PHYSICS OF COATING TENSIONED-WEB OVER SLOT DIE

A DISSERTATION

SUBMITTED TO THE FACULTY OF THE GRADUATE SCHOOL

OF THE UNIVERSITY OF MINNESOTA

BY

Eungsik Park

IN PARTIAL FULFILMENT OF THE REQUIREMENTS

FOR THE DEGREE OF

DOCTOR OF PHILOSOPHY

L. E. Scriven, M. S. Carvalho, Advisers

November 2008

Contents

List of figure

List of Tables

Chapter 1

Introduction

1.1. BACKGROUND

Coating deposited in liquid form and then solidified is basic technology being used in many industries, of which example ranges from plastic packaging to up-to-date semiconductor and display devices. Coating can perform many functions, whether optically, chemically, electrically, magnetically or mechanically, as they are required in various applications.

Numerous methods have been invented for depositing a liquid film on a substrate according to the properties of coating liquid, the thickness, structure and quality of the coated layer, the nature of the substrate, and the speed of the process.

In some mature industry, coating is already well-established technology. But still, they are trying to improve their processes for better quality and better productivity, because even small improvements can lead to big reductions in production cost.

Today's fast developing industries are driving advances in coating technology toward thinner coating, strict coating thickness control, and structured multi-layers. Magnetic storage media, for instance, are growing explosively in storage density and the manufacturers are developing new coating processes for thinner and multi-layered coating. A thinner magnetic layer is necessary for higher storage density and soon the thickness will reportedly be as thin as 40nm solidified. Even if the wet coating as deposited is 25 times as thick, i.e. 1μm, that will be a record for a fast and continuous manufacturing process. Coatings for optical properties are good examples of applications requiring strict thickness control on the scale of the wavelength of light, because thickness is most crucial factor for their functions.

As technology evolves, the number of applications where several coating layers are needed grows. More and more functions are demanded of a single product and it gets impossible to perform all of the functions adequately in a single layer: the way out is to apply several layers. Furthermore multilayer coating can make functions possible that are impossible in single layer. For example a thin enough single layer which cannot be coated at all can be coated by simultaneous two-layer coating with relatively thicker second layer.

Coating processes are necessarily followed by solidification step, in which the microstructure of the coating is determined. Microstructure of coated layer plays crucial role in determining its property. Simultaneous mutilayer coating followed by drying may give enhanced properties ranging from simple interlayer adhesion enhancement to some advanced nanostructure.

1.2. ELASTOHYDRODYNAMICS IN COATING SYSTEM

Constant coating gap, the clearance between the substrate and coating head, is one of the most important process conditions to ensure the coating uniformity. For example, in conventional slot die coating, where a substrate to be coated is backed by a roll of big radius, if there is a periodic gap variation between backup roll and slot die uniform coating is hard to obtain; gap variation in fixed gap slot coating usually comes from roll run-out or dynamic behavior of the bearing of backup roll.

As technologies advance and diversify, more and more applications require thin coating layer; applications of optical films and magnetic storage tapes are good examples. Importance of constant coating gap grows as coating thickness becomes thinner. The conventional approach, which relies on precision machining for thin and constant gap, reached its limitation. One of the possible solutions to overcome this difficulty is the use of elastohydrodynamics, the interaction between elastic force and hydrodynamic force.

Several examples of elstohydrodynamic coating system include die coating, tensioned web roll coating, and tensioned web slot die coating, of which deformable parts are backup roll made of elastic material in the die coating system and flexible web in tensioned web coating systems (Fig. 1-1). Beside the small gap clearance, one of the main advantages of elastohydrodynamic coating systems is that the small gap clearance is made possible with cheap cost. The

needs for expensive precision machining of rolls, bearing and dies are reduced.

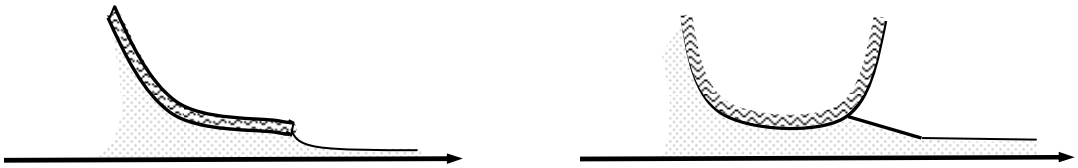

(a) Flexible blade coating (b) Membrane coating

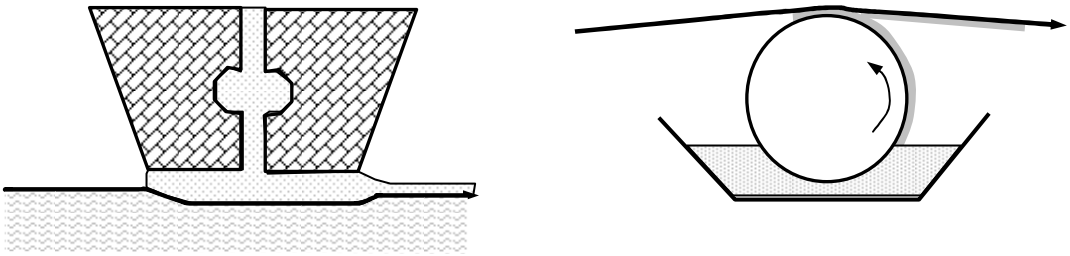

(c) Die coating (d) Tensioned web roll coating

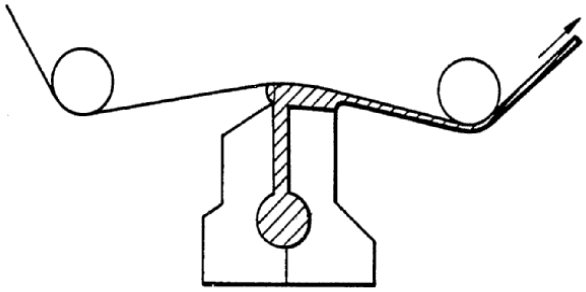

(e) Tensioned web slot die coating

Fig. 1-1. Elastohydrodynamic coating system

Tensioned web slot coating is special among the elastohydrodynamic coating system in that it is pre-metering coating method and that two layer coating is

possible. Tensioned web slot coating is strong candidate for the future applications requiring thin and structured layered coating.

1.3. SLOT COATING

Slot die coating method is one of the premier pre-metered coating methods in use today. Pre-metered methods deposit a specified layer thickness by delivering liquid at a controlled rate to a moving substrate; *if* the resulting layer is uniform, its thickness is simply the volume flow rate divided by the substrate width and speed. Fig. 1-2 is a cross-section of typical slot coater, showing upstream lip, downstream lip, feed gap between the two lips, and back-up roll bearing substrate. Flexible substrate in the form of extremely long sheet that is stored and transported in rolls, then unwound to process and wound up again, is called web. Coating liquid issues from feed gap and forms what is called the coating bead in the space between lips and substrate, or web. The coating bead is bounded by web, die lips, two curved air-liquid interfaces or menisci, and three contact lines in which the air/liquid interfaces meet the lip surfaces and web surface. In projection a contact line is a point as in Fig. 1-2. At the dynamic contact line the liquid first wets the moving web and the meniscus there makes apparent dynamic contact angle with the web. The other two are static contact lines where upstream and downstream menisci meet the stationary slot die lips. The static contact lines may move freely along the slot die lip surfaces, or pin on them, depending on lip shape and the operating parameters.

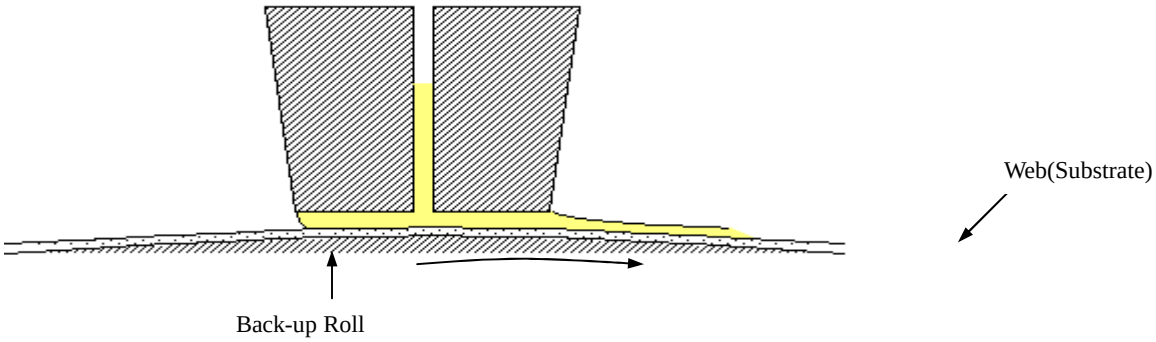

Fig. 1-2. Schematic of single layer slot coater.

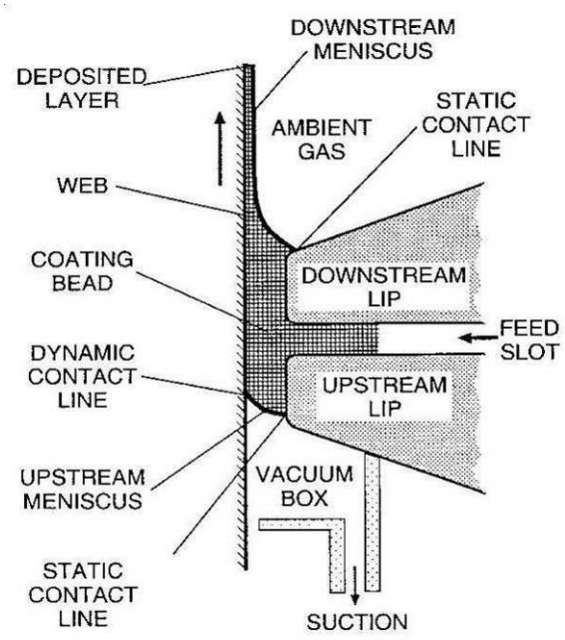

Fig. 1-3. Single-layer slot coating flow. (From Gates 1999; after Sartor 1990)

A slight vacuum is often applied to the upstream meniscus as is shown in Fig. 1-3 in order to produce a pressure difference across the bead that makes faster, uniform coating possible. Beguin (1954) was the first who used the vacuum box upstream of the slot die. He reduced the pressure of the gas in the upstream meniscus to make positive pressure gradient through the coating bead. Beguin

claimed that this pressure difference across the coating bead delays the coating liquid from entraining air bubble to higher speed and holds the bead in position against the moving web.

The coating bead can be maintained only in a particular range of pressure difference across the bead. With quasi-static lubrication theory, Ruschak (1976) and Higgins and Scriven (1981) analyzed why the coating bead requires these pressure differences to maintain a stable bead. Ruschak made the simplified analysis by assuming that the viscous effects in the bead are negligible and that the pressure difference in the bead is caused solely by capillary effects. Higgins and Scriven included viscous effects by separating the bead into two distinct rectilinear flows; one upstream of the feed slot and the other downstream of it. In these two regions, the flow is a superposition of obligatory Couette flow and Poiseuille flow, and the pressure drop due to viscous effect can be simply calculated by lubrication approximation of slider bearings. These analyses provided not only reasonable coating window diagrams but also some insight on the coating bead behavior.

Coating window is a parameter space within which the coated film is free of unacceptable defects. The typical examples of parameters that determines the state of slot coating include vacuum pressure, web speed, coating thickness, and the other operating and physical variables. Fig. 1-4 shows coating window predicted by Higgin's visco-capillary model. The dotted line is the result when viscous effects are neglected. The coating window is a parallelogram bounded on right by an optimal film thickness (Higgins 1980):

$$\frac{1}{h_{opt}} = \frac{1.34}{d_d}\left(\frac{\mu V_w}{\sigma}\right)^{-\frac{2}{3}} \qquad (1\text{-}1)$$

The top and bottom boundaries are the pressure difference bounds set by capillary effect. The solid line represents the case viscous effect is included. The viscous effect distort the total pressure drop shifting the window upward to a slightly greater pressure difference, whereas in the greater coating thickness region the pressure drop should be small because the action of Poiseuille flow have to assist the Couette flow instead of opposing it.

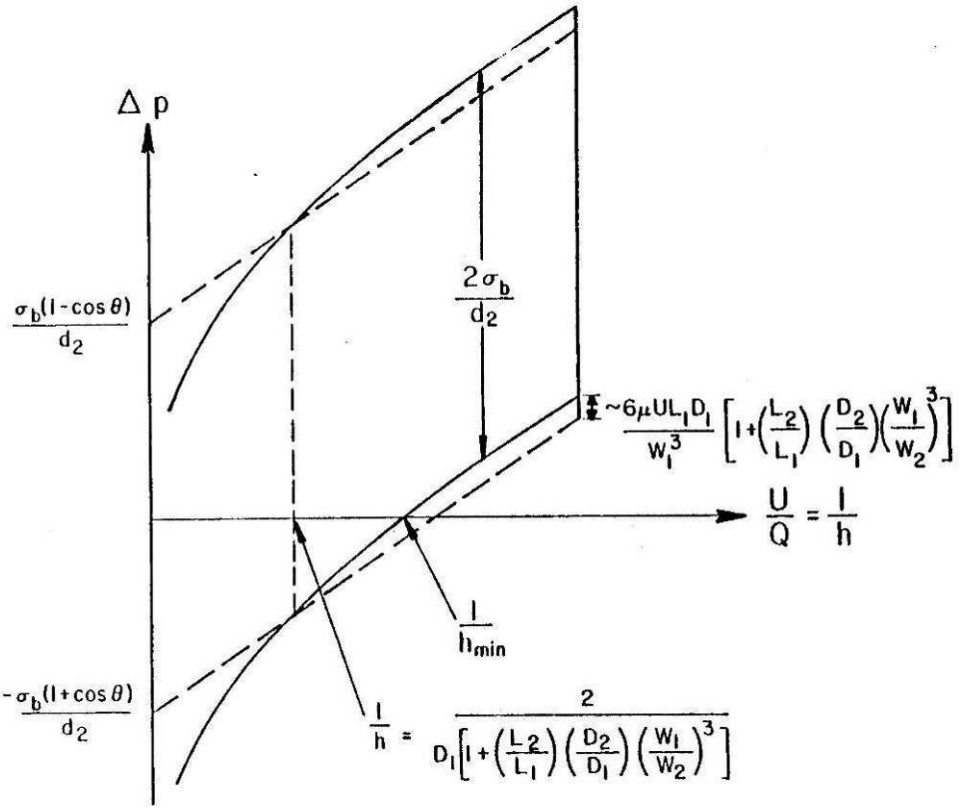

Fig. 1-4. Allowable operating region for a visco-capillary coating bead with upstream meniscus pinned (adapted from Higgins (1980)).

The next major contribution to the slot coating was made by Sartor (1990). He is the first who try flow visualization to identify when and where recirculations appear in the bead. He observed a variety of microrecirculations and measured contact line positions and angles and the shapes of upstream and downstream menisci. Following Silliman (1979), he used Galerkin's method with finite element basis functions to solve the Navier-Stokes equation system for steady, Newtonian, two-dimensional free surface flows in the slot coating bead. The dynamic contact angle was measured from experiment to be used in the calculation. The calculation result based on the theoretical model showed good agreement with that of visualization experiment. The calculated velocity fields and streamlines measured from visualization, agreed well those observed in the flow visualization. He found many recirculations inside the coating bead, which is undesirable for stable coating operation in the visualization experiments and theoretical calculation.

Recirculations were classified into four kinds; in the feed slot, under the downstream die lip, on the downstream die shoulder, and under the upstream die lip. Recirculation on the downstream die shoulder (Fig. 1-5(d)) occurs when liquid occupies the surface of die shoulder. In this case the recirculation is usually accompanied by a contact line that is not straight, which causes non-uniform coating layer thickness. Recirculation under the downstream die lip (Fig. 1-5(c)) is most common. Simple rectilinear flow theory predicts recirculation under the downstream lip, when the coating thickness is less than one-third of the

downstream gap and recirculation under upstream die lip is predicted to be when coating thickness is less than $\frac{4}{27}$ of upsteam gap; Sartor's experiments validated this prediction. Sometimes a recirculation is present just inside the feed slot (Fig. 1-5(e)). Sartor showed through his theoretical analysis with the Navier-Stokes system that the feed slot recirculation appears when the coating thickness is less than approximately one-fifth of the slot gap:

$$h_\infty < 0.2\, h_f$$

These recirculations can interweave with each other in combination - and fusion - as shown in Fig. 1-5.

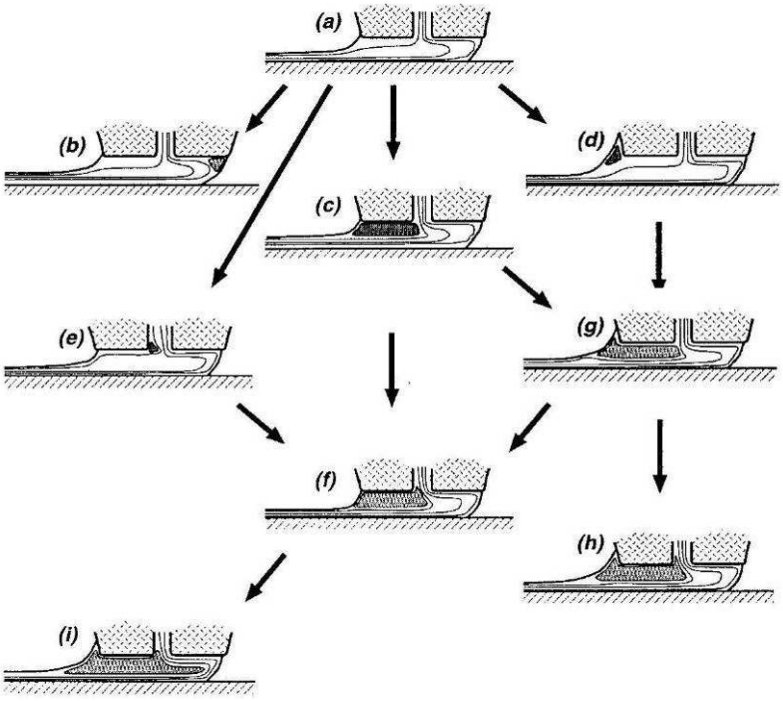

Fig. 1-5. Map of vortices observed in the single layer slot coating bead (adapted form Sartor 1990).

Whereas Sartor concentrated on situations where die lips are parallel to substrate so that the upstream and downstream gaps are uniform and equal, Gates (1999) in his experiments with interchangeable lips observed the effects of different gap configurations. In general, shorter die lips and convergent downstream lip (Fig.1-6) permitted higher web speed and thinner coated layer than uniform gap and longer lips. Gates also made theoretical predictions of steady state with both the one-dimensional lubrication approximation and the two-dimensional Navier-Stokes system, which he augmented with analysis of stability to small perturbation and of response to time-periodic disturbances. In the analysis with Navier-Stokes system using pseudo arc-length continuation to explore the parameter space, turning points marked limits on the possible parameter space to give operating windows, which agreed well both with the flow visualization results and the results from one-dimensional approximate model. The dynamic contact angle data used in the analysis was measured in the visualization.

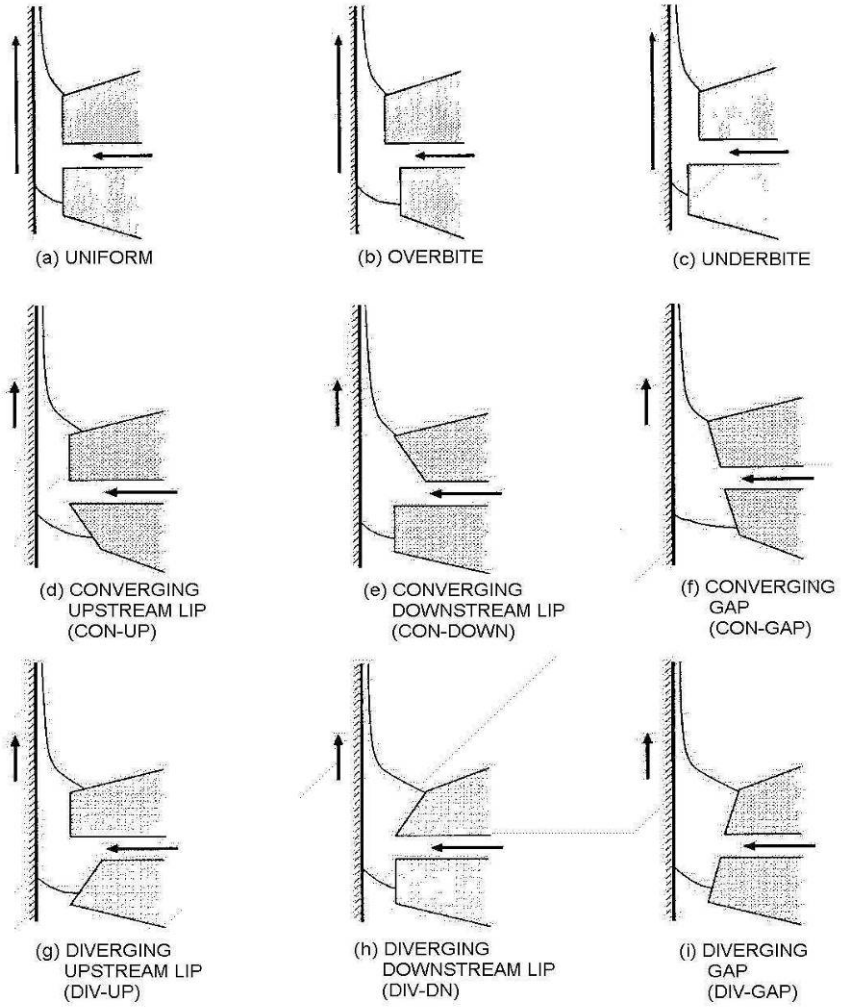

Fig. 1-6. Die geometries used in Gates' experiments.

Overbite configuration (Fig.1-6), a convergent downstream gap configuration, and a knife-edge configuration in place of downstream lip (the shortest in lip length considered) were predicted to make coating bead stable against the three-dimensional perturbation than uniform and underbite configuration, diverging downstream lip, and flat downstream lip configuration, respectively. These configurations make it possible to raise the speed at which the break-up occurs when other conditions are fixed, which means minimum coating thickness can be

lowered because higher speed can be achieved before bead breakup.

When the web speed is too high or the vacuum is too low, upstream meniscus recedes to the feed slot and encroaches on it, which leads to bead breakup from the upstream. But bead breakup can occur at the downstream in the fast web speed or low feeding rate provided that the vacuum applied in the upstream meniscus is strong enough, which is called “low-flow limit”. The minimum coating thickness is obtained near this condition. Low-flow limit can be predicted by viscocapillary analysis of Ruschak (1976) in low capillary number flow.

Kheshgi and Carvalho (2000) found that the minimum coating thickness in high capillary number flow is different from the value predicted by viscocapillary theory. They analyzed the low-flow limit in slot coating by solving Navier-Stokes system equation and compared the result with experimental value. In the low-flow limit condition, the downstream meniscus recedes into the coating bead followed by bead breakup from downstream, but according to Kheshgi and Carvalho the momentum of liquid tend to counteract this receding action of downstream meniscus as inertia effect becomes significant. Fig. 1-7 shows their experimental result and the coating windows predicted by viscocapillary theory. In high capillary number region, i.e. high inertia regime, coating window was larger than the prediction of viscocapillary model but well explained by viscous boundary layer theory. When the web speed is high, the viscous boundary layer inside the bead grows slowly to make the coating thickness thin. In this flow regime, coating thickness is also affected by the length of the bead.

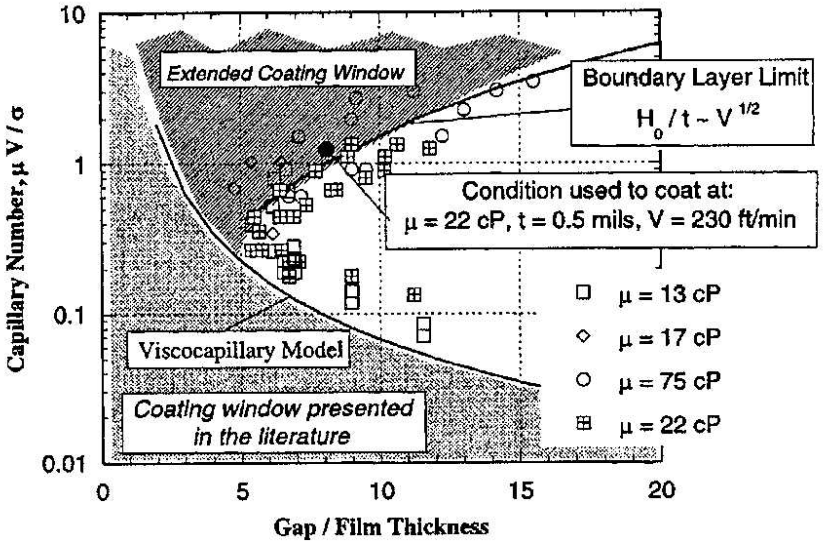

Fig. 1.7. Experimental result of minimum coating thickness as a function of capillary number and coating windows predicted by viscocapillary theory.

1.4. COATING TENSIONED WEB OVER SLOT DIE

In tensioned web slot coating there is no back-up roll; instead the web under tension moves over the lips and slot of the die and is slightly bent over them. In other words the web wraps slightly the die as shown in Fig. 1-8. In successful operation the normal stress resultant that tends to drive the web into contact with the die surface is countered by the force of the pressure field that develops in the gap.

Tensioned web slot coating is similar to the conventional slot coating, in that pre-metered liquid issues from the slot into the gap between the die lip and the substrate which carries liquid away as a layer coated on it. But tensioned web slot die coating has several advantages over conventional slot die coating, which needs a back-up roll. Moreover the surface of the backup roll must turn precisely through a circle in order to maintain a fixed gap.

Fig. 1-8 illustrates the typical arrangement of tensioned web slot coating. Two idler rolls support the moving web, which is under tension. Between them, the slot coating head comprising two lips (three in two-layer coating) and feed slot is pushed against the moving web, so that it makes a certain angle with the web. The normal force arises from the resultant of the tension in the curved substrate, which balances hydrodynamic forces exerted by the flowing coating liquid. The moving web, die lips and the viscous coating liquid in the clearance between web and lips constitute an elastohydrodynamic system, and the balance of forces in

this system enables thin uniform liquid layer to be coated. In this arrangement, no precision back-up roll is needed, and less precise positioning of die may be acceptable, i.e. thinner coating becomes possible at relatively small cost.

Instead of vacuum upstream of the coating head, often parameters such as web tension and web's incidence and departure angles can manage the pressure profile in tensioned web coating system. The geometries of die lip have bigger effect on controlling the pressure profile than in the case of conventional slot die coating.

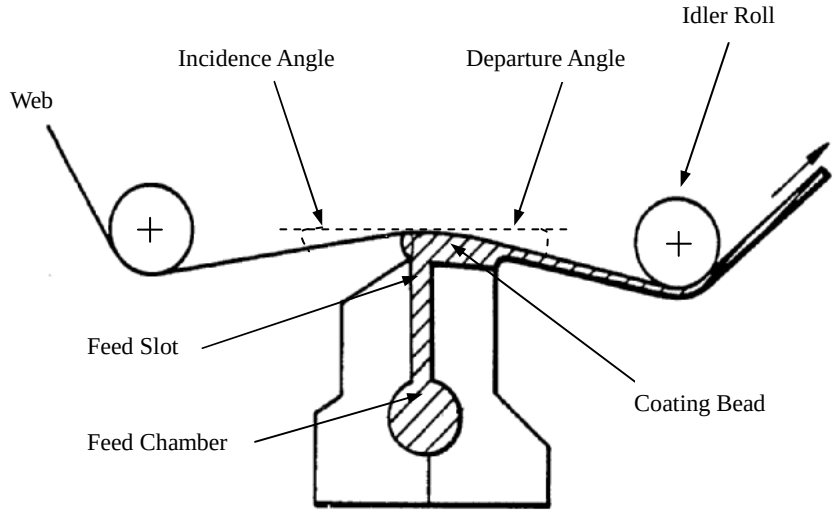

Fig. 1-8. Schematics of typical tensioned web slot coating (Chino et al. 1988)

The incidence and departure angle of the web makes wrap around die, in which gap height is sustained by elastohydrodynamic force balance between pressure and the web tension. One of the benefits of the tensioned web coating system is the flexibility: different operation conditions can be accommodated by relatively simple change of operation conditions.

Tensioned web slot coating was originally developed for thin, uniform layers of shear-thinning magnetic suspension. The technology subsequently advanced to simultaneous deposition of two layers. Magnetic storage media remain the chief application. The two-layer coating was a major innovation that overcomes certain technical and economical dilemmas: an extremely thin top layer that could not be applied as single layer was coated simultaneously with a relatively thick bottom layer to get the best technical compromise among electromagnetic and mechanical performances.

The major developments of tensioned web slot coating were made by the magnetic memory industry beginning in the early 1980's. The unique features that distinguish this technology from conventional slot coating have evolved through modification of die lips. Various shapes of the die lips designed to act in concert with the wrap of the tensioned web, are the subjects of the leading patents on single-layer coating in the 1980's. It was Pipkin and Schaefer (1979) who first described a slot coating system having the die pushed against a tensioned web without backup roll (Fig. 1-9). They showed a V-shaped die having acute angles between die lip surfaces and shoulders, and a rounded upstream edge of the downstream lip to prevent trapping of particles. They incorporated several design factors from conventional slot coating, but they didn't show how to manage pressure profile by manipulating tension force.

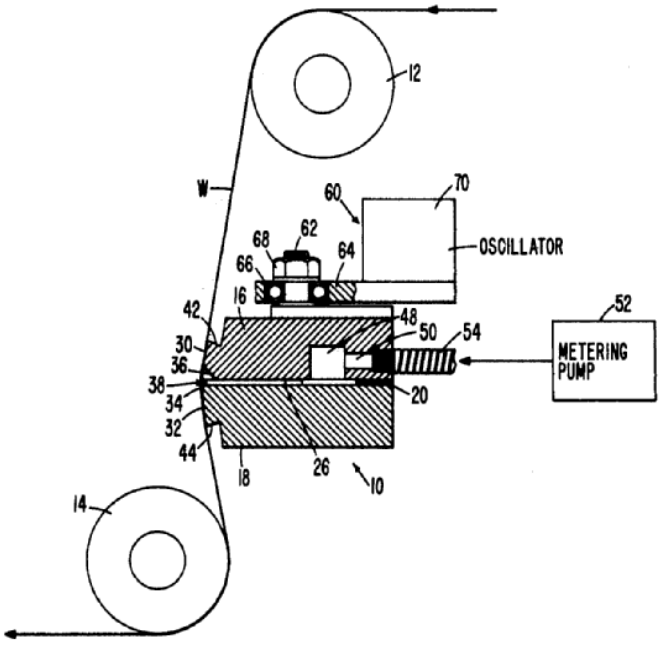

Fig. 1-9. Schematic of Pipkins and Schaefer's (1979) tensioned-web slot coating.

Subsequently, a variety of patents on tensioned-web slot coating appeared. The important issues in the claims of these patents are preventing recirculation in the coating bead and protecting the die lip surfaces from damage. According to them, when the recirculation exists in the bead, foreign materials are easily trapped and stuck, which can cause damage to and contamination of the lip surface. Both can have direct impact on the uniformity of coating, most often by causing long streaks deficient in particles or in thickness. Most of these patents claimed better designs of die lips for uniform coating at higher speeds. Topics other than lip design include surface hardness of the die, treatment of slot side edge, viscosity of liquids, and so on. A variety of lip shape was claimed in the

patents, but clear explanation about why that shape is good was hard to find. Several patents are introduced in the following section with brief explanations.

Several die designs in the patents are illustrated in Fig. 1-10. Among them, (a) and (b) have angled surfaces in the middle of the lip. These angled salients, when pushed against the tensioned web, make it curve over them and thereby cause a higher normal stress resultant toward the surface, which produces smaller gap and high pressure around the salient. High pressure in coating bead is good for high speed coating, whereas too smaller gap is not: in high speed coating these angled surfaces are easy to be attacked by unexpected foreign particles and to be chipped, which have direct effect on uniformity of coating. To overcome this problem, smooth surface die shape was claimed (Fig. 1-10).

In most patents on tensioned web slot die shapes the claims are expressed in terms of angles, radius of arc, or polynomial equations describing the surface shape. All those are eventually ways of expressing the radius of curvature of the die surface as a function of distance along the surface. That function controls the distribution of normal force induced by the curvature of the tensioned web, as it passes over the die.

The incidence web angle and the shape of upstream die lip determine the upstream wrap force, and likewise the departure web angle and the downstream lip shape determines the downstream wrap force. Incidence angle affects the pressure in the upstream air layer, which is unfavorable to delay bead breakup. Capability of adjusting incidence web angle brings flexibility to the other process conditions (Fig. 1-10(d)). Detailed discussion on the pressure build-up in

upstream air layer was put in Chapter 4.

The pressure distribution along the die surface is determined not only by die shape, but also by the process conditions, namely incidence and departure angles of the web, web tension, and the rheological property of coating liquid.

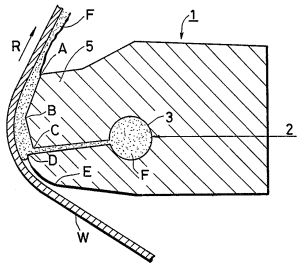

(a) Tanaka et al. (1984b).
USP 4480583

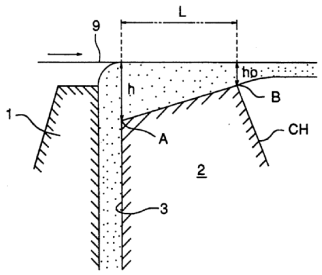

(b) Yoshida (1994).
USP 5318804

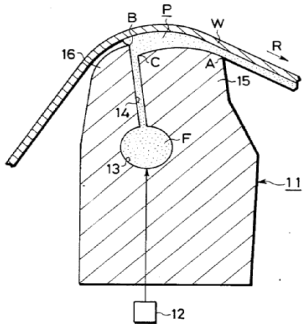

(c) Shibata et al.(1987).
USP 4681062

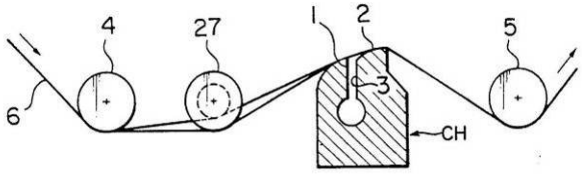

(d) Tobisawa et al. (1991).
USP 5042422

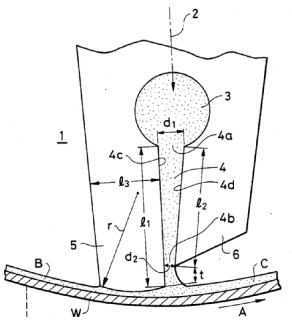

(e) Shibata et al. (1990)
USP 4907530

Fig. 1-10. Die shapes for single-layer tensioned web slot coating shown in patents.

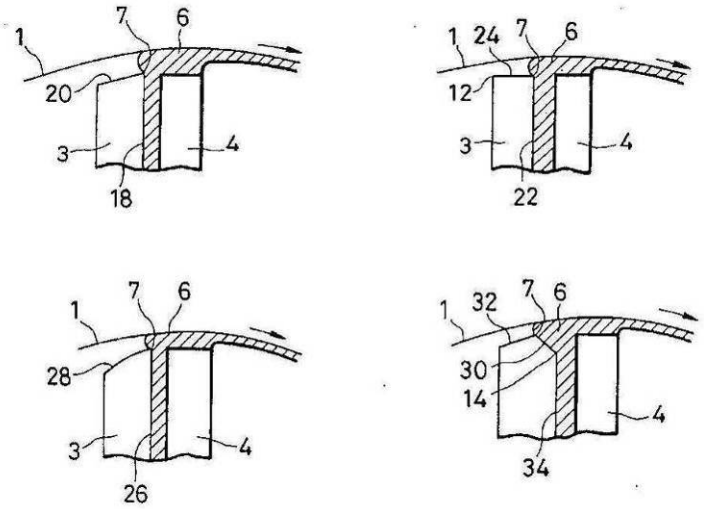

(a) Good downstream meniscus location

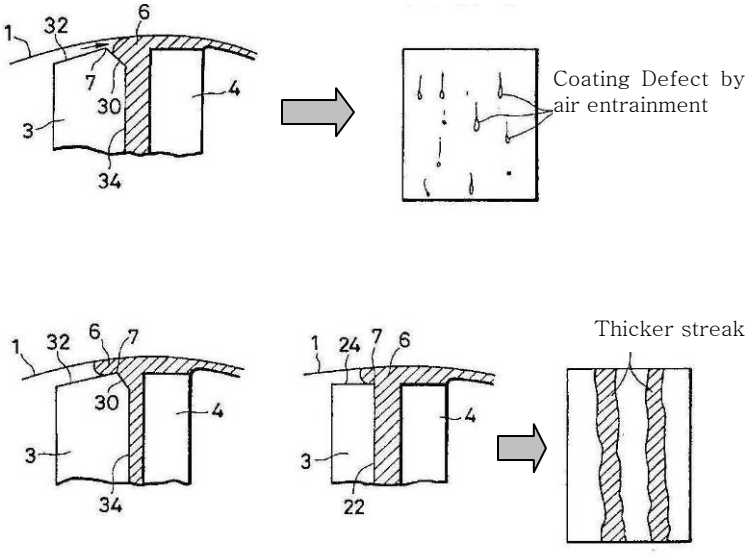

(b) Bad downstream meniscus location

Fig. 1-11. Downstream meniscus location and resultant coating qualities (Shibata et al. 1988).

Shibata et al. (1988) claimed based on the lots of experimental experience,

that the upstream meniscus should be located at the feed slot corner of the upstream lip as shown in Fig. 1-11(a). According to their patent, if meniscus is receded to the feed slot the upstream air invades to cause defects on the coated layer, and on the contrary, if the meniscus advanced to the surface of the upstream lip coating uniformity will be deteriorated by thick streak.

In some patents, use of tension force is different. Patents of this kind deal with web carrying a pre-coated layer and describe a knife-edge shaped downstream lip in under-bite configuration. Making the downstream lip a knife-edge makes the coating bead stabilized against breakup according to the findings of Gates (1999). This arrangement is shown in Fig. 1-10 (e). This configuration can be regarded as conventional slot die coating with a very narrow downstream gap, much narrower than can be maintained in conventional slot coating hardwares. Narrow gap height is kept stable by the difference between the heights of upstream lip and downstream lip. Instead of vacuum in conventional slot coating, air attack from the upstream side is effectively blocked by upstream die lip and the pre-coated liquid layer. This type of coating is called “wet-on-wet coating”.

Despite the practical importance of the tensioned web coating system, only one theoretical study has been published in the literature. Feng (1998) analyzed the flow in the coating bead by solving the Navier-Stokes system by means of Galerkin’s method with finite element basis function. Mechanical behavior of the web he treated by membrane theory (Flűgge 1973) in which flexural rigidity, bending and twisting moments are neglected. With these arrangements, Feng

succeeded in calculating reasonable pressure profiles and showed how they are changed by altering process conditions such as web tension, incidence angle and departure angle. He showed that gap height of tensioned web coating system, i.e. the local distance between the web and the die surface, is regulated automatically by the action of elasto-hydrodynamics, i.e. the interaction between the normal stress resultant of the tensioned web and the viscous stress and the pressure in the liquid of the coating bead, when feed rate of liquid is changed, or equivalently the final coating thickness is changed. But only one of the die lip shapes described by Tanaka et al. (1984) was studied in his work, and he didn't consider the effect of the upstream air layer.

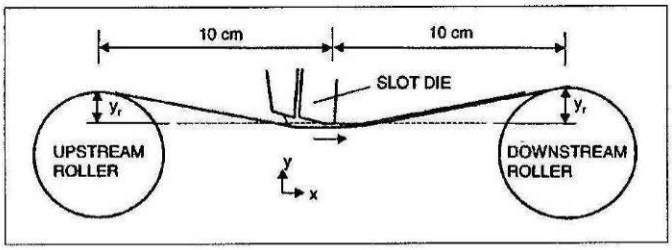

(a) Tensioned web slot coating system studied by Feng

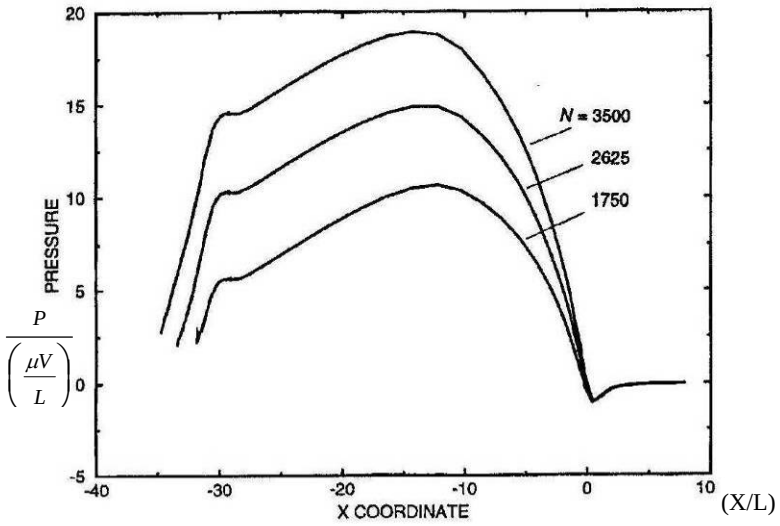

(b) Pressure distribution in coating bead corresponding to web tension at 1,750, 2,625 and 3,500 (N/(μV))

Fig. 1-12. Coating a web tensioned over a slot die as modeled theoretically by Feng (1998); and his prediction of the pressure distribution in the coating bead along the die. (L= size of feed slot; V=web speed, μ=viscosity of liquid).

Lee (2001) studied the die shape effect in tensioned web slot die coating system experimentally by visualizing the coating beads from the top side and observed bead breakup behavior in various conditions. He recorded the minimum thickness possible varying upstream wrap angle and downstream wrap angles using circular shape slot die lip. He found that higher total wrap angle with

higher departure angle is good for delaying bead break-up. Several kind of lip designs were tested in 3° symmetric wrap angle, among wh ich flat shaped lip was found to be good for maintaining bead in high speed to make a thinner coating layer.

1.5. TWO LAYER COATING

As technology evolves, the number of applications where several coating layers are needed grows. More and more functions are demanded of a single product and it gets impossible to perform all of the functions adequately in a single layer: the way out is to apply several layers. In the past, layers were often coated in tandem, i.e. the second layer was deposited on the surface of first layer which had already been dried. This is not only expensive, because the capacities of facilities must be doubled or their productivities halved, but is also unfavorable with respect to the quality. The surface of the product is exposed to the production process, which can inflict damage to it.

The alternative is to apply all the layers simultaneously and solidify them together. Tensioned-web coating is an attractive option for coating two layers simultaneously. One of particular features of the tensioned-web slot coating is that it can make one of the layers to be exceptionally thin. It is the magnetic recording media industry that makes best use of the capacity of tensioned-web slot coating system, coating thin top layer; thin top magnetic layer enables high

recording density. Fujifilm announced that they had developed, using a two-layer tensioned-web slot coating process, a high-recording-density magnetic media tape of which the recording density had been only possible through a metal-evaporating deposition process; the coating thickness of the top magnetic layer of the tape was said to be 0.2 micron. Moreover according to their recent announcement, they have advanced their technology so that they can coat even thinner layer by a factor of ten.

Though not even a single fundamental study on two-layer tensioned-web slot coating has been published, while a lot of patents were claimed on it, many fundamental principles found in conventional two-layer slot coating, which shares lots of features in common, are thought to be valid in two-layer tensioned-web slot die coating system.

Cohen (1993) analyzed the bead of two-layer slot coating with a uniform gap by means of a simple rectilinear flow model. He neglected effects of capillary pressure in the menisci and worked out equations that predict limits of operation, the location of interlayer and separation line. The interlayer is a thin diffusion zone that separates the bulk of the two liquid layers. This zone is the result of the interdiffusion between the two miscible liquids, which is the usual in simultaneous multiplayer coating. The interdiffusion destroys the interfacial character of liquid-liquid interface, thus there’s no interfacial tension. The interlayer begins at the separation line on the solid wall where the velocity is zero. Cohen also visualized slot coating flows with same methods used by Sartor. He succeeded in observing the sequence of flow patterns, recirculations, location of interlayer and separation

lines as the flow rates of the two layers, their viscosity ratio, and the vacuum pressure applied at the upstream meniscus were varied. Increasing vacuum pressure tended to pull the interlayer upstream, and in the low vacuum, the interlayer separated from the downstream corner (Fig. 1-13). He also observed that the less viscous layer as the upper layer tended to lead to ribbing, which implies that coating with the more viscous layer on top is the more stable configuration.

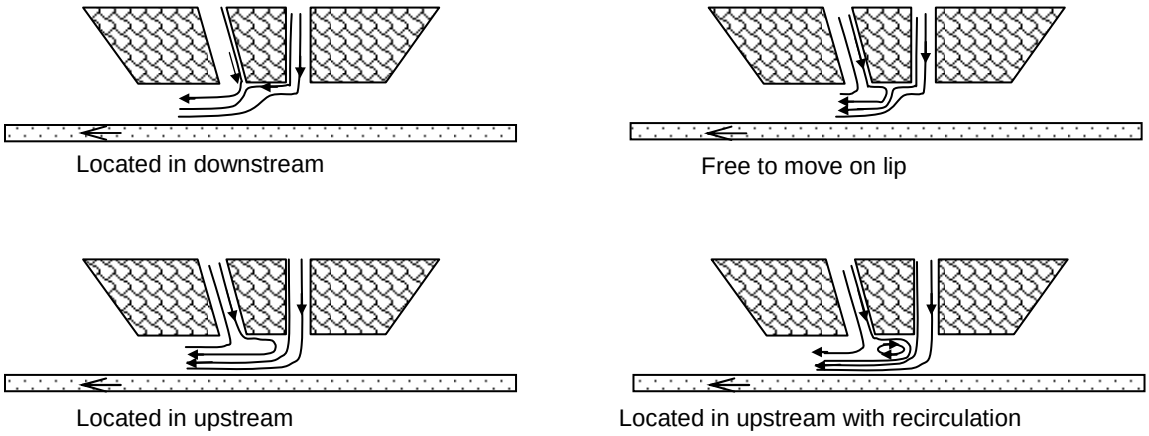

Fig. 1-13. Flow pattern observed in the intermediate section (from Cohen 1993)

Sartor et al. (1996, 1998) in their patents described in some detail a multilayer slot coater and how to control the pressure gradients in the coating bead. To achieve “stable two-dimensional flow in coating bead, they claimed that the recirculations that can appear under the intermediate and downstream lips should be avoided and that the separating streamline should be pinned at the

downstream edge of the intermediate lip, which they called stability point, as shown in Fig. 1-14. To pin the separating streamline at the stability point, Sartor et al. adjust the geometry so that the positive pressure gradient under the intermediate lip is avoided. Fig. 1-14 shows the die geometries Sartor et al. reported for stable two-layer coating.

They also claimed that the clearance between the intermediate lip and web, called the intermediate gap, should be twice the bottom layer thickness and that the downstream gap should be less than twice the total thickness of the top and bottom layers. This is to avoid the recirculation which will lead to the mixing of the two layers.

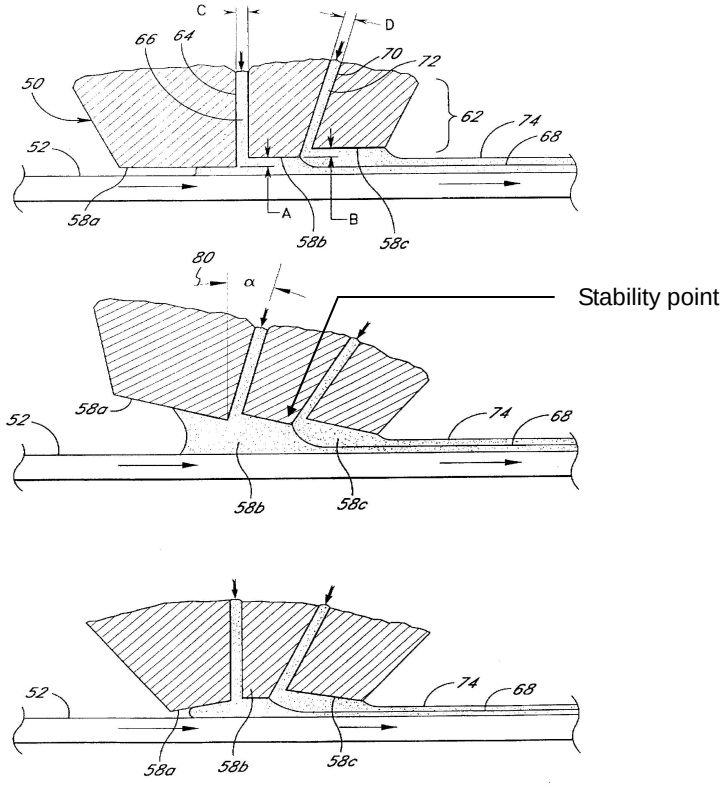

Fig. 1-14. Schematics of two layer slot coating lip configurations by Sartor et al. (1998)

Musson(2001) analyzed two-layer slot coating by solving Navier-Stokes equation system with Galerkin's method and finite element basis functions. The two-dimensional model was coupled with arc-length continuation methods to trace out steady state solution path in the parameter space. Each steady state solution was checked for its stability and sensitivity to perturbations. He also made visualization experiment from which the results are shown in Fig. 1-15 with the result of theoretical prediction of his model. The dotted line in Fig. 1-15 shows the operation window prediction from the viscocapillary model (Cohen 1990), which shows good agreement with experimental data.

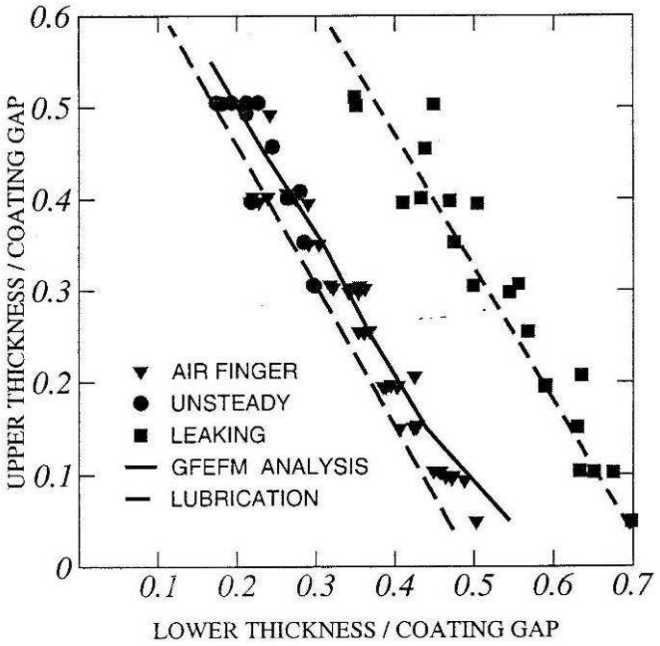

Fig. 1-15. Theoretical predictions and experimental determination of the low flow limit of the operation in two-layer slot coating. Conditions: Viscosity ratio=1; P_{vac}=0; Re=2; Ca=0.4. (from Musson 2001).

In the study of one parameter, the viscosity ratio(upper layer viscosity over lower layer viscosity), Musson found that only a limited range of viscosity ratio could be accommodate by the pressure difference between the downstream ambient air and the upstream vacuum chamber pressure. If the viscosity ratio was raised too much, the upstream meniscus moves toward upstream lip end and at above the upper limit of viscosity ratio, meniscus invades the vacuum chamber. If the viscosity ratio was lowered too much, the upstream meniscus moves forward to the region under the lower-layer feed slot and at above the lower limit of the viscosity ratio the bead became unstable to the three-dimensional disturbances. His frequency response showed that the most detrimental disturbance in the two-layer slot coating is the fluctuation of coating gap and that the system becomes more sensitive to the coating gap disturbance as the top layer viscosity rises. In a two-parameter study, he tried to keep the upstream meniscus in same position as changing viscosity ratio, by manipulating other parameters, e.g. the upstream vacuum pressure and checked the stability and sensitivity of the system to the disturbances. He found that the system becomes unstable to the three-dimensional perturbation and sensitive to the coating gap disturbances as the top layer viscosity falls.

Patents on the multi-layer tensioned slot coating began with that of Chino et al. (1989) most of the subsequent patents on tensioned web slot coating dealt with multi-layer coating. Fig. 1-16 (a) shows the die design of Chino et al. (1989).

They claimed that if the upper layer coating quantity C2 is larger than that of bottom layer coating quantity C1, the radius of curvature of the downstream lip surface R2 should be bigger than the radius of curvature of intermediate lip surface R1. On the contrary, when C2 is sufficiently lower than C1, R1 may be smaller or larger than R2, but the difference between R1 and R2 should be small: -3mm $\leq$R2-R1$\leq$15mm. If R2 is too big, air bubble will be infiltrated to the upper layer. If R2 is too small, coating bead will overflow to the downstream lip edge.

The die shapes have become smoother since the salients in the lip may make the larger gap height in a certain operation condition, and can cause recirculation, which is the biggest danger in separate two-layer coating. Takahashi et al. (1995) claimed that the height difference between downstream lip surface and intermediate lip surface should be small: 5μm$\leq$ t $\leq$30μm (Fig. 1-16 (b)). According to their experiment, the smaller height difference than 5μm will cause entrapment of foreign particles, and the larger height difference than 30 μm will disturb the interlayer of the flows.

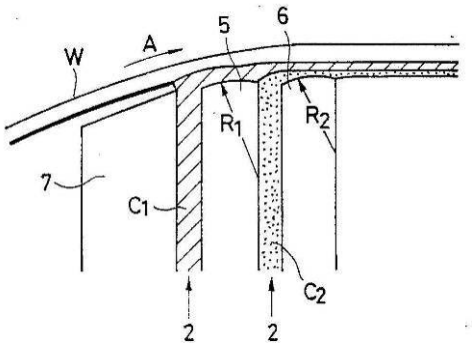

(a) Chino et al. (1989)

USP 4854262

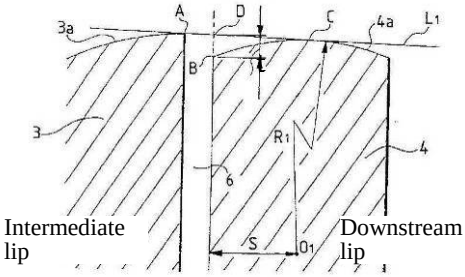

(b) Takahashi et al. (1995)

USP 5384162

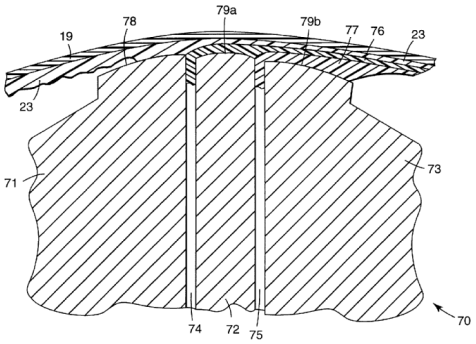

(c) Kistler et al. (2000)

USP 6033723

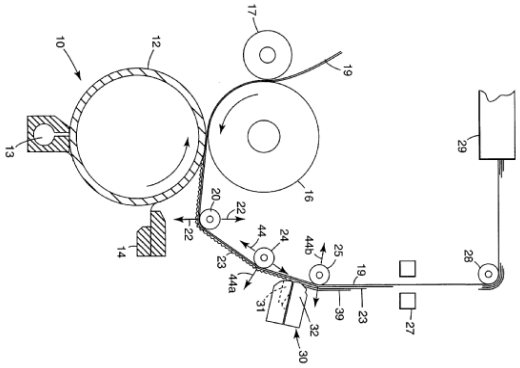

(d) Kistler et al. (2000)

USP 6033723

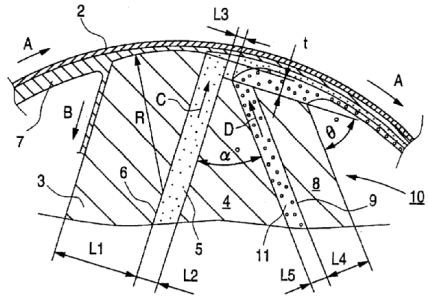

(e) Tomaru et al. (1997)

USP 5677004

Fig. 1-16. Die shapes of tensioned web slot die for multi-layer coating shown in patents.

Chapter 2

Foil Bearings:
Back-Pressured and Forward-Pressured

2.1. INTRODUCTION

A foil bearing consists of a thin and flexible sheet, strip, web, or foil running over a cylinder, which is also called a spindle, and entraining a thin lubricating layer of fluid between foil and cylinder. The thickness of the entrained fluid film, a classical subject of elastohydrodynamics, is decided by a force balance between the pressure in the lubrication layer and elastic force from the curved and tensioned foil. Understanding the foil bearing is useful in designing many industrial devices such as magnetic tape recording systems, web handling processes, etc. Researches related with elastohydrodynamics of the foil bearing were reviewed by Muftu (2005).

The first publication on the foil bearing seems to be that of Blok and van Rossum (1953). They conducted an experiment with a cellophane foil stretched round a journal and oil as lubricant. The result from their experiment agrees well

with their theoretical prediction based on the assumption that the film thickness over the angle of wrap is constant. Eshel and Elrod (1965) in their paper solved, by numerical integration, the elastohydrodynamics of the foil bearing consisting of lubrication flow approximation for the incompressible lubricant flow and membrane theory for the foil deformation with boundary conditions from asymptotic foil shape. They divided the calculation zone into entrance region and exit region and solved the gap profiles of each zone with boundary conditions from three asymptotic foil shapes; two from asymptotic shapes of the foil, flat lines, in far upstream and far downstream and one from asymptotic configuration of the foil in the center of foil bearing, uniform clearance between foil and cylinder. Their approach led to the following expression for the height of the gap clearance in uniformity zone:

$$h_m = 0.6430 r_0 \left(\frac{6\mu V}{N} \right)^{2/3} \qquad \text{(2-1)}$$

Here h_m is the thickness of the gap where the pressure gradient is zero; r_0 is the radius of the cylindrical spindle; V is the speed of foil; μ is the viscosity of the fluid; and N is the tension of the foil.

Barlow (1967) solved the same equations set as Eshel and Elrod(1965), but he solved for the gap profiles of both entry and exit zones simultaneously with boundary conditions derived from given wrap angle. He checked effect of wrap angles and found that the coefficient in Eq. (2-1) hold constant value of 0.643 when wrap angle is big enough—dimensionless wrap angle, $B = \frac{\beta}{2}\left(\frac{6\mu V}{N} \right)^{-1/3}$ is

bigger than 5, where β is wrap angle in radians. He also showed that the coefficient in Eq. (2-1) should change as wrap angle is reduced; when B is smaller than 0.5, the deviation from the prediction of Eq. (2-1) exceeds 10%.

Renshaw (1999a) presented an approximate analytical solution of the classical foil bearing problem by using the first few terms of a scaled exponential power series and deciding the scale constant by minimizing the residual numerically in the least square sense. The approximate solution produced by this approach differed by no more than 7.6% from the result of Eshel and Elrod (1965).

Beside the papers on the classical foil bearing, many others dealt with the compressibility of lubricant, stiffness of the foil, effect of asperity of the foil or cylinder, and porosity of the foil using one-dimensional or two-dimensional elastohydrodynamic models. But no study was published about the effects of pressure upstream and pressure downstream of the foil bearing that differed from ambient pressure on the exposed side of the foil. Understanding the effects of such pressure differences upstream and downstream is critical to dealing with related elastohydrodynamic systems like tensioned-web slot die coating, where the action of a narrow coating gap that facilitates thin coating is an elastohydrodynamics one almost identical to that of the foil bearing. Hence study of foil bearings provides bases for understanding such systems.

In this chapter, two theoretical models of pressured foil bearing are descrived. One is the classical one-dimensional elastohydrodynamic model of the foil bearing, the equation system of which was solved by Galerkin’s weighted residual method with finite element basis functions. The solution space of this

equation system was explored by arc-length continuation to study the effects of pressure differences upstream and downstream of the narrowest part of the gap. The second theoretical model is new and is based on approximating a foil bearing as consisting of three asymptotic zones. This model's prediction of h_m, the gap in a certain place in the uniform zone where the lubricant flow is a pure Couette type, is less accurate than that of Eq. (2-1) because the approximations in each asymptotic zone do not hold true in the short intervals between zones (see section 2.5). But this model is helpful in building systematic insights on the structure of foil bearing and the effect of downstream pressure of foil bearing.

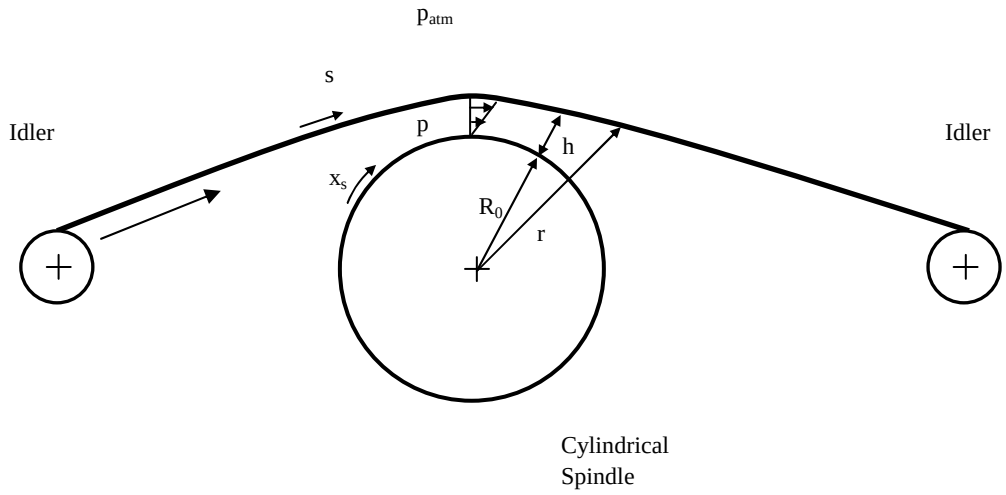

Fig. 2-1. Schematic of foil bearing. p, h, and r are the pressure, gap, and foil position profiles along the foil. s is the arc length spanning along the foil. R_0 is the radius of the cylinder.

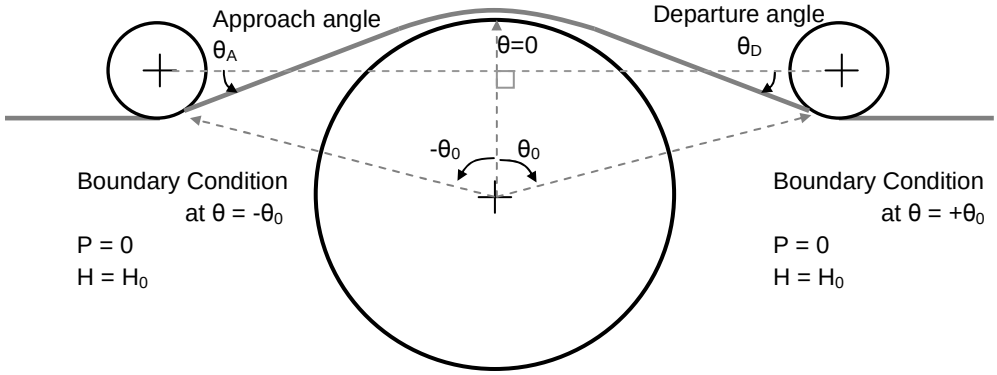

Fig. 2-2. Boundary conditions. Approach angle and departure angle of the foil are defined as angles between the straight line asymptotes to the foil and the horizontal line which connects the centers of the idlers.

2.2. ELASTOHYDRODYNAMIC DESCRIPTION OF THE FOIL BEARING.

Shell theory describes the deformation of a flexible web provided it is wide enough that the deformation in the cross-web direction is negligible [Flügge 1973]. If the tangent direction at a point is denoted s, and arc length is too, conservation of momentum leads to two force balance equations and one moment-of-momentum balance equation:

$$\frac{dN_s}{ds} - \kappa_s Q_s + P_s = 0 \qquad (2\text{-}2)$$

$$\frac{dQ_s}{ds} - \kappa_s N_s + P_r = 0 \qquad (2\text{-}3)$$

$$\frac{dM_s}{ds} - Q_s = 0 \qquad (2\text{-}4)$$

κ_s is the sole curvature of the cylindrical shell; P_s and P_r are external loads per unit area in the tangential direction s and the normal-to-the-shell direction r, respectively; P_s is viscous shear stress and P_r's pressure difference across the shell, i.e. the foil bearing. The normal stress resultant in tangential direction, N_s, is called web tension. Q_s is transverse shear stress resultant acting on a plane normal to the tangential direction. M_s is bending moment about cross-web direction.

If the web is described by Hook's elasticity law and the standard Kirchhoff-Love

assumptions about the deformation (e.g. Pranckh 1989) are adopted, the bending moment, M_s is simply related to the curvature along the web profile.

$$M_s \cong -K\kappa_s \tag{2-5}$$

K is the flexural rigidity defined as

$$K \equiv \frac{Et^3}{12(1-\nu^2)} \tag{2-6}$$

E is the elastic Young's modulus of the web, t is thickness of web, and v is its Poisson ratio.

With Eqs. (2-4) and (2-5), $Q_s = -K\frac{d\kappa_s}{ds}$. Eqs. (2-3) and (2-4) become

$$\frac{dN_s}{ds} + \kappa_s K\frac{d\kappa_s}{ds} + P_s = 0 \tag{2-7}$$

$$-K\frac{d^2\kappa_s}{ds^2} + \kappa_s N_s - P_r = 0 \tag{2-8}$$

Usually web tension is the dominant force in the foil bearing, so that the tangential load in tangential direction, P_s, can be ignored. In this case Eq.(2-7) becomes

$$N_s = -\frac{1}{2}\kappa_s{}^2 K + N_0 \tag{2-9}$$

N_0 is the web tension when the curvature of web is not deformed. Eq. (2-9) combines with force balance in the normal to the shell surface, Eq. (2-8), to yield

$$-K\frac{d^2\kappa_s}{ds^2} + \kappa_s\left(-\frac{1}{2}\kappa_s{}^2 K + N_0\right) - P_r = 0 \tag{2-10}$$

Curvature in cylindrical coordinate is

$$\kappa_s = \frac{2(\frac{dr}{d\theta})^2 - r\frac{d^2r}{d\theta^2} + r^2}{\left((\frac{dr}{d\theta})^2 + r^2\right)^{3/2}} \tag{2-11}$$

When the radial load across the shell is the pressure difference across it, the force balance in normal direction to the shell, Eq. (2-10), becomes

$$-K\frac{d^2\kappa_s}{d\theta^2}\left(\frac{d\theta}{ds}\right)^2 + \kappa_s\left(-\frac{1}{2}{\kappa_s}^2 K + N_0\right) - \Delta p = 0 \tag{2-12}$$

where $\frac{\partial s}{\partial \theta} = \sqrt{r(\theta)^2 + r'(\theta)^2}$, $\Delta p = p - p_{atm}$ (2-13)

Flows in the lubricating layer which flows through a narrow passage are described by the Reynolds equation of incompressible steady flow of a Newtonian flow:

$$\frac{\partial}{\partial x_s}\cdot\left(\frac{hV}{2} - \frac{h^3}{12\mu}\frac{\partial p}{\partial x_s}\right) = 0 \tag{2-14}$$

Here h is gap between the surfaces of foil and spindle, p is the pressure in the lubricating layer, V is the speed of the foil, μ is viscosity of the lubricating layer, and x_s is arc length along a given reference surface. The terms inside the bracket in the Reynolds equation are the flow rate of the lubrication flow, q.

$$q = \frac{hV}{2} - \frac{h^3}{12\mu}\frac{\partial p}{\partial x_s} \tag{2-15}$$

In foil bearing analysis the reference surface of the lubrication equation is chosen to be cylinder surface and x_s is arc length coordinate along the cylinder surface, so that $x_s = R_0\theta$, where R_0 is the radius of the cylindrical spindle, and θ is

a angle measured from the vertical coordinate line passing the center of spindle and perpendicular to the horizontal line connecting centers of the idlers [see figure 2-2]. When cylindrical coordinate are taken as the base coordinate system for calculation and measure the gap clearance, h, between the foil and the cylinder surface is measured in radial direction:

$$h = r - R_0 \tag{2-16}$$

Eqs. (2-11), (2-12), (2-15) and (2-16) are the system of equations that describe elastohydrodynamics of foil bearing.

The base coordinate system for calculation was chosen to be a polar coordinate system because the lubricant flows on the cylindrical surface and is described most efficiently by polar coordinate. The origin of the coordinate is set on the center of cylindrical spindle, and angle zero is set to be perpendicular to the horizontal line connecting the centers of idlers.

Boundary conditions on this system come from the idlers. The point at which foil departs from upstream idler or, arrives at the downstream one, was set as passage point. For simplicity in calculation, when the approach angle or the departure angle changes, the idler is assumed to move on prescribed path so that the angular coordinate of passage point is unchanged. In this chapter, only symmetric configurations of idlers and spindle were considered; i.e., the distances between the center of idlers and that of spindle are same.

$$p(-\theta_0) = p_{up} \tag{2-17}$$

$$r(-\theta_0) = r_0 \tag{2-18}$$

$$\kappa(-\theta_0) = \frac{p_{up}}{N} \quad (2\text{-}19)$$

$$p(\theta_0) = p_{Down} \quad (2\text{-}20)$$

$$r(\theta_0) = r_0 \quad (2\text{-}21)$$

$$\kappa(\theta_0) = \frac{p_{down}}{N} \quad (2\text{-}22)$$

where θ_0 is angle of right idler position measured from the vertical coordinate line at which θ is zero, r_0 is distance between the origin and the passage point at given wrap angle, and p_{down} and p_{up} are the pressures relative to that of ambient set at downstream passage point and upstream passage point respectively.

2.3. THREE-ASYMPTOTIC-ZONE MODEL.

Looking at the pressure profiles along the flow passage of foil bearings, one might try to approximate the foil bearing as consisting of three asymptotic regions over each of which the pressures is nearly uniform; those are an virtually uniform gap zone in the middle, an upstream zone, and a downstream zone to each side. The pressure profile is not uniform in short transition intervals between the different regions. The characteristics of each zone allow gap profiles to be expressed in simplified equations whose solutions can be matched at appropriate matching locations. This produces a simpler theoretical model for the total gap profile of foil bearing.

The upstream and downstream parts of three-asymptotic-zone model

presented here are similar to those in Langlois' approach (1963), which he developed to analyze an almost flat foil bearing with zero wrap angle. To build a model which can describe a foil bearing of non-zero wrap angle, Langlois' model is divided into upstream zone and downstream zones, between which a uniform zone is inserted [Figure 2-3].

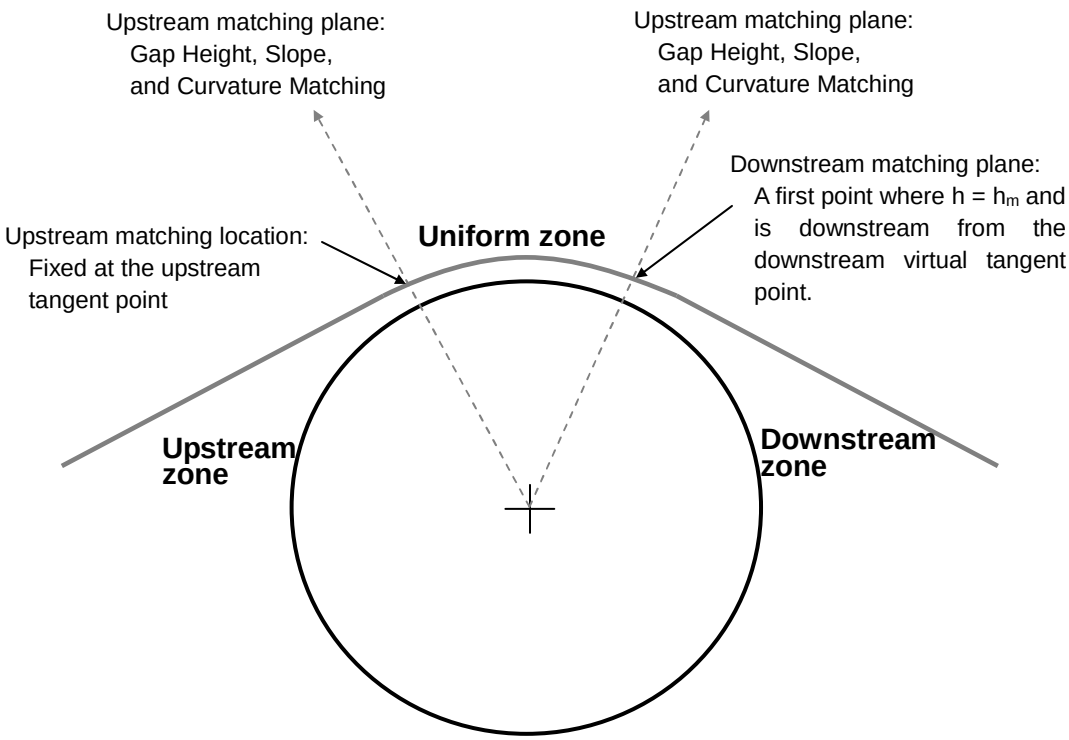

Fig. 2-3. Dividing a foil bearing into three asymptotic zones. Gap clearances, foil slopes, and curvatures of the two adjacent zones are matched in an upstream matching plane and a downstream matching plane.

Uniform zone

In the uniform gap zone, almost uniform and high pressure arises to counterbalance the normal tension-resultant force from the tension in the curved foil. Based on this asymptotic condition of almost uniform pressure, the gap profile, which is measured in radial direction, can be linearized around the h_m, the gap clearance at a certain point of the almost uniform pressure part in the middle. The system equations of elastohydrodynamics are simplified to produce a closed form solution as Eshel and Elrod (1965) and successors did.

When a foil is so thin that the flexural rigidity becomes negligible, Eq. (2-12) becomes:

$$N\kappa_s = \Delta p \tag{2-23}$$

When gap clearance h and $\frac{\partial h}{\partial s}$ are much smaller than R_0, Eq. (2-23) can be approximated by

$$N\left(\frac{1}{R_0} - \frac{\partial^2 h}{\partial s^2}\right) = \Delta p \tag{2-24}$$

Substituting p in Eq. (2-15) with Eq. (2-24), noticing that $q = \frac{h_m V}{2}$, and nondimensionalizing variables with $\varepsilon_6 \equiv \frac{6\mu V}{N}$, $\tilde{h} \equiv \frac{h}{h_m}$, and $\xi \equiv \frac{s\varepsilon_6^{1/3}}{h_m}$, gives

$$\frac{\partial^3 \tilde{h}}{\partial \xi^3} = \frac{1-\tilde{h}}{\tilde{h}^3} \tag{2-25}$$

When the gap profile doesn't differ much from h_m, i.e., $\tilde{h} \cong 1$, Eq. (2-25) can be solved giving general solution of the following form,

$$\tilde{h}(\xi) = 1 + C_{m1} * e^{-\xi} + C_{m2} * e^{\frac{\xi}{2}} * Cos[\frac{\sqrt{3}}{2}\xi + C_{m3}] \qquad (2\text{-}26)$$

where C_{m1}, C_{m2}, and C_{m3} are integration constants. Eq. (2-26) shows that $\tilde{h} = 1$, or $h = h_m$ in one or more isolated points due to the growing undulation that the last term in Eq. (2-26) makes.

$\bar{h}_{mid}$ is the gap height profile in uniform zone expressed in units of R_0. $\bar{h}_m$ is the gap height in units of R_0 when $\frac{\partial P}{\partial s} = 0$.

$$\bar{h}_{mid}(s) = \frac{\tilde{h}(s) h_m}{R_0} \qquad (2\text{-}27)$$

$$\bar{h}_m \equiv \frac{h_m}{R_0} \qquad (2\text{-}28)$$

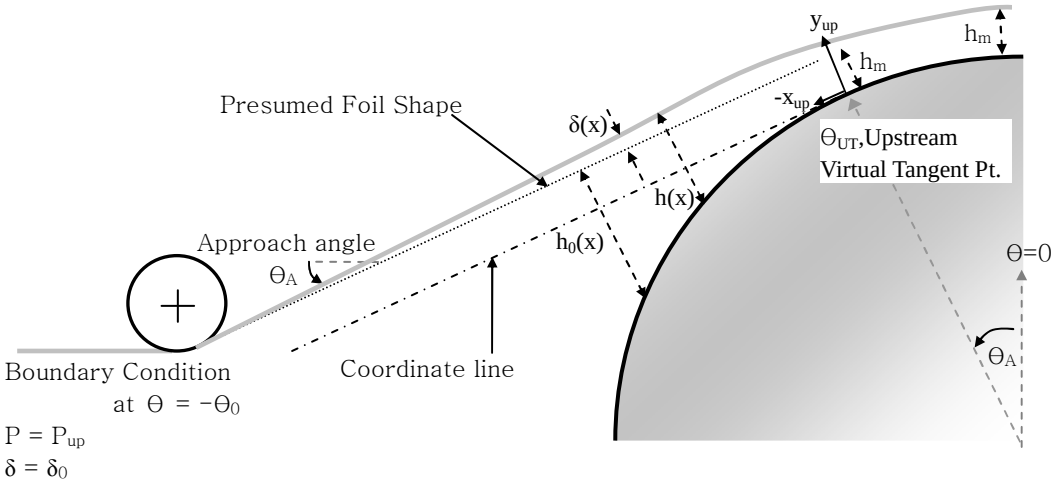

Fig. 2-4 Definition of gap clearance to the asymptotic foil shape, deviation from it, and arc length coordinate x in upstream asymptotic zone.

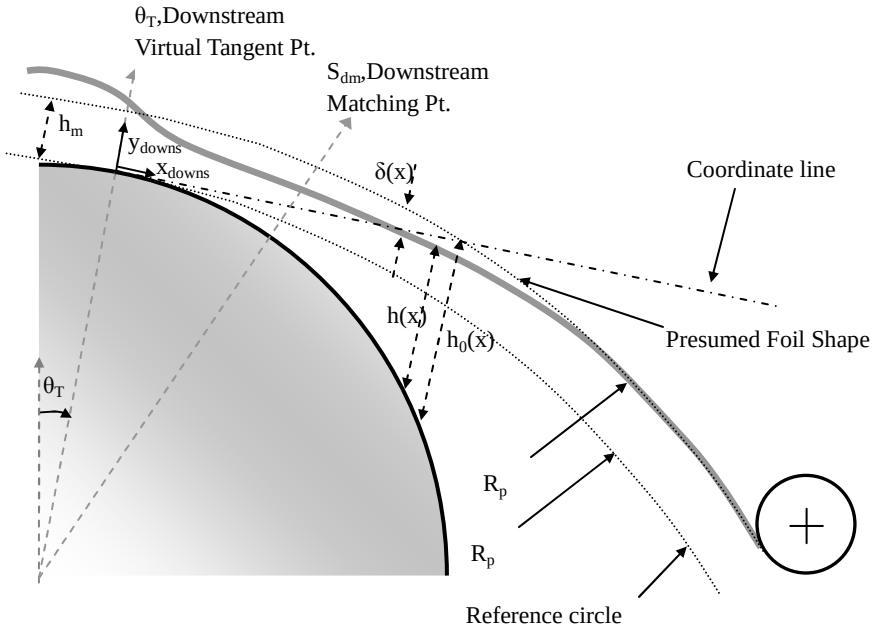

Fig. 2-5 Definition of gap clearance to the asymptotic foil shape, deviation from it, and arc length coordinate x in downstream asymptotic zone of back-pressured foil bearing.

Upstream zone and downstream zone

In most of the upstream and downstream zones, the gap is so wide that the pressures there are virtually constant. Hence, if the imposed pressure upstream or downstream is ambient, the asymptotic foil configuration there is a straight line. However, if pressure is not ambient, the foil takes a shape of an arc of circle to balance the pressure difference with its normal stress resultant.

Whatever the asymptotic shapes of the upstream and downstream zones, straight or arc of circle, they must be almost tangent to the cylindrical spindle; actually they are not quite tangent to the spindle because of the thin lubrication layer of fluid between it and the foil. Near the spindle the asymptotic foil shape is unknown because the thickness of lubrication layer, h, is unknown. So it is useful to define “presumed foil shape”, a convenient choice close to the asymptotic foil shape. The presumed foil shape is chosen to be an arc of circle which has the radius decided by pressure difference upstream or downstream, passes through the passage point, and has the radial distance of h_m from the spindle at virtual tangent point, which is defined as a point at which the presumed foil shape would osculate with the spindle if the distance between the arc of circle and the spindle is zero.

The base coordinates for upstream zone and downstream zone, shown in Fig. 2-4 and Fig. 2-5 respectively, are chosen to be rectangular coordinates that are

defined to have origins at the upstream virtual tangent point and downstream virtual tangent point, respectively, and to have abscissas running along the tangent lines which become tangent to the cylinder surface at each virtual tangent point.

Because the pressure in each zone is virtually uniform except in the narrow length near the tangent point, the foil shape doesn't deviate much from the asymptotic shape elsewhere in the upstream zone and elsewhere in the downstream zone. Actual foil shape can be effectively described with linearized equations for deprarture from the presumed foil shape, as follows.

Figure 2-4 and figure 2-5 show how coordinates, x_{up} and x_{down}, and deviation from the presumed foil shape, δ, are defined. The gap heights and δ are measured in the direction perpendicular to the coordinate line. By definition, gap clearance is the sum of the presumed gap, $h_0(x)$, and the deviation $\delta(x)$:

$$h_i(x) = h_{0,i}(x) + \delta_i(x) , \qquad \text{i = up, down} \qquad (2\text{-}29)$$

The radius R_p of the asymptotic foil shape, an arc of circle in general case, was found from Eq. (2) by setting curvature to be the inverse of R_p. The equations of circles for the downstream presumed foil shapes and θ_T, the locations of the downstream virtual tangency, are found from the conditions that the arcs should pass through the foil's downstream passage point and be tangent to the cylindrical spindle.

In the same manner the equation of a circle for the upstream presumed foil shape and θ_{UT}, the locations of the upstream virtual tangency, can be found. But

the analyses of three-asymptotic-zone model in this study is limited to the cases with ambient upstream pressure because non-ambient upstream pressure destroys the virtual uniformities of pressure and gap profile in the uniform zone [see figure. 2-10] and limits the use of Eq. (2-26). In these cases, the downstream virtual tangent point in polar angle coordinate coincides with the upstream web angle of the web.

The gap between presumed foil shape and cylinder is measured in a perpendicular direction to the coordinate line. This distance can be approximated by means of the parabola that osculates the circular arc at x = 0, i.e., at the virtual tangent point:

$$h_{0,i}(x) = h_m + \frac{x^2}{2R_{mean,i}} \qquad \text{i = up, down} \qquad (2\text{-}30)$$

R_{mean} is a geometric mean of R_p and R_0:

$$\frac{1}{R_{mean,i}} \equiv \frac{1}{R_0} - \frac{1}{R_{p,i}} \qquad \text{i = up, down} \qquad (2\text{-}31)$$

An overbar on a length variable designates that it is non-dimensionalized in units of R_0.

$$\overline{h}_{0,i}(x) \equiv \frac{h_{0,i}}{R_0} \qquad \text{i = up, down} \qquad (2\text{-}32)$$

$$\overline{R}_{p,i} \equiv \frac{R_{p,i}}{R_0} \qquad \text{i = up, down} \qquad (2\text{-}33)$$

$$\bar{x} \equiv \frac{x}{R_0} \qquad \text{(2-33-a)}$$

When δ is much smaller than h_0, Eq. (2-15) becomes

$$\frac{dP_i}{d\bar{x}_i} = \varepsilon_6 \left(\frac{1}{\bar{h}_{0,i}(\bar{x})^2} - \frac{\bar{h}_m}{\bar{h}_{0,i}(\bar{x})^3} \right) \qquad \text{i = up, down} \qquad \text{(2-34)}$$

where $P \equiv \frac{(p - p_{atm})}{N / R_0}$. Eq. (2-34) was integrated with the boundary condition

$P = P_i = 1/R_{p,i}$ at $\bar{x} = \pm\infty$ (2-35)

The position of the idler is far enough from the virtual tangent point in the foil bearing that Eq. (2-35) can be considered to be true in passage points.

Integrating Eq. (2-34) with boundary condition Eq. (2-35) gives the pressure profile in downstream zone:

$$P_{down}(x_{down}) = \frac{1}{R_{p,down}} + \varepsilon_6 \left(\begin{array}{l} -\dfrac{\pi}{8\sqrt{2}h_m^{3/2}\sqrt{1-\dfrac{1}{R_{p,down}}}} - \dfrac{x_{downs}}{\left(2h_m + (1-\dfrac{1}{R_{p,down}})x_{downs}^2\right)^2} \\ + \dfrac{x_{downs}}{4h_m\left(2h_m + (1-\dfrac{1}{R_{p,down}})x_{downs}^2\right)} + \dfrac{ArcTan[\sqrt{1-\dfrac{1}{R_{p,down}}}\, x_{downs} / \sqrt{2h_m}]}{4\sqrt{2(1-\dfrac{1}{R_{p,down}})}h_m^{3/2}} \end{array} \right)$$

(2-36)

Bars are suppressed in Eq. (2-36) and in the following equations.

As mentioned above, the upstream pressure is limited to the ambient because the three-asymptotic-zone model in this chapter is valid only with ambient upstream pressure; with non-ambient upstream pressure, Eq. (2-26) is no longer valid because the upstream pressure causes, in the gap of the uniform zone, a Poiseuille flow contribution that increases or decreases the lubricant flow and the gap in the uniform zone, which weakens the assumption of Eq. (2-26), $\tilde{h} = 1$. This is discussed in detailed in next section. The upstream pressure profile is obtained by integrating Eq. (2-34) again for the upstream with boundary condition, $P_{up} = 0$ at $\bar{x} = -\infty$ is

$$P_{up}(x_{up}) = \varepsilon_6 \left(\frac{\pi}{8\sqrt{2}h_m^{3/2}} - \frac{x_{up}}{\left(2h_m + x_{up}^2\right)^2} + \frac{x_{up}}{4h_m\left(2h_m + x_{up}^2\right)} + \frac{ArcTan[x_{up}/\sqrt{2h_m}]}{4\sqrt{2}h_m^{3/2}} \right) \quad (2\text{-}37)$$

When P is small or when the deviation from the presumed foil shape is only significant within the narrow length from the virtual tangent point—the second condition is generally effective in the back-pressured foil bearing because the significant length for calculating foil shape deviation from the presumed foil shape reduces as the downstream pressure rises—Eq. (2-23) is approximated by

$$\frac{1}{R_{p,i}} - \frac{d^2\delta_i}{dx^2} = P_i(x) \qquad \text{i = up, down} \qquad (2\text{-}38)$$

See appendix 2-B for a detailed derivation of Eq. (2-38).

Integrating this twice with the downstream pressure profile, Eq. (2-36), yields the foil deviation:

$$\delta_{down}(x_{down}) = C_{d3} + C_{d2}x_{down} + \varepsilon_6 \left(\begin{array}{l} \dfrac{x_{down}}{8h_m(1-\dfrac{1}{R_p})} + \dfrac{\pi x_{down}^{\ 2}}{16\sqrt{2}h_m^{\ 3/2}\sqrt{1-\dfrac{1}{R_p}}} \\ -\dfrac{ArcTan[x_{down}\sqrt{1-\dfrac{1}{R_p}}\Big/\sqrt{2h_m}]}{4\sqrt{2h_m}}\left(\dfrac{3}{(1-\dfrac{1}{R_p})^{2/3}} + \dfrac{x_{down}^{\ 2}}{2h_m\sqrt{1-\dfrac{1}{R_p}}} \right) \end{array} \right) \quad \text{(2-39)}$$

Here C_{d2} and C_{d3} are integration constants.

Upstream pressure in the present analysis with three-asymptotic-zone model is ambient, which makes the $R_{p,up} = \infty$—an ambient upstream pressure makes flat upstream presumed foil shape, of which the radius of curvature is infinite. The same integration of Eq. (2-38) with the upstream pressure profile, Eq. (2-37), gives

$$\delta_{up}(x_{up}) = C_{u3} + C_{u2}x_{up} + \varepsilon_6 \left(\frac{x_{up}}{8h_m} - \frac{\pi x_{up}^{\ 2}}{16\sqrt{2}h_m^{\ 3/2}} - \frac{ArcTan[x_{up}\Big/\sqrt{2h_m}]}{4\sqrt{2h_m}}\left(3 + \frac{x_{up}^{\ 2}}{2h_m} \right) \right) \quad \text{(2-40)}$$

where C_{u2} and C_{u3} are integration constants. Substitution of Eq. (2-39) or Eq. (2-40) into Eq. (2-30) completes gap clearance profiles.

Solution Procedure

To obtain the overall gap profile, it is necessary to find unknown h_m and seven integration constants, C_{m1}, C_{m2}, C_{m3}, C_{u2}, C_{u3}, C_{d2} and C_{d3} in Eq. (2-26), Eq. (2-

39), and Eq. (2-40). Equations needed to solve for the unknowns come from boundary conditions and matching conditions. [See Table 1]

Gap heights, slopes, and curvatures of the three asymptotic zones were matched at two matching planes. As shown in figure 2-3(b) the upstream zone and the uniform zone were matched at the upstream matching plane, and the uniform zone and the downstream zone were matched at the downstream matching plane. The upstream matching point was chosen to be the virtual tangent point of the upstream presumed foil shape, which was reasonable enough because the foil shape deviation was tiny in the conditions of this study. Moreover, the calculation result was pretty insensitive to the location of upstream matching point once it is near the virtual upstream tangent point. The downstream matching point location needs to be downstream of the downstream virtual tangent point since near the downstream virtual tangent point there is a wiggle, which is a typical of foil bearing and is better described by the sinusoidal term in Eq. (2-26). The location of downstream matching plane was chosen to be a point which is downstream of the downstream virtual tangent point and the first point at which the clearance is h_m. To guarantee the matching location between downstream zone and uniform zone to be positioned appropriately, the location of downstream matching point, s_{dm}, was solved for as an unknown in addition to the other eight unknowns listed above by setting the gap height at the matching point to be h_m. The location of upstream matching point was chosen to be the upstream virtual tangent point of the presumed foil line on the cylinder.

9 unknowns	9 Equations	
C_{m1}	Boundary Condition	Eq. (2-41)
C_{m2}	Boundary Condition	Eq. (2-42)
C_{m3}	Downstream matching conditions:	
C_{u2}	Height matching	Eq. (2-46)
C_{u3}	Slope matching	Eq. (2-47)
C_{d2}	Curvature matching	Eq. (2-48)
C_{d3}	Upstream matching conditions:	
h_m	Height matching	Eq. (2-43)
s_{dm}	Slope matching	Eq. (2-44)
	Curvature matching	Eq. (2-45)
	At downstream matching point	$h_{mid}(s_{dm}) = h_m$

Table 1. Unknowns and equations in three-asymptotic-zone model.

Boundary conditions fill two equations among the nine equations needed for solving for the unknowns. At both passage points the deviations from the presumed foil shapes are taken to be zero:

$$\delta_{up}(-x_0) = 0 \qquad (2\text{-}41)$$

$$\delta_{down}(x_0) = 0 \qquad (2\text{-}42)$$

x_0 is the position of passage point on the downstream idler in downstream coordinate.

The other six equations are from matching conditions; gap clearances, slopes, and curvatures must match in both the upstream and downstream matching planes.

Since upstream matching position is at the tangent point, the equations of matching gap height, slope, and curvature are straightforward.

$$\bar{h}_{mid}(\theta_A) = \bar{h}_{up}(0) \tag{2-43}$$

$$\bar{h}_{mid}'(\theta_A) = \bar{\delta}_{up}'(0) \tag{2-44}$$

$$\frac{2(\bar{h}_{mid}'(\theta_A)^2 - (\bar{h}_{mid}(\theta_A)+1)\bar{h}_{mid}''(\theta_A) + (\bar{h}_{mid}(\theta_A)+1)^2}{\left((\bar{h}_{mid}'(\theta_A)^2 + (\bar{h}_{mid}(\theta_A)+1)^2\right)^{3/2}} = \frac{\bar{\delta}_{up}''(0)}{(1+\bar{\delta}_{up}'(0)^2)^{3/2}} \tag{2-45}$$

The downstream matching equations are more complicated because the matching point is not at the virtual tangent point which is the origin of the rectangular coordinates of downstream. Gap height, slope, and curvature matching gives

$$\bar{h}_{down}(Tan(s_{dm})) = \bar{h}_m(\theta_T + s_{dm})Cos(s_{dm}) \tag{2-46}$$

$$\bar{\delta}_{down}'(Tan(s_{dm})) = \frac{\bar{h}_m'(\theta_T + s_{dm})Cos(s_{dm}) - (1+\bar{h}_m(\theta_T + s_{dm}))Sin(s_{dm})}{\bar{h}_m'(\theta_T + s_{dm})Sin(s_{dm}) + (1+\bar{h}_m(\theta_T + s_{dm}))Cos(s_{dm})} \tag{2-47}$$

$$\frac{\bar{\delta}_{down}''(Tan(s_{dm}))}{(1+\bar{\delta}_{down}'(Tan(s_{dm}))^2)^{3/2}} = \frac{2(\bar{h}_{mid}'(\theta_T + s_{dm})^2 - (\bar{h}_{mid}(\theta_T + s_{dm})+1)\bar{h}_{mid}''(\theta_T + s_{dm}) + (\bar{h}_{mid}(\theta_T + s_{dm})+1)^2}{\left((\bar{h}_{mid}'(\theta_T + s_{dm})^2 + (\bar{h}_{mid}(\theta_T + s_{dm})+1)^2\right)^{3/2}} \tag{2-48}$$

See Appendix 2-A for detailed derivations of these matching conditions.

All unknowns are solved for simultaneously by Newton iteration until the residual errors become less than 10^{-10}.

2.4. EQUATIONS OF THE 1D-ELASTOHYDRODYNAMIC MODEL SOLVED WITH GALERKIN'S WEIGHTED RESIDUAL METHOD

When equations (2-11), (2-12), (2-15), and (2-16) are non-dimensionalized with the length unit, R_0, which is chosen from characteristic lengths of die geometry, flow rate unit, $R_0V/2$, and pressure unit, N_0/R_0,

$$h^*(\theta) = r^*(\theta) - D^*(\theta) \tag{2-49}$$

$$\kappa_s^* = \frac{2(\frac{dr^*}{d\theta})^2 - r^* \frac{d^2 r^*}{d\theta^2} + r^{*2}}{\left((\frac{dr^*}{d\theta})^2 + r^{*2}\right)^{3/2}} \tag{2-50}$$

$$q^* = h^* - \frac{h^{*3}}{6N_{EL}} \frac{\partial P^*}{\partial \theta} \frac{\partial \theta}{\partial x^*_s}, \qquad \frac{\partial x^*_s}{\partial \theta} = \sqrt{D^*(\theta)^2 + D^{*\prime}(\theta)^2} \tag{2-51}$$

$$-N_{SF} \frac{d^2 \kappa^*_s}{d\theta^2} \left(\frac{d\theta}{ds^*}\right)^2 + \kappa^*_s \left(-\frac{N_{SF}}{2} \kappa^{*2}_s + 1\right) - \Delta P^* = 0, \tag{2-52}$$

$$\frac{\partial s^*}{\partial \theta} = \sqrt{r^*(\theta)^2 + r^{*\prime}(\theta)^2}$$

The asterisks mean non-dimensional variables, but they are suppressed from now on. N_{EL} is elasticity number, ratio of viscous force to the elastic force from tensioned web, and N_{SF} is stiffness number, the ratio of web stiffness to the web tension.

$$N_{EL} \equiv \frac{\mu V}{N_0}, \qquad N_{SF} \equiv \frac{K}{{R_0}^2 N_0} \tag{2-53}$$

The system equations of Eqs. (2-49), (2-50), (2-51), and Eq. (2-52) was solved with boundary condition, Eq. (2-17) ~ Eq. (2-22) by Galerkin's weighted residual method with finite element basis functions for the pressure profiles and gap height profiles. Weighted residuals were obtained by multiplying Eqs. (2-49), (2-50), (2-51), and (2-52) by basis functions and integrating the products over the calculation domain, which spans from the upstream passage point to the downstream passage point.

$$\int_{\Omega} \left(r^*(\theta) - D^*(\theta) - h^*(\theta) \right) \phi_i d\theta = 0 \qquad \text{i = 1 ·· n} \tag{2-54b}$$

$$\int_{\Omega} \left(2\left(\frac{dr^*}{d\theta}\right)^2 - r^* \frac{d^2 r^*}{d\theta^2} + r^{*2} - {\kappa_s}^* \left(\left(\frac{dr^*}{d\theta}\right)^2 + r^{*2} \right)^{3/2} \right) \phi_i d\theta = 0$$

$$\text{i = 1 ·· n} \tag{2-55b}$$

$$\int_{\Omega} \left(h^* - \frac{{h^*}^3}{6N_{EL}} \frac{\partial P^*}{\partial \theta} \frac{\partial \theta}{\partial {x^*}_s} - q^* \right) \phi_i d\theta = 0, \qquad \frac{\partial {x^*}_s}{\partial \theta} = \sqrt{D^*(\theta)^2 + D^{*\prime}(\theta)^2}$$

$$\text{i = 1 ·· n} \tag{2-56b}$$

$$\int_{\Omega} \left(-N_{SF} \frac{d^2 {\kappa^*}_s}{d\theta^2} \left(\frac{d\theta}{ds^*} \right)^2 + {\kappa^*}_s \left(-\frac{N_{SF}}{2} {\kappa^*}_s^{\,2} + 1 \right) - \Delta P^* \right) \phi_i d\theta = 0,$$

$$\frac{\partial s^*}{\partial \theta} = \sqrt{r^*(\theta)^2 + r^{*\prime}(\theta)^2} \qquad \text{i = 1 ·· n} \tag{2-57b}$$

Beside the profile of pressure difference from the ambient P, gap profile, curvature profile κ, web shape function r, and gap profile h, the lubricant flow

rate q was solved for as an unknown.

Solution Method.

The basis functions used in both pressure residuals and gap height residuals, ϕ_i were standard quadratic finite element polynomial functions. All the integrals were evaluated by Gaussian quadrature with three Gauss points per element.

Once the field variables, pressure and gap height, were represented in terms of the basis functions, the system of differential equation Eqs. (2-49), (2-50), (2-51), and (2-52) reduced to system of algebraic equations for the coefficient of basis functions in finite element representations of field variables. This non-linear set of equations was solved by Newton iteration, which required evaluation of the full Jacobian matrix:

$$\mathbf{u}_{(k+1)} = \mathbf{u}_{(k)} + \delta\mathbf{u} \qquad (2\text{-}58)$$

$$\mathbf{J}(\delta\mathbf{u}) = -\mathbf{R} \qquad (2\text{-}59)$$

$\mathbf{u}$ is the vector of the unknown coefficients of the basis functions for pressure and gap height. $\mathbf{R}$ is the vector of the weighted residuals, and $\mathbf{J}$ is the Jacobian matrix of sensitivity of the residuals to the unknowns.

The first case solved was zero wrap angle case with initial approximation of flat web configuration and ambient pressure profile along the gap profile. Cases with nonzero wrap angles were solved by continuation technique explained in next section.

The linear solver used during Newton iteration was a direct band matrix solver

from LINPACK. Iteration proceeded until both the L2-norms of the updates $\|\mathbf{u}\|_{L_s 2}$ and residuals $\|\mathbf{R}\|_{L2_s}$ are less than 10^{-9}.

Figure 2-6 shows pressure profiles computed with uniform tessellations of 500 nodes and 1000 nodes. The difference of the two solutions was evaluated in a L2-norm of which the form is $\Delta = \left(\oint \left(P(s)_{n=1000} - P(s)_{n=500} \right)^2 ds \right)^{0.5}$, and turned out to be less than 1×10^{-5}. Considering that the value of pressure in uniform zone is around one, the error is thought to be small enough to guarantee the accuracy of solution. The two solutions are practically identical, which means discretization is fine enough. 1000 nodes uniformly distributed over the whole calculation domain were used in calculation of this study.

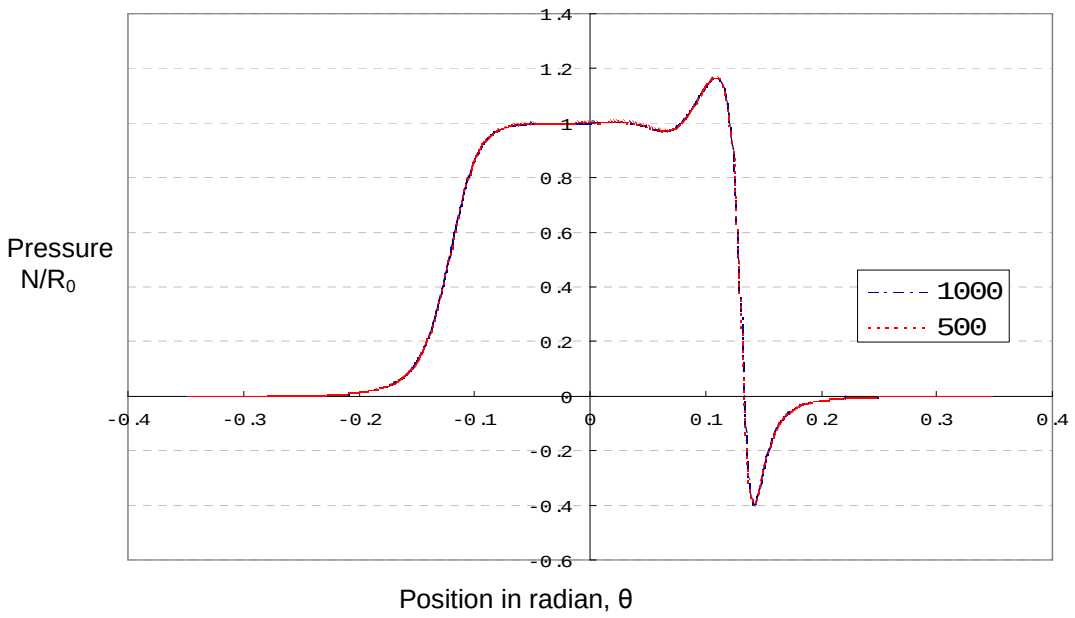

Fig. 2-6. Calculated pressure profiles with different node-densities. $N_{EL} = 10^{-6}$, $\theta_A = \theta_D = 7°$, $\theta_0 = 20°$, $p_{Up} = p_{Down} = 0$.

Pseudo Arc-Length Continuation

To explore the solution space around turning points, pseudo arc-length continuation was used to get the initial guess for the next Newton iteration. When $\mathbf{u}_0$ is a solution vector obtained at parameter a_0, the pseudo arc-length Δs to the another solution point of parameter a and the solution $\mathbf{u}$ was defined as

$$\Delta s = \sqrt{(\mathbf{u} - \mathbf{u_0}) + (a - a_0)^2} \tag{2-60}$$

The parameter for the next calculation, a was calculated simultaneously with solution $\mathbf{u}$ for the distance between the solution points to be arc-length of Δs. To solve for the augmented solution vector, the Newton iteration scheme shown in Eq. (2-54) and Eq.(2-55) was modified:

$$\begin{bmatrix} \mathbf{J} & \dfrac{\partial \mathbf{R}}{\partial a} \\ \dfrac{\partial N}{\partial \mathbf{u}} & \dfrac{\partial N}{\partial a} \end{bmatrix} \bullet \begin{bmatrix} \delta \mathbf{u} \\ \delta a \end{bmatrix} = -\begin{bmatrix} \mathbf{R} \\ N \end{bmatrix} \tag{2-61}$$

$$\mathbf{u}_{(k+1)} = \mathbf{u}_{(k)} + \delta \mathbf{u}, \quad p_{(k+1)} = p_{(k)} + \delta a \tag{2-62}$$

where, $N = \Delta s^2 - (\mathbf{u} - \mathbf{u_0}) \cdot (\mathbf{u} - \mathbf{u_0}) - (a - a_0)^2$ (2-63)

The initial guess for the next iteration was obtained by solving for the sensitivity to the continuation parameter and predicting it with linear Eq. (2-61). [Musson, 2001]

$$\begin{bmatrix} \mathbf{J}\big|_{\mathbf{u}_0} & \left.\frac{\partial \mathbf{R}}{\partial a}\right|_{\mathbf{u}_0} \\ \left.\frac{\partial N}{\partial \mathbf{u}}\right|_{\mathbf{u}_0} & \left.\frac{\partial N}{\partial a}\right|_{\mathbf{u}_0} \end{bmatrix} \bullet \begin{bmatrix} \frac{\partial \mathbf{u}}{\partial s} \\ \frac{\partial a}{\partial s} \end{bmatrix} = -\begin{bmatrix} \mathbf{R}\big|_{\mathbf{u}_0} \\ N\big|_{\mathbf{u}_0} \end{bmatrix} \tag{2-64}$$

$$\mathbf{u} = \mathbf{u}_0 + \frac{\partial \mathbf{u}}{\partial s}\Delta s\,, \quad a = a_0 + \frac{\partial a}{\partial s}\Delta s \tag{2-65}$$

The distance Δs was adjusted to make the Newton iteration converge in 6 steps and also to maintain the distance between solution points not too far. When iteration didn't converge in 6 steps, Δs was reduced by half, and when iteration converges in less than 4 steps, Δs was raised by 1.5 times.

The linear system equation, Eq. (2-57) or Eq. (2-60), was solved with an arrow matrix solving algorithm to utilize the band structure of J [Musson 2001].

2.5. BASIC FOIL BEARING

Gap profile in basic foil bearing case, where both the upstream and downstream pressures are ambient, was obtained by solving the equation sets of the three-asymptotic-zone model listed in Table 1 and compared with the result from the classical 1D-elastohydrodynamic model which is presented in section 2.4 and was solved by Galerkin / Finite element method. The computation results are shown in figure 2-7. Both the calculations of the gap profile agree well in most of the region. The biggest difference between the two is around the minimum gap clearance near the downstream virtual tangent

point: the gap profile of the three-asymptotic-zone model has a minimum clearance near the downstream tangent, whereas the classical 1D-elastohydrodynamic model has the minimum gap shifted to the downstream from the downstream virtual tangent point.

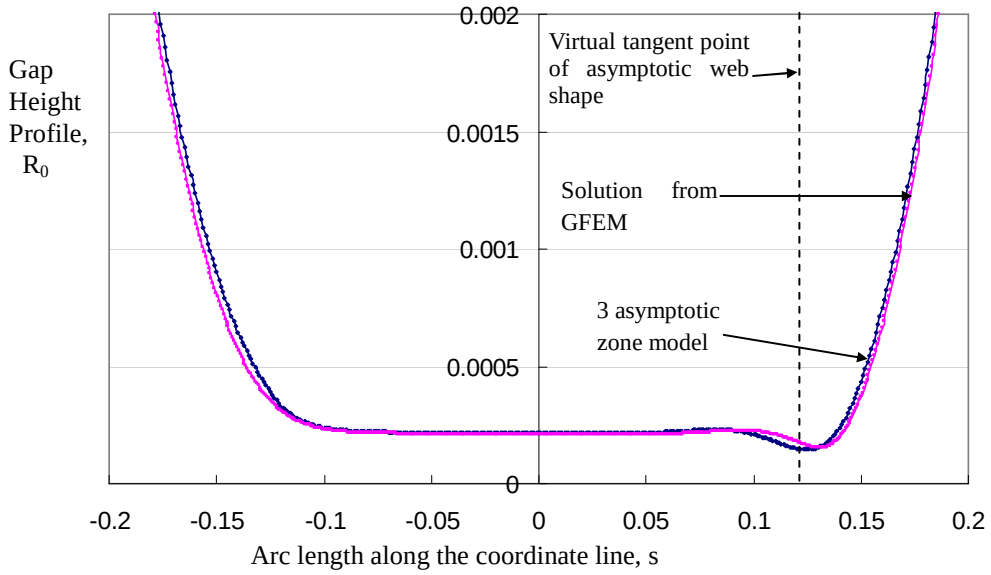

Fig. 2-7. Comparison of gap profiles calculated by 3-asymptotic-zone model with results from Galerkin/Finite Element Method **(** $N_{EL} = 10^{-6}$ **,** $\theta_A = \theta_D = 7°$ **,** $\theta_0 = 20°$ **,** $p_{Up} = p_{Down} = 0$ **)**

The downstream zone forms a diverging channel, which is destined to make the negative pressure profile along the channel; the viscous drag from moving web induces negative pressure profile in diverging channel. The strong negative pressure that forms in the downstream zone, especially at the close gap near the virtual tangent point, draws down the web and shifts the point of minimum

clearance downstream.

This minimum gap plays an important role in keeping the pressure in the uniform zone high. At the upstream exit of the uniform zone, viscous drag at the foil surface contributes to building the high pressure in the uniform zone and, at the same time, to keeping it high. But at the downstream exit, the direction of viscous drag is to lower the pressure of the uniform zone. Instead, at the downstream exit the minimum gap caused by negative pressure from the diverging channel acts like a shutter and keeps the pressure of the uniform zone high; the deviation from the presumed foil shape is positive in upstream zone whereas it is negative in the downstream zone.[see figure 2-8]

In the three-asymptotic-zone model, the equations of which are derived on the assumption, $\delta << h_{0,up}$, the interaction between the pressure and foil deformation is underestimated, and the minimum clearance point shifts slightly less than the shift in the solution of the classical 1D elastohydrodynamic model.

Deviation of the foil shape from the presumed foil shape, which is a part of solution of three-asymptotic-zone model, is shown in figure 2-8 by the ratio $\frac{\delta}{h_{0,up}}$, which is the measure showing the validity of assumption $\delta << h_{0,up}$. In the upstream zone the ratio $\frac{\delta}{h_{0,up}}$ reaches up to 0.75 in the vicinity of the upstream virtual tangent point. This ratio is too big to guarantee good accuracy of calculation. Actually the prediction from the three-asymptotic-zone model is less precise than predictions from the other model, the classical elastohydrodynamic model descibed in section 2.4. But the value of the three-

asymptotic-zone model is that it provides insight into the structure of foil bearing flow, as discussed here and in the discussion on the back-pressured foil bearing in section 2.6.

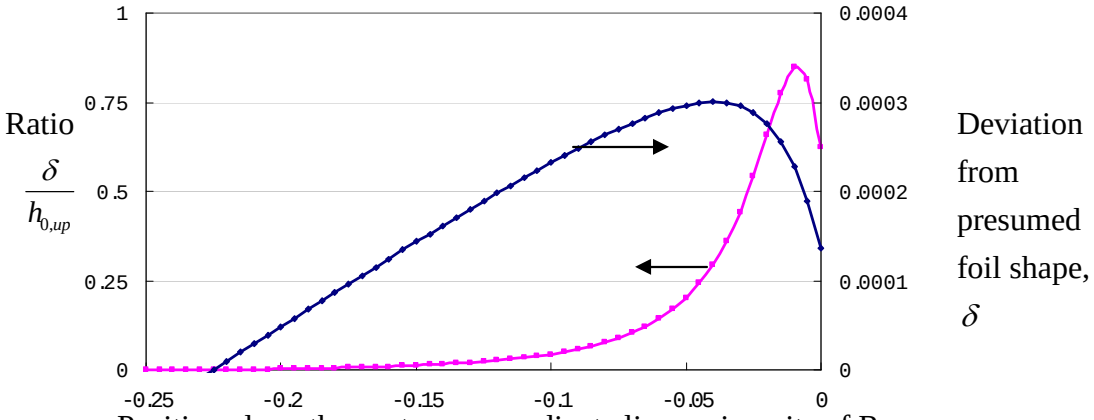

(a) Upstream

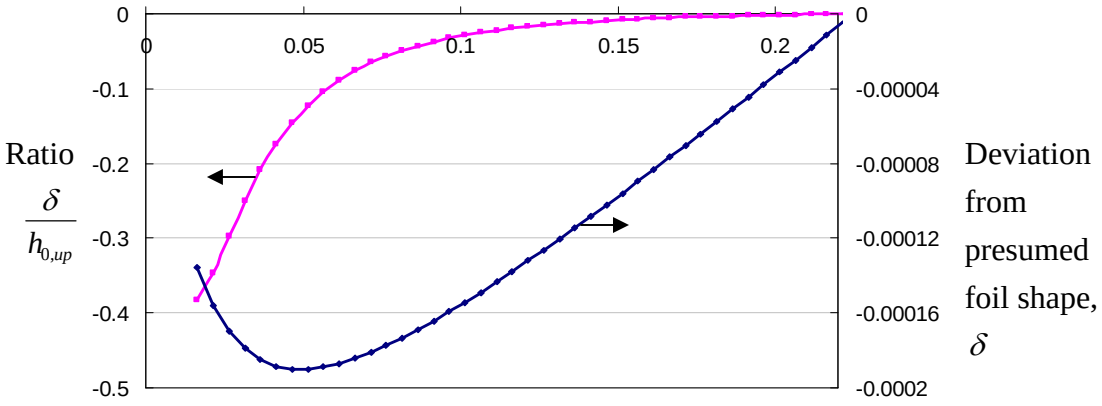

(b) Downstream

Fig. 2-8. Deviation from the asymptotic shape, δ, and the ratio of $\frac{\delta}{h_{0,up}}$ in upstream zone and downstream zone in three-asymptotic-zone model. **(**$N_{EL}=1.0\times10^{-6}$**,** $\theta_A=\theta_D=7°$**,** $\theta_0=20°$**,** $p_{Up}=p_{Down}=0$**).**

2.6. PRESSURE UPSTREAM AND PRESSURE DOWNSTREAM

Forward-Pressurized Foil Bearing

When the pressure upstream of a foil bearing rises above ambient pressure, the upstream part of foil is bent and locally lifted away from the spindle and the gap profile swells over the whole upstream zone. Fig. 2-9 shows the change of the lubricant flow rate through the gap, which was obtained from the theoretical model in section 2.4 with the Galerkin / Finite element method. The flow rate of lubricant into and through the gap grows as the upstream pressure rises. Evidently, it does so for two reasons; one is the rise of Poiseuille flow through the gap with stronger favorable pressure gradient laid across the foil bearing, and the other is the expansion of the channel for the lubricant flow. The increase in flow rate is small until the upstream pressure reaches a critical value, approximately $P^* = 0.76$ in units of N/R_0 in the condition of Fig. 2-9; thereafter the flow rate increases sharply as shown in Fig. 2-9. This behavior arises in the geometric restriction that is placed on the foil configuration. When the upstream pressure is lower than the critical value, $P^* = 0.76$ in the condition of Fig. 2-9, the asymptotic foil shape, which is an arc of circle passing the upstream passage point, can osculate on the spindle surface with the tangent point upstream of the downstream virtual tangent point so that foil can make a narrow gap on the spindle. But when the pressure upstream is bigger than the critical value, the asymptotic foil shape either osculates at the downstream of the downstream

virtual tangent point or can’t make a tangent point because the radius of arc of circle is too small. Since a narrow channel is impossible to make with a pressure higher than the critical value, the lubricant flow rate rises more sensitively to the pressure upstream; in lubrication type flow, the Couette flow contribution is proportional to the gap whereas the Poiseuille flow contribution is proportional to cube of gap.

Figure 2-10 shows changes in the pressure profiles and the gap profiles as the pressure upstream is raised. When dimensionless pressure upstream is higher than the critical value, 0.76, with the other conditions the same as in Fig. 2-9, the foil is totally lifted and the pressure gradient over the whole foil bearing becomes favorable to the fluid flow. The strong pressure upstream bends the web at high curvature, the flow channel cannot make narrow gap, and the increase of flow rate mainly comes from stronger pressure-gradient. When the dimensionless pressure upstream is lower than the critical value, gap is lifted partly, and the small gap, which still exists at some part, shaves the lubricant flow making the pressure gradient around the center of the foil bearing still remain adverse to the flow direction. Though the net flow is not as sensitive as in the other branch, increasing the pressure upstream still raises the lubricant flow rate.

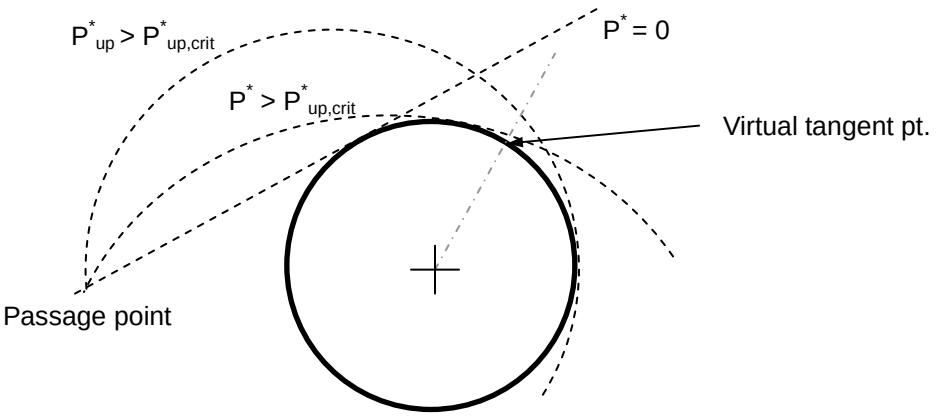

(a) Configurations of asymptotic foil shapes.

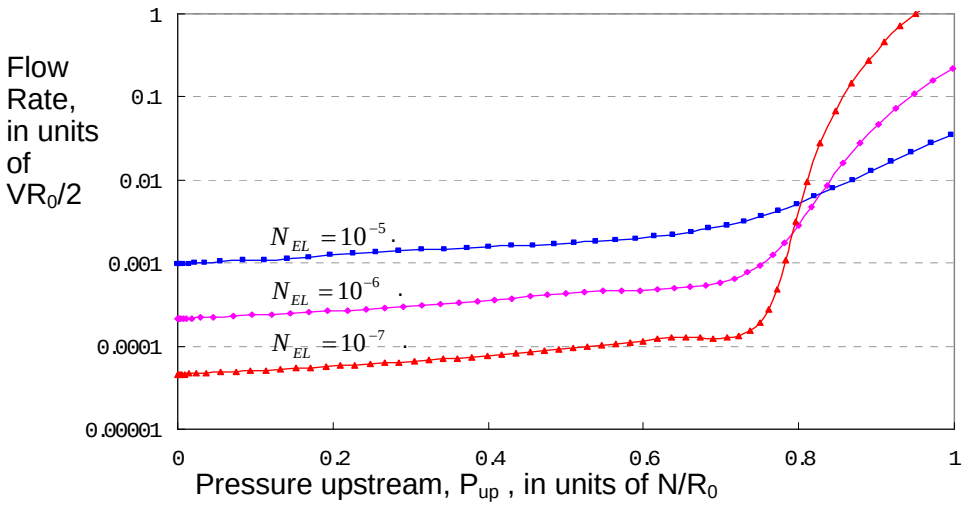

(b) Flow rate change caused by pressure upstream

Fig. 2-9. Effect of pressure upstream. ($N_{EL} = 10^{-6}$, $\theta_A = \theta_D = 7°$, $\theta_0 = 20°$, $P_{down} = 0$)

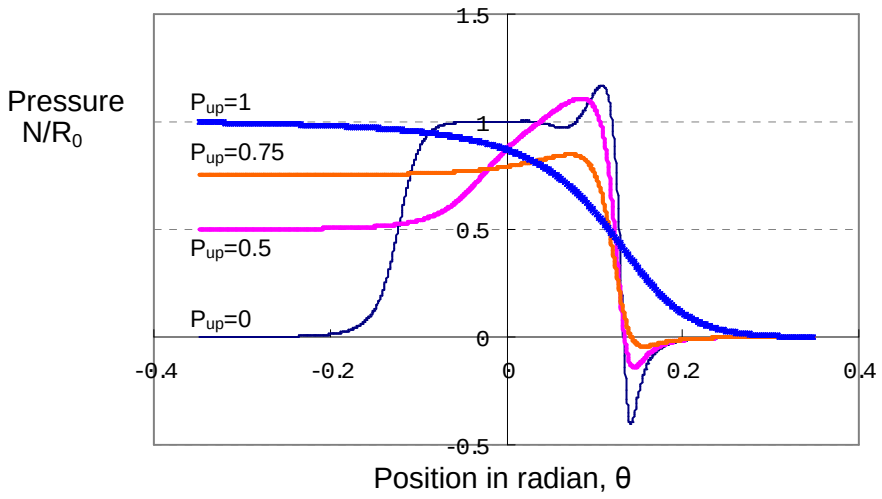

(a) Calculated pressure profiles.

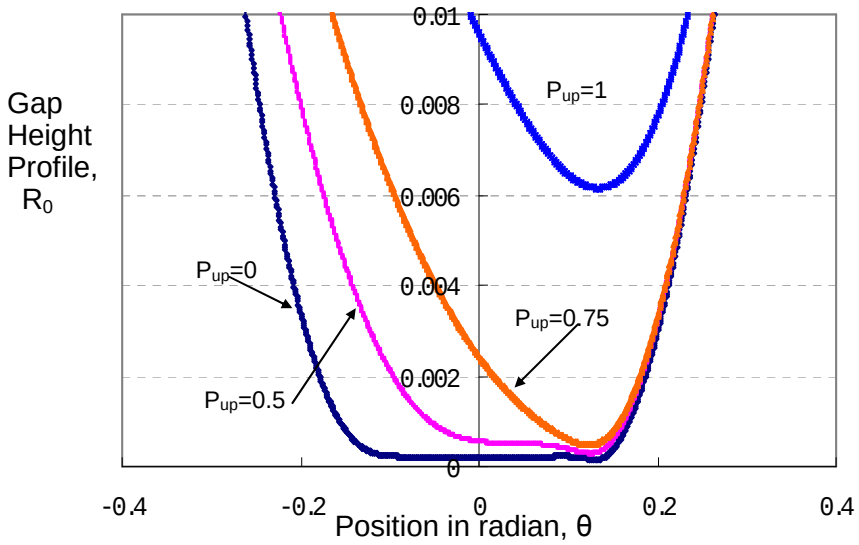

(b) Calculated gap height profiles

Fig. 2-10. Effect of the pressures upstream, P_{up}. ($N_{EL}=10^{-6}$, $\theta_A=\theta_D=7°$, $\theta_0=20°$, $p_{Down}=0$)

Back-Pressurized Foil Bearing

Figures 2-11, 2-12, 2-13, 2-14, and 2-15 are from the theoretical model described in section 2.4, which was solved by the Galerkin method with finite element functions.

Figure 2-11 shows the change in flow rate as the pressure downstream rises. Unlike raising the upstream pressure, raising the pressure downstream of the foil bearing above ambient pressure doesn't change the flow rate of lubricant until it approaches a critical value, which is a little short of a turning point in the plane of flow rate versus pressure downstream shown in figure 2-11. The reason for the unchanging flow rate is that the minimum gap, which is at the downstream exit of the uniform zone acts like a shutter, as discussed in section 2.5, so that the characteristics of uniform zone, virtually-uniform pressure and gap profiles, are maintained and so the flow rate of lubricant remains unchanged.

As the pressure downstream approaches the turning point, the flow rate decreases a little and start turning around in a loop-like path in a q-P_{down} parameter space. Further increase of the pressure downstream decreases the flow rate drastically, and then reverses the flow when the back pressure from the downstream is big enough. Figure 2-11 shows that there are three solution trajectories for three elasticity numbers and that loop-shaped turning points exist for all three elasticity numbers. The origin of this turning point is explained in the latter part of this section.

The turning point divides the solution trajectory into two branches. The one in the lower downstream pressure side of the turning point can be called the “partly-closed foil bearing branch”. The other one in the higher pressure downstream side of the turning point can similarly be called the “open foil bearing branch”.

Similar to the discussion on the critical pressure upstream, the critical value of pressure downstream at which loop-shaped turning point can be roughly estimated by a geometrical consideration [See figure 2-14]. When the asymptotic downstream foil shape can osculate on the spindle at the downstream of the upstream virtual tangent point, the foil forms a partly-closed foil bearing; otherwise it pertains to the open foil bearing branch. When downstream pressure difference from the ambient is bigger than the critical value, which is 0.76 in the unit of N/R_0 at the condition of Fig. 2-11 and elasticity number 10^{-6}, the radius of the presumed foil shape becomes too small to make a tangency to the cylindrical spindle while passing the passage point [see Fig. 2-14].

On the partly-closed foil bearing branch, the pressure downstream is not so big that the asymptotic downstream foil shape still can become tangent to the spindle at a point downstream of the upstream virtual tangent point. Figure 2-12 shows the pressure profiles and gap height profiles for several downstream pressures in the “partly-closed branch”. The minimum clearance shifts upstream as the pressure downstream climbs. While the foil in the downstream side of the minimum gap is swollen by the increased downstream pressures, the upstream side of the foil keeps the structure of the foil bearing, the virtually-uniform-gap

zone and the pressure swing before the minimum clearance. The gap profile plotted in rectangular coordinates [figure 2-13] clearly shows the two parts of the foil bearing in the partly closed branch: the remaining foil bearing structure in the upstream part and back-pressure swollen foil in the downstream part.

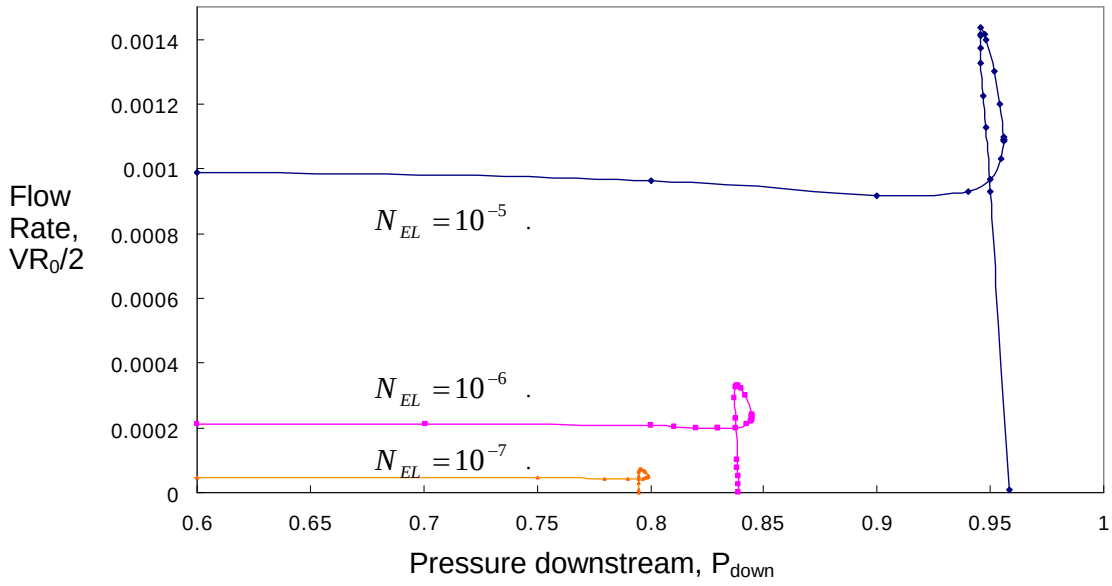

Fig. 2-11. Flow rate, Q versus the difference of pressure downstream from the ambient, P_{down}, at three elasticity numbers $N_{EL} \equiv \frac{\mu V}{N_0}$. ($\theta_A = \theta_D = 7°$, $\theta_0 = 20°, \theta_A = \theta_D = 7°,\ p_{Up} = 0$)

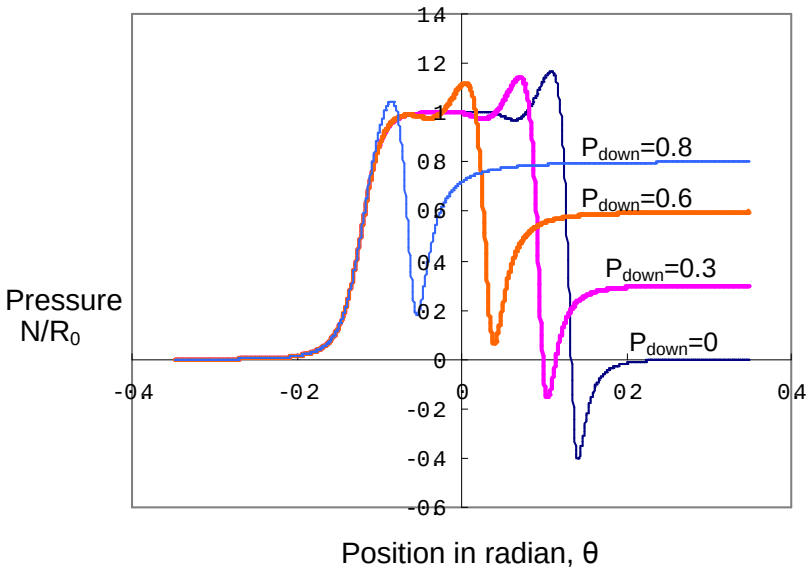

(a) Calculated pressure profiles.

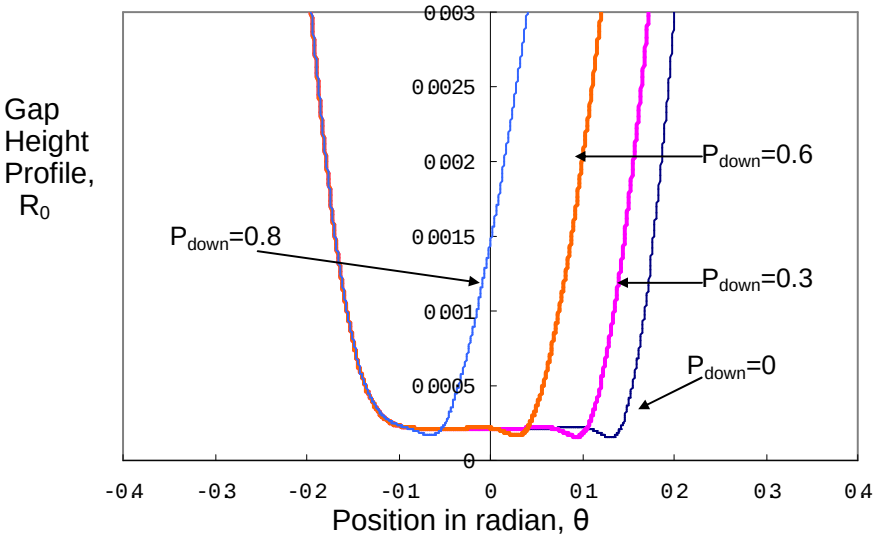

(b) Calculated gap height profiles

Fig. 2-12. Effect of downstream pressure difference from ambient in partly-closed foil bearing branch. ($N_{EL} = 10^{-6}$, $\theta_A = \theta_D = 7°$, $\theta_0 = 20°$, $p_{Up} = 0$)

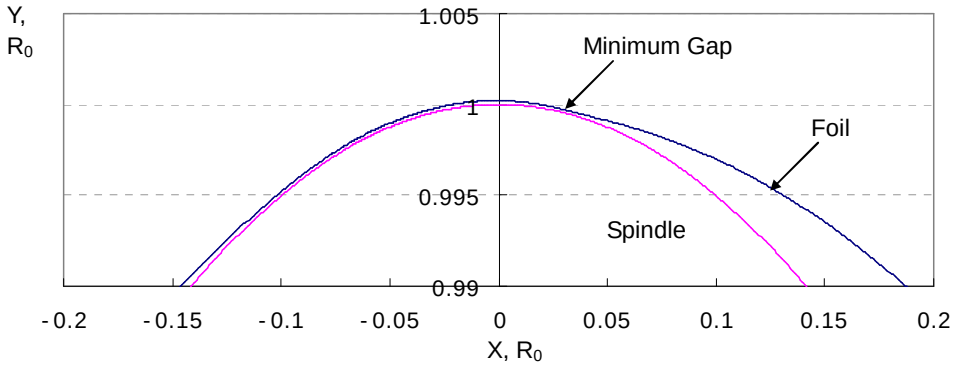

Fig. 2-13. Calculated shape of the foil in the partly-closed foil bearing branch. ($P_{down} = 0.6, P_{up} = 0,\ N_{EL} = 10^{-6},\ \theta_A = \theta_D = 7°,\ \theta_0 = 20°$)

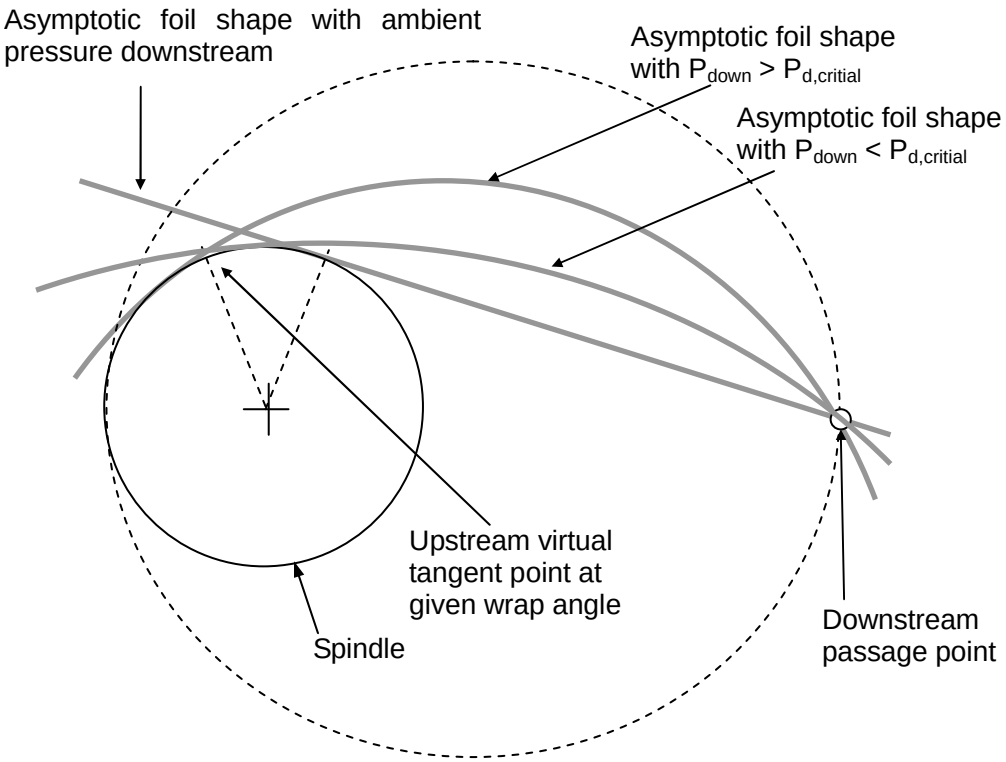

Fig. 2-14. The downstream pressure difference from ambience has range limited by foil shape restriction that the downstream asymptotic foil shape should osculate, at least be close to osculate, at the spindle surface wrapped by foil.

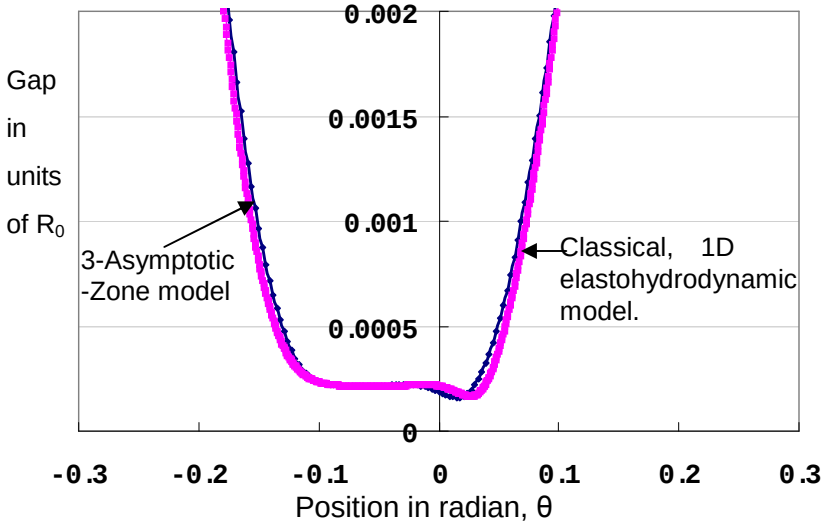

Fig. 2-15. Comparison of gap profiles calculated by 3-asymptotic-zone model with results from classical elastohydrodynamic model solved by Galerkin's weighted residual method ($N_{EL} = 1.0 \times 10^{-6}$, $\theta_A = \theta_D = 7°$, $\theta_0 = 20°$, $P_{down} = 0.6$, $P_{up} = 0$).

In the foregoing consideration of the location of the turning point, the asymptotic downstream foil shape was taken to be tangent to the spindle. This tangency can be established by the facts that the foil is a membrane and so must have continuous slope at every point, and that the foil shape in uniform zone is almost an arc of circle, close to the shape of the spindle. This tangency requirement can be verified with the three-asymptotic-zone model. In figure 2-15, the result from the three-asymptotic zone model for the back-pressured case with P_{down} = 0.6 is compared with that from the Galerkin/Finite element analysis(GFEM) with the elastohydrodynamic model presented in section 2.4.

Three-asymptotic-zone model sets the presumed downstream foil shape to be tangent to the spindle and computes the deviation of the foil shape from the presumed foil shape. The calculation results show that the deviation is small so that the calculated foil shape is not much different from the presumed foil shape which osculates the spindle. Figure 2-15 shows that the gap profile computed from the three-asymptotic-zone model agrees well with the result of classical elastohydrodynamic model solved by the Galerkin / Finite element method also in the case of non-zero downstream pressure difference from the ambient.

The use of three-asymptotic-zone model for back-pressured foil bearing cases is limited by the tangency requirement of the presumed foil shape. When the downstream pressure difference from the ambient is so big that the presumed foil shape downstream cannot osculate at the downstream of the upstream virtual tangent point, the model can’t describe the case properly because the uniform zone cannot be assigned since two side zone overlaps even without an uniform zone.

In the open foil bearing branch, the pressure downstream lifts the web throughout the whole span. The characteristics of the general foil bearing—the virtually uniform gap and the pressure swing—disappear. Within this regime a small increase of the pressure downstream leads to a big backward flow contribution because the downstream pressure lifts the foil raising the gap height; the Poiseuille contribution to the flow rate is proportional to the cube of the gap height. Fig.2-16 shows the pressure and gap profiles in this part.

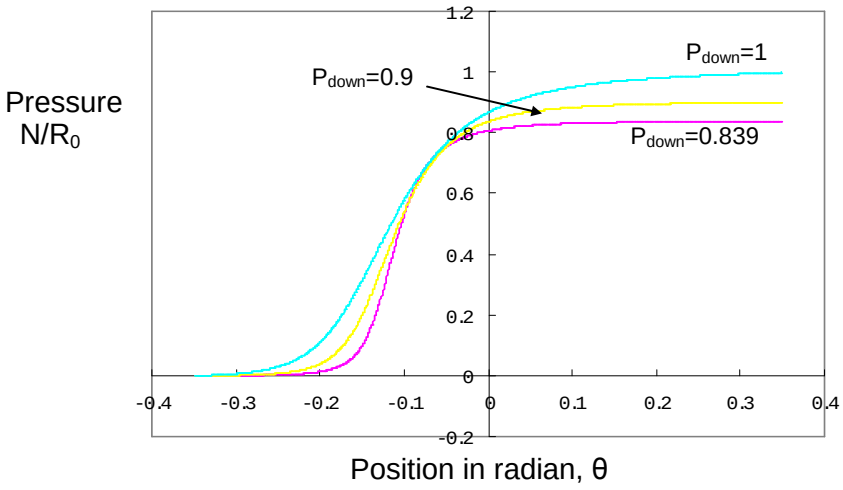

(a) Calculated pressure profiles.

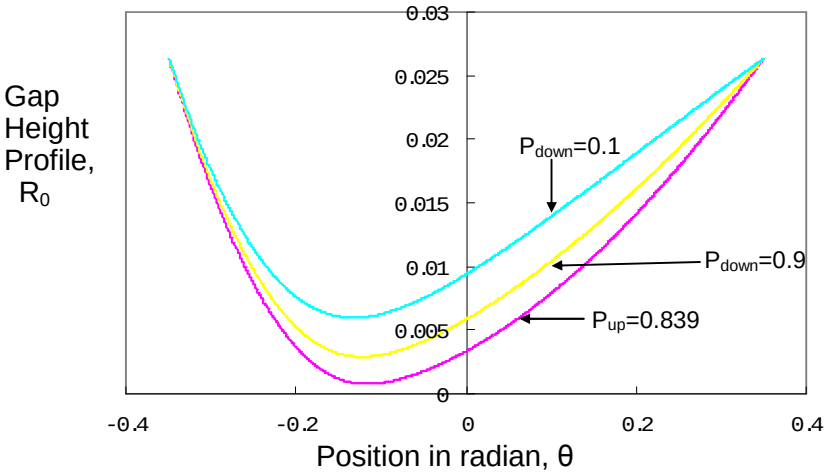

(b) Calculated gap profiles

Fig. 2-16. Effect of downstream pressure difference from ambient in the open foil bearing branch. ($P_{Up}=0$, $N_{EL}=10^{-6}$, $\theta_A=\theta_D=7°$, $\theta_0=20°$)

As is shown in figure 2-11, the turning points of the loop-shaped solution trajectories in P_{down}-q plain do not coincide with the critical downstream pressure,

$P_{d,crit}$, which is obtained by geometric consideration that asymptotic foil shape should osculate the cylinder within the wrapped surface; in the condition of figure 2-11 with elasticity number 10^{-6}, the geometry restriction gives the critical downstream pressure difference from the ambient of 0.76 while the turning point is around P_{down} = 0.84. This difference is generated by the strong negative pressure in the narrow and diverging gap in the exit of uniform zone. As mentioned above, the strong negative pressure sucks down the foil and makes the minimum gap. This suction effect delays the transition from the partly-closed foil bearing to the open foil bearing branch. Another consequence from the suction is the fold in the solution trajectory, i.e. its loop-shape around the turning point. The delaying action is stronger when the transition starts from the partly closed foil bearing than in the transition in reverse direction; thereby the open foil bearing branch and partly-closed foil bearing branch overlap each other, forming the loop-shaped turning points in Fig. 2-11.

In Fig. 2-17, solution trajectories for several wrap angles are shown in the plane of flow rate versus downstream pressure difference. When wrap angles are smaller than the critical angle of a given condition, which is around 6° in the condition of Fig. 2-17, solution trajectories do not have the turning point. As wrap angles rise, two branches, open foil bearing and partly closed foil bearing start overlapping and forming loop-shaped turning points.

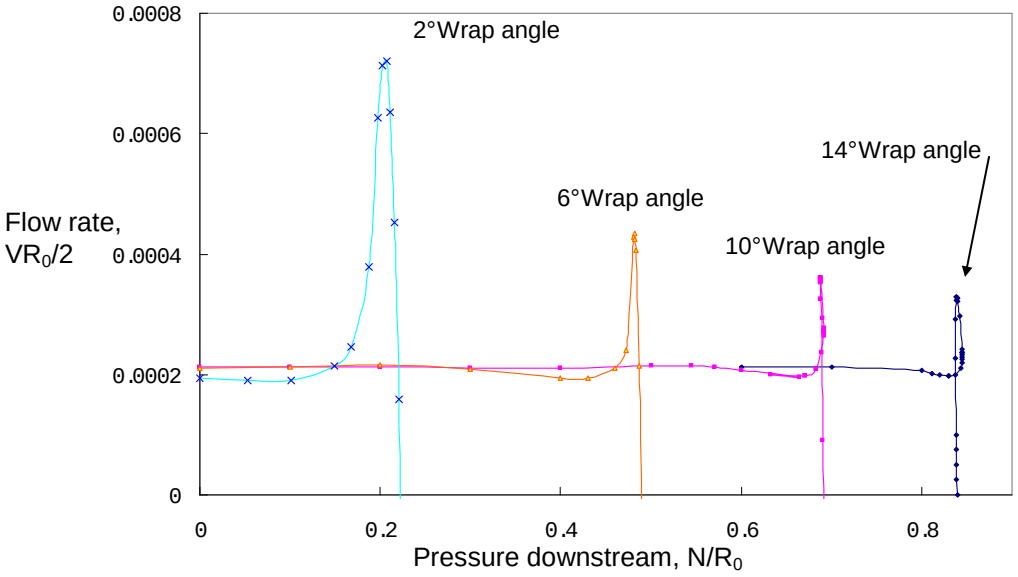

Fig. 2-17. Effect of the wrap angle on the turning point. ($N_{EL} = 10^{-6}$, $\theta_A = \theta_D = 7°$, $\theta_0 = 20°$, $P_{Up} = 0$)

Again the consideration with three-asymptotic-zone model provides useful perspective of the reason for the angle dependence of the fold forming. Figure 2-18 shows the presumed gap profiles in the downstream zone with several downstream pressure differences from the ambient. This plot sheds light on why the turning point forms a fold only in a wrap angle higher than the critical value. The higher the downstream pressure, the narrower and longer the diverging channel that forms in the downstream zone. A longer and narrower diverging channel makes stronger consequence of negative pressure in forming the minimum gap. In figure 2-17, when the wrap angle is small, the transition between the two branches occurs too early for the diverging channel to be long enough to form a strong negative pressure at the minimum gap and to exert its

influence on the foil deformation strongly to make a fold. As the wrap angle rises, the diverging gap at the critical downstream pressure becomes narrower and longer and forms negative pressure around the minimum gap strong enough to make a fold in the solution trajectory.

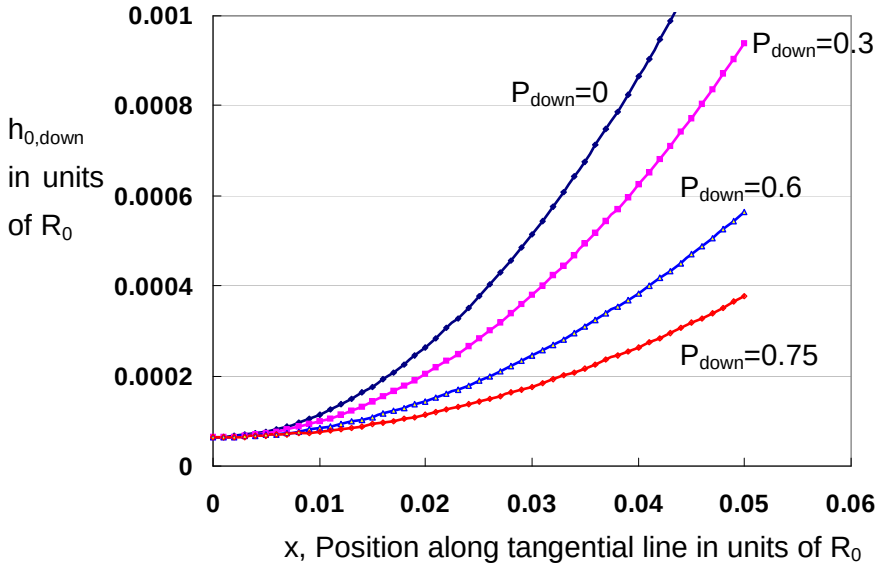

Fig. 2-18. Gap profile from asymptotic foil shape of downstream zone in several downstream pressures difference from the ambient

Blocked Foil Bearing

In the solution trajectory of back-pressured foil bearing, there is a special point at which the lubricant flow rate is zero; it is special in that it can bring out insights into the working mechanisms of the parts of web-based elastohydrodynamic processes, e.g., tensioned-web slot coating system. In reality there's no such a foil bearing of which the gap is blocked in some part. But the name, blocked foil

bearing, was chosen since it expresses well the state of no net flow. Figure 2-19 shows two possible configurations of blocked foil bearing. In the configuration shown in figure 2-19(a), foil bearing is operating like a pump which pressurizes the downstream zone by applying the drag force which is supported by tension resultant force into the lubrication layer. In configuration 2-19 (b), the foil bearing pump is vacuuming the upstream zone. To ensure proper operation of the blocked foil bearing of this configuration, the downstream pressure has to be high enough, if it is not enough to drive adverse Poiseulle flow to compensate the drag flow, the foil would touches the spindle—but such situations are out of the capability of the steady state models.

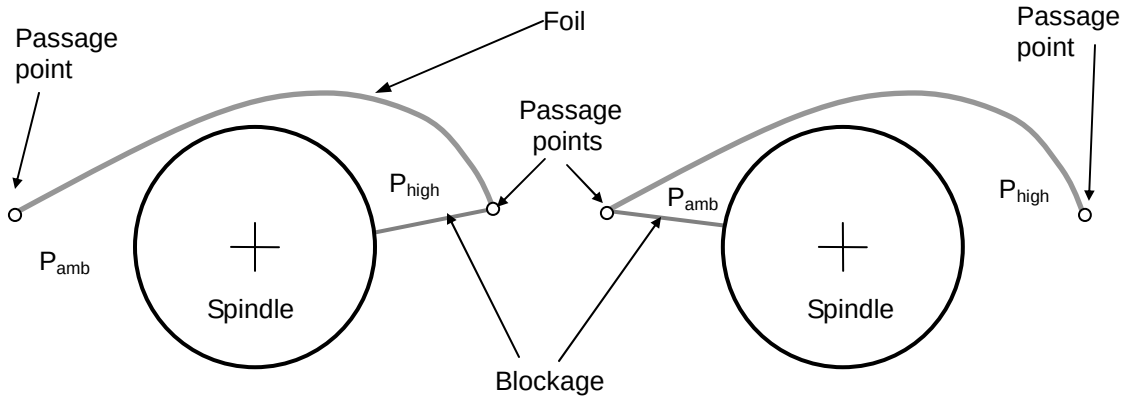

(a) Blockage downstream (b) Blockage upstream

Fig. 2-19. Two possible locations of the blockage in blocked foil bearing

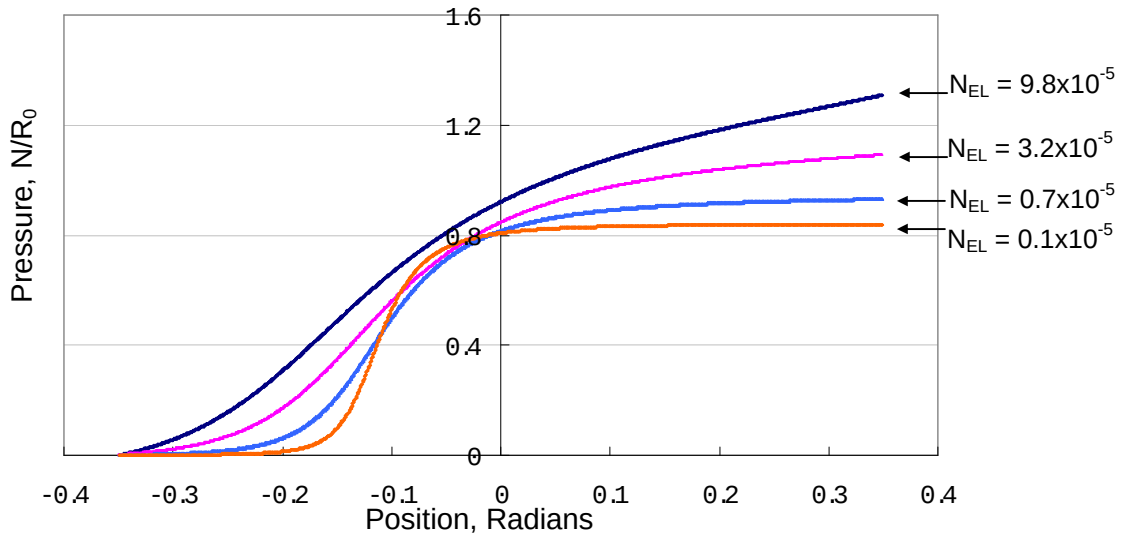

(a) Pressure profiles of blocked foil bearings

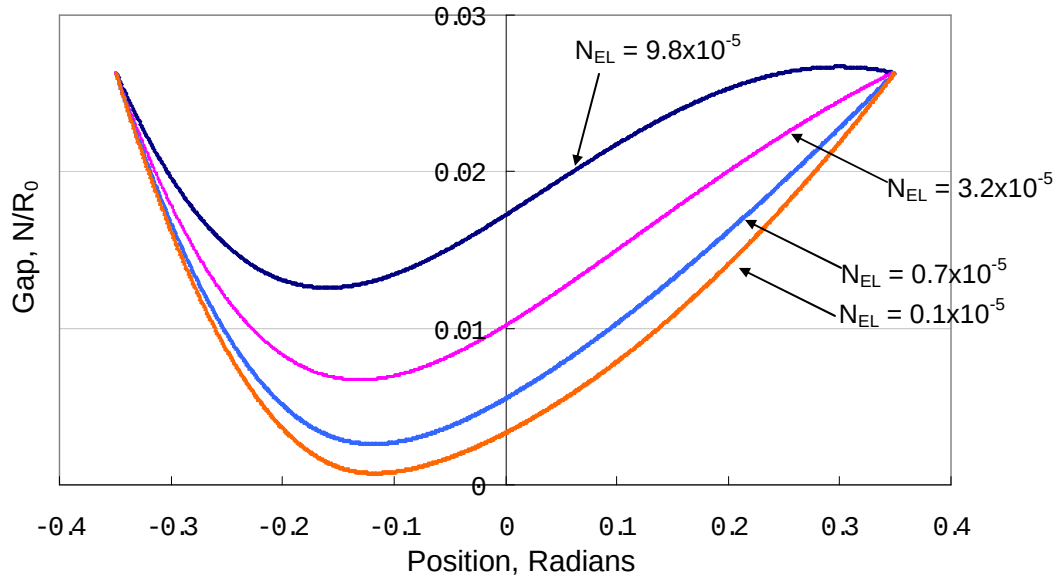

(b) Gap profiles of blocked foil bearing

Fig. 2-20. Effect of elasticity number in blocked foil bearing. ($P_{up} = 0$, $\theta_A = \theta_D = 7°$, $\theta_0 = 20°$, q = 0)

Though the interpretations of the pressure profiles for the both cases in figure 2-19 are different, the pressure profiles are the same. The pressure and gap profiles predicted by the elastohydrodynamic model described in section 2.4 are shown in figure 2-20. Blockage downstream, case (a) in figure 2-19, is the case chosen for interpretation of pressure and gap profiles because configuration (a) seems easier to understand intuitively.

Figure 2-20(a) shows that pressures downstream are made by the viscous drag throughout the span, though the part of smaller gap pumps more significantly. Figure 2-20 shows that where the gap is small the pressure gradient is bigger. Increase of elasticity number means stronger viscous force. As the elasticity number rises, the pressure downstream rises. When the viscous drag force at a given condition of the system is sufficiently big, the pressure downstream rises high yet a small gap does not arise, as illustrated by case $N_{EL}=9.8x10^{-5}$ in figure 2-20.

The effect of wrap angle in the blocked foil bearing is shown in figure 2-21. Raising wrap angle boosts the power of the viscous drag pump because more wrap angle lead to a bigger the tension resultant force. As a result, bigger wrap angle makes higher pressure downstream.

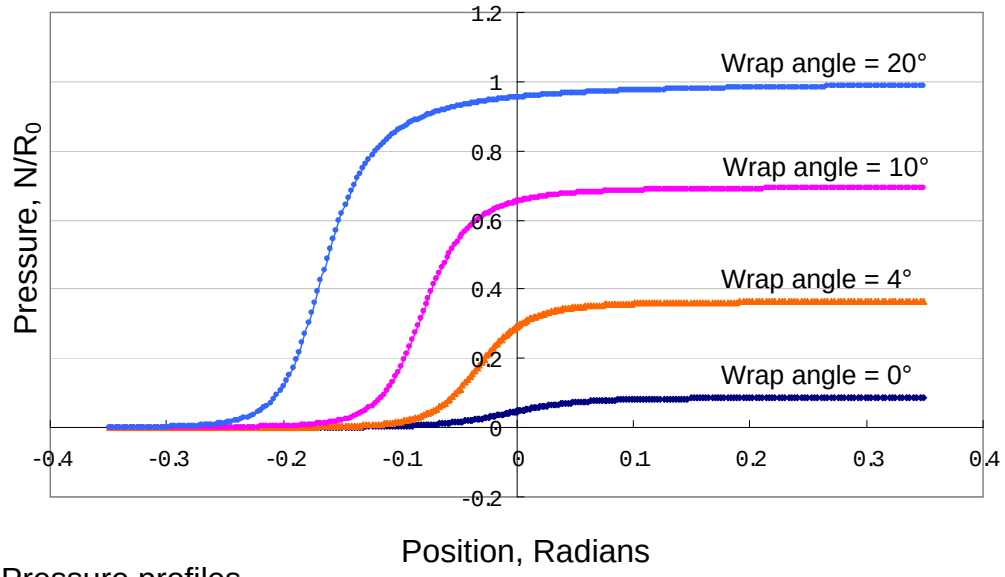

(a) Pressure profiles

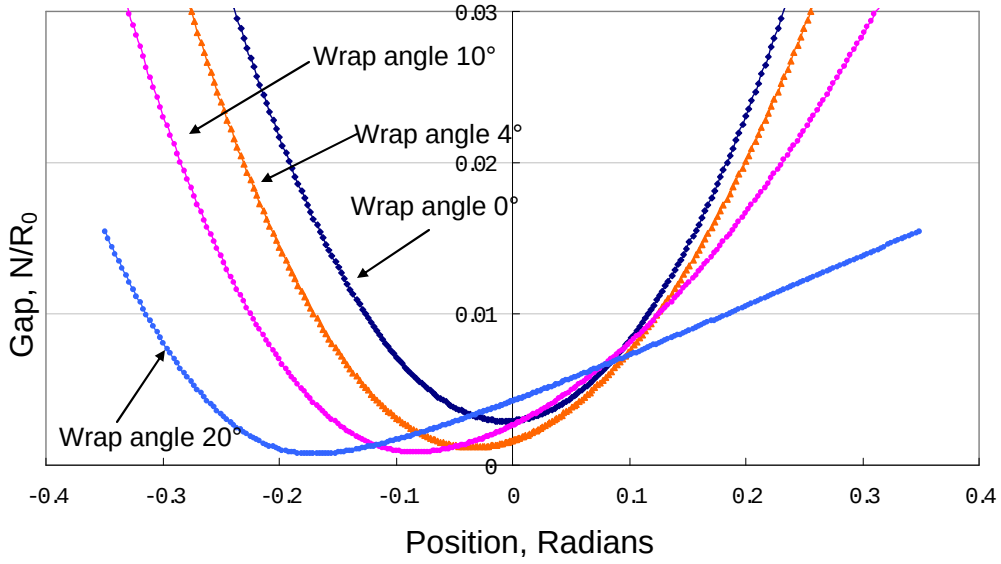

(b) Gap profiles

Fig. 2-21. Effect of wrap angle in blocked foil bearings. ($P_{up} = 0$, $N_{EL} = 10^{-6}$, $\theta_0 = 20°$, q = 0)

2.7. Effect of Stiffness

When an infinitesimal membrane segment which is a foil without flexural rigidity is subject to a load across it, the membrane deforms until it finds balance between the normal load and the normal tension-resultant force [Eq. 2-23]; the tangential load is negligible in the conditions of this study. The deformation of infinitesimal membrane fragment doesn't affect the configurations of adjacent foil segments. However, when a foil has stiffness—it's then called a shell—the deformation of foil segment is not free from the configuration of adjacent portions of foil; bending a foil exerts a force to the adjacent foil segments [Eq. 2-12]. The equilibrium foil shape needs a balance of three forces: external load, tension resultant force, and the elastic force of the shell.

The effects of foil stiffness were studied by the elastohydrodynamic model in section 2.4. Shown in figure 2-22 are the results with the basic case foil bearing, where both the upstream and downstream pressures are ambient. As the foil gets stiffer, its deformation takes longer length. With zero flexural rigidity the characteristic structure of foil bearing, the minimum gap and pressure swing at the end of uniform zone, develops in a relatively short interval. But as the stiffness rises, the wider interval is needed for developing the structure; figure 2-22 shows that when stiffness number is 10^{-2} the interval needed for developing foil bearing structure exceed the length of given wrap angle so that we cannot see the uniform zone.

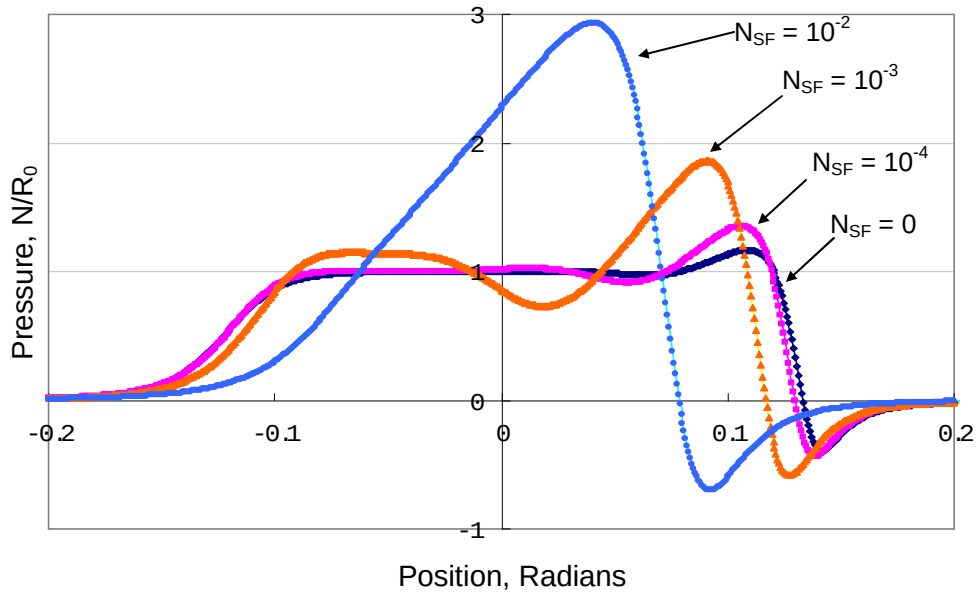

(a) Pressure profile

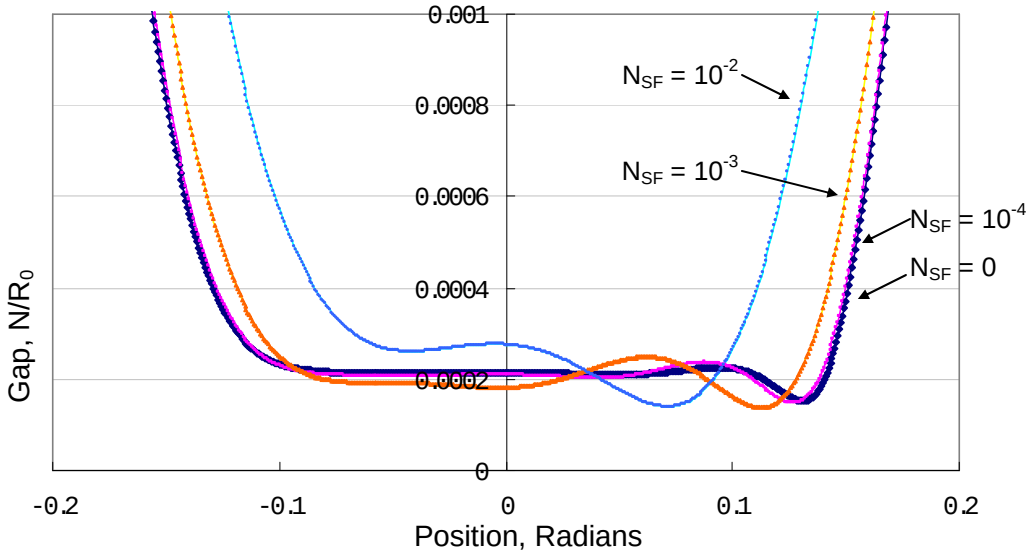

(b) Gap profile

Fig. 2-22 Effect of stiffness in basic foil bearings. ($P_{up} = P_{down} = 0$, $N_{EL} = 10^{-6}$, $\theta_0 = 20°$, $\theta_A = \theta_D = 7°$,).

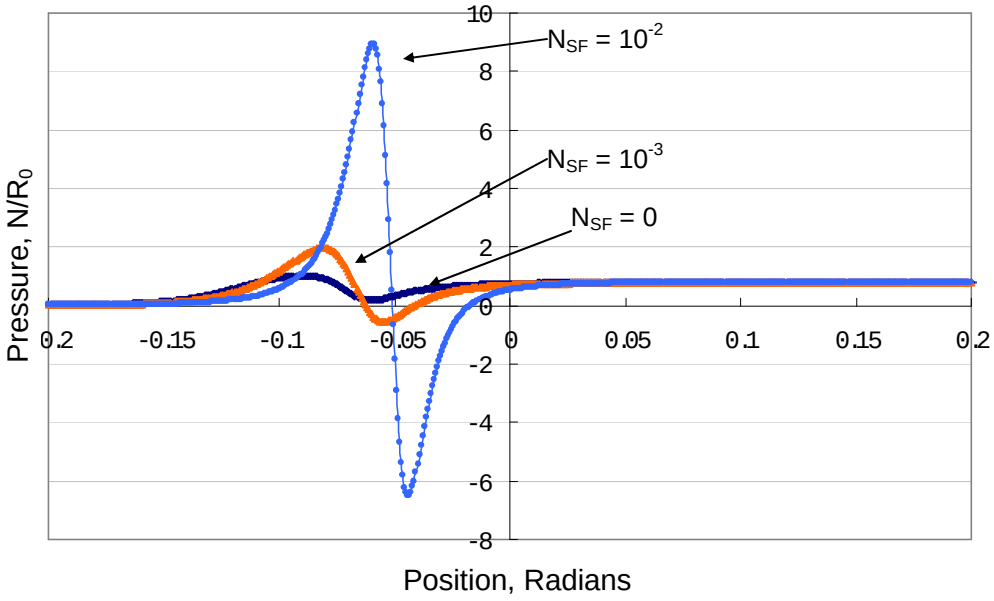

(a) Pressure profiles

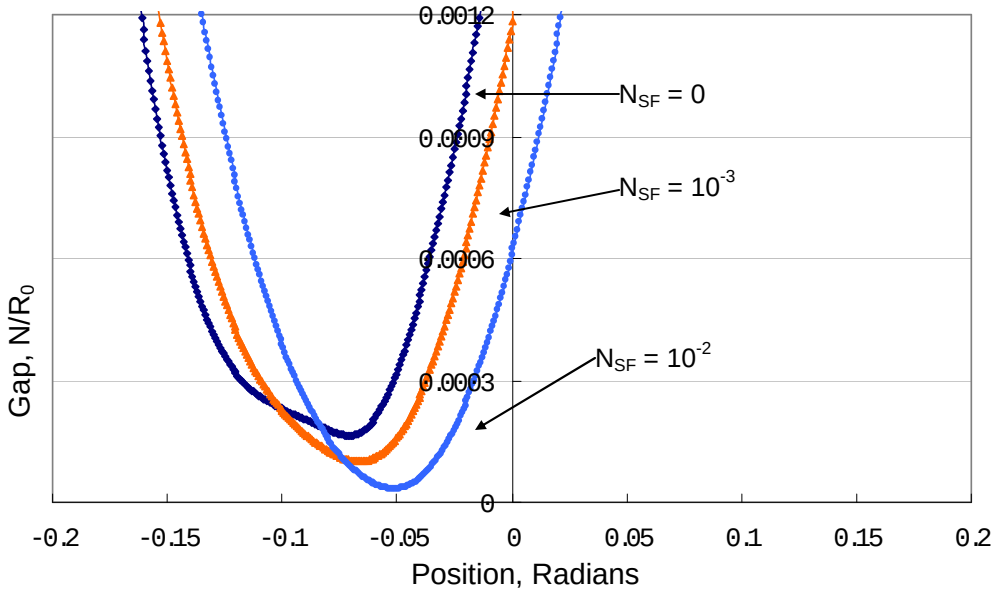

(b) Gap profiles

Fig. 2-23. Effect of stiffness in back-pressured foil bearings. ($P_{up} = 0$, $P_{down} = 0.81$, $N_{EL} = 10^{-6}$, $\theta_0 = 20°$).

Stiffness of the foil makes the flow channel more rigid and makes the pressure profile resemble that of fixed channel flow more as the stiffness rises. Due to this stiffness effect the pressure peak just before the minimum gap rises high with the foil stiffness increase. [figure 2-22] The same tendency is observed in figure 2-23, which shows the pressure and gap profiles of pressured foil bearing with downstream pressure difference from the ambient 0.81. Another remarkable thing is that the minimum gap near the downstream virtual tangent point falls as the stiffness rises; that is due to the rigidity of the diverging channel, which makes deeper pressure valley downstream of the minimum gap, combined by the longer diverging channel effect, which is discussed with figure 2-18.

A smaller minimum gap caused by rigidity of the foil in the back-pressured foil bearing lowers the lubricant's flow rate. Figure 2-24 shows that the higher rigidity not only moves the location of the turning points in the loop-shaped solution trajectories to the higher downstream pressure but also expands the size of the loop in flow rate dimension, of which the reasons are discussed with figures 2-22 and 2-23.

Figure 2-24 also shows that the foil stiffness draws down overall flow rate and that the transition of structure is expanded to the wider interval of downstream pressure.

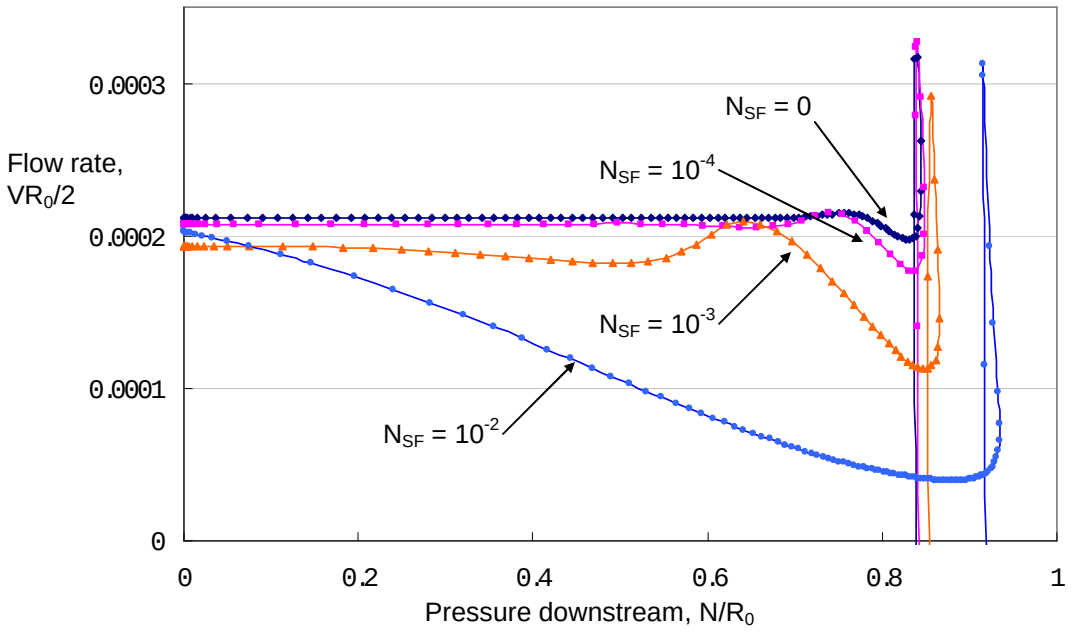

Fig. 2-24. Flow rate, q versus the difference of pressure downstream from the ambient, P_{down}, at four different stiffness numbers, $N_{SF} \equiv \frac{K}{R_0^{\,2} N_0}$, in back-pressured foil bearing. ($N_{EL} = 10^{-6}$, $\theta_A = \theta_D = 7°$, $\theta_0 = 20°$, $P_{up} = 0$)

2.8. CONCLUSION

The system equation of elastohydrodynamics of foil bearings was solved by Galerkin's method with finite element basis functions. The pressure and gap profiles agreed well with the data published previously.

The effects of the upstream and downstream pressure differences from the ambient were studied. The upstream pressure difference increases the flow rate of the lubricant, whereas the effect of the downstream pressure difference on the lubrication flow rate is not appreciable until the downstream pressure difference approaches the turning point because the upstream part of the foil bearing keeps the characteristic structure of the foil bearing, the virtually-uniform-gap zone and the minimum clearance.

The loop-shaped turning point was found when downstream pressure was increased. The turning point come from the structure near the downstream virtual tangent point, the minimum gap and pressure swing, which cuts the pressure effect from transferring from the downstream of it to the upstream of it, or in the reverse way also. This structure is kept by the negative pressure valley forming at the diverging channel downstream of the downstream virtual tangent point.

The stiffness of the foil makes the flow channel rigid so that the pressure peak and valley are intensified and that the foil bearing structure forms in wider length. The study of this wider class of foil bearings brought us further insights on the foil bearing structure, which is useful in understanding more complicated elastohydrodynamic system like tensioned-web over slot die coating.

Chapter 3

Elastoviscocapillary Model of Single Layer Tensioned-Web Coating.

3.1. INTRODUCTION

Coating gap, the clearance between the substrate and lip surface of the slot die, should be kept constant in time, which is one of the most important process conditions to ensure the coating uniformity in slot die coating. For example, in conventional slot die coating, where a substrate to be coated is backed by a roll of big radius, if the gap between backup roll and the lips of the slot die varies with time, the wet coating is non-uniform in the downstream direction. Gap variation in fixed gap slot coating usually comes from run-out or dynamic behavior of the bearing of the backup roll, and sometimes from mechanical vibration of the die and its mounting.

As technologies advance and diversify, more and more applications require thin coating layers; applications of optical films and magnetic storage tapes are good examples. The importance of constant coating gap grows as coating

thickness becomes thinner. Slot die coating with back-up roll, which relies on precision machining and mounting to main for narrow and constant gap, seems to have reached its limits. One of the possible solutions to overcome this difficulty is the use of elastohydrodynamics, the interaction between elastic force and hydrodynamic force. The prime example of elastohydrodynamic coating systems is tensioned-web slot die coating.

In tensioned-web slot die coating system no backup roll is needed; instead web wraps the slot die and moves over them (as is shown in Fig. 3-1). The coating liquid issued from slot die forms lubricating layer between web surface and lips surfaces of the slot die. The coating gap is maintained by the elastohydrodynamic force balance between the elastic force from the curved and tensioned web and the pressure force from the liquid of the coating bead. The price for the thin coating gap of tensioned-web coating is the necessity of good web-handling system to ensure constant web tension around the coating station.

In many cases, properly designed one-dimensional theoretical model gives clear and efficient picture about the mechanism by which a given system works. The viscocapillary model for the coating bead flows in the slot die coating is a good example of successful model; not only its predictions agreed reasonably with experimental results, but also it gave the coating engineers a clear understanding on the pressure profile in the coating bead so that they can expect how pressure profile changes by process conditions change. The coating bead can be maintained only in a particular range of pressure difference across the bead. With quasi-static lubrication theory, Ruschak (1976) and Higgins and

Scriven (1981) analyzed why the coating bead requires these pressure differences to maintain a stable bead. Ruschak made the simplified analysis by assuming that the viscous effects in the bead are negligible and that the pressure difference in the bead is caused solely by capillary effects. Higgins and Scriven included viscous effects by separating the bead into two distinct rectilinear flows; one upstream of the feed slot and the other downstream of it. In these two regions, the flow is a superposition of obligatory Couette flow and Poiseuille flow, and the pressure drop due to viscous effect can be simply calculated by lubrication approximation of slider bearings. These analyses provided not only reasonable coating window diagrams but also some insight on the coating bead behavior.

For tensioned-web slot die coating, no successful one-dimensional model has been published yet, although Lee (2002) reported one in his M. S. thesis. Hyunil Lee proposed a one-dimensional model for tensioned-web slot coating system by adapting the foil bearing model of Barrow (1967) to tensioned web slot die. But his model's application was limited to simple die shapes consisting of two arc-shaped lips without offset between them, and he didn't present any analysis result from his model. In this chapter, a one-dimensional elastohydrodynamic model of the tensioned-web slot die coating is presented. The model consists of combined equations of the lubrication approximation of flow and the shell theory of flexible web. The proposed model can be used for analyzing any shape of die lips and any set of process conditions including departure web angle, approach web angle, flow rates, liquid viscosity, web speed, and web tension.

The approach web angle θ_A and the departure web angle θ_D are measured from the imaginary horizontal line which is perpendicular to the upstream inner wall of the feed slot. [Fig. 3-1]

Convenient simplifications, in particular considering tensioned-web slot die coating to be a combination of basic foil bearings, are proposed in a later part of this chapter. It proves useful to design die geometries or assess suitable process condition with die lip design given.

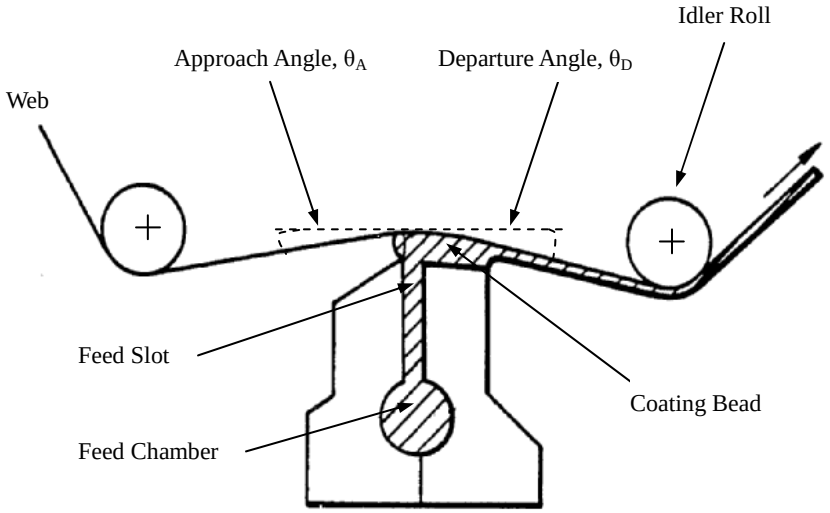

Fig. 3-1. Schematic of typical tensioned web slot coating (Chino et al. 1988)

3.2. Elastoviscocapillary model of tensioned-web slot coating

In tensioned-web slot die coating, the lubricating fluids filling the gap between the surfaces of the substrate and slot die are coating liquid and the ambient air; both fluids are separated by upstream and downstream menisci. The fluids in the

lubricating film flowing through a thin and narrow passage are described by Reynolds equation for incompressible steady flow of a Newtonian fluid. Since the cross-web direction flow is negligible in the cases considered,

$$\frac{\partial}{\partial x_s}\cdot\left(\frac{hV}{2}-\frac{h^3}{12\mu}\frac{\partial p}{\partial x_s}\right)=0 \qquad (3\text{-}1)$$

where h is gap between the surfaces of substrate and slot die, p is the pressure in the lubricating layer, V is the speed of the substrate web, μ is viscosity of the lubricating layer, and x_s is arc length running along the die lip surface [see figure 3-2]. The terms inside the bracket in the Reynolds equation is the flow rate of the lubrication flow, q.

$$q=\frac{hV}{2}-\frac{h^3}{12\mu}\frac{\partial p}{\partial x_s} \qquad (3\text{-}2)$$

Shell theory describes the deformation of a flexible web [Flügge 1973]. When deformation of the web in the cross-web direction is neglected, shell theory gives two force balance equations and one moment-of-momentum balance equation:

$$\frac{dN_s}{ds}-\kappa_s Q_s+P_s=0 \qquad (3\text{-}3)$$

$$\frac{dQ_s}{ds}-\kappa_s N_s+P_r=0 \qquad (3\text{-}4)$$

$$\frac{dM_s}{ds}-Q_s=0 \qquad (3\text{-}5)$$

s denotes the tangent direction. κ_s is the principal curvature of the shell, and P_s and P_r are external loads per unit area in tangential direction and normal-to-the-shell direction, r, respectively. P_s is viscous shear and P_r pressure difference across the shell. The normal stress resultant in tangential direction, N_s, is web

tension. Q_s is transverse shear stress resultant acting on a plane normal to the tangential direction. M_s is bending moment.

If the web is described by Hooke's elasticity law is adopted, the bending moment, M_s is simply related to the principal curvature along the web profile.

$$M_s \cong -K\kappa_s \qquad (3\text{-}6)$$

K is the flexural rigidity defined as

$$K \equiv \frac{Et^3}{12(1-\nu^2)} \qquad (3\text{-}7)$$

E is the elastic Young's modulus of the web, t is thickness of web, and v is its Poisson ratio.

With Eqs. (3-6) and (3-7), $Q_s = -K\frac{d\kappa_s}{ds}$. Eqs. (3-4) and (3-5) become

$$\frac{dN_s}{ds} + \kappa_s K\frac{d\kappa_s}{ds} + P_s = 0 \qquad (3\text{-}8)$$

$$-K\frac{d^2\kappa_s}{ds^2} + \kappa_s N_s - P_r = 0 \qquad (3\text{-}9)$$

Usually web tension is a dominant force in the tensioned-web slot die coating system, so that the tangential load in tangential direction, P_s, can be ignored. In this case Eq.(3-9) becomes

$$N_s = -\frac{1}{2}\kappa_s{}^2 K + N_0 \qquad (3\text{-}10)$$

N_0 is the tension of flat web, i.e. web tension when the curvature of web is zero. Eq. (3-11) combines with force balance in the normal to the shell surface, Eq. (3-10), to yield

$$-K\frac{d^2\kappa_s}{ds^2} + \kappa_s\left(-\frac{1}{2}\kappa_s{}^2 K + N_0\right) - P_r = 0 \qquad (3\text{-}11)$$

When cylindrical coordinates are chosen as base coordinate system for calculation and when the gap profile, h(θ), is measured in radial direction, the gap profile is the difference of die shape function D(θ) and web shape profile r(θ).

$$h(\theta) = r(\theta) - D(\theta) \qquad (3\text{-}12)$$

Expression of curvature in cylindrical coordinate is [Weatherburn 1927]

$$\kappa_s = \frac{2(\frac{dr}{d\theta})^2 - r\frac{d^2r}{d\theta^2} + r^2}{\left((\frac{dr}{d\theta})^2 + r^2\right)^{3/2}} \qquad (3\text{-}13)$$

When the reference surface of lubrication approximation is defined to be the slot die surface, Eq. (3-3) becomes

$$q = \frac{hV}{2} - \frac{h^3}{12\mu}\frac{\partial p}{\partial \theta}\frac{\partial \theta}{\partial x_s}, \qquad \frac{\partial x_s}{\partial \theta} = \sqrt{D(\theta)^2 + \left(\frac{dD}{d\theta}\right)^2} \qquad (3\text{-}14)$$

When the radial load across the shell is the pressure difference from the ambient, the force balance in normal direction to the shell, Eq. (3-12), becomes

$$-K\frac{d^2\kappa_s}{d\theta^2}\left(\frac{d\theta}{ds}\right)^2 + \kappa_s\left(-\frac{1}{2}{\kappa_s}^2 K + N_0\right) - \Delta p = 0, \qquad (3\text{-}15)$$

where $\frac{\partial s}{\partial \theta} = \sqrt{r(\theta)^2 + \left(\frac{dr}{d\theta}\right)^2}$, $\Delta p = p - p_{atm}$

Equations (3-13), (3-14), (3-15), and (3-16) forms the basic system equation set for the elastohydrodynamics of the tensioned-web slot die coating system.

Since, in tensioned-web coating system, gap between substrate and die surface is not fixed, a coating gap is inadequate to be chosen as a length unit. Instead, length unit can be found from the die shape, i.e. feed gap or radius of

curvature of the most critical part on die lip surface, good example of which is an arc of circle confronting the biggest portion of wrap angle. When equations (3-13), (3-14), (3-15), and (3-16) are non-dimensionalized with length unit, R_0, flow rate unit, $R_0V/2$, and pressure unit, N_0/R_0,

$$h^*(\theta) = r^*(\theta) - D^*(\theta) \tag{3-16}$$

$$\kappa_s^* = \frac{2(\frac{dr^*}{d\theta})^2 - r^* \frac{d^2 r^*}{d\theta^2} + r^{*2}}{\left((\frac{dr^*}{d\theta})^2 + r^{*2}\right)^{3/2}} \tag{3-17}$$

$$q^* = h^* - \frac{h^{*3}}{6N_{EL}} \frac{\partial p^*}{\partial \theta} \frac{\partial \theta}{\partial x^*_s}, \qquad \frac{\partial x^*_s}{\partial \theta} = \sqrt{D^*(\theta)^2 + \left(\frac{dD^*}{d\theta}\right)^2} \tag{3-18}$$

$$-N_{SF} \frac{d^2 \kappa^*_s}{d\theta^2} \left(\frac{d\theta}{ds^*}\right)^2 + \kappa^*_s \left(-\frac{N_{SF}}{2} \kappa^{*2}_s + 1\right) - \Delta p^* = 0, \quad \frac{\partial s^*}{\partial \theta} = \sqrt{r^*(\theta)^2 + \left(\frac{dr^*}{d\theta}\right)^2} \tag{3-19}$$

The asterisks mean non-dimensional variables but they are be suppressed from now on. N_{EL} and N_{SF} are elasticity number and stiffness number respectively.

$$N_{EL} \equiv \frac{\mu V}{N_0}, \qquad N_{SF} \equiv \frac{K}{R_0^2 N_0}$$

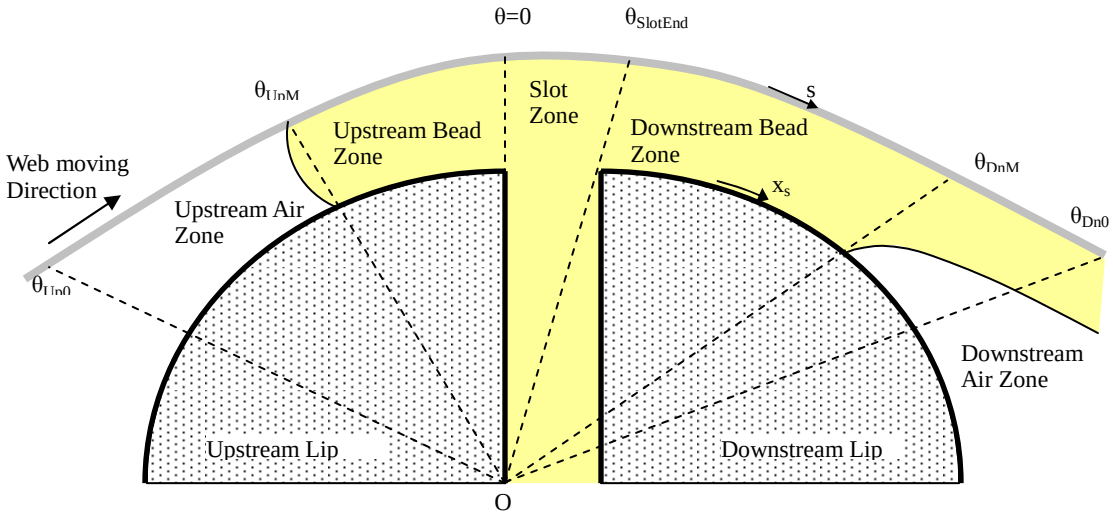

Fig. 3-2. Five zones of different lubrication flows in single layer tension-web slot coating.

Five zones in single-layer tensioned-web slot die coating.

As shown in Fig. 3-2, a lubricating flow in single-layer tensioned-web slot die coating is divided into five zones by the fluid type and their flow rates.

Upstream meniscus, downstream meniscus, and both the ends of feed slot set the boundaries of each zone. Upstream bead zone is where coating liquid flows on the upstream lip, bounded by the upstream meniscus and the upstream end of the feed slot. In steady state operation, net flow rate is zero in the upstream zone. Downstream bead zone is where the coating liquid flows on the downstream lip, bounded by the downstream meniscus and the downstream end of feed slot. Flow rate in the downstream zone is equal to the feed rate, q_f.

Upstream air zone occupies the upstream of the upstream meniscus and reaches to the far upstream end point, θ_{up0}, where boundary conditions are given. When the upstream meniscus is located near the feed slot and the approach angle is appreciable, higher than 3 degree when the upstream lip surface is smooth, high pressure develops in the upstream air zone as a consequence of elastohydrodynamic interaction on the lip and affects greatly the bead-break condition. In this condition, the surface roughness of the upstream lip also affects the bead breakup condition greatly. In elastohydrodynamics of tensioned-web system, thin gap is necessary to draw high pressure from the elastic force because the viscous drag force of the moving web acts stronger as the gap gets thinner. When gap height of the air lubrication layer is small so that it can be comparable to surface roughness of the upstream die lip, the rough lip surface can delay bead breaking as high peaks on the lip surface suppresses the development of high pressure [see chapter 4]. Downstream air layer is the downstream of the downstream meniscus to the far downstream end point, θ_{dn0}, where downstream boundary condition is set. In both air zones, net flow rates of air are zero. The liquid film in the most part of the downstream air zone moves in virtual solid body translation except at relatively short length near downstream meniscus.

The pressure profile over the slot zone can be regarded constant. Since there is no lip surface limiting the flow channel in the web moving direction in slot zone, the pressure change in the slot zone is not much compared to the other parts on the lip surface. Though the two dimensional flow effects, which are discussed in

Chapter 6, produces pressure change in this zone, it is small enough to be ignored in this one-dimensional model. The normal stress resultant of the web tension is dominant among forces in the tensioned-web slot die coating flow. Significant pressure change is mainly made by the elastohydrodynamic interaction especially in narrow gap area. The pressure change over the feed slot is relatively small.

The coordinate of the upstream end position of feed slot zone is set as $\theta = 0$.

Matching conditions at Menisci and Boundary conditions

Pressure and gap profile must be continuous at the borders of the zones, except the upstream and downstream menisci, where capillarity makes discontinuity in pressure. Pressures in each zone were matched at the borders with adjacent domains, with capillary pressure considered at the each meniscus. But no matching has been introduced for web shape profile, gap profile, and web curvature profile, since the web was treated as a single object over the whole calculation domain of the five zones. The positions of upstream meniscus and downstream meniscus, denoted by θ_{UpM} and θ_{DnM} respectively, are also unknowns to be found by solving the entire system equation including the pressure matching conditions and geometric relations.

The downstream meniscus was located at the position where the pressure jump across it is matched by the capillary pressure given by static and dynamic

contact angles and the shape of meniscus. Ruschak's extension(1976) of Landau-Levich equation, solution of film profile equation, can give the estimate of pressure difference across the downstream meniscus, when capillary number is small.

$$\frac{h_\infty}{R_{DnM}} = 1.34 N_{CA}^{\ 2/3}, \qquad N_{CA} \equiv \frac{\mu V}{\sigma} \tag{3-20}$$

$$p_{DownstreamBead} - p_{DownstreamAir} = \frac{\sigma}{R_{DnM}} \tag{3-21}$$

σ is surface tension of coating liquid. h_{00} is wet coating thickness. R_{DnM} is the radius of curvature of the downstream meniscus when viscous stress is negligible. The Landau-Levich equation is known to be precise when capillary number N_{CA} is smaller than 0.01 [Kheshgi 1983]. In some cases of this study, capillary numbers were bigger than 0.01 up to 0.1, but the inaccuracy from Landau-Levich equation didn't make significant changes in the total pressure profiles because the contributions of the capillary pressure at the menisci to the total pressure profile are small. The shape of the meniscus was approximated as an arc of circle connected with flat free surface of coated layer. This approximation gives the geometric relation to be met at the downstream meniscus.

$$h(\theta_{DnM}) Sin\left(\frac{\pi}{2} - \theta_{DnM} + \theta_{web}\right) = h_\infty + R_{DnM}\left\{1 + Cos(\theta_{die} + \theta_s - \theta_{web})\right\} \tag{3-22}$$

θ_{web}, θ_{die} and θ_s are slopes of the web and the die surface at the downstream meniscus, and static contact angle, respectively. Downstream meniscus should

locate so that both the pressure matching condition, Eq. (3-22), and the geometric relation, Eq. (3-23), are met.

The upstream meniscus locates at the balance of pressure. The pressure profiles in the upstream air lubrication layer and that in the upstream bead flow at the upstream meniscus must balance the capillary pressure difference there, which is given by Laplace-Young's equation. By assuming that shape of meniscus is an arc of circle:

$$p_{upstreamBead} - p_{UpstreamAir} = \frac{\sigma}{R_{UpM}} \qquad (3\text{-}23)$$

From the assumption on the shape of the meniscus, another geometric relation is given:

$$h\left(\theta_{UpM}\right) = R_{UpM}\left\{Cos\left(\theta_d + \theta_{UpM} - \theta_{web}\right) + Cos\left(\theta_s - \theta_{UpM} + \theta_{die}\right)\right\} \qquad (3\text{-}24)$$

R_{UpM} is a radius of curvature of the upstream meniscus. θ_d is dynamic contact angle. By combining Eq. (3-24) and Eq.(3-25), the equation for locating upstream meniscus is obtained.

$$p_{upstreamBead} - p_{UpstreamAir} = \frac{\sigma}{h\left(\theta_{UpM}\right)}\left\{Cos\left(\theta_d + \theta_{UpM} - \theta_{web}\right) + Cos\left(\theta_s - \theta_{UpM} + \theta_{die}\right)\right\} \qquad (3\text{-}25)$$

The locations where boundary conditions are set, θ_{Up0} and θ_{Dn0}, are chosen to be far enough from the virtual tangent points of the web to the die surface so that any variations in coating gaps at virtual tangent points do not make appreciably change the approach web angle and departure web angle. The upstream virtual tangent point is that at which straight web passing the passage point of the

boundary condition touches the die lip. The downstream virtual tangent point is defined in the downstream side in the same way the upstream virtual tangent point is defined. Pressure, web position, and curvature are set at both boundary points. Pressures at both boundary points are set to be ambient. The curvatures of the web there are set zero, which are in accordance with the ambient pressure condition. The positions of the web at both boundary points are fixed. The radial distances of the upstream and downstream passage points, r_{Up0} and r_{Dn0}, are set by the value meeting the approach and departure angles, respectively. Each radial distance is measured from the origin of the polar coordinate system, which is on the inner upstream wall of the feed slot and away from the top corner of the feed slot and upstream lip by R_0, the characteristic radius of curvature of upstream or downstream lip.

$$p(\theta_{Up0}) = p_{Ambient} \tag{3-26}$$

$$r(\theta_{Up0}) = r_{Up0} \tag{3-27}$$

$$\kappa(\theta_{Up0}) = 0 \tag{3-28}$$

$$p(\theta_{Dn0}) = p_{Ambient} \tag{3-29}$$

$$r(\theta_{Dn0}) = r_{Dn0} \tag{3-30}$$

$$\kappa(\theta_{Dn0}) = 0 \tag{3-31}$$

Solution method

To solve elastohydrodynamic system equation consisting of (3-17), (3-18), (3-19), and (3-20) for pressure profile p, web shape profile r, gap profile h, and curvature profile of the web κ, Galerkin's weighted residual method was used with finite element basis function. Quadratic polynomial functions were used to represent field variables. All the integrals were evaluated by Gaussian quadrature with three Gauss points per element. The resulting nonlinear system of algebraic equations for the coefficients of the basis functions were solved by Newton's method. Iteration proceeded until both $\|\mathbf{u}\|_{L_s}$ and $\|\mathbf{R}\|_{L_s}$ are less than 10^{-9}.

Except the slot zone, all zones were divided into 100 elements respectively when die lip surface doesn't have sharply curved portion; when the non-dimensional radius of curvature at the sharpest part is bigger than 0.5. The slot zone was divided into 10 elements since slot zone is narrow and the pressure change there is small. One-dimensional version of spine scheme [Kistler 1984] was used to distribute the nodes inside the zones since both the upstream and downstream menisci are unknown and moving during the calculation. Nodes were equally spaced in each zone. As the meniscus moves, the positions of the other nodes were decided proportionally by the ratio of the distance to the node from the stationary point to the distance of the meniscus to the stationary position at the other end of the zone. Stationary positions are θ_{Up0} and θ_{Dn0} in upstream air zone and downstream air zone respectively, and 0 and $\theta_{SlotEnd}$ in upstream bead zone and downstream bead zone respectively. The solution space was

explored by arc-length continuation [Musson 2000]. The shape of the resulting Jacobian matrix is bordered due to the entries related to the menisci positions and arc-length continuation variables. Keller's bordering algorithm [1977] was used to solve the linear system without losing the benefits of banded structure. Linear solver used in calculation was direct band-matrix solver from LINPACK.

3.3. ELASTOHYDRODYNAMICS ON THE CYLINDRICAL DIE

Cylindrical lip shapes were chosen for the first die shapes to be analyzed by theoretical model described in section 3.2, since cylindrical surface has uniform curvature profile, with which the elastohydrodynamic effect, the interaction of web deformation and pressure, can be isolated from the die shape effect. The die shapes analyzed are shown in Fig. 3-3. Each die lip surface is an arc of circle, of which the end at the feed slot side is tangent to the base circle of radius R_0; at lease one out of upstream lip radius and downstream lip radius was set as R_0 and the feed slot width was kept smaller than 0.01 radian, so that the feed slot doesn't change the overall die shape from the combination of upstream and downstream lip arcs.

Pressure profiles and gap profiles along the cylindrical die surfaces of $R_d^* = R_u^* = 1$ about three different flow rates with speeds, tensions, and fluid viscosities held fixed are shown in Fig. 3-4.

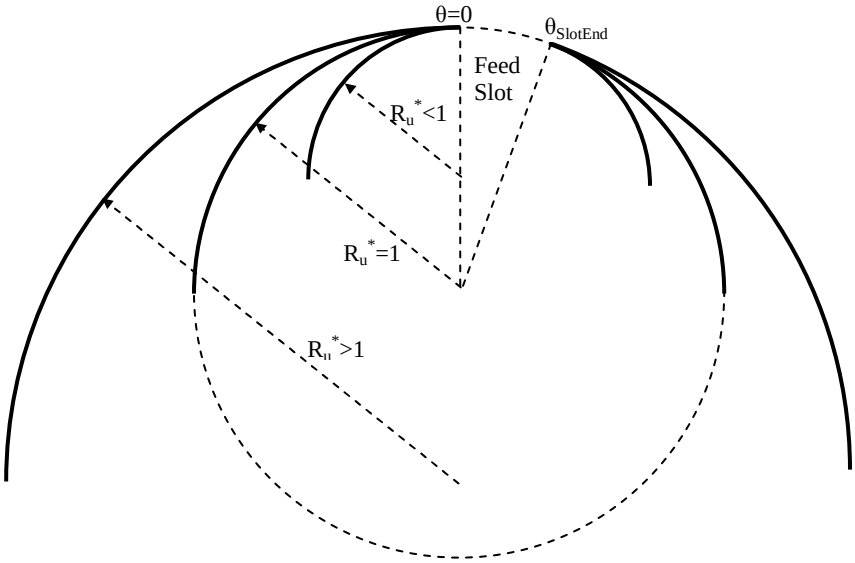

Fig. 3-3. Cylindrical die shapes with different radius of curvature. At least one die lip was designed to have $R^* = 1$.

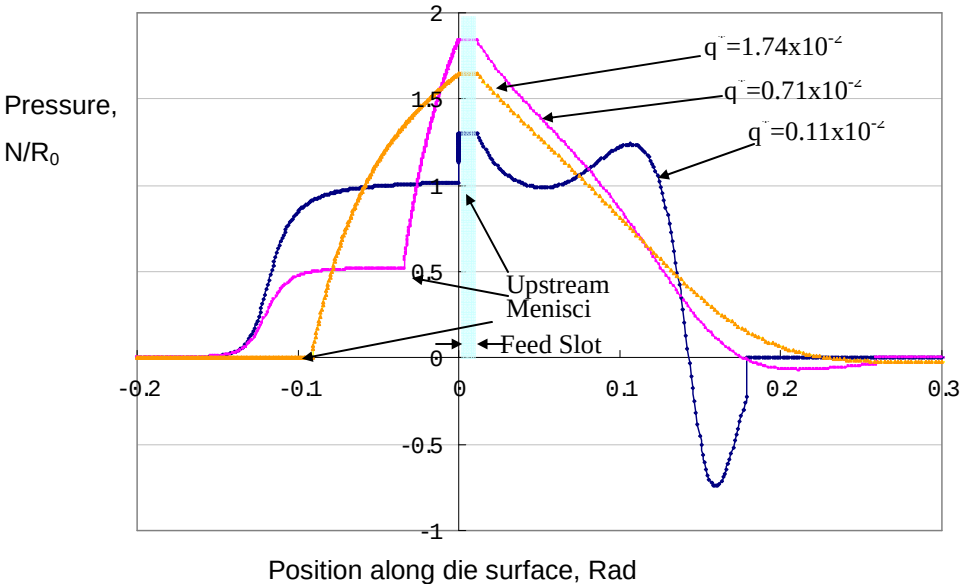

(a) Pressure profiles along the cylindrical die surface.

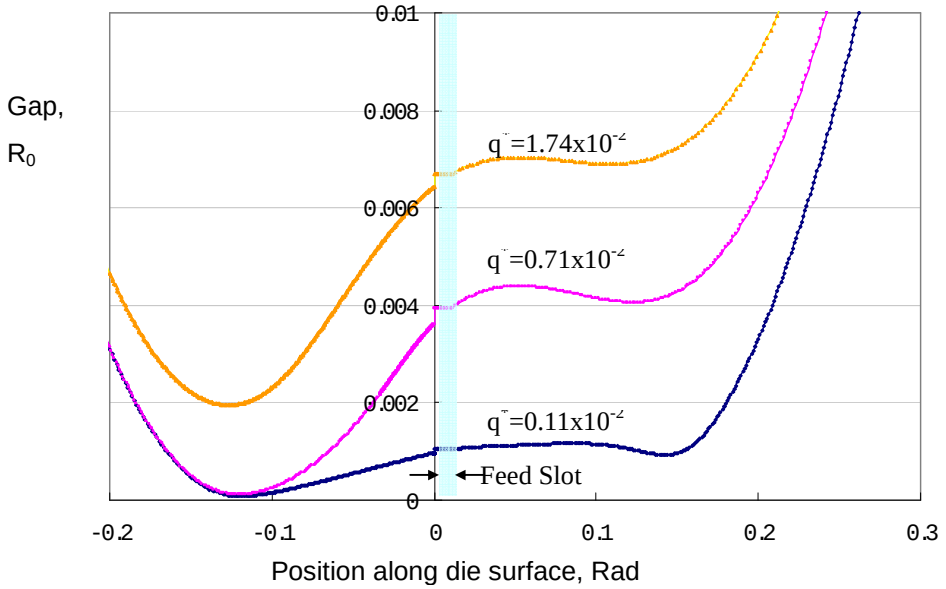

(b) Gap profiles along the cylindrical die surface.

Fig. 3-4. Pressure profiles and gap profiles in tensioned-web coating with cylindrical die when $R_d^* = R_u^* = 1$, $\theta_A = \theta_D = 7°$, $\theta_{Dn0} = \theta_{Up0} = 30°$, $N_{SF} = 0$, and $N_{EL} = 5x10^{-5}$.

The other parameters conditions in Fig. 3-4 are: θ_s =95°, θ_d = 105°, σ = 66.5 dyne/cm, μ = 22.5cp, and N_{SF} = 0. These conditions are the same throughout this chapter when there's no condition specified. On the upstream lip the net flow rate of lubricant is zero both in the air lubrication layer and coating liquid lubrication layer. When feed rate $q^* = 0.11 \times 10^{-2}$, upstream meniscus advances to the feed slot with most part of the upstream lip covered with air lubrication layer. The pressure profile of this air lubrication layer on upstream lip is similar to that of the "blocked foil bearing", a special case of back-pressured foil bearing with the net lubricant flow rate zero [Chapter 2]. As the feed rate rises, the upstream meniscus recedes to the upstream so that both the upstream air zone and the upstream bead zone occupies appreciable lengths on the upstream lip as is the case of $q^* = 0.71 \times 10^{-2}$ in Fig. 3-4(a). The upstream air zone still has the pressure profile of blocked foil bearing, but the upstream bead zone is different from the blocked foil bearing though its net flow rate is also zero. The pressure peak in the upstream bead zone originates from the feed slot, where pumping coating liquid generates high pressure to lift up the substrate expanding the narrow flow channel over the feed slot. The steep pressure gradient in the upstream bead zone induces the backward Poiseuille flow, which is counterbalanced by the forward Couette flow made by substrate movement. When the feed rate is high as in the case of $q^* = 1.74 \times 10^{-2}$ in Fig. 3-4, the pressure peak generating from the feed slot pushes the upstream meniscus to the near of the upstream virtual tangent point, so that further increase in feed rate makes the coating liquid spill out of the upstream meniscus to the upstream.

Fig. 3-5 shows movement of upstream meniscus with feed rate changing when die shape is cylindrical with $R_d^* = R_u^* = 1$. As the feed rate rises the upstream meniscus moves back to the upstream until it reaches turning point, where the sign of gradient of solution trajectory changes as well as stability of solution [D. Joseph 1989]. The turning points in Fig. 3-5 are flooding points beyond which coating liquid starts spilling over to the upstream so that pre-metering is lost, Stable steady-state solution doesn't exist beyond these points until the feed rate reaches another turning point, which is not shown in Fig. 3-5.

Physical interpretation of the turning point on flooding point is effectively given by blocked foil bearing consideration. For the net flow rate of coating liquid in the upstream bead zone to be zero, the flow in the upstream bead zone must have balance between the Couette flow caused by moving substrate and the Poiseuille flow caused by the pressure gradient arising from the feed slot. When the feed rate rises, it raises the gap height around feed slot, especially the gap on the upstream lip. The gap height affects the Couette flow by order one and the Poiseuille flow by order of three [see Eq. 3-3]. Since the rise of the gap height affects the Poiseuille flow more, the upstream meniscus recedes to the upstream until it finds a new balance point of narrow gap. But if the feed rate is on the turning point, the upstream meniscus is at some point near the virtual upstream tangent point, at which further increase in the feed rate will push the upstream meniscus to the direction of raising gap clearance. In this geometrical condition, which is the case of the lower branches of the curves in fig. 3-5, the upstream meniscus cannot find a new balance point. Therefore the solution obtained with

this feed rate is in flooding condition and is instable.

The other limit in feed rate occurs when upstream meniscus reaches the downstream corner of upstream lip. Reducing feed rate moves the upstream meniscus downstream. When the upstream meniscus reaches downstream corner of upstream lip, it cannot move any further to the downstream; this situation is beyond the capability of this one-dimensional model. This condition is considered as the bead-break points beyond which air invades into the coating bead. Locating the upstream meniscus right on the downstream corner of upstream lip i.e., the $\theta = 0$ position, brings a difficulty in the numerical calculation scheme of present approach because length of the upstream bead zone would shrink to zero. To prevent this singularity condition, the position of $\theta = -10^{-4}$ was taken as the limit position for the upstream meniscus to reach before coating bead breaks. The range of possible feed rate is limited by two extreme points; the minimum feed rate is set by bead-break limit point and the maximum feed rate is set by the turning point where flooding occurs.

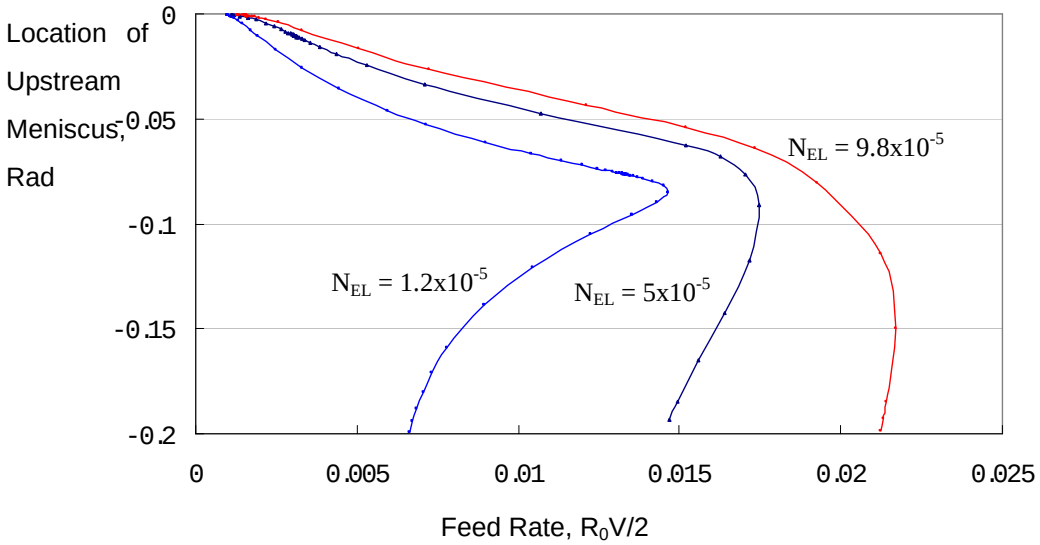

Fig. 3-5. Movement of the upstream meniscus as feed rate changes. Process conditions: Cylindrical die with $R_d^* = R_u^* = 1$, $\theta_A = \theta_D = 7°$, $\theta_{Dn0} = \theta_{Up0} = 30°$.

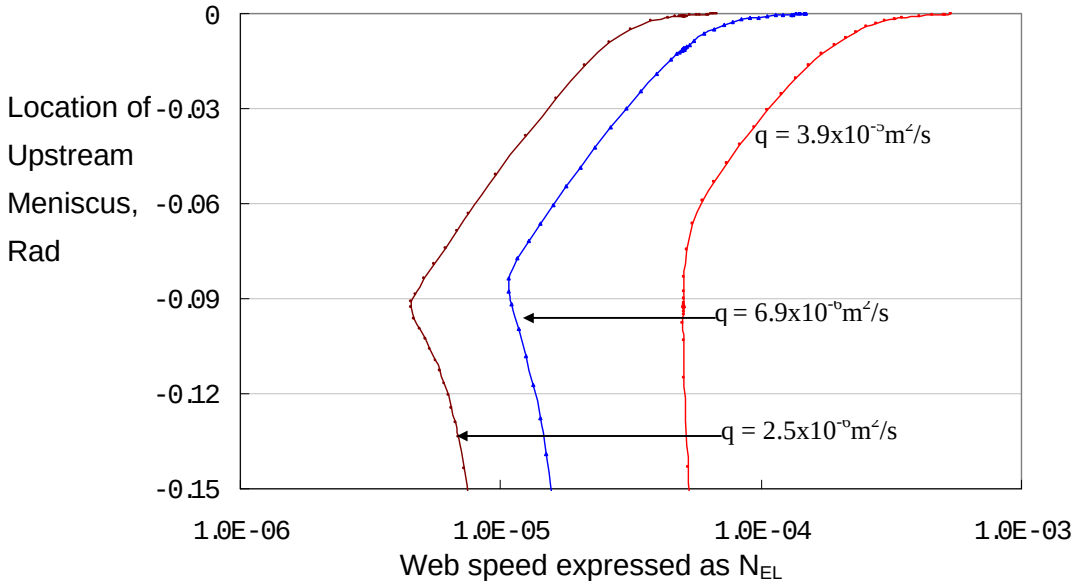

Fig. 3-6. Movement of upstream meniscus when web speed changes. Process conditions: Cylindrical die with $R_d^* = R_u^* = 1$, $\theta_A = \theta_D = 7°$, $\theta_{Dn0} = \theta_{Up0} = 30°$, $R_0 = 1$ cm.

Fig. 3-6 shows the movement of upstream meniscus as web speed changes with feed rate fixed. As web speed slows, the upstream meniscus moves upstream. When the upstream meniscus reaches some point near the virtual tangent point of the web, a turning point, which is taken to be flooding point, appears. As web speed rises, upstream meniscus advances downstream toward the bead-break point.

Fig. 3-7 shows the pressure profiles and gap profiles of several flow rates near the bead-break points. The pressure profiles in the downstream bead zone are those of the forward-pressured foil bearings of which the upstream pressure difference from the ambient is negative, and the pressure profiles on the upstream are those of typical blocked-foil bearings. Big pressure valleys, characteristic feature of negative-upstream-pressured foil bearing, appear near the downstream menisci since, at bead-break points with cylindrical dies, web runs faster than the speed of the standard foil bearing of which the pressures downstream and upstream is ambient. Another contribution to the pressure profiles comes from feeding effects. As are shown in Fig. 3-4(a) and Fig. 3-7(a) feeding generates pressure peak around feed slot to lift web and make channel wider for fed liquid to flow.

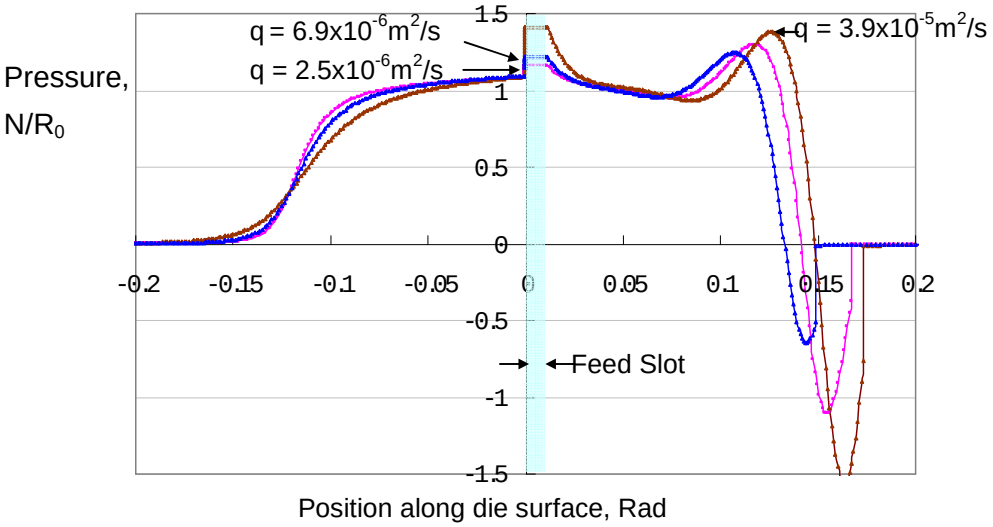

(a) Pressure profiles near bead-break points

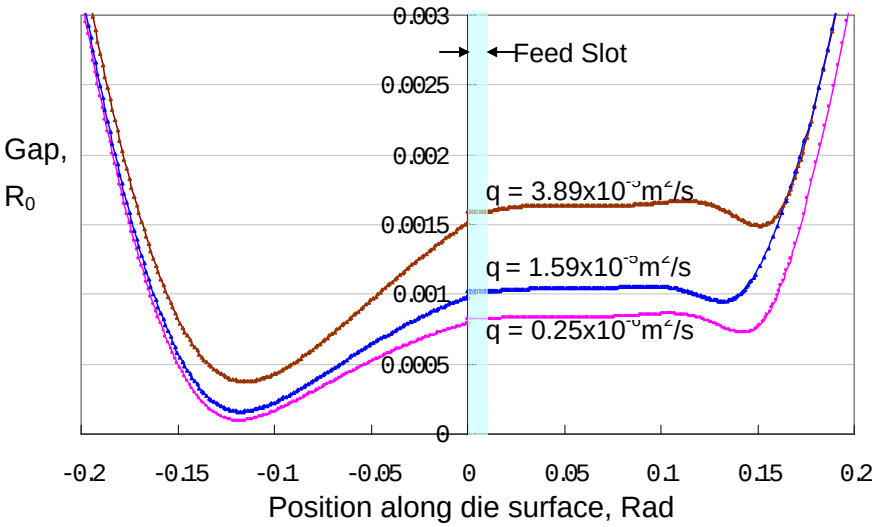

(b) Gap profiles near bead-break points

Fig. 3-7. Pressure and gap profiles near bead-break point with different feed rates. Process conditions: Cylindrical die with $R_d^* = R_u^* = 1$, $\theta_A = \theta_D = 7°$, $\theta_{Dn0} = \theta_{Up0} = 30°$, $R_0 = 1$ cm.

3.4. EFFECT OF WEB STIFFNESS

The effects of web stiffness in tensioned-web elastohydrodynamic system are discussed in the chapter 1 with foil bearings. With non-zero stiffness of the web, the elastic force of the shell is added to the force balance, which was between the tension resultant force and the pressure difference across the web. The elasticity of the shell makes the change of the web slow so that the pressure profile of the elastohydrodynamic system of elastic shell resembles more that of fixed gap flow.

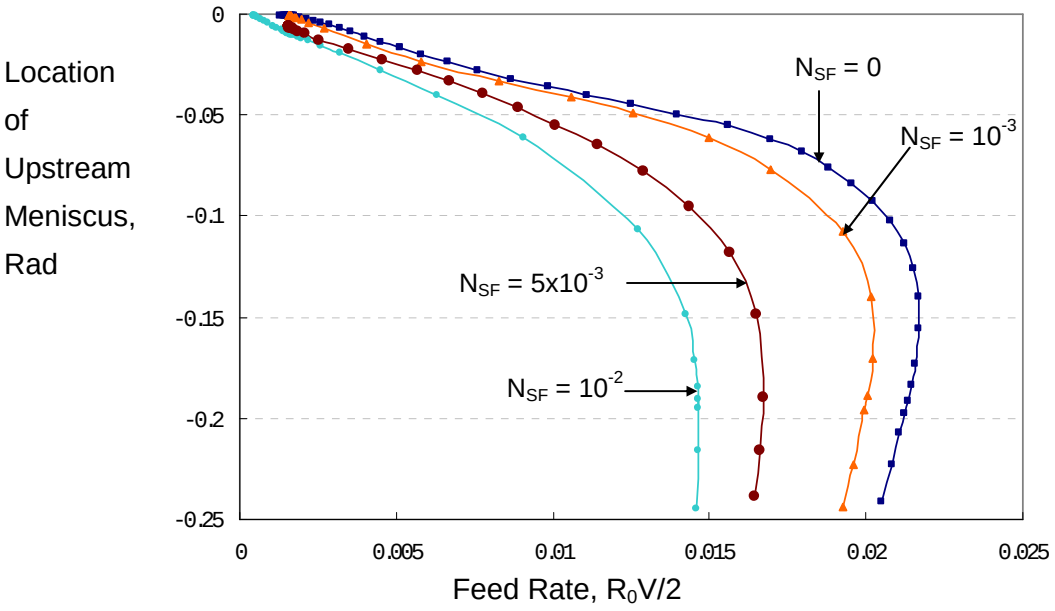

Fig. 3-8. Effect of web stiffness on the movement of the upstream meniscus as feed rate change. Process conditions: cylindrical die with $R_d^* = R_u^* = 1$, $\theta_A = \theta_A = 7°$, $\theta_{Dn0} = \theta_{Up0} = 30°$ and $N_{EL} = 1x10^{-4}$..

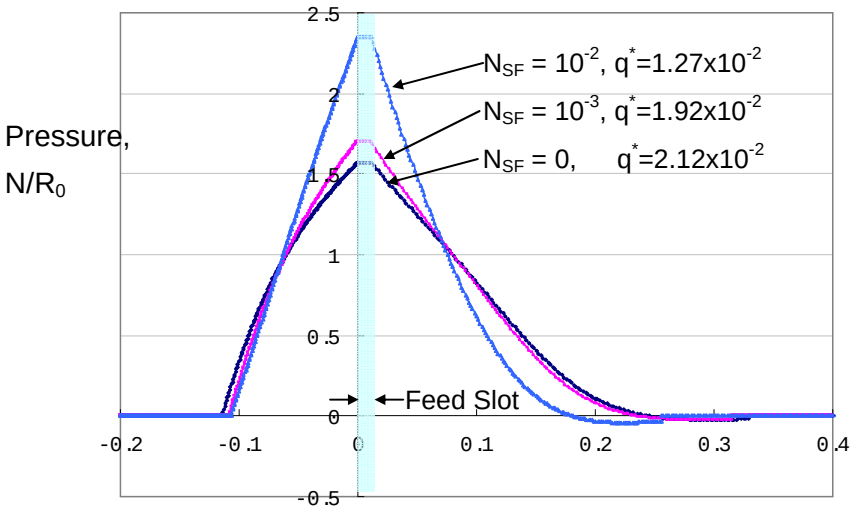

(a) Calculated pressure profiles with the upstream menisci around θ = 0.11 rad.

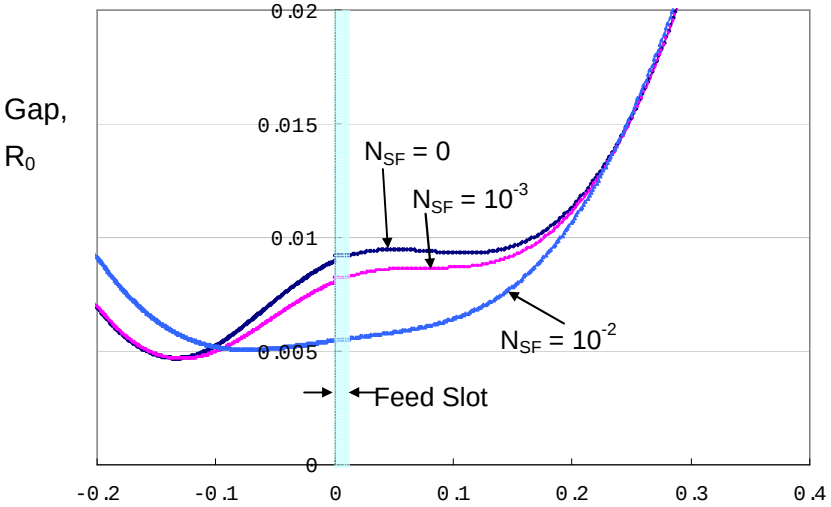

(b) Calculated gap profiles with the upstream menisci around θ = 0.11 rad.

Fig. 3-9. Pressure and gap profiles when the upstream menisci are near flooding point with different web rigidities. Process conditions: cylindrical die with R_d^*= R_u^*= 1, θ_A= θ_D= 7°, θ_{Dn0}= θ_{Up0}= 30°, and N_{EL} = 1x10^{-4}.

Fig. 3-8 shows the movement of upstream meniscus over the cylindrical die shape wrapped by webs of 3 different rigidities as feed rate changes. As the web stiffens, the range of possible feed rate, the part of solution trajectory between bead-break point and flooding point, shrinks and shifts to the lower feed rate. The shifts are bigger in flooding point side than those in the bead-break points. Fig. 3-9 shows the pressure and gap profiles on the cylindrical die when upstream menisci are near $\theta = 0.11$, i.e., when upstream menisci are near the upstream virtual tangent point. As the web stiffens, the gaps on the upstream and downstream lips get narrow since the elastic force of the stiff web presses down the coating bead more strongly with web stiffness increased. Higher pressure also develops around the feed slot with the web stiffness increase to sustain the flow channel over the feed slot against the elastic force of the stiff web and to issue the liquid through the narrower channel. This high pressure pushes the upstream meniscus to the outside and causes the earlier flooding as shown in Fig. 3-8.

A stiff shell also takes longer span to adapt to the new force balance than the flexible membrane. Fig. 3-10 shows the pressure and gap profiles on the cylindrical die when the upstream meniscus is near the bead-break point. When the web is stiff ($N_{SF} = 10^{-2}$), the span of close gap shrinks since the stiffness of the web is partly supporting the web near the virtual contact points. As a result of narrower span in close gap, the higher pressure in the coating bead is generated since same amount of the tension resultant force should be balanced in the shorter span.

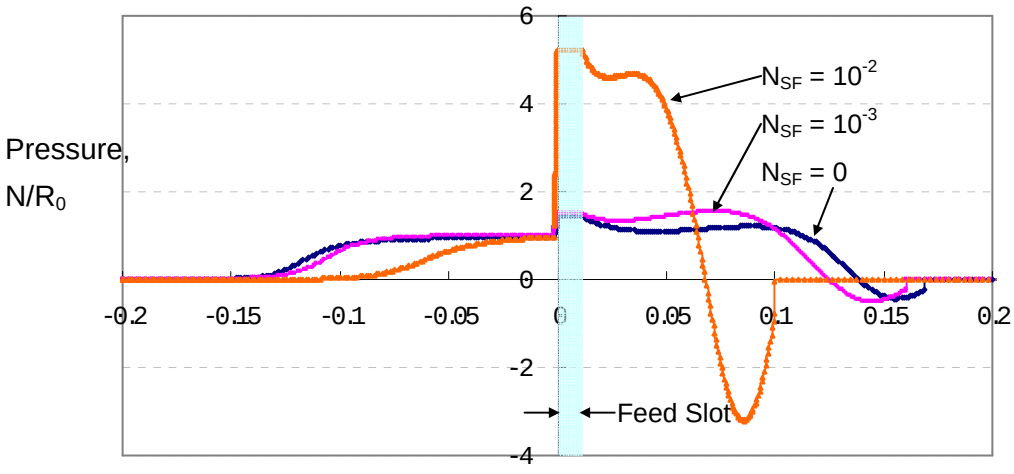

(a) Pressure profiles when the upstream menisci are around θ = 0.013 rad.

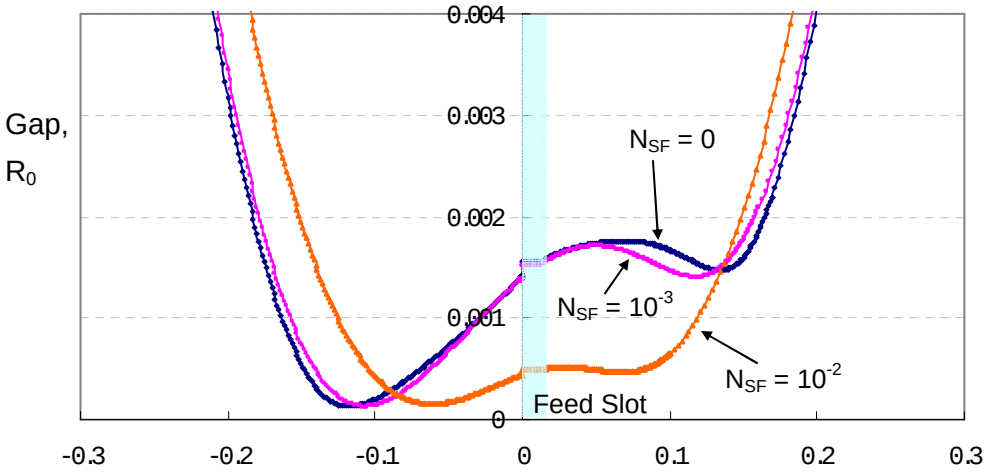

(b) Gap profiles when the upstream menisci are around θ = 0.013 rad.

Fig. 3-10. Pressure and gap profiles when the upstream menisci are near bead-break point with different web rigidities. Process conditions: cylindrical die with $R_d^* = R_u^* = 1$, $\theta_A = \theta_D = 7°$, $\theta_{Dn0} = \theta_{Up0} = 30°$, and $N_{EL} = 1x10^{-4}$.

3.5. EFFECT OF RADIUS OF CURVATURE OF THE DIE LIP

The pressure in the approximately uniform zone in a foil bearing is necessarily proportional to N/R_0 [Eshel et al. 1965], which implies that the pressure profile along the gap of the tensioned-web coating can be controlled by manipulating the curvature profile of the die; higher curvature of the die induces higher curvature of the web, which raises the normal stress resultant and hence induce higher pressure on it. To check this idea, die shapes consisting of two cylindrical lips, as explained in Fig. 3-3, were altered by changing the radius of curvature of each lip surfaces, and pressure and gap profiles of each shape were checked with theoretical model in section 3.2.

The effect of downstream lip curvature on the pressure profiles and gap profile is shown in Fig. 3-11. With each die shape, the feed rate was manipulated to position the upstream meniscus at same location of $\theta = 0.01$ radian, which is near the corner of feed slot. As expected from the theory, the higher pressure forms on the downstream lip of higher curvature. The upstream meniscus positions itself at the balance of pressure. The pressure upstream of it, i.e. the pressure in the upstream air zone, is formed by elastohydrodynamic interaction on the upstream lip, and its profile is similar to the pressure profile of blocked foil bearing. Since in the three cases in Fig. 3-11 the upstream air layer conditions are almost same, i.e. same elasticity number and same lip surface, the pressure profiles in the upstream air zones are very similar each other. The only difference between the cases is the gap height on the upstream meniscus, which is in the

right end of upstream air layer. The pressure in the upstream bead zone is contributed by the pressure ridge of feeding effect and the pressure fields generated by elastohydrodynamics on both the lips. Not only the upstream lip shape but also the downstream lip shape affects the pressure in the upstream bead zone, especially when the upstream meniscus is near the feed slot; since the pressure fields in the every zone are in a balance. When the downstream lip has high curvature, the pressure there forms high and also affects the pressure in the upstream bead zone. Fig. 3-11 shows that when the downstream lip curvature is raised the feed rate should be manipulated to be smaller to keep the upstream meniscus at the same location. In another words, when the thin coating layer is required, high curvature in the downstream lip is favorable.

Fig. 3-12 shows the solution trajectories solved with downstream lips of three different radii in the space of feed rate and upstream meniscus position. In the trajectory with higher curvature on the downstream lip, the flooding point, which is on the turning point in the right side of the curve, occurs at smaller feed rate than that in the trajectory of flatter downstream die lip. This tendency agrees well with the discussion in the previous paragraph; higher pressure on the downstream lip pushes the upstream meniscus backward. The difference in the feed rates of the bead-break points by changing downstream lip curvature is not so big as compared to the difference made in the flooding points. The reason is that the feeding effect dominates the pressure field around the feed slot when the gap over the feed slot is small; when the upstream meniscus is near the bead-break point, at least with the smooth die shapes shown in Fig. 3-3, pressure peak

rises over the feed slot to expand the flow channel around it. The effect of the lip curvature is small in such conditions.

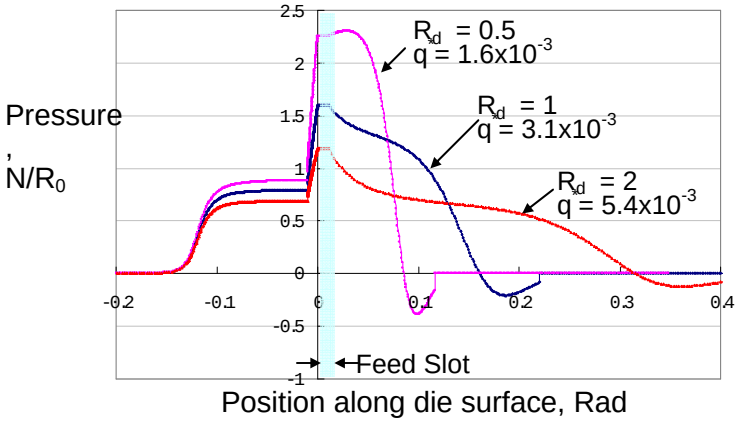

(a) Pressure profiles along the die surfaces

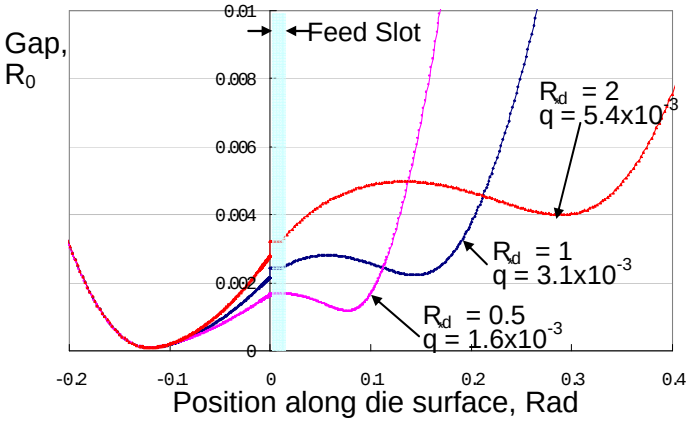

(b) Gap profiles along the die surfaces

Fig. 3-11. Effect of the curvature of the downstream lip on the pressure profile, gap profile, and feed rate q^* with upstream meniscus kept in $\theta = 0.01$. Process conditions: Cylindrical die with $R_u^* = 1$, $N_{EL} = 5x10^{-5}$, $\theta_A = \theta_D = 7°$, $\theta_{Dn0} = \theta_{Up0} = 30°$.

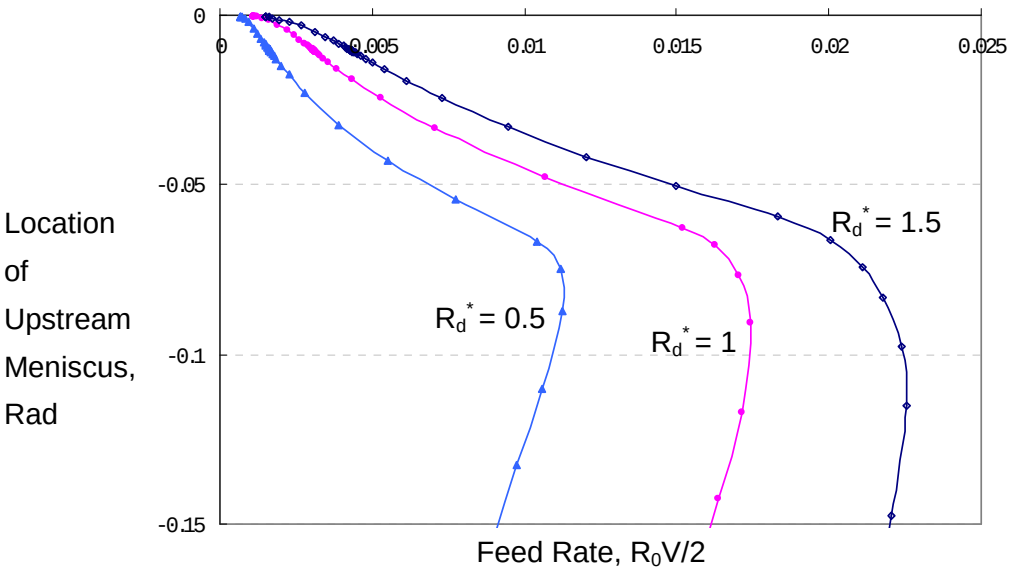

Fig. 3-12. Effect of downstream lip curvature on the the upstream meniscus position as feed rate changes. Process conditions: Upstream lip shape is arc of circle with $R_u^* = 1$, $\theta_A = \theta_D = 7°$, $\theta_{Dn0} = \theta_{Up0} = 30°$, and $N_{EL} = 5x10^{-5}$.

Fig. 3-13 shows how upstream lip curvature does indeed affect pressure and gap profiles. Again the feed rate was manipulated to fix the upstream meniscus positioned in some point near the feed slot; it was fixed at $\theta = 0.01$. As is expected from the consideration of blocked foil bearing, which is simpler and similar to the upstream air zone of the tensioned-web slot coating, pressure at the upstream meniscus was almost proportional to the upstream lip curvature. When R_u^* is reduced from the base value of $R_u^* = 1$, higher pressure is formed in the upstream air zone and feed rate should be raised to keep the upstream meniscus in same place; when the upstream lip is flattened, lower pressure is formed in the upstream air zone, and the feed rate should be reduced to maintain the upstream meniscus in the same spot.

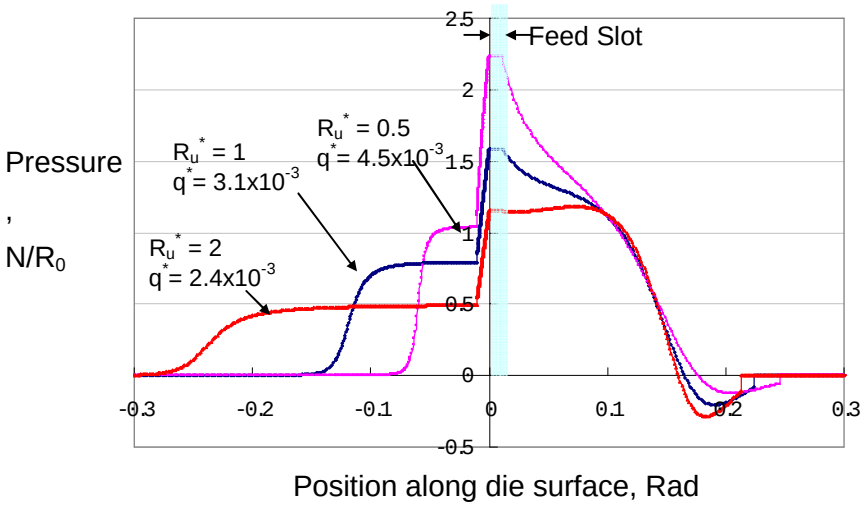

(a) Pressure profiles along the die surfaces

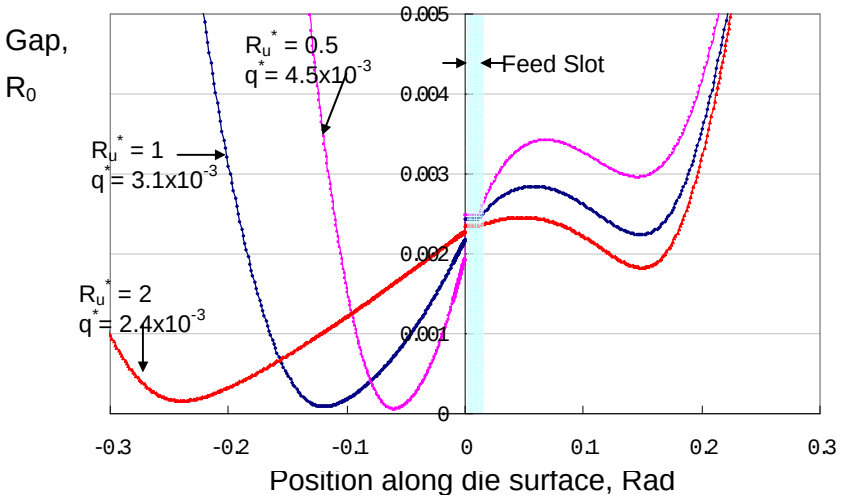

(b) Gap profiles along the die surfaces

Fig. 3-13. Effect of the curvature of the upstream lip on the pressure profile, gap profile, and feed rate q^* with upstream meniscus kept in θ = 0.01. Process conditions: Cylindrical die with R_d^* = 1, $\theta_A = \theta_A = 7°$, $\theta_{Dn0} = \theta_{Up0} = 30°$.

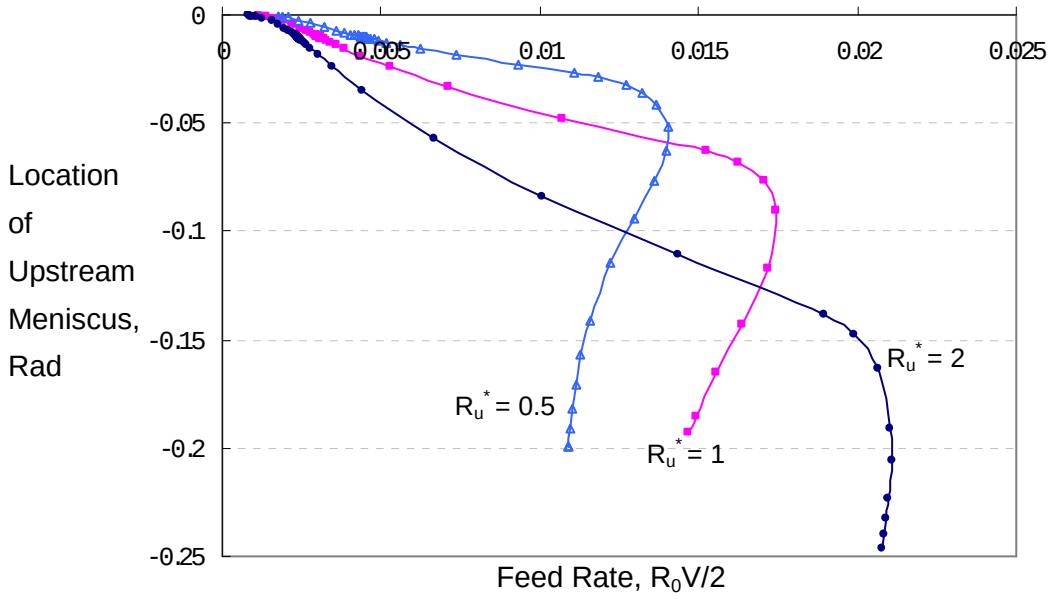

Fig. 3-14. Effect of downstream lip curvature on the the upstream meniscus position as feed rate changes. Process conditions: Upstream lip shape is arc of circle with $R_d^* = 1$, $\theta_A = \theta_D = 7°$, $\theta_{Dn0} = \theta_{Up0} = 30°$, and $N_{EL} = 5x10^{-5}$..

The solution trajectories in the feed rate and upstream meniscus position plane were calculated with three die shapes of different upstream lip radii [Fig. 3-14]. Higher curvature on the upstream lip not only generates higher pressure in upstream air zone but also makes the back-flow passage in the upstream bead zone narrower. Both of these effects, with the feed rate same, make the upstream meniscus located closer to the feed slot when the upstream lip is more curved. Though these effects are also favorable for expanding feed rate operation range, which is from the bead-break point to the flooding point, the operation range shrinks by mounting smaller radius upstream lip in Fig. 3-14.

That is because reducing the lip radius shortens the length of the close wrap on the upstream lip, and the effect of shortening length of flow passage is bigger than that of making lip curved. Again the feed rate of the bead-break point is not so sensitive to the upstream lip radius since the feeding effect dominates when feed rate is small and the gap over the feed slot is thin.

3.6. FOIL BEARINGS IN SERIES SIMPLIFICATION

Reflections on the previous sections lead to a simple model of tensioned-web slot die coating, which otherwise has to be understood in terms of system of the nonlinear governing equation, viz. membrane equation and lubrication approximation. What becomes evident is that single layer tensioned-web slot die coating behaves similarly to a system consisting of two foil bearings in series with the feed source between them; one upstream of the slot and one downstream of it, with pressure continuous at the feed slot between them. The elastohydrodynamic interaction in the upstream air zone is the same as in a foil bearing blocked downstream so that the net flow rate of lubricant is zero. The elastohydrodynamic interaction over the downstream lip is the same as that in a forward-pressured foil bearing. The feeding effect adds another pressure mountain around the feed slot. Especially, its effect on the pressure profile in the upstream bead zone is dominant. The pressure profile of tensioned-web slot die coating is a combination in series of a blocked foil bearing's pressure profile and

a forward pressured foil bearing through which the flow rate is feed rate, added by a contribution of the feeding, as shown in Figs 3-4, 3-7, 3-11, and 3-13.

In fact, separating contributions of the each part to the total pressure profile is not possible, since the all pressure contributions—contributions from upstream lip and downstream lip, and feeding, and capillary pressure changes over the menisci—are interconnected and should be balanced as a whole for the steady state operation. This simplified structure enables handy idea about how the system will respond to the changes and how the system should be designed.

3.7. MORE GENERAL DIE SHAPES

Another class of die shapes having offset between the heights of upstream lip corner and downstream lip corner was analyzed by one-dimensional elastoviscocapillary model. Fig 3-15 shows the three die shapes, of which the radii of curvatures of the upstream lips are all 10mm and the radii of curvature of the downstream lip are all 6mm. Three shapes denoted by M, ML, and MR are different by the location of downstream lip's apex point.

Pressure profiles and gap profiles were calculated with die shapes M, ML, and MR for the same process condition, $N_{EL} = 2.8 \times 10^{-6}$, $q^* = 4.2 \times 10^{-4}$. As shown in Fig. 3-16, pressure field in the coating bead rises and the upstream meniscus position approaches to the bead-break point, as apex point on the downstream lip moves upstream. The explanation on the pressure rise comes from force balance

between the tension-resultant force of the web membrane and the pressure force acting on the web. Total amount of web-tension-resultant forces pressing on the downstream lip are same for all three die lips, since same departure web angle is given. But as downstream lip's apex point moves to the feed slot, the area where significant tension-resultant force is applied gets narrow. Therefore, to keep the force balance between the total pressure force and the total tension resultant force, higher pressure should develop within the area between the downstream tangent point and the feed slot. Higher pressure in the coating bead pushes the upstream meniscus back to the downstream. High pressure on the downstream lip is also not a favorable condition for a thin coating because it will induce Poiseuille flow downstream.

According to this consideration, a die designer might want to put downstream lip's apex point at the downstream part of the downstream lip for fast operation speed or for thin coating. But a designer also should be careful not to make recirculation on the downstream lip by putting sharp point on the downstream part or by making deep offset on the upstream corner of downstream lip

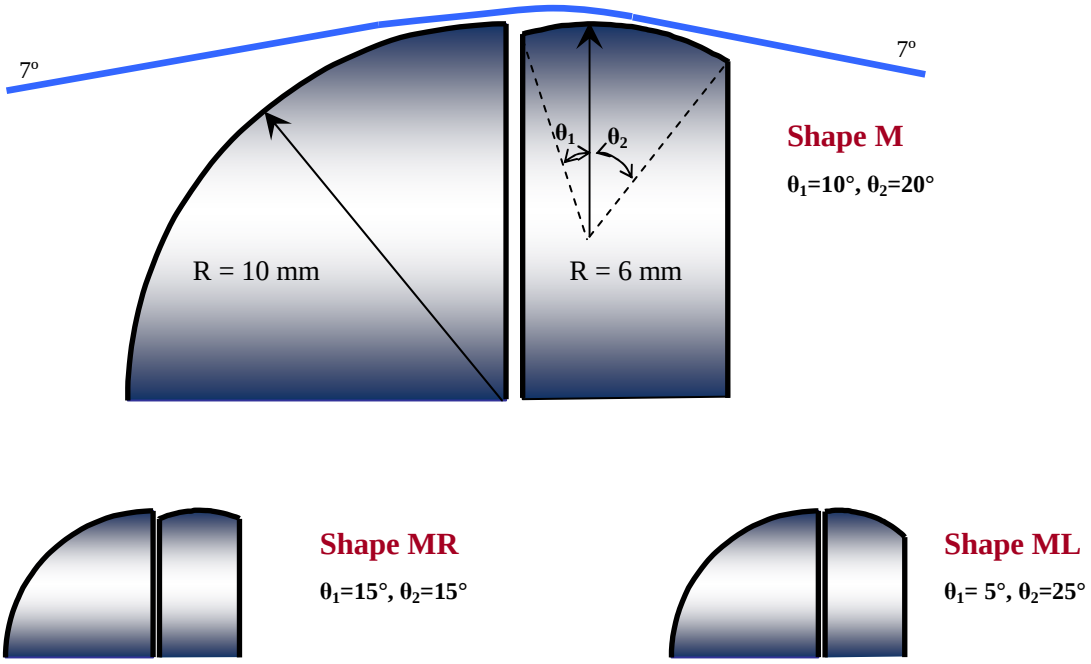

Fig. 3-15. Shape M, Shape MR, and Shape ML

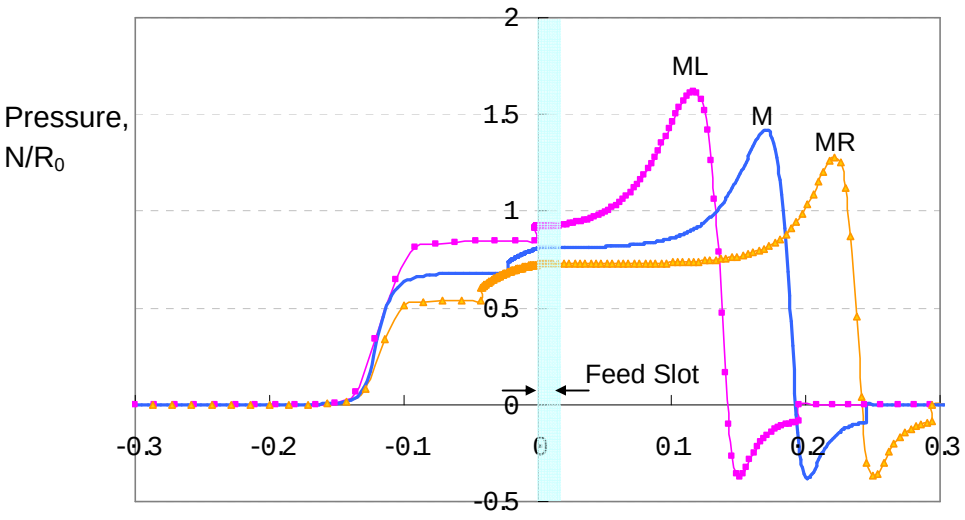

(a) Pressure profiles

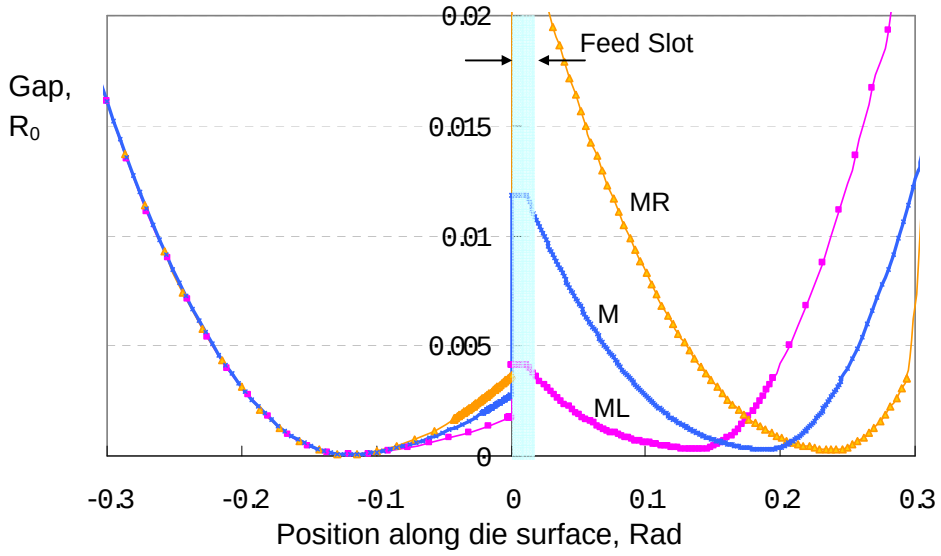

(b) Gap profiles

Fig. 3-16. Pressure and gap profiles with die shapes M, MR, and ML. Process conditions: $\theta_A = \theta_A = 7°$, $\theta_{Dn0} = \theta_{Up0} = 60°$, $N_{EL} = 2.8 \times 10^{-6}$, $q^* = 4.2 \times 10^{-4}$, $R_0 = 11.25$mm.

3.8. CONCLUSION

One-dimensional elastohydrodynamics model of tensioned web slot coating , which is based on the lubrication equation and shell theory, was solved and gave its prediction on the pressure profiles and gap profiles inside the coating bead and menisci positions. By tracking the upstream meniscus position as feeding rate or web speed changes, bead breakup condition and flooding condition was found; the bead breakup condition was defined to be the condition when the upstream menisci is at the downstream corner of upstream lip, and the flooding condition is found to be the turning point condition, beyond which the upstream meniscus would recede drastically.

Foil-bearing-in-series simplification that the pressure profile of tensioned-web coating bead is balanced combination of blocked foil bearing and forward pressured foil bearing added with feeding effect turned out to be efficient to understand the force balances in tensioned-web slot die coating system and useful for designing die geometries.

The curvature of the die lip and the position of apex point, when there’s offset in the die shape, are important design factor to manage and distribute the tension resultant force over the lip surface and to control the pressure profile inside the coating bead.

Chapter 4

Single-Layer Tensioned-web slot coating: Visualizations

4.1. INTRODUCTION

Tensioned-web coating is an attractive way of coating thin and uniform layers at high speed with a relatively simple setup—a combination of slot die and carefully controlled web transport. Tensioned web slot coating is similar to the conventional slot coating, in that pre-metered liquid issues from the slot into the gap between the die lip and the substrate which carries liquid away as a layer coated on it. But tensioned-web slot die coating has several advantages over conventional slot die coating: tensioned web slot coating doesn’t needs a back-up roll of which the surface must turn precisely through a circle in order to maintain a fixed gap, and coating gap is self-adjusting to coating thickness.

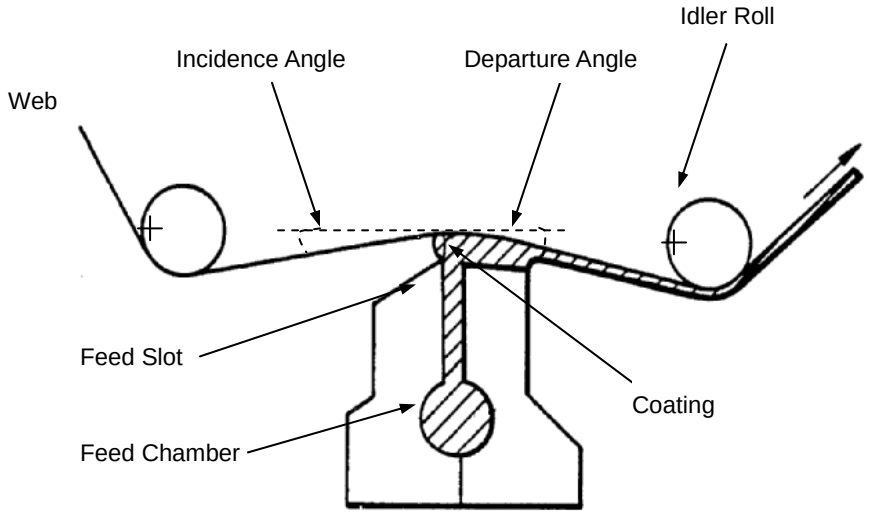

Fig. 4-1. Schematics of typical tensioned web slot coating (Chino et al. 1988)

Fig. 4-1 illustrates the typical arrangement of tensioned web slot coating. Two idler rolls support the moving web, which is under tension. Between them, the slot coating head comprising two lips (three in two-layer coating) and feed slot is pushed against the moving web, so that it makes a certain angle with the web. The normal force arises from the resultant of the tension in the curved substrate, which balances hydrodynamic forces exerted by the flowing coating liquid. The moving web, die lips and the viscous coating liquid in the clearance between web and lips constitute an elastohydrodynamic system, and the balance of forces in this system enables thin uniform liquid layer to be coated. In this arrangement, no precision back-up roll is needed, and less precise positioning of die may be acceptable, i.e. thinner coating becomes possible at relatively small cost. Vacuum upstream of the coating head is also unnecessary, since properly-designed die lip and proper process conditions including web tension and

approach web angles can manage the pressure profile inside the coating bead to keep the bead from breakup.

Die lip geometry plays central role in deciding pressure distribution inside the coating bead in tensioned web slot coating system. Understanding the relation of die geometry to the pressure distribution is indispensable in designing a tensioned-web slot coating system, since pressure distribution decides gap profile and operation limits such as maximum operating speed and minimum coating thickness. But it is not well-understood how to manage the pressure profile in tensioned –web slot coating. Lots of patents were claimed on the die lip shape for tensioned-web slot coating since Pipkin and Schaefer (1979) first claimed tensioned-web coating system with V-shaped slot die. Most of patent disclosed fragmentary pieces of information on the die shape. None of the patents gave clear explanation about how the die shapes changes pressure profiles inside the coating bead and how they affect the system's capabilities.

Despite the practical importance of the tensioned web coating slot coating system, only one theoretical study has been published in the literature. Feng (1998) analyzed the flow in the coating bead by solving the Navier-Stokes system by means of Galerkin's method with finite element basis function Mechanical behavior of the web he treated by membrane theory (Flűgge 1973) in which flexural rigidity, bending and twisting moments are neglected. With these arrangements, Feng succeeded in calculating reasonable pressure profiles and showed how they are changed by altering process conditions such as web tension, incidence angle and departure angle. He showed that gap height of

tensioned web coating system, i.e. the local distance between the web and the die surface, is regulated automatically by the action of elastohydrodynamics, when feed rate of liquid is changed, or equivalently the final coating thickness is changed. But only one type of the die lip shapes described by Tanaka et al. (1984) was studied in his work, and the effect of die lip shape was not discussed.

Lee (2001) studied the die shape effect in tensioned web slot die coating system experimentally by visualizing the coating beads from the top side and observed bead breakup behavior in various conditions. He recorded the minimum thickness possible varying upstream wrap angle and downstream wrap angles using circular shape slot die lip. He found that higher total wrap angle with higher departure angle is good for delaying bead break-up. Several kind of lip designs were tested in 3° symmetric wrap angle, among wh ich flat shaped lip was found to be good for maintaining bead in high speed to make a thinner coating layer.

Considering die lip shape of tensioned-web slot coating, we have to pay attention to sharply angled point, which will be called as “salient” in this paper, because a sharply angled point on the lip surface will receive concentrated tension resultant force which induces high pressure around it when web wraps the salient with sufficient angle. In this paper the effect of salient curvature and salient location is studied both by visualization and by theoretical model presented in chapter 3.

When sufficient approach angle is given on the upstream lip and upstream

meniscus is located in the downstream of the virtual tangent point, the point where the web will touch the die first if is no lubrication, air lubrication layer forms with pressure field generated by elastohydrodynamic interaction. In this condition pressure of air lubrication layer grows high enough to make a considerable contribution to the whole pressure distribution and affect operating conditions of whole coating system. Air lubrication layer thickness is so thin that sometimes the surface roughness of the die lip or those of substrates is comparable to the air layer thickness and that the web may touch the die surface. In these cases, pressure profile becomes lower than it should be formed by elastohydrodynamic interaction. These situations of thin air lubrication layer was discussed and analyzed with theoretical model in chapter 3 added by contact pressure estimation given by Lacey and Talke(1993).

4.2. Visualization of coating bead of tensioned-web slot die coating

4.2.1. Coating Apparatus

Fig. 4-2 is a schematic and a diagram of coating equipment and photograph of the coating station. The coating system is divided into roughly three parts; coating station, liquid pumping system, and web moving system.

In the coating station, the web is positioned by two 5.08 cm-diameter idler rolls, of which the horizontal positions can be changed and between which the slot die

is located. The die is mounted on a stand whose position can be adjustable in vertical direction. By manipulating the horizontal positions of idler rolls and the vertical position of slot die, adjustments of incidence and departure angle become possible.

The width of the slot die is 5.08 cm. In normal operation, this width is wide enough to secure the center portion of the slot head from side effects. But this narrow width does make it possible for the side effects to govern the whole width of the coating head, especially in the flooded condition. The coating die is designed to adjust its slot gap up to about 1600 μm by adding or removing steel shims between the die block and the lips [Fig. 4-3]. Slot lips were made of stainless steel to stand corrosion, wear, and scratches during the operation.

Coating liquid is supplied at a fixed rate up to 123 cc/min by syringe pump with 60 cc syringe (Havard Apparatus, Model 55-226, Southnatick, MA). The syringe pump was chosen to provide accurate pumping rate. The coated liquid is removed from the web by a squeegee roll with a soft rubber cover, which is installed so that it contacts the web after the departure idler roll. The squeezed liquid was collected and discarded. The still damp web is rewound and then discarded.

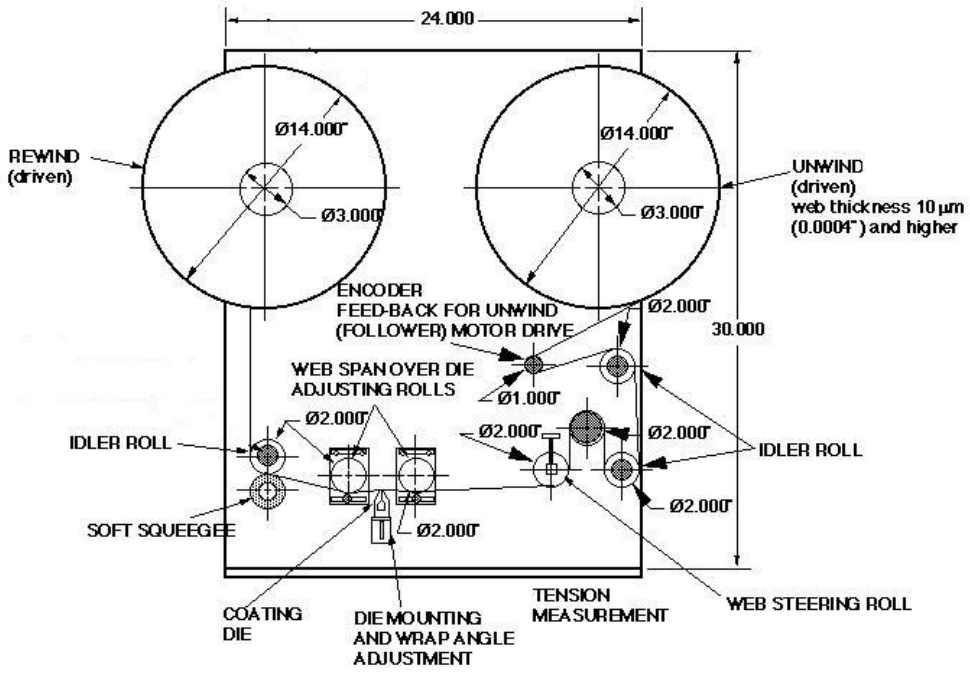

a) Schematic of the coating apparatus

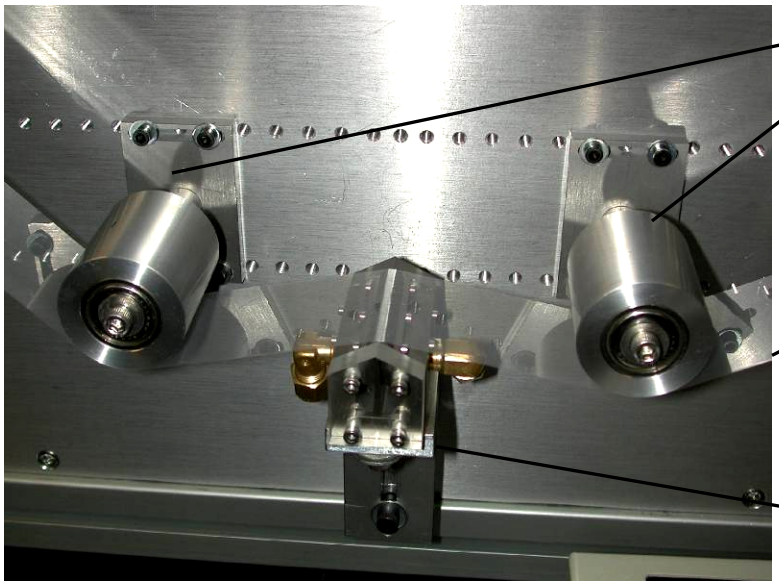

b) Photograph of coating station showing slot die, two idle rolls and position adjusting devices. The coating bead can be viewed through the transparent web.

Fig. 2. Structure of tensioned web slot die coating apparatus.

The web moving system is designed to control both web tension and speed. Two DC motors (Adjustable speed drive motor, Model 5BPB 56PA101, General Exlectric, Fort Wayne, ID: max.1750) and two motor controllers (Model M-drive, Contrex, MN) are used. Web speed is monitored by speed sensor (Model 711-S Accu-Coder, Encorder Product Company, Sandpoint, ID) and web tension is measured by load cell (Model RF, Dover Flexo Electronics, INC, Rochester, NH; Model TI-14 Indicator, maximum capacity, $10kg_f/2in.$). Both monitored signals are fed back to the controller.

Offset logic programmed in the motor controller is used for web speed and tension control. A schematic of its control logic was shown in Fig. 4-3. The motor that drives the rewinding wheel is named as “Master” and the motor that drives the unwinding wheel is named as “Follower”. The Master controller receives the signal from the speed sensor and drives the Master motor to maintain the web speed at a set value. The follower controller receives signals from the speed sensor, the load cell measuring tension, and the magnetic pickup on the follower motor and drives the follower motor to control tension at a set value. The offset parameter which is set by operator produces the difference in the speeds of the two motor to make tension in the running web. The motor controllers control the motor speeds by PID logic, of which parameters were adjusted to minimize oscillation in the web speed and tension through repeated trials.

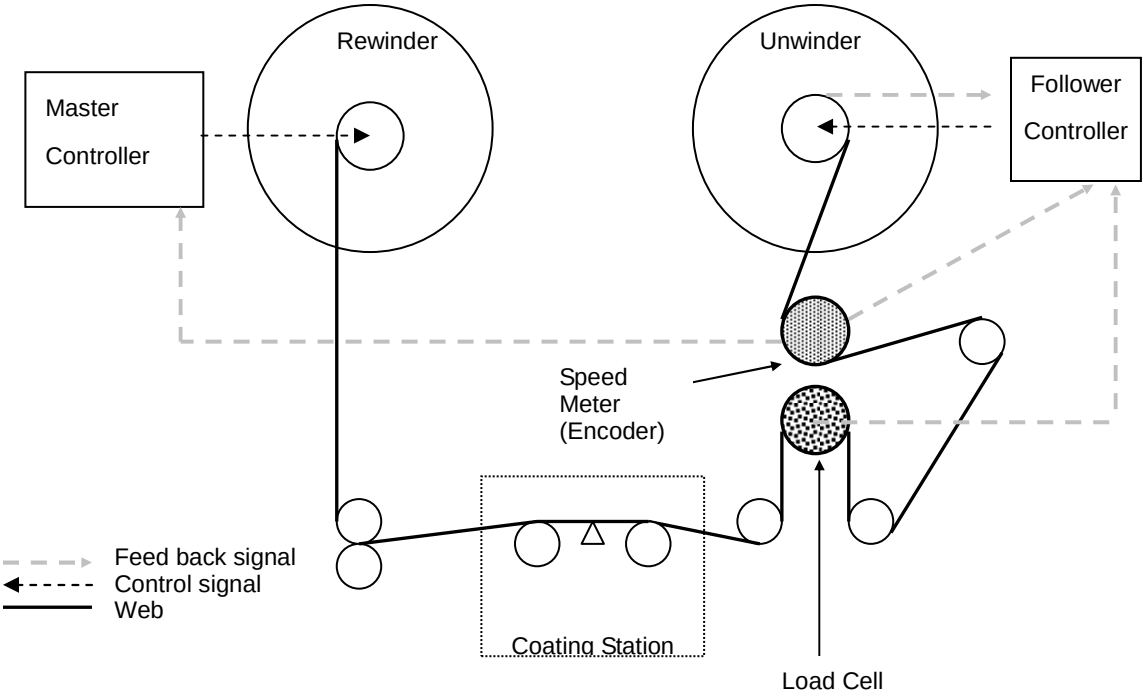

Fig. 4-3. Schematic of the control logic in web moving system.

4.2.2. Coating liquid and web material

As coating liquid, solutions of glycerin and water were used. Both are well known as Newtonian liquid and their mixture is also Newtonian liquid. 70% aqueous solutions of 99.7% pure glycerin (Item 599811, Milsolv Corporation, Menomonee Falls, WI) were used. The physical properties listed in CRC Handbook of Chemistry and Physics are shown in Table 4.1.

Glycerin %	Viscosity (cps)	Surface Tension(dyne/cm)	Density (g/cc)
100	1410	62.5	1.2611
70	22.5	66.5	1.1821
30	2.4	68.5	1.0713

Table 4.1. Surface tension & viscosity values of glycerin & water mixtures. (from CRC Handbook of Chemistry and Physics, 83rd Ed.).

The viscosity values were verified with Brookfield shear viscometer (YULA-15 ULA Spindle, Model DV-II+, Brookfield Eng. Labs., Stoughton, MA). To improve visibility of thin liquid film in the gap, less than 0.05%wt of organic die was added. (FDOC Blue No.1, Fischers' United Supply Inc., Minneapolis, MN)

12 μm PET film was used as substrate. Most of the substrate used was supplied by Mitsubishi Polyester Film, LLC. (Product ID: 24CT, 12μm) 24CT is transparent one-side corona treated film. In this experiment, untreated side was use.

4.2.3. The optics and imaging

A 35mm camera (Model NX18A, NEC, Tokyo, Japan) with magnifying lens attachment (Magnazoom 6000 with 1X adapter, Navitar, Rochester, NY) was placed above the web at the coating die to observe the minute movement of coating bead and its menisci. Fiber optic illumination was used to get better image. Figure 4 shows positions of the camera and illumination. Only top view

visualization was made in this experiment. The side view position was tried, but the coating gap is too small to observe bead with optical magnifying lens.

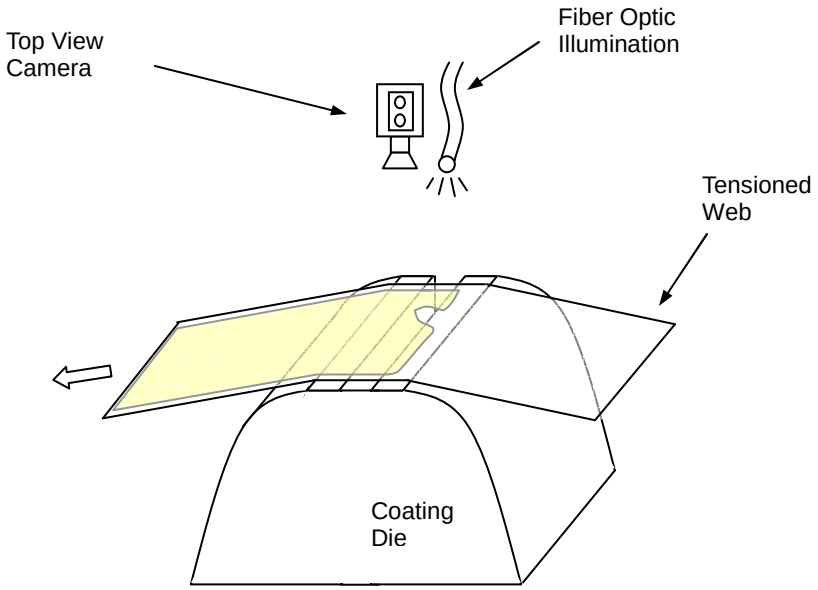

Fig. 4-4. Positions of camera and illumination.

4.2.4. Start-up procedure

After the die was assembled, its surface was cleaned with detergent and tap water followed by acetone cleaning and mounted on the die stand of which the height had already been adjusted for the desired web angles. The horizontal positions of each idler roll are also set for the incidence and departure web angles respectively.

When the die is mounted on the stand and the web is properly connected through the web moving system, operation can be started. The syringe pump

was turned on first to make liquid issued from the slot so that when the web was set in motion it would not scratch the surface of the lips. Next, the web speed was gradually increased by changing the Master controller speed setting. After web speed reached its set value, the Follower motor was turned on to control the web tension. Web speed and pumping rate were adjusted to the desired value for the experiment.

After one experiment was done, web speed, tension, and pumping rate were changed without shutting down, but to change incidence and departure web angle web moving system had to be shut down and start up again.

As web speed is reduced, or feed rate is raised, upstream meniscus moves back to the upstream. When further increase of feed rate or further reduction of web speed bring out spilling of coating liquid out of upstream meniscus, that point was recorded as flooding point. Conversely, upstream meniscus moves forward to the downstream as feed rate is reduced, or web speed rises. When air entrains into the coating bead though upstream meniscus with further rise of web speed or further reduction in feed rate, the condition is recorded as bead breakup point.

Most of experiments in this chapter were done by web speed sweeping; web speed was changed with feed rates fixed. Upstream meniscus locations were recorded as the web speed changed and bead breakup point and flooding point are checked at given feed rate.

4.2.5. Die geometry

In the study of die shape effect, the surface of high curvature is of the highest interest since it concentrates the tension resultant force on narrow area and can affect the whole pressure profile; the high pressure developed on the sharp surface can swell the web over the whole lip surface. In this thesis the surface of high curvature, especially the one around which the web wraps, is called by salient. Without wrapping of web around a salient, it doesn't receive the tension resultant force and is out of importance. The existence of salient on the die lip might not be favorable for some applications since it will be easy to be damaged by foreign particles in the coating liquid or can cause a recirculation under the swelled gap which it makes. But studying the effect of salient gives basic idea to understand the design of slot die for tensioned web coating.

To study the effects of salient curvature and its position, several die lip shapes were prepared. Die geometries are shown in Fig. 4-5. Each lip piece was designed to have same width, 1mm. Each lip was made differently by its salient curvature and its location; two flat surfaces were jointed with curved salient in the middle. Two kinds of curvatures were given on the salients; radii of curvatures were 25μm for sharp corner and 300μm for dull corner. The name of lip piece was named by its salient position and curvature; for example, the lip having salient in the middle of top surface was denoted as SM (sharp middle), and the other lip piece with dull salient at the end was denoted as DE (dull end). The shapes of the lips were checked with optical microscopes, and its salient

curvatures were verified by measuring height profiles of the lip surfaces with surface profiler (P10 profilometer, Tencor, San Jose, CA) and fitting a circle to the corner height profile measured. The error in measured radius of curvature in this way is within 15%. The angles at which two flat lip surfaces meet at the salient were 7°, which is equal to the approach and departure web angles given in experiments, so that all the tension-resultant force is applied around the salient.

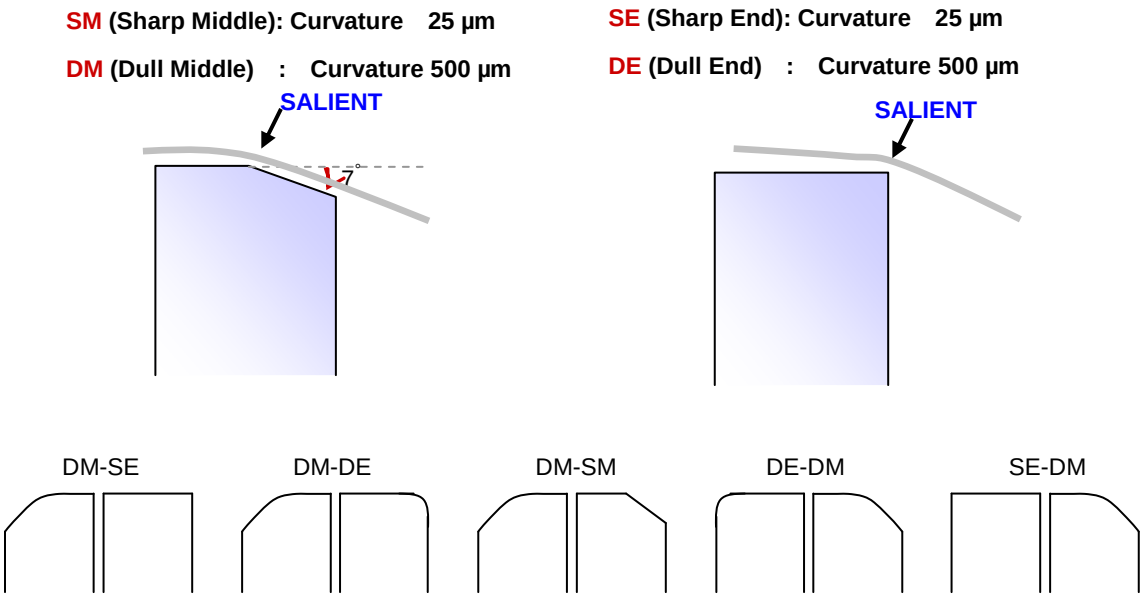

Fig. 4-5. Die geometries used in the experiments.

4.2.6. Effect of curvature on the downstream salient

A coating window is a parameter space within which the coated film is free of unacceptable defects. Coating windows of tensioned-web slot coating with couple of die lip geometries were shown in coating thickness versus elasticity plain in figure 6, where changes in elasticity were made by changing web speed. As shown fig. 4-6, coating windows are bound by two lines; one consisting of flooding points in low elasticity side and the other consisting of bead break up points in high elasticity side. Figure 6 shows two coating windows of two die geometries which are almost same except the curvatures of the downstream salients. In both geometries salients were put in the end corner of the downstream lip. The coating window was shifted to the higher speed and thinner coating thickness side as the salient gets sharper. Sharper salient on the downstream lip forms higher pressure profiles in the upstream of the salient; therefore bead breakup is delayed and flooding comes earlier by higher pressure in the coating bead.

4.2.7. Effect of downstream salient position

The effect of the downstream salient location on the coating window is shown in Fig. 4-7. Putting a salient in the downstream side of the downstream lip moved the bead breakup line to the higher speed and thinner coating. But the coating windows was wider when downstream salient is in the upstream side of the lip.

As is shown in chapter 3, the salient positioned in the upstream side on the downstream lip induces higher maximum pressure in the upstream of the salient since same amount of tension-resultant force, when same approach web angle and downstream web angle are given, should be balanced in narrower area. Higher pressure in the coating bead makes bigger contribution of Poiseuille flow in the coating liquid flow over the downstream lip, and results in thicker coating.

4.2.8. Effect of upstream salient curvature

Fig. 4-8 shows the effect of upstream salient on the coating bead. Two coating windows from experiments with the almost same die shapes except the upstream salient curvature show almost same bead breakup points while appreciable differences exist in the flooding point. In the bead-breakup situation, upstream salient is covered by air lubrication layer, of which the thickness can be comparable to the roughness of the die lip surface or that of the substrate. When lubrication layer thickness is smaller than the surface roughness, the elastohydrodynamic interaction around the high peaks will become very high, and the considerable portion of tension-resultant normal force will be supported by these peaks; it may touch web. When this situation happens, the effect of salient curvature on the upstream lip is weakened; pressure in the air layer near the upstream meniscus would not form high as it would be on smooth lip surface because the tension resultant force, which should develop high pressure in the lubrication layer via elastohydrodynamic interaction, is partly supported by the

sum of local forces at the high peaks. Detailed explanation is given with theoretical analysis results in section 4.3.

On the other hand, coating liquid covers the upstream salient in flooding situation. Conventionally lubrication layer thickness is thicker than the surface roughness of die lip or that of substrate when the lubrication layer has the viscosity of liquid. The sharper the upstream salient is, the slower the web can run without flooding; the leaking flow into the upstream need to suffer higher pressure change when upstream salient is shaper.

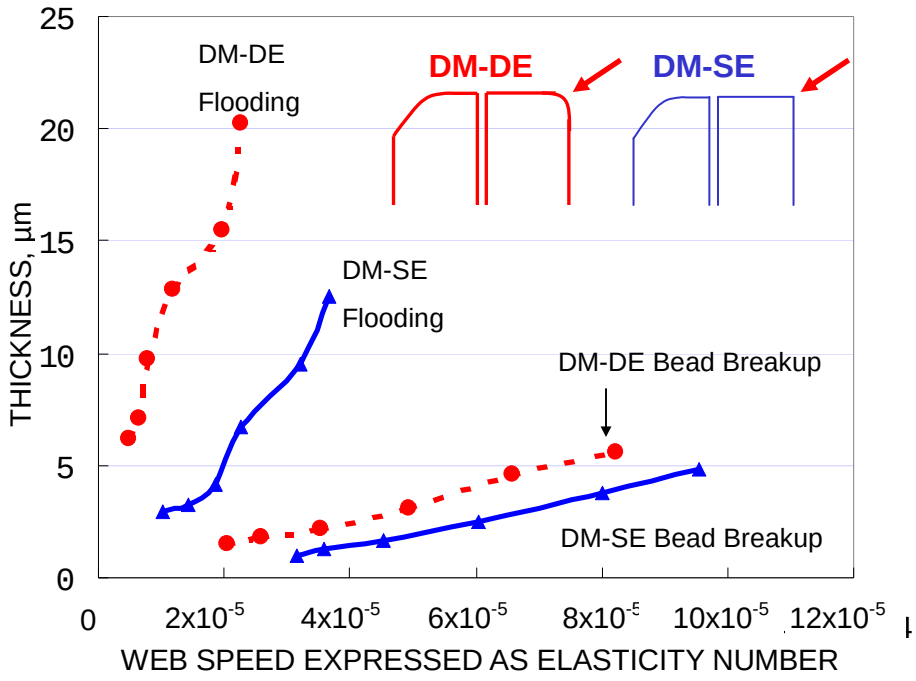

Fig. 4-6. Effect of downstream salient curvature. Sharp downstream salient shifts coating window to the higher speed and thinner coating. Experimental condition: coating liquid 70% glycerin aqueous solution, N=100 N/m, 7°approach angle and 7°departure angle.

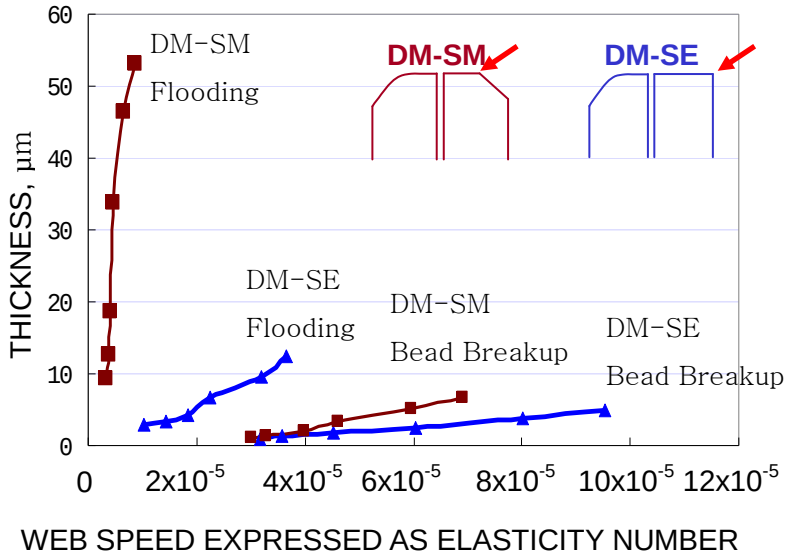

Fig. 4-7. Effect of downstream salient location. Putting salient in the downstream side of the downstream lip enables thin and fast coating. Experimental condition: coating liquid 70% glycerin aqueous solution, N=100 N/m, 7° approach angle and 7° departure angle.

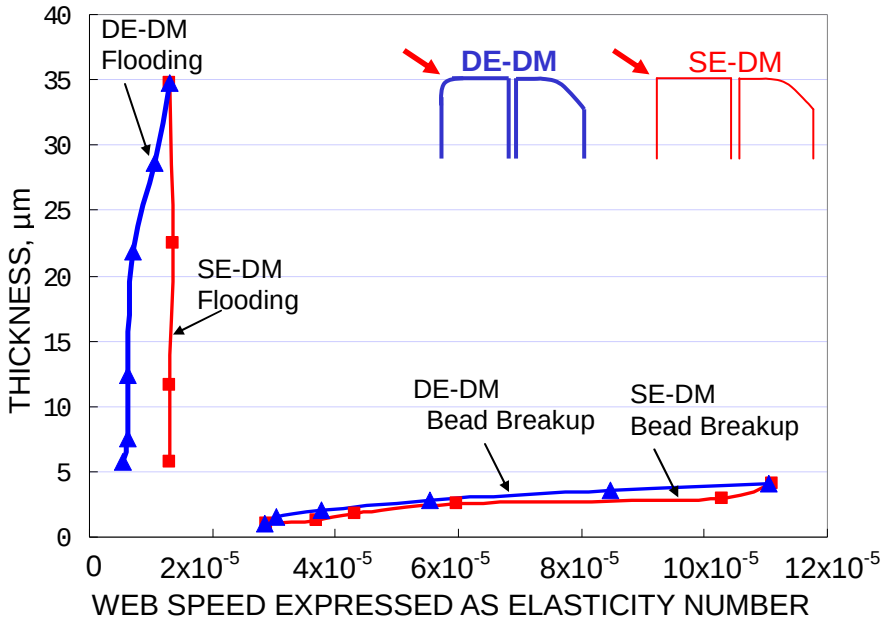

Fig. 4-8. Effect of upstream salient curvature. Upstream salient didn't affect the bead beak point but the flooding point condition. Experimental condition: coating liquid 70% glycerin aqueous solution, N=100 N/m, 7° ap proach angle and 7° departure angle.

4.3. COMPARISON WITH THEORETICAL PREDICTION.

The one dimensional elastohydrodynamic model presented in chapter 3 was used to make theoretical prediction to compare with the experimental results. In this model the pressure field in the coating bead is described by lubrication approximation, and the web deformation was described by shell theory; but since in this chapter the flexural rigidity is ignored, the web deformation equation is essentially the membrane equation. The gap clearance between the web and the

die surface was measured in radial direction of polar coordinate. Equation set are as follows:

$$h(\theta) = r(\theta) - D(\theta) \tag{4-1}$$

where h, r, and D are gap profile, web position function, and Die Shape function.

Expression of curvature, κ_s, in cylindrical coordinate is

$$\kappa_s = \frac{2(\frac{dr}{d\theta})^2 - r\frac{d^2r}{d\theta^2} + r^2}{\left((\frac{dr}{d\theta})^2 + r^2\right)^{3/2}} \tag{4-2}$$

When we take the reference surface to be the slot die surface, of lubrication approximation becomes

$$q = \frac{hV}{2} - \frac{h^3}{12\mu}\frac{\partial p}{\partial \theta}\frac{\partial \theta}{\partial x_s}, \qquad \frac{\partial x_s}{\partial \theta} = \sqrt{D(\theta)^2 + D'(\theta)^2} \tag{4-3}$$

q is flow rate of lubricant, V is web speed, μ is viscosity, and x_s is arc length coordinate along the die surface.

When the radial load across the shell is the pressure difference, the force balance in normal direction to the shell equation becomes

$$-K\frac{d^2\kappa_s}{d\theta^2}\left(\frac{d\theta}{ds}\right)^2 + \kappa_s\left(-\frac{1}{2}{\kappa_s}^2 K + N_0\right) - \Delta p = 0, \tag{4-4}$$

where, $\frac{\partial s}{\partial \theta} = \sqrt{r(\theta)^2 + r'(\theta)^2}$, $\Delta p = p - p_{atm}$

N_0 is the web tension when the curvature of web is not deformed. K is the flexural rigidity defined as

$$K \equiv \frac{Et^3}{12(1-\nu^2)} \quad (4\text{-}5)$$

E is the elastic Young's modulus of the web, t is thickness of web, and v is its Poisson ratio. The locations of upstream and downstream menisci are decided by geometry relations and pressure balance. Boundary conditions are set in upstream and downstream idler positions, θ_{Up0} and θ_{Dn0} :

$$p(\theta_{Up0}) = p_{Ambient} \quad (4\text{-}6)$$

$$r(\theta_{Up0}) = r_{Up0} \quad (4\text{-}7)$$

$$\kappa(\theta_{Up0}) = 0 \quad (4\text{-}8)$$

$$p(\theta_{Dn0}) = p_{Ambient} \quad (4\text{-}9)$$

$$r(\theta_{Dn0}) = r_{Dn0} \quad (4\text{-}10)$$

$$\kappa(\theta_{Dn0}) = 0 \quad (4\text{-}11)$$

where r_{Up0} and r_{Dn0} are radial distance from the origin of polar coordinate to the passage points set on the idlers upstream and downstream respectively.

4.3.1. Contact pressure model.

Both the surfaces of web and the die are rough in microscopic scale. Generally the surface of the web is designed to be rougher to easy its handling. When lubrication layer becomes so thin that the tiny peaks on the web may contact the

die lip surface, the web could be supported partly by the lubrication layer and partly by the “contact” of tiny peaks with the die lip surfaces. But the “contact” may not be a right word, since the peaks on the web surface may not practically touch the die lip surface. The lubrication layer may still be formed in the even thinner gap between the peaks and die surface and generates much higher pressure around the peaks to support the web far more strongly than the other lower area. With respect to the force balance between the die lip and the web, the effect of this “lubricated contact” is thought to be same to that of the real contact with the die. In case a peak is by far greater and sharper than the other peaks around it, it would be inevitable for the peak to practically touch the die surface. Detailed consideration on this topic is beyond the scope of this thesis. For this study the empirical non-linear contact model for contact pressure versus spacing given by Lacey and Talke(1992) is effective enough to describe the situation.

$$p_{contact} = \begin{cases} 0 & h \geq \alpha \\ \beta\left(1 - \dfrac{h}{\alpha}\right)^2, & h < \alpha \end{cases} \qquad \text{(4-12)}$$

where, α is a constant denoting the spacing for which initial contact occurs between the lip and the web and β is a constant denoting the contact pressure that exists if the head-tape spacing is zero. Its contribution appears in the normal force balance equation of shell equation:

$$-K\frac{d^2\kappa_s}{d\theta^2}\left(\frac{d\theta}{ds}\right)^2 + \kappa_s\left(-\frac{1}{2}\kappa_s{}^2K + N_0\right) - \Delta p - p_{contact} = 0 \qquad \text{(4-13)}$$

Lacey and Talke decided the values of parameter α and β by matching eq. (4-12)

with experimental measurement of head-tape spacing and the contact pressure applied, or equivalently the web tension. He found that the parameter α has similar value to the peak-to-valley roughness of the substrate. In this study, the parameter value of α is given as 3.6μm which was the peak-to-valley roughness of the substrate used in the experiment. The value of β was given as 16.1 in units of (N/R_0), which is a dimensionless pressure applying on the upstream salient of DMDC when the web is stagnant so that all the web-tension-resultant force is balanced by the contact on the lip surface.

4.3.2. Prediction of coating window with die shape DMDC.

Coating window calculated from theoretical model with die shape DMDC is compared with experimental coating window and shown in thickness versus elasticity plain [Fig. 4-9]. Two coating windows showed discrepancies in both flooding conditions and bead breakup conditions. Since the experimental apparatus was not perfect, there were several possible sources of errors in the experiment. Sensitivities of the flooding points and bead breakup points to several parameters are checked to see if they can be the cause of these discrepancies. The bead breakup points and flooding points were calculated as the parameters to be checked were varied with the other conditions fixed, so that the sensitivity of flooding and bead breakup conditions to the upstream salient curvature, downstream salient curvature, approach web angle, and departure

web angle could be checked. The slopes of the graph in figure 10 represent the sensitivities of the parameters. Under the experimental condition with die shape DMDC and 14° symmetric angle, both bead breakup and flooding points turned out to be insensitive to the upstream salient curvatures, but they were sensitive to the downstream salient curvature and both the web approach angle and departure web angle.

The most sensitive parameter was downstream web angle. This sensitivity information gives us an idea that how the process will react to the ongoing disturbances in real operation. Since the tensioned-web slot coating is lacking in the fixed support compared to the other coating method, the web fluctuation, which can be interpreted as the fluctuation in the web angle, can be detrimental to the coating uniformity.

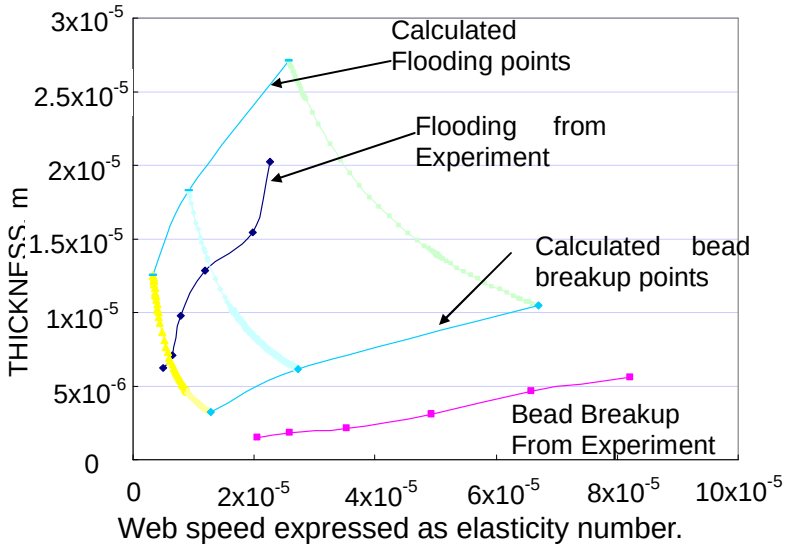

Fig. 4-9. Comparison of coating window calculated from theoretical model with experimental result. The die geometry used is DMDC. N=100 N/m.

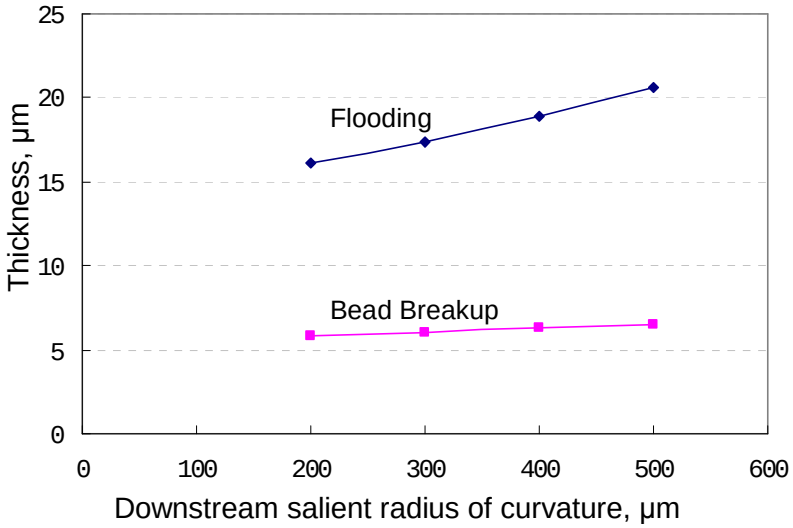

(a) Sensitivity to the downstream salient curvature.

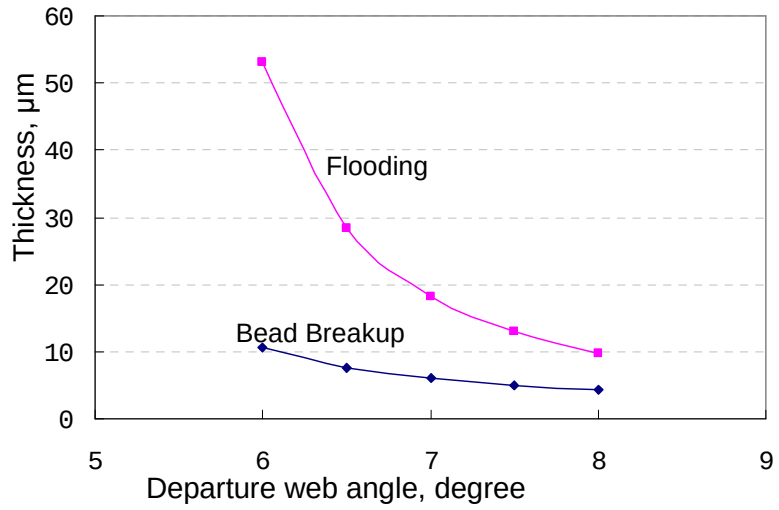

(b) Sensitivity to the departure web angle.

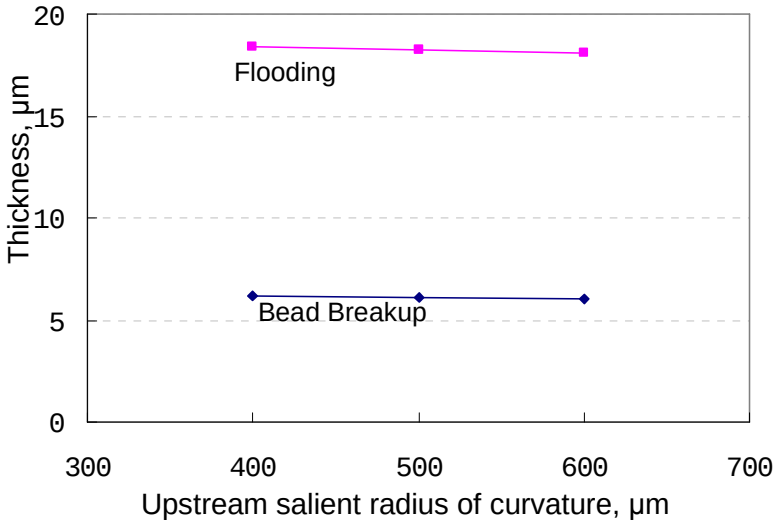

(c) Sensitivity to the upstream salient curvature.

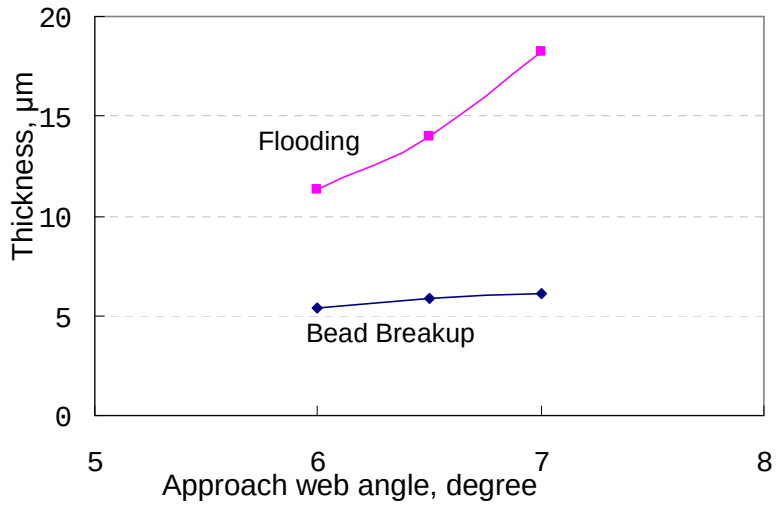

(d) Sensitivity to the approach web angle.

Fig. 4-10. Sensitivity of flooding point and bead breakup point to the parameters. Process conditions: q=0.89 cm^2/min, N=100 N/m7°, approach angle and 7° departure angle.

As figure 4-10 shows, the flooding conditions are much more sensitive than the bead breakup conditions to the parameters checked, i.e., downstream curvature, departure web angle, and approach web angle. The flooding points could be matched by making a very small change in the web angles given to the calculation, but the bead breakup points were remain unmatched with little changes of parameters because their sensitivities are low. Fig. 4-11 shows the coating window calculated with both the approach and the departure angle tilted by as small as 0.3°, this could be from the error in leveling the die assembly mount in the experiment. The flooding points were shifted close to the experimental value, but the bead breakup point didn't approach enough to the experimental value leaving big discrepancies with experimental values.

4.3.3. Contact of the web on die surface.

In section 4.2.8, local contacts of web around the high peaks of the die surface were discussed when the experimental result on the upstream salient was discussed. The discrepancy in bead breakup points between experiment and theoretical calculation is another evidence of contacting force between the high peaks and opposite surface. When web is partly supported by high asperities on the die lip or on the substrates, the gap clearance becomes larger than the value which would be without high asperities. With larger gap, lower pressure develops on the upstream lip since the pumping of viscous fore from the moving web is

weaker. With lower pressure in the air lubrication layer on the upstream lip, upstream meniscus will locate at the more upstream on the upstream die lip, and the bead breakup will be delayed when the thickness of air lubrication layer is comparable to the asperities on the salient.

The contact pressure model presented in section 4.3.1 was added to the theoretical model of tensioned-web slot die coating, and the calculation results were shown in Fig. 4-12; the movements of upstream meniscus with and without the effect of contact pressure model are compared with the results from visualization. Without incorporating the contact pressure model the theoretical calculation shows big difference from the visualization result. But the incorporation of the contact pressure into the model made the calculation results closer to the experimental results expanding the coating window to the faster speed condition [Fig. 4-13].

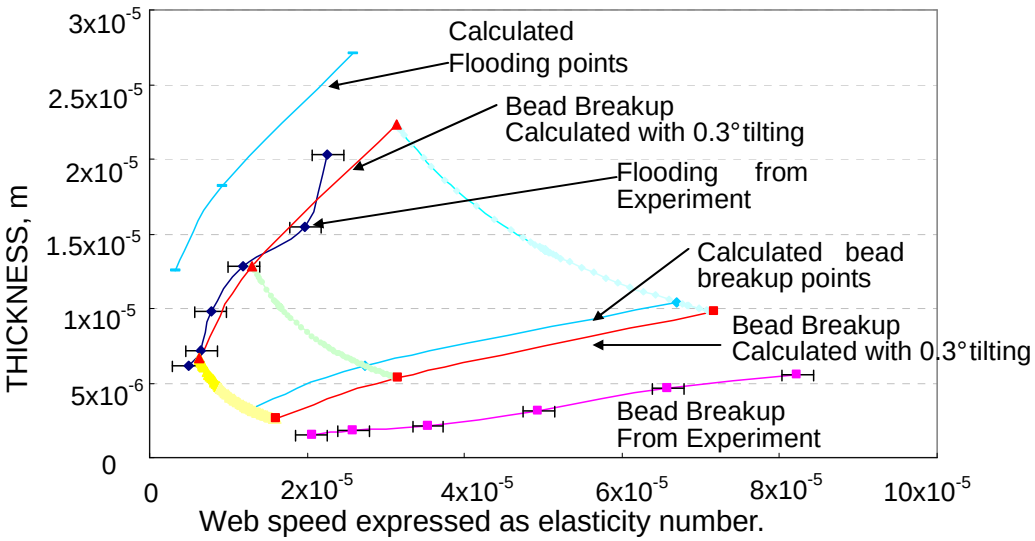

Fig. 4-11. Coating window shifted by tilting the die assembly by 0.3°. The die geometry used is DMDC. N=100 N/m.

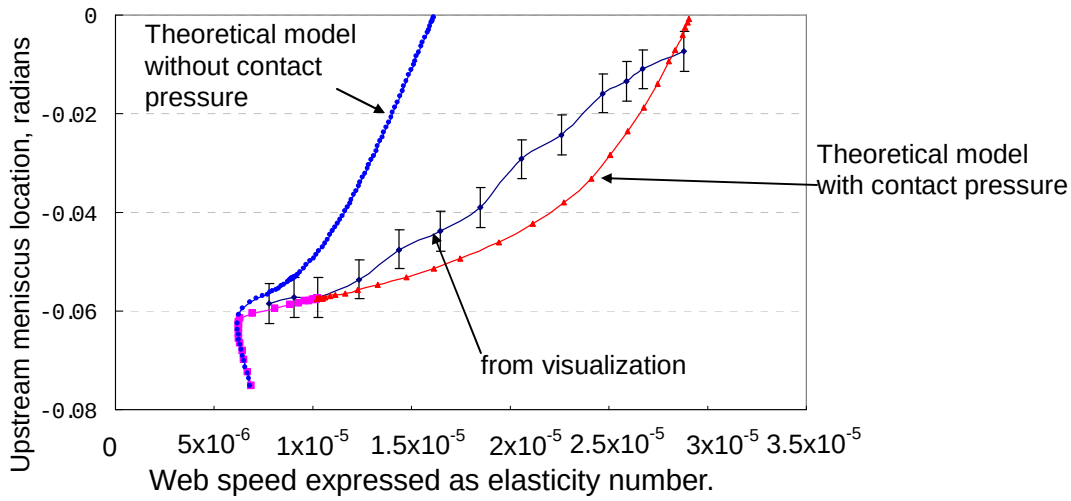

Fig. 4-12. Movement of upstream meniscus when web speed changes in DMDC. Process conditions: approach web angle 6.7°, departure w eb angle 7.3°, q=0.89 cm^2/min, N=100 N/m.

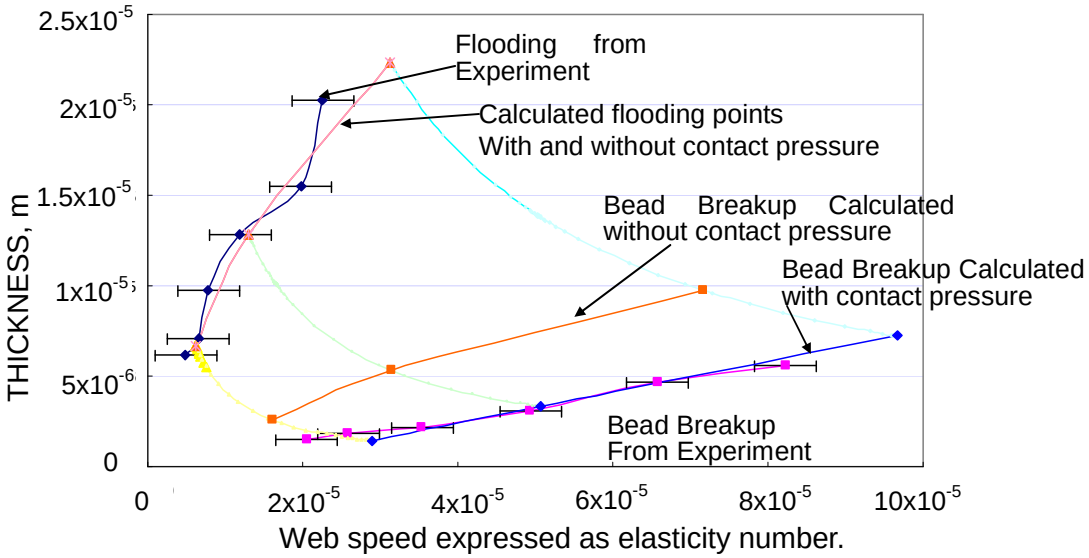

Fig. 4-13. Coating windows shifted by incorporation of contact pressure into the theoretical model. Process conditions: approach web angle 6.7°, departure web angle 7.3°, q=0.89 cm^2/min, N=100 N/m.

4.4. Conclusion

Coating bead in tensioned web slot coating is visualized from the top side of the die lip assembly to study the die geometry effect on the coating window. Upstream meniscus movement, flooding condition, and the bead breakup condition was recorded from the visualization and compared with the result from theoretical model analysis.

To facilitate understanding die geometry research was focused on the effect of a salient, which has sharply curved surface and receive big tension-resultant force. Sharper salient on the downstream lip is found to effective for faster coating operation and thinner coating. As a salient is positioned at the more downstream side on the downstream lip, the coating window was extended to the faster operation speed and thinner coating.

The results from the experiment and the theoretical model didn’t show good agreement. To explain this discrepancy sensitivity analysis was tried, and the contact pressure consideration was added to the theoretical model, expanding the understanding on the tensioned-web slot coating system.

The sensitivities of the coating window location to the parameters including departure web angle, approach web angle, and downstream salient curvature were checked. The flooding conditions were found to be more sensitive to the parameters changes than the bead breakup conditions. The approach web angle and departure web angle is shown to have big influence on the coating window.

Therefore, fluctuation of the web, which can affect the approach web angle and departure web angle, can be detrimental to the uniform coating.

The surface roughness of the upstream lip or that of substrate seems to affect the bead breakup condition. Peaks on the lip surface can exert contact force on the substrate and support the web, possibly by the “lubricated contact”, of which the result is lowering pressure in the air lubrication layer on the upstream lip. If the surface roughness is properly designed to exert a lubricated contact force against the web’s elastic force, it could be utilized to delay the bead breakup.

Chapter 5

Elastoviscocapillary model of double layer tensioned-web slot coating

5.1. INTRODUCTION

Tensioned-web coating is an efficient way of depositing thin and uniform layers on flexible web at high speed with a relatively simple set-up, a combination of slot die pre-metering and carefully controlled web transport. A particularly attractive feature of such tensioned-web coating is that two layers can be coated simultaneously, which makes it possible for one of the layers to be exceptionally thin. It is the magnetic recording media industry that makes best use of the capacity of tensioned-web slot coating system, for a thin top magnetic layer enables high recording density. Fujifilm announced that they had developed, using a two-layer tensioned-web slot coating process, a high-recording-density magnetic media tape of which the recording density had previously been possible only through a metal-evaporating deposition process; the coating thickness of the

top magnetic layer of the tape was said to be 0.2 micron. Moreover according to their recent announcement, they have advanced their technology so that they can coat even thinner layers by a factor of five.

Though no fundamental study of two-layer tensioned-web slot coating has been published, a lot of patents deal with it and most of the fundamental principles that have been worked out for fixed-gap two-layer slot coating, which shares many features with the tensioned-web version, are evidently relevant to the latter.

Cohen (1993) analyzed the bead of two-layer slot coating with a uniform fixed gap by means of a simple rectilinear flow model—a viscocapillary model, except that he neglected effects of capillary pressure in the menisci. He worked out equations that predict limits of operation, the location of interlayer and separation line. The interlayer is a thin diffusion zone that separates the bulk of the two liquid layers. This zone is the result of the interdiffusion between the two layers of miscible liquids; miscible liquids are the rule in simultaneous multilayer coating. Interdiffusion extremely rapidly broadens any interface created between miscible liquids that there's no interfacial tension. The interlayer begins at the separation line on the solid wall where the velocity is zero. Cohen (with Suszynski) also visualized slot coating flows with same methods used by Sartor (and Suszynski). He succeeded in observing the sequence of flow patterns, recirculations, location of interlayer and separation lines as the flow rates of the two layers, their viscosity ratio, and the vacuum pressure applied at the upstream meniscus were varied. Increasing vacuum pressure tended to pull the interlayer upstream, and at

low vacuum, the interlayer separated from the downstream corner (Fig. 5-1). He also observed that the less viscous layer in the upper layer tended to lead to ribbing, which implies that coating with the more viscous layer on top is the more stable configuration.

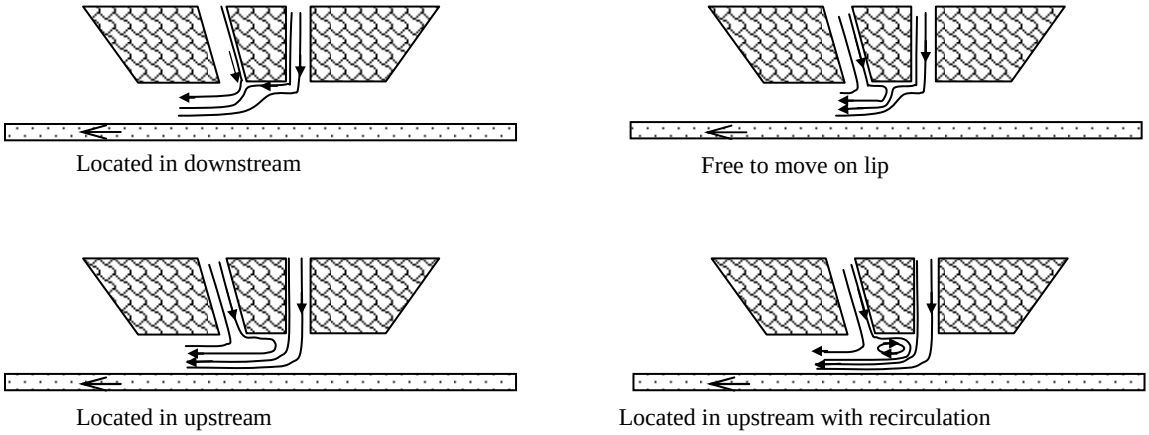

Fig. 5-1. Flow pattern observed in the intermediate section (from Cohen 1993)

Sartor et al. (1996, 1998) in their patents described in some detail a multilayer slot coater and how to control the pressure gradients in the coating bead. To achieve “stable two-dimensional flow in coating bead”, they claimed that the recirculations that can appear under the intermediate and downstream lips should be avoided and that the separating streamline should be pinned at the downstream edge of the intermediate lip, which they called the stability point, as shown in Fig. 5-2. To pin the separating streamline at the stability point, Sartor et al. adjust the geometry so that a positive pressure gradient under the

intermediate lip is avoided. Fig 5-2 shows the die geometries Sartor et al. reported for stable two-layer coating.

They also claimed that the clearance between the intermediate lip and web, called the intermediate gap, should be twice the bottom layer thickness and that the downstream gap should be less than twice the total thickness of the top and bottom layers. This is to avoid the recirculation which will lead to the mixing of the two layers.

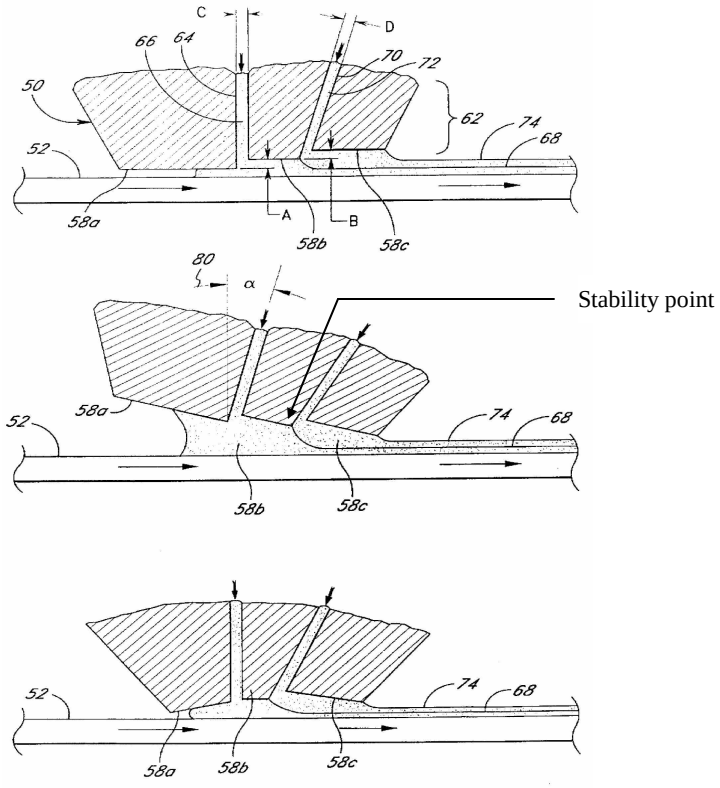

Fig. 5-2. Schematics of two layer slot coating lip configurations by Sartor et al. (1998)

Musson(2001) analyzed two-layer slot coating by solving the Navier-Stokes

equation system with Galerkin's method and finite element basis functions. He coupled two-dimensional model to arc-length continuation methods to trace out steady-state solution paths in the parameter space. Each steady state solution was checked for its stability and sensitivity to perturbations. He also made visualization experiments the results of which are shown in Fig. 5-3, where they are coupled with the results with theoretical prediction of his model. The dotted line in Fig. 5-3 shows the operating window prediction by Cohen (1990) from his viscocapillary model, which agrees well with experimental data.

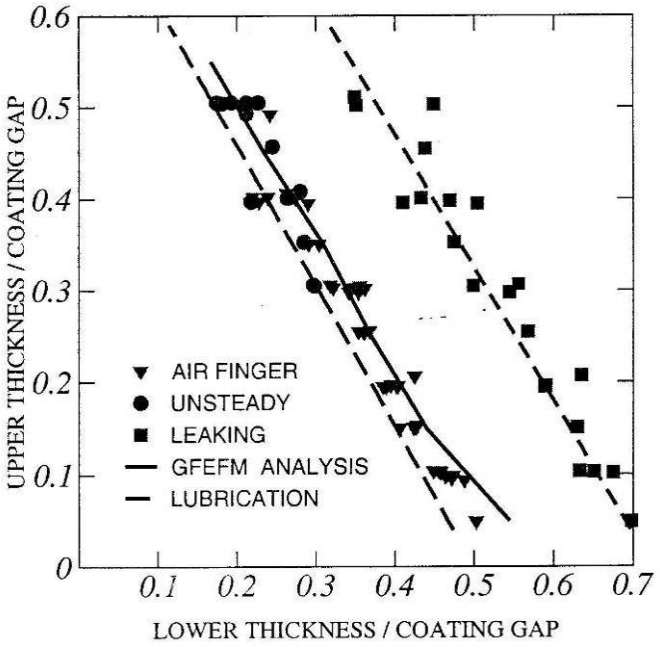

Fig. 5-3. Theoretical predictions and experimental determination of the low flow limit of the operation in two-layer slot coating. Conditions: Viscosity ratio = 1; P_{vac} = 0; Re = 2; Ca = 0.4. (from Musson 2001).

In the study of one parameter, the viscosity ratio (upper layer viscosity over

lower layer viscosity), Musson found that only a limited range of viscosity ratio could be accommodated by the pressure difference between the downstream ambient air and the upstream vacuum chamber pressure. If the viscosity ratio was raised too much, the upstream meniscus moved toward upstream lip end and at above the upper limit of viscosity ratio, meniscus invaded the vacuum chamber. If the viscosity ratio was lowered too much, the upstream meniscus moved forward to the region under the lower-layer feed slot and at above the lower limit of the viscosity ratio the bead became unstable to three-dimensional disturbances. His frequency response analysis showed that the most detrimental disturbance in the two-layer slot coating is the fluctuation of coating gap and that the system becomes more sensitive to the coating gap disturbance as the top layer viscosity rises. In a two-parameter study, he tried to keep the upstream meniscus in same position as the viscosity ratio changed by manipulating other parameters, e.g. the upstream vacuum pressure; he checked the stability and sensitivity of the system to disturbances. He found that the system becomes unstable to a three-dimensional perturbation and sensitive to coating gap disturbances as the top layer viscosity falls.

In this chapter an elastoviscocapillay model of two-layer tensioned-web slot coating is assembled by combining a two-layer flow model with the single-layer tensioned-web slot coating model presented in Chapter 2. Effects of flow rate ratio, viscosity ratio, and die geometry were examined by calculating predictions of the theoretical model. The radius of curvatures of upstream lip and downstream die lip were varied, and the mid-lip’s surface was bulged.

5.2. Elastoviscocapillary model of two-layer coating bead

5.2.1. One-dimensional model of two-layer coating flow

Cohen (1993) made a one-dimensional flow model of two-layer bead flow in the fixed-gap slot coating based on the lubrication approximation, in which he ignored the effect of normal stress on the interface location. Musson (2001) showed that the prediction of Cohen's model was satisfactory compared with the experimental results and computed predictions of the two-dimensional Navier-Stoke equation system.

Because the coating gap of tensioned-web slot coating is narrower than that of fixed-gap slot coating, it is to be expected that the Cohen's one-dimensional model would also work well in describing two-layer bead flow in tensioned-web slot coating. A schematic of two-layer flow in a narrow channel is shown in Fig. 5.4. With the rectilinear flow approximation, both top layer flow and bottom layer flow are represented by

$$0 = -\frac{\partial P}{\partial s} + \mu_i \left. \frac{\partial^2 v_i}{\partial z^2} \right|_{i=T,B} \qquad (5\text{-}1)$$

where, the subscripts, T and B denote top layer and bottom layer, respectively. P is pressure in the coating bead, v is flow speed in streamline direction, s is arc length coordinate along the die surface, and z is a coordinate perpendicular to the die surface. The boundary conditions are no-slip at the top and bottom solid surfaces, and the interface conditions are continuities of flow velocity and shear

stress at the interlayer.

$$u_T = 0 \qquad \text{at} \quad z=0 \qquad (5\text{-}2)$$

$$u_B = V \qquad \text{at} \quad z=h \qquad (5\text{-}3)$$

$$u_T = u_B = V_m \qquad \text{at} \quad z=\delta \qquad (5\text{-}4)$$

$$\mu_B \frac{du_B}{dz} = \mu_T \frac{du_T}{dz} \qquad \text{at} \quad z=\delta \qquad (5\text{-}5)$$

Here δ denotes the location of interlayer, h is the gap height, V is the top surface's translating speed, and V_m is the liquid flow speed at the interlayer.

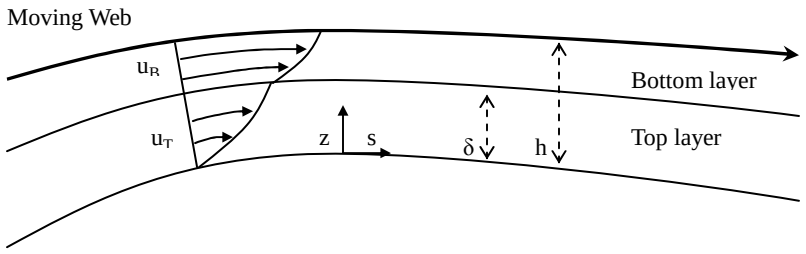

Fig. 5-4. Schematic of two-layer rectilinear lubrication flow in a coating bead

Solving Eq. (5-1) with boundary conditions Eq. (5-2), Eq. (5-3), Eq. (5-4), and Eq. (5-5) gives expression for V_T, V_B, and V_m:

$$u_T = \frac{z}{\delta} V_m + \frac{z(z-\delta)}{2\mu_T} \frac{\partial p}{\partial s} \qquad (5\text{-}6)$$

$$u_B = \frac{(\delta - z)V - (h - z)V_m}{\delta - h} + \frac{(\delta - z)(h - z)}{2\mu_B}\frac{\partial p}{\partial s} \tag{5-7}$$

$$V_m = \frac{\mu_B \delta V + \frac{1}{2}\frac{\partial p}{\partial s} h\delta(\delta - h)}{\delta(\mu_B - \mu_T) - \mu_T h} \tag{5-8}$$

Flow rates of bottom layer and top layer are calculated by integrating flow velocity over the thickness:

$$q_B = \int_{\delta}^{h} u_B dz \tag{5-9}$$

$$q_T = \int_{0}^{\delta} u_T dz \tag{5-10}$$

After replacing the V_m with Eq. (5-8), Eq. (5-9) and Eq. (5-10) become

$$q_T = -\frac{\delta^2\left(\frac{dp}{ds}\delta^2\mu_B + \frac{dp}{ds}(h-\delta)(3h+\delta)\mu_T - 6V\mu_B\mu_T\right)}{12\mu_T\left(\delta(\mu_B - \mu_T) + h\mu_T\right)} \tag{5-11}$$

$$q_B = -\frac{(h-\delta)\left(\frac{dp}{ds}\delta\mu_B(4h-\delta)(h-\delta) + \frac{dp}{ds}(h-\delta)^3\mu_T - 6V\mu_B(2\delta\mu_B + (h-\delta)\mu_T)\right)}{12\mu_B\left(\delta(\mu_B - \mu_T) + h\mu_T\right)} \tag{5-12}$$

When Eq. (5-11) and Eq. (5-12) are non-dimensionalized with length unit, R_0, which is chosen as a characteristic length of the die geometry; flow rate unit, $R_0V/2$; and pressure unit, N_0/R_0, where N_0 is web tension where web is flat, they become

$$Q_T^{\ *} = -\frac{\delta^{*2}\left(N_{EL}\frac{dP^*}{d\theta}\frac{d\theta}{ds^*}\delta^{*2} + N_{EL}\frac{dp}{ds}(h^* - \delta^*)(3h^* + \delta^*)m - 6m \right)}{6m\left(\delta^*(1-m) + h^* m\right)} \qquad (5\text{-}13)$$

$$Q_B^{\ *} = -\frac{\left(h^* - \delta^*\right)\left(\frac{1}{N_{EL}}\frac{dP^*}{d\theta}\frac{d\theta}{ds^*}(h^* - \delta^*)\left(\delta^*(4h^* - \delta^*) + (h^* - \delta^*)^2 m\right) - 6(2\delta + (h^* - \delta^*)m) \right)}{6\left(\delta^*(1-m) + h^* m\right)} \qquad (5\text{-}14)$$

Here $m \equiv \frac{\mu_T}{\mu_B}$ and $N_{EL} \equiv \frac{\mu_B V}{N_0}$. Q_T and Q_B are the non-dimensional flow rate of top layer and bottom layer, respectively. The asterisks mean non-dimensional variables and will be suppressed from now on.

5.2.2. Eight zones in two-layer tensioned-web slot die coating.

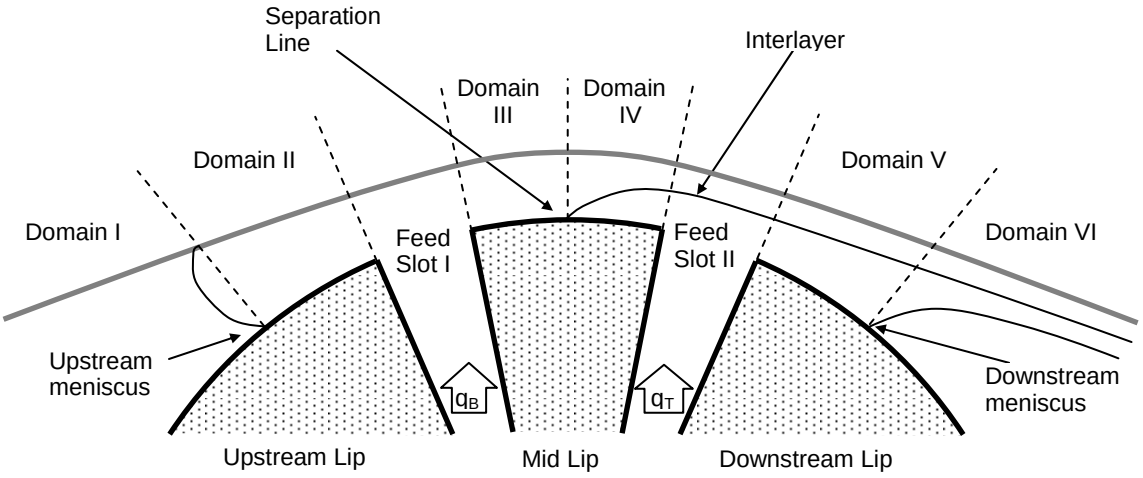

Fig. 5-5. Eight zones in two-layer tensioned web slot die coating.

Two-layer tensioned-web slot die coating flow can be divided into eight zones according to the fluid type, number of layers, and type of flow, as is done in table 5-1. Flow models in upstream air zone, upstream bead zone, mid-lip single-layer zone, and downstream air zone are same as those in the elastoviscocapillary model of single-layer tensioned-web slot die coating. But flows in mid-lip double layer zone and downstream bead zone consist of two layers, and the two-layer flow model developed in section 5.2.1 is used in those zones. The flow rates of bottom layer and top layer in downstream bead zone are set by feeding rates from the upstream feed slot and the downstream feed slot, respectively. The net flow rate in the top layer of the mid-lip double-layer zone is zero, and that of bottom layer is set by upstream feed slot's feed rate.

	Zone name	Type of Fluid	# of layers	Flow rate, q
Domain 1	Upstream Air	Air	1	0
Domain 2	Upstream Bead	Liquid B	1	0
Slot 1	Upstream slot	Liquid B	1	-
Domain 3	Mid-lip single layer	Liquid B	1	q_B
Domain 4	Mid-lip double layer	Liquid B / Liquid T	2	q_B / 0
Slot 2	Downstream slot	Liquid B / Liquid T	2	-
Domain 5	Downstream Bead	Liquid B / Liquid T	2	q_B / q_T
Domain 6	Downstream Air	Air	1	0

Table 5.1. Different characteristics in each flow domain; Liquid T = top layer coating liquid; Liquid B = bottom layer coating liquid.

5.2.3. Matching conditions at menisci and boundary conditions

The locations of upstream meniscus and downstream meniscus are dictated by the balance of the pressures of either sides of menisci with offset of capillary pressures and by satisfying the geometric restrictions laid by contact angles and web-die configurations as are done in single layer model in Chapter 3. As an approximation, the capillary number at the downstream meniscus is calculated with top layer's surface tension and bottom layer's viscosity. In most cases, the effect of capillary pressure on the overall pressure profile is small; it is less than 3% of the maximum pressure in the coating bead, and so this approximation does not change much the result presented in this Chapter.

The boundary conditions were given in same way as in the single-layer tensioned-web slot coating model in Chapter 3, namely the locations where boundary conditions are set, θ_{Up0} and θ_{Dn0}, are chosen to be far enough from the virtual tangent points of the web to the die surface that any changes in coating gaps at virtual tangent points do not appreciably alter the approach web angle and departure web angle. Pressure, web position, and curvature are given at both boundary points.

5.2.4. Locating the separation line

At a separation line where the interface intersects a solid surface viscous shear

stress goes to zero when two liquids are miscible. Because the flow velocity profile is assumed to be quadratic in the lubrication approximation, the location of a separation line can be found by solving

$$\left.\frac{\partial u}{\partial y}\right|_{y=0} = 0 . \qquad (5\text{-}15)$$

The flow velocity profile in the mid-lip single-layer zone is found by solving Eq. (5-1) with the no-slip boundary conditions at both y = 0 and y = h:

$$u = -\frac{h^2}{2\mu}\frac{dp}{ds}\left(\frac{y}{h} - \left(\frac{y}{h}\right)^2\right) + \frac{Vy}{h} \qquad (5\text{-}16)$$

By integrating Eq. (5-16) over the lubrication film thickness, the flow rate, q, is found to be

$$q = \frac{hV}{2} - \frac{h^3}{12\mu}\frac{\partial p}{\partial s} \qquad (5\text{-}17)$$

By differentiating Eq. (5-16) and applying Eq. (5-15) the pressure gradient is found to be

$$\frac{\partial p}{\partial s} = \frac{2\mu V}{h^2} \qquad (5\text{-}18)$$

Combining Eq. (5-17) and Eq. (5-18) gives the equations for locating separation line:

$$q = \frac{hV}{3} \qquad (5\text{-}19)$$

Separation line location was determined by solving Eq. (5-19) in the mid-lip single layer domain.

When the separation line locates at the downstream corner of the mid-lip, the

width of the mid-lip double-layer domain is zero and the equation set is singular, because gradients of field variables cannot be numerically calculated on a point. Same thing happens to the mid-lip single layer domain when the separation line locates in the upstream corner of mid-lip. To prevent these difficulties, an upstream bound on the separation line location was set at the point which is $1x10^{-3}$ radian downstream of upstream corner; and a downstream bound was set at the point which is $1x10^{-3}$ radian upstream of downstream corner of the mid-lip.

5.2.5. Solution method

The equation set of elastohydrodynamics of two-layer tensioned-web slot coating was solved by the same method used in Chapter 3, Galerkin's weighted residual method with finite element basis functions. The equation system is the same except that new field variable δ, height of interlayer, and the separation line location appear in the mid-lip single layer zone and downstream bead zone.

The height of the interlayer, δ, was of course taken to be zero at the separation line. Interlayer height in the downstream slot zone was not calculated because the flow in the slot zone is two-dimensional and out of the capability of one-dimensional model.

Again constant pressure profiles were assumed in both feed slot zones, since the pressure changes in slot zones are negligible compared to that in the other parts. The pressure was approximated as uniform along the feed slot zones.

5.3. ELASTOHYDRODYNAMICS OF TWO-LAYER COATING

The equations of the elastoviscocapillary model explained in previous section were solved with cylindrical die shape shown in Fig. 5-6 (a). As shown in Fig. 5-6(b), the changes in die shape were made on each lip at a time while the other two lips stay unchanged from the base cylindrical shape. The radius of base cylinder is taken as a length unit.

The total wrap angle on the die assembly was chosen to be 19°. 7° wrap angles were chosen at the upstream lip and downstream lip, 0.5° angle over each feed slot, and 4° angles were applied on the mid-lip. The locations of passage points are set at Θ = -30° and Θ = 35°, which are away from the upstream and downstream virtual tangent points by 23°. Boundary con ditions given at passage points are that the pressure is ambient and that web positions are fixed to align web with a given approach and departure angles.

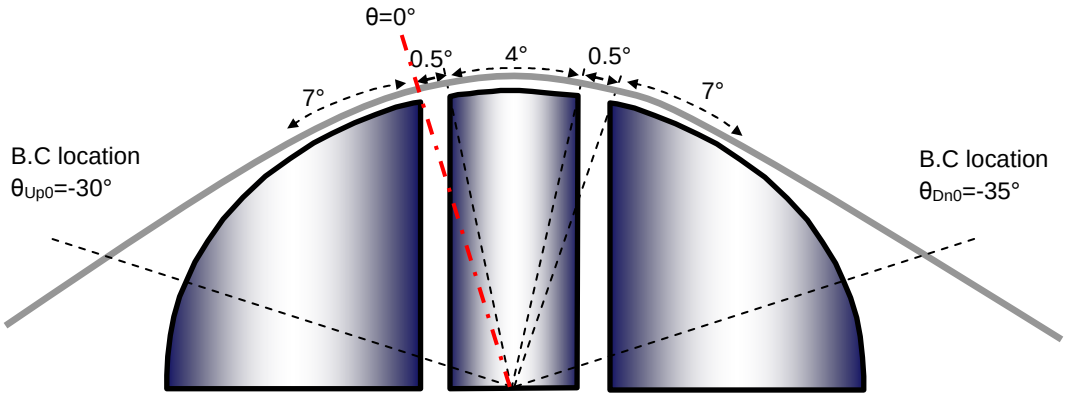

(a) Base die, cylindrical geometry.

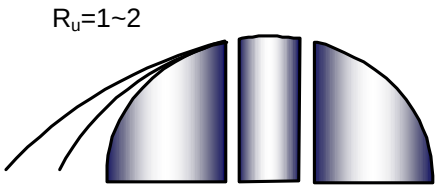

(b) Upstream lip radius rise

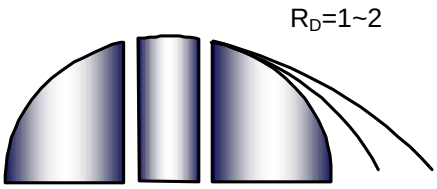

(c) Downstream lip radius rise

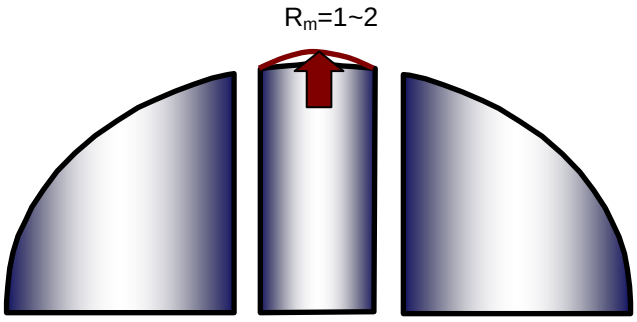

(d) Bulging mid-lip

Fig. 5-6. From the base die shape, namely a circular cylinder, the radius of upstream lip or downstream lip was changed keeping its tangency at the connection with base arc. When mid-lip was changed, it was bulged from the base arc. The web wraps the die at 19° total angle is given; upstream and downstream lips are wrapped by 7°, respectively, and 5° is given to mid-lip and feed slots.

5.3.1. Bottom-layer feed rate

Fig. 5-7 and Fig. 5-8 show effects of bottom-layer feed rate on the locations of separation line and upstream meniscus. The bottom layer feed rate's effect is the same to that of the feed rate of single layer coating, When bottom layer feed rate falls the upstream meniscus advances along the upstream lip surface toward the

feed slot, and coating bead breaks as the bottom feed rate falls below the bead-break value. The upstream meniscus recedes upstream when the bottom feed rate rises. When bottom layer feed rate rises over a flooding value, which is shown as turning point in Fig. 5-6, the coating bead spills out of the upstream meniscus.

The separation line stays at the downstream corner of mid-lip when bottom layer feed rate is big enough to prevent the backflow of the top layer liquid from the downstream feed slot onto the mid-lip surface. The position of separation line was decided by Eq. 5-19. When the bottom layer feed rate is dropped below the the value calculated by Eq. 5-19 at the downstream corner of the mid-lip, which below 2.9×10^{-3} in condition of Fig. 5-8, the separation line starts to move back toward the upstream. Further recession was stopped by bead breakup in the condition of Fig. 5-8.

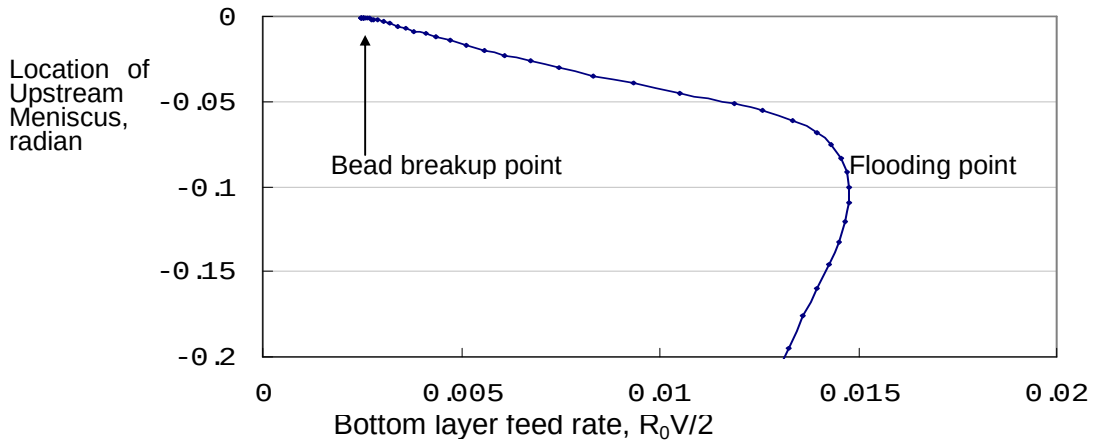

Fig. 5-7. Effect of bottom-layer feed rate on the upstream meniscus location with cylindrical die geometry. $N_{EL} = 8.7 \times 10^{-5}$, $N_{CA} = 0.276$, m = 1, and $Q_t = 2.5 \times 10^{-3}$.

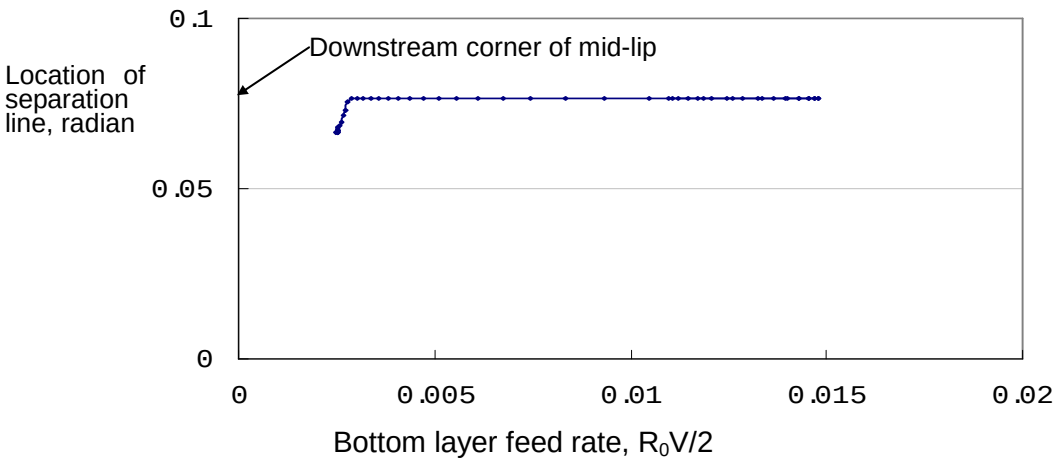

Fig. 5-8. Effect of bottom-layer feed rate on the separation location.

$N_{EL} = 8.7x10^{-5}$, $N_{CA} = 0.276$, m = 1, and $Q_t = 2.5x10^{-3}$.

5.3.2. Top-layer feed rate

Generally when feed rate is raised in the feed slot of single layer coating or in the bottom layer feed slot of two-layer coating, the upstream meniscus moves upstream due to the rise of pressure around the feed slot. But the feed rate of top layer in two-layer tensioned-web slot coating makes two different effects depending on its intensity. When the top-layer feed rate is low, as in the left branch in the Fig. 5-8, upstream meniscus slightly moves downstream as the top-layer feed rate rises. This is because the expansion of gap over the mid-lip made by top-layer feeding reduces the pressure peak at the bottom layer feed slot [Fig. 5-11]. But when the top-layer feed rate is big enough, as in the right branch of the Fig. 5-9, the upstream meniscus moves upstream as top-layer feed rate is raised

because the gap height over the bottom feed slot is already widened enough so that the effect of the widening gap is small. Instead, the pressure rise that accompanies raising the top layer feed rate starts to contribute strongly and pushes the upstream meniscus upstream, so that bead breakup is avoided.

Fig. 5-10 shows the movement of separation line when the top layer feed rate changes. Separation line moves back along the mid-lip surface when the top layer feed rate is raised because the pressure peak accompanying the rise of the top-layer feed slot not only lifts the gap height around the top-layer feed slot but also causes adverse Poiseuille flow on the mid-lip [Fig. 5-11].

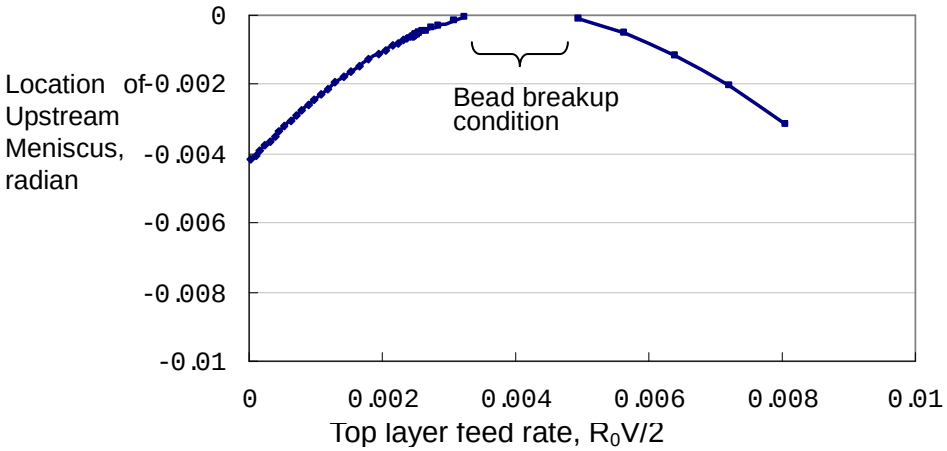

Fig. 5-9. Effect of top-layer feed rate on the upstream meniscus location. N_{EL} = $8.7x10^{-5}$, N_{CA} = 0.276, m = 1, and Q_B = $2.5x10^{-3}$.

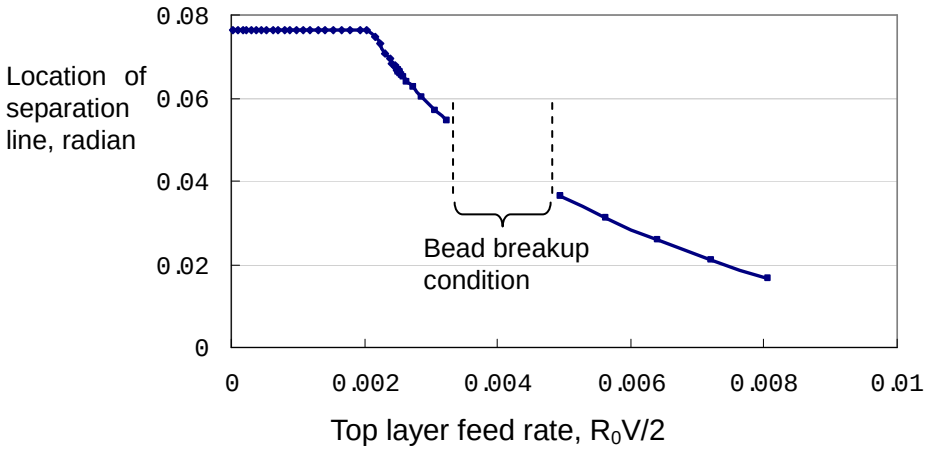

Fig. 5-10. Effect of top-layer feed rate on the separation location with cylindrical die geometry. N_{EL} = $8.7x10^{-5}$, N_{CA} = 0.276, m = 1, and Q_B = $2.5x10^{-3}$.

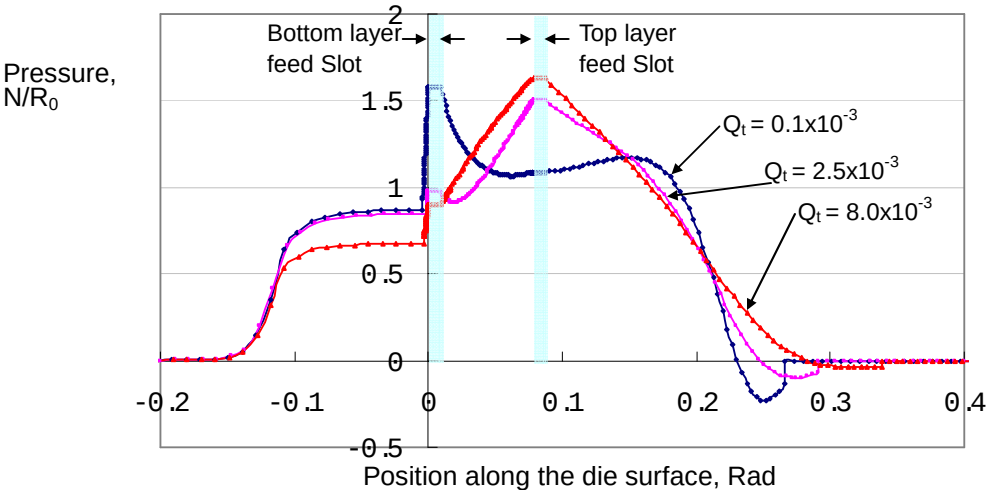

(a) Pressure profiles along the cylindrical die surfaces

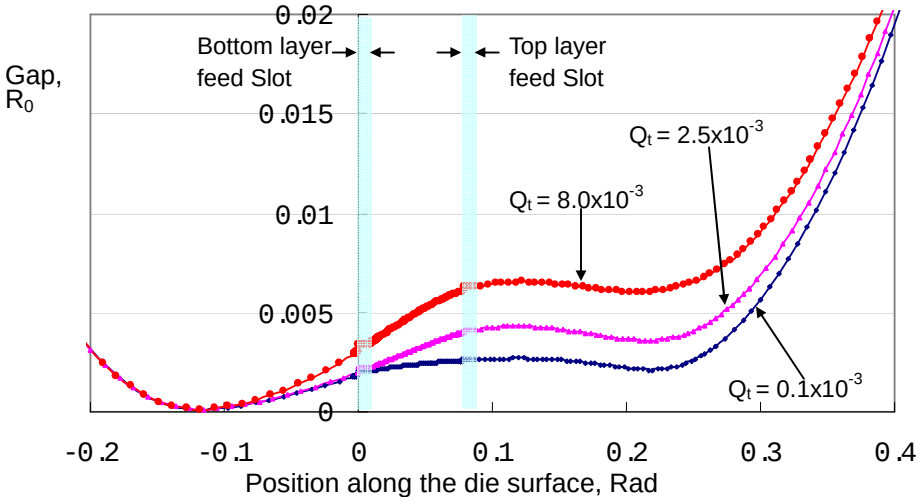

(b) Gap profiles along the cylindrical die surfaces

Fig. 5-11. Pressure and gap profiles of the two-layer tensioned-web slot die coating with cylindrical die shape. N_{EL} = 8.7x10^{-5}, N_{CA} = 0.276, m = 1, and Q_B = 2.5x10^{-3}.

5.3.3. Effect of viscosity ratio

Raising top layer's viscosity builds higher pressure over the mid-lip, because the flow channel should be expanded to accommodate more viscous liquid at same flow rate. Its effect on the pressure profile is similar to that of increasing top layer flow rate, which is shown in Fig. 5-11. When top viscosity is smaller or comparable to the bottom layer viscosity, as in the left branch in Fig. 5-12, raising top layer viscosity reduces the pressure peak at the bottom layer feed slot by widening the channel for the issued liquid to flow out of the bottom layer feed slot, so that upstream meniscus moves forward as the top-layer viscosity rises. But in the right branch in Fig. 5-12 viscosity ratio is high enough for the pressure peak from the top-layer feed slot to expand the flow channel over the second feed slot. Raising viscosity makes the higher pressure, the effect of which reaches to the upstream meniscus and pushes the upstream meniscus against bead breakup.

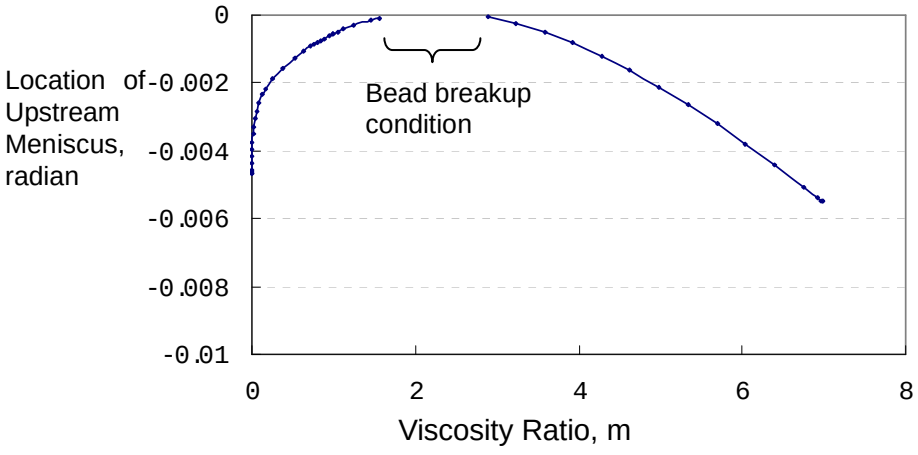

Fig. 5-12. Effect of viscosity ratio to the upstream meniscus location in cylindrical die geometry. $N_{EL} = 8.7 \times 10^{-5}$, $N_{CA} = 0.276$, and $Q_T = Q_B = 2.5 \times 10^{-3}$.

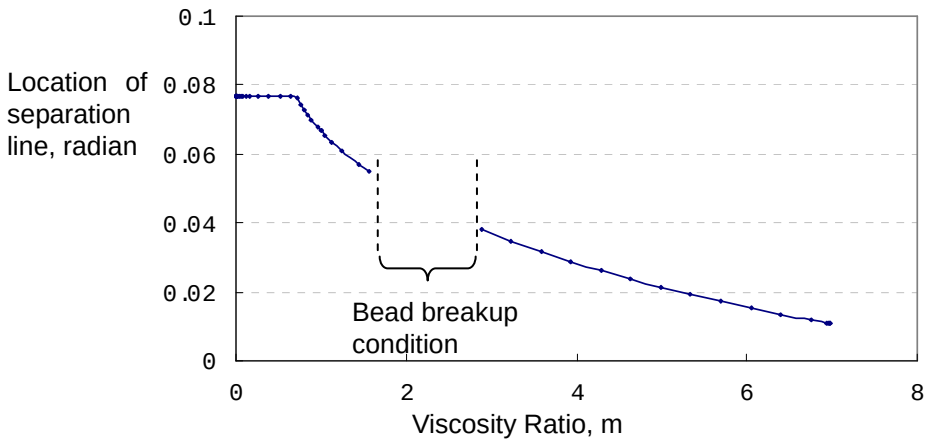

Fig. 5-13. Effect of viscosity ratio to the separation line location in cylindrical die geometry. $N_{EL} = 8.7x10^{-5}$, $N_{CA} = 0.276$, and $Q_T = Q_B = 2.5x10^{-3}$.

5.4. DIE SHAPE EFFECT IN TWO-LAYER TENSIONED-WEB COATING

The cylindrical die geometry was shaped from the basic cylindrical die. Each die lip was changed as shown in Fig. 5-6 (b and c). The radius of curvature of upstream die lip was changed to see its effects on the pressure profiles and on the locations of upstream meniscus and separation line. When one lip was changed the other two lips stayed on the base arc. The change in the upstream lip was made keeping the arc of upstream lip surface tangent to the base arc at the downstream end of upstream lip. Likewise, the radius of curvature of the downstream lip was changed with keeping its tangency at its upstream end with base arc of circle.

Because mid-lip is located between two feed slots, its effect is easily buried by high pressures generated at the two. To amplify its effect on the pressure profile, the mid-lip surface was bulged from the base arc of circle while its radius of curvature was reduced.

5.4.1. Effect of upstream lip curvature

In Fig. 5-14, movements of upstream menisci on the two upstream lips of different radii of curvatures are compared. The position of upstream meniscus is shifted upstream when the upstream lip is flattened, since the pressure profile on the upstream lip is lower, the flatter the upstream lip surface. The differences in the upstream meniscus location at same flow rate are not so big when top-layer flow rate is small. But the difference grows as the top layer feed rate rises. The movements of separation lines over the two upstream lips of different curvatures are compared in Fig. 5-15. At the same flow rates, with a flatter upstream lip the separation line locates at the closer to upstream side than that with more curved upstream lip; again, since the flatter upstream lip lead to the lower pressure profile, as Fig. 5-16(a) shows. When the upstream lip is flatter, the pressure gradient on the mid-lip is steeper since the pressure on the upstream lip is lower. This steeper pressure gradient induces the adverse Poiseuille flow, which leads to the reverse flow on the mid-lip when pressure gradient is strong enough. The gap profile also shows that with less-curved upstream lip gap on the mid-lip rises, which makes also favorable condition for the reverse flow on the mid-lip.

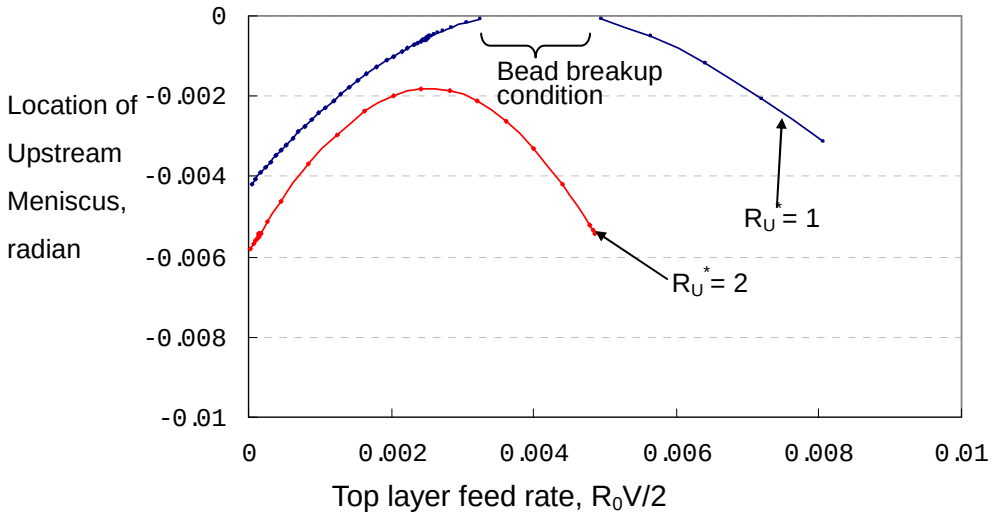

Fig. 5-14. Effect of radius of curvature of upstream lip on the location of upstream meniscus. N_{EL} = 8.7x10^{-5}, N_{CA} = 0.276, m = 1, R_D = R_m = 1, and Q_B = 2.5x10^{-3}.

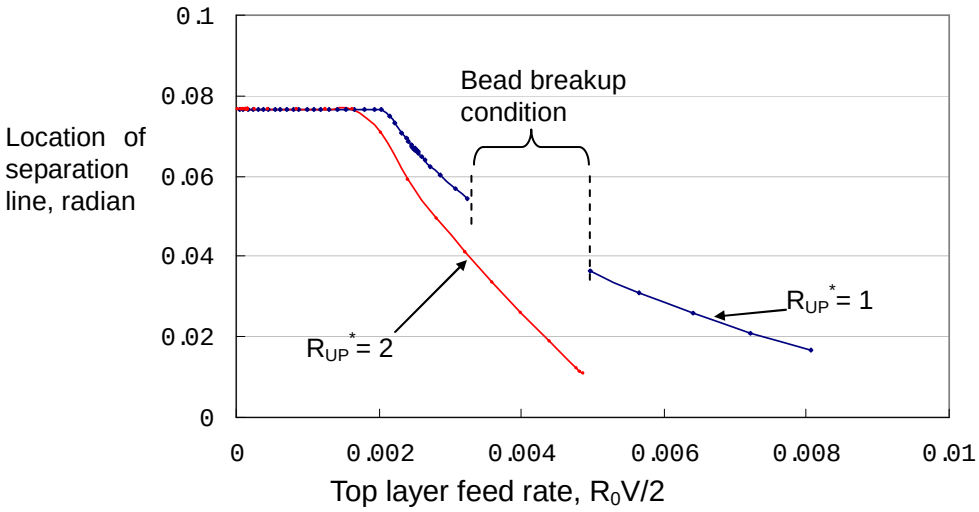

Fig. 5-15. Effect of radius of curvature of upstream lip on the location of separation line. N_{EL} = 8.7x10^{-5}, N_{CA} = 0.276, m = 1, R_D = R_m = 1, and Q_B = 2.5x10^{-3}.

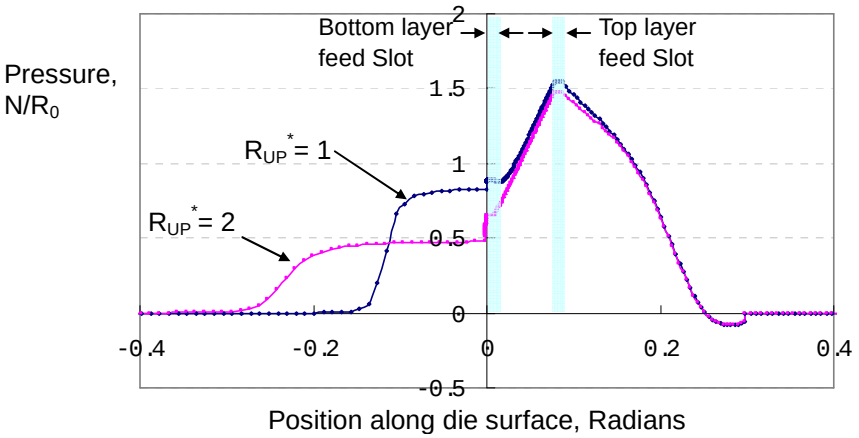

(a) Pressure profile along the die lip surface

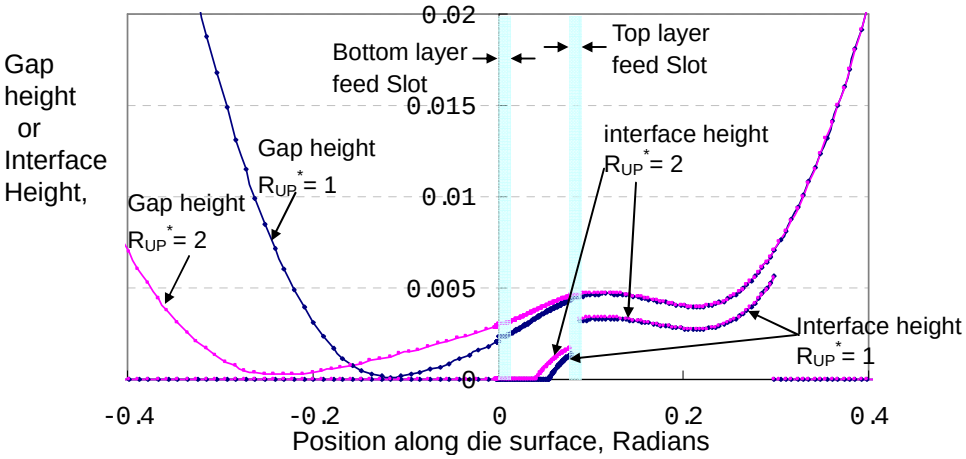

(b) Gap height and interlayer height profiles along the die surface

Fig. 5-16. Comparison of pressure and gap profiles of two die geometries with different upstream lip curvatures. $N_{EL} = 8.7x10^{-5}$, $N_{CA} = 0.276$, m = 1, $R_D = R_m = 1$, $Q_T = 3.2x10^{-3}$, and $Q_B = 2.5x10^{-3}$.

For successful two-layer coating, the best location of the separation line is reportedly at the downstream corner of the mid-lip—the “stability point” of Sartor et al. (1998). Fig. 5-15 shows that a more curved upstream lip is better at keeping separation line at stability point.

5.4.2. Effect of downstream lip curvature

The more curved the downstream lip, the higher the pressure over the downstream lip. When the downstream lip surface is more curved than the upstream lip surface and the intensities of feed rate is similar, the pressure gradient on the mid-lip becomes positive. [Fig. 5-19(a)] The adverse pressure gradient on the mid-lip induces backward Poiseuille flow and moves the separation line upstream. Fig. 5-19 shows the pressure and gap profiles of the case of same curvatures on the upstream and downstream lips, where the pressure gradient on the mid-lip is not so steep and is mainly determined by the feed rate effects.

Fig. 5-18 shows movement of separation line as the top layer feed rate is varying. As expected, separation line easily detached from the “stability corner” and moves upstream at lower top layer feed rate when the downstream lip is more curved. The effect of downstream lip curvature on the upstream meniscus location is shown in Fig. 5-17. When the downstream lip is more curved, the resultant higher pressure on the downstream lip and mid-lip expand the gap there

and makes the transition from the left branch to the right branch early in the condition of Fig. 5-17. But when the curvature of the downstream lip is same with that of upstream lip, the transition from the left branch to right branch is shifted to the higher top layer feed rate.

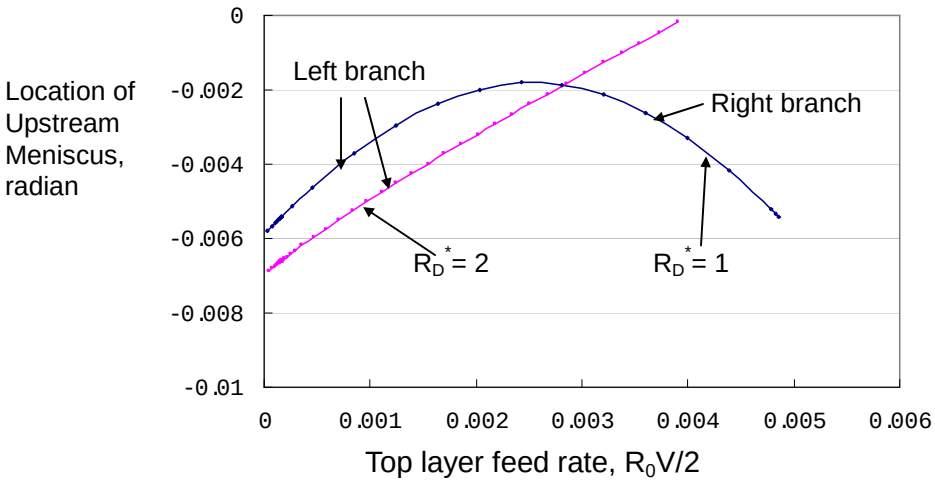

Fig. 5-17. Effect of radius of curvature of downstream lip on the location of upstream meniscus. $N_{EL} = 8.7x10^{-5}$, $N_{CA} = 0.276$, m = 1, $R_U = 2$, $R_m = 1$, and $Q_B = 2.5x10^{-3}$.

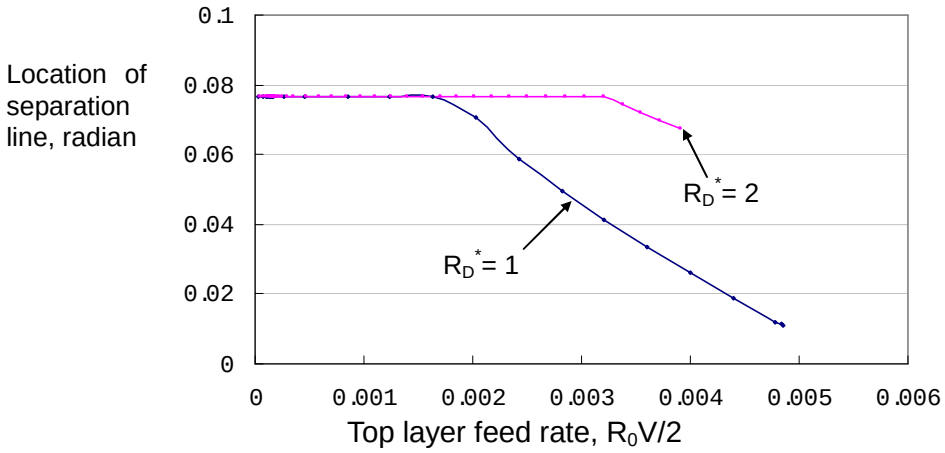

Fig. 5-18. Effect of radius of curvature of upstream lip on the location of separation line. $N_{EL} = 8.7x10^{-5}$, $N_{CA} = 0.276$, m = 1, $R_U = 2$, $R_m = 1$, and $Q_B = 2.5x10^{-3}$.

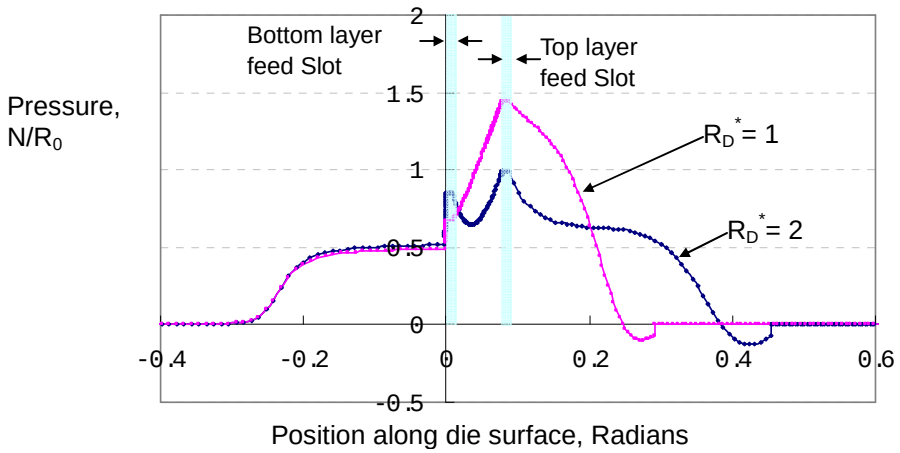

(a) Pressure profiles along the die surface

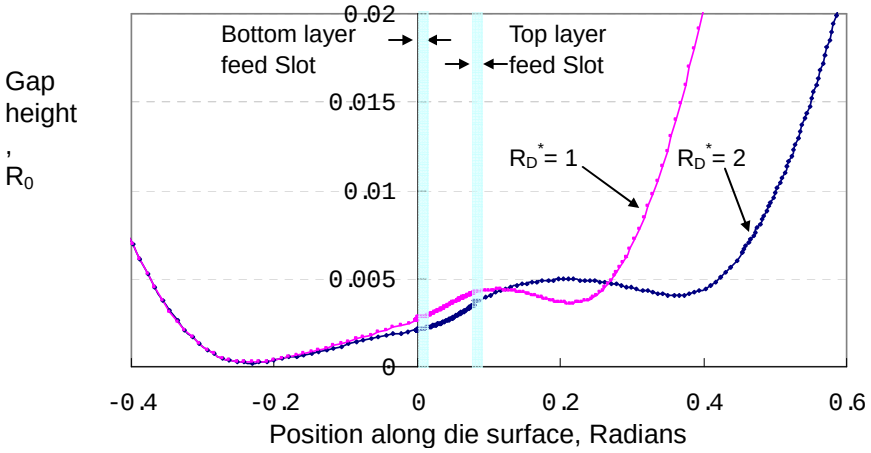

(b) Gap height profiles along the die surface

Fig. 5-19. Comparison of pressure and gap profiles of two die shapes with different upstream lip curvatures. N_{EL} = 8.7x10^{-5}, N_{CA} = 0.276, m = 1, R_U = 2, R_m = 1, Q_T = 2.5x10^{-3}, and Q_B = 2.5x10^{-3}.

5.4.3. Bulging mid-lip

The effect of the mid-lip in two-layer tensioned-web coating is easily buried by the pressure peaks at the two feed slots on either side of it. A mid-lip bulging out of the base arc of circle produces interesting effects: it not only sharpens the mid-lip but also concentrates the normal resultant force of the tension in the web on the liquid in the mid-lip zones while weakening the normal resultant force acting on the liquid in both the upstream and downstream lip zones. During the successive stages of bulging the mid-lip out of the base arc, the upstream meniscus was kept at the same place by adjusting the bottom layer flow rate. Otherwise the coating bead would flood at early stage of bulging mid-lip. Fig. 5-20 shows how the bottom layer feed rate should change to keep the upstream meniscus at same position. As mid-lip sharpens and receives more wrap angle, it builds higher pressure on the mid-lip and shaves more liquid so that the bottom layer feed rate should be reduced to keep the upstream meniscus on the upstream lip without flooding.

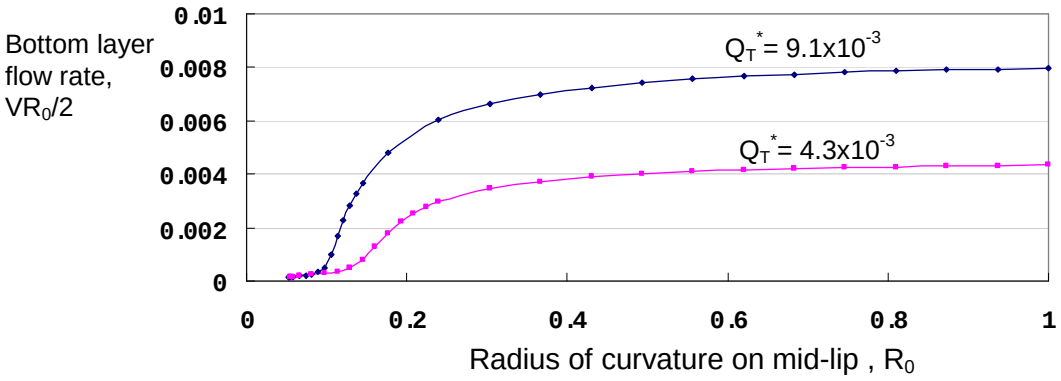

Fig. 5-20. Bottom layer feed rate needed to keep the upstream meniscus at same position with the mid-lip surface bulging out of base arc of circle. $N_{EL} = 5.0x10^{-5}$, $N_{CA} = 0.16$, m = 1, and $R_D = R_U = 1$.

Fig. 5-21 shows the movement of separation line in the same succession as in Fig. 5-20. As the mid-lip is bulged, the gap heights at both ends of mid-lip, at the upstream corner and the downstream corner of the mid-lip, all rise because the apex point of the mid-lip lifts the web. As described in section 5.2.4, high gap for the flow rate through it makes reverse flow on the die surface. As the mid-lip bulges out, reverse flow occurs at the downstream corner of the mid-lip and the separation line climbs up the shoulder of the mid-lip. This succession teaches that protrusion out of smoothly curved die surface shape—generally arc of circle—is unfavorable for preventing the recirculation or for keeping the separation line on the “stability corner”.

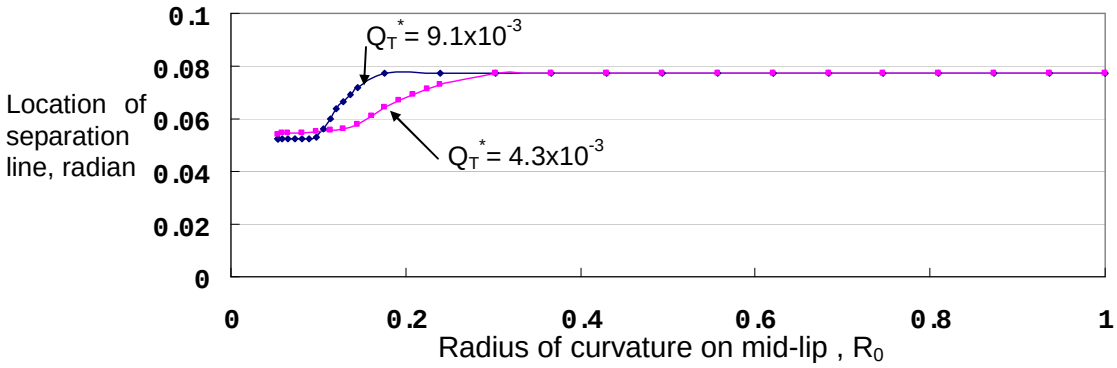

Fig. 5-21. Movement of separation line as the mid-lip surface bulges out of the base arc of circle, with the upstream meniscus kept at same position by adjusting Q_B. $N_{EL} = 5.0x10^{-5}$, $N_{CA} = 0.16$, m = 1, and $R_D = R_U = 1$.

In Fig. 5-22 the movement of upstream meniscus with a bulged mid-lip is compared with that of cylindrical die geometry as the web speed changes, to show the change in the range of possible operation speed. With the die shape of bulged mid-lip, the range of coating speed is expanded to the higher coating speed — twice the coating speed with $R_m^* = 0.2$ than with the base shape. This shift to the higher speed is due to the higher pressure forming on the bulged mid-lip which is resulted from concentrating bigger normal resultant force of the tensioned web on the narrow area in the bulged mid-lip. Fig. 5-23 shows the pressure and gap profiles with the die shape of bulged mid-lip compared with those of cylindrical base die geometry at same condition. The pressure profile with bulged mid-lip has a higher pressure peak over the mid-lip, which reaches to the bottom layer feed slot and to the upstream lip and push the upstream meniscus upstream against bead breakup.

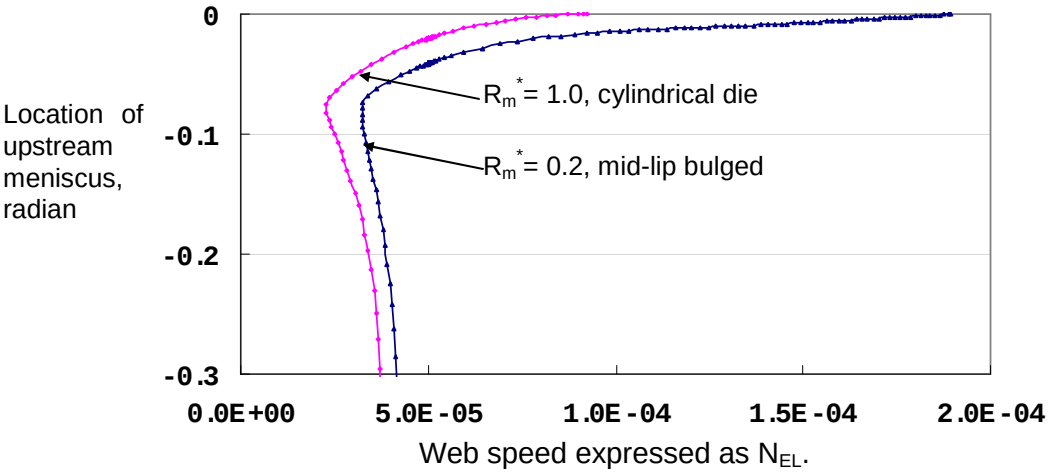

Fig. 5-22. Movement of upstream meniscus as the web speed changes. $Q_T = Q_B = 4.3x10^{-3}$, m = 1, and $R_D = R_U = 1$

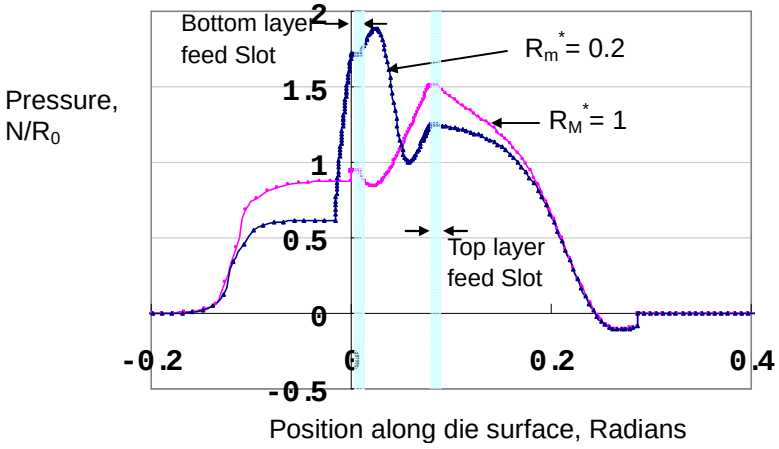

Fig. 5-23. Comparison of pressure profiles of die shapes of bulged mid-lip with cylindrical base die geometry. $N_{EL} = 9.2x10^{-5}$, $Q_T = Q_B = 4.3x10^{-3}$, m = 1, and $R_D = R_U = 1$

This type of die configuration, where most of the normal resultant force of the web tension is applied on a single die lip, the one upstream or the one in the middle, has merits over the other configurations: bead breakup is delayed by high pressure on the bulged lip, and the overall gap except over the bulged part gets narrow and less sensitive to the web fluctuations, since the bulged lip supports the web by high pressure in the thin liquid film over it. In Fig. 5-24 the die geometry from one of the patents using this configuration is shown. Shibata et al. (1990) in that patent claimed that they could avoid a streak-like irregularity by introducing this type of die configuration with pre-coated layer instead of bottom layer in two-layer coating.

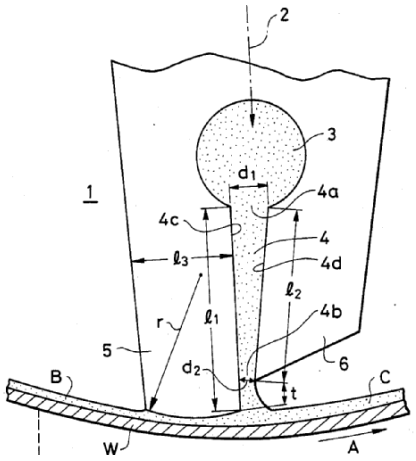

Fig. 5-24. Die geometry from Shibata et al. (1990, US4907530)

5.5. CONCLUSION

The Elastoviscocapillary model presented in the chapter is effective in describing the elastohydrodynamics on the two-layer tensioned web slot coating die and studying the die shape effects. Separation line location, which is reported to be important for the successful two-layer coating operation, could be predicted by zero shear stress condition.

The effects of process conditions were checked with cylindrical base die geometry. The effect of bottom-layer feed rate to the movement of upstream meniscus and to the bead breakup is almost similar to the feed rate effect in the single layer coating. But the effect of top-layer feed rate can be different from the feed rate effect in single layer coating depending on the process condition: a rise in top-layer feed rate in two layer tensioned web coating can cause bead breakup, Separation line is released from the so-called stability point, the downstream corner of the mid-lip, and moves upstream when top layer feed rate is raised enough to cause recirculation on the mid-lip.

Flattening the upstream die lip can release the separation line from stability corner, but high top-layer feed rate is still needed to move separation line backward to the upstream. Flattening downstream lip seems to tend to hold separation line on the stability corner, but two-dimensional flow analysis is needed to see if it stays on the stability corner or moves into the top-layer feed slot.

Chapter 6

1D/2D hybrid model of double layer tensioned-web slot coating

6.1. INTRODUCTION

As technology evolves, the number of applications where several coating layers are needed grows. More and more functions are demanded of a single product and it becomes impossible to perform all of the functions adequately in a single layer: the way out is to apply several layers. In the past, layers were often coated in tandem, i.e. the second layer was deposited on the surface of first layer, which had already been dried, at least partly dried. This is not only expensive, because the capacities of facilities must be doubled or their productivities halved, but is also unfavorable to quality. The surface of the partially completed product is exposed to the second stage of the production process, which can inflict damage to it.

The alternative is to apply all the layers simultaneously and solidify them

together. Tensioned-web coating is an attractive option for coating two layers simultaneously. One of particular features of tensioned-web slot coating is that it can make one of the layers exceptionally thin. It is the magnetic recording media industry that makes best use of this capability of tensioned-web slot coating system; a thin top magnetic layer enables high recording density. Fujifilm published in their web site on the ATOMM technology that they had developed, using a two-layer tensioned-web slot coating process, a high-recording-density magnetic media tape of recording density that had been only possible through a metal-evaporating deposition process; the coating thickness of the top magnetic layer of the tape was said to be 0.2 micron. Moreover, according to their more recent announcement, they have advanced their technology so that they can coat an even thinner layer by a factor of five.

Not even one fundamental study on two-layer tensioned-web slot coating has been published, although a lot of patents have issued on it. However, many fundamental principles that applied to conventional fixed-gap two-layer slot coating, which shares lots of features in common, are thought to pertain to two-layer tensioned-web slot die coating system.

Cohen (1993) analyzed the bead of two-layer slot coating with a uniform fixed gap by means of a simple rectilinear flow model—a viscocapillary model, except that he neglected effects of capillary pressure in the menisci. He worked out equations that predict limits of operation, the location of interlayer and separation line. The interlayer is a thin diffusion zone that separates the bulk of the two liquid layers. This zone is the result of the interdiffusion between the two layers of

miscible liquids; miscible liquids are the rule in simultaneous multilayer coating. Interdiffusion extremely rapidly broadens any interface created between miscible liquids that there's no interfacial tension. The interlayer begins at the separation line on the solid wall where the velocity is zero. Cohen (with Suszynski) also visualized slot coating flows with same methods used by Sartor (and Suszynski). He succeeded in observing the sequence of flow patterns, recirculations, location of interlayer and separation lines as the flow rates of the two layers, their viscosity ratio, and the vacuum pressure applied at the upstream meniscus were varied. Increasing vacuum pressure tended to pull the interlayer upstream, and at low vacuum, the interlayer separated from the downstream corner (Fig. 6-1). He also observed that the less viscous layer in the upper layer tended to lead to ribbing, which implies that coating with the more viscous layer on top is the more stable configuration.

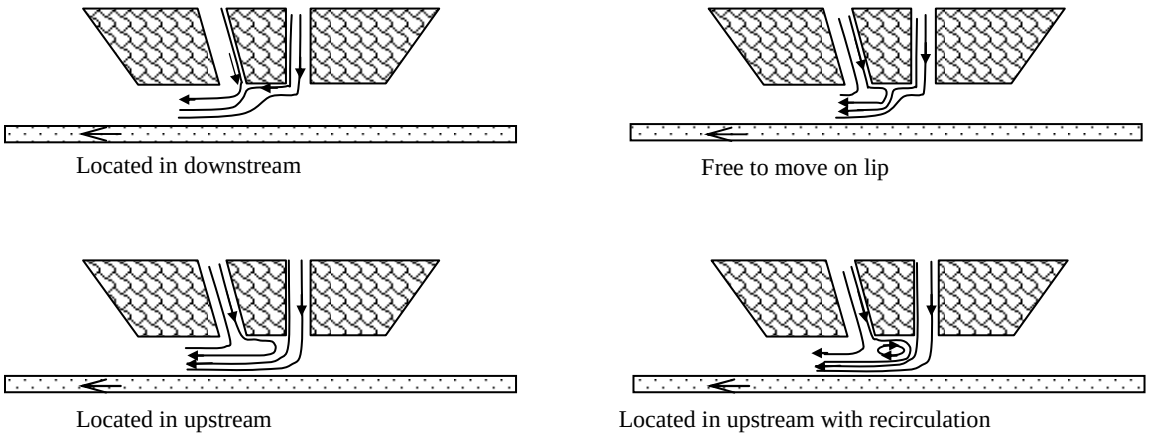

Fig. 6-1. Flow pattern observed in the intermediate section (from Cohen 1993)

Sartor et al. (1996, 1998) in their patents described in some detail a multilayer slot coater and how to control the pressure gradients in the coating bead. To achieve “stable two-dimensional flow in coating bead”, they claimed that the recirculations that can appear under the intermediate and downstream lips should be avoided and that the separating streamline should be pinned at the downstream edge of the intermediate lip, which they called the stability point, as shown in Fig. 6-2.

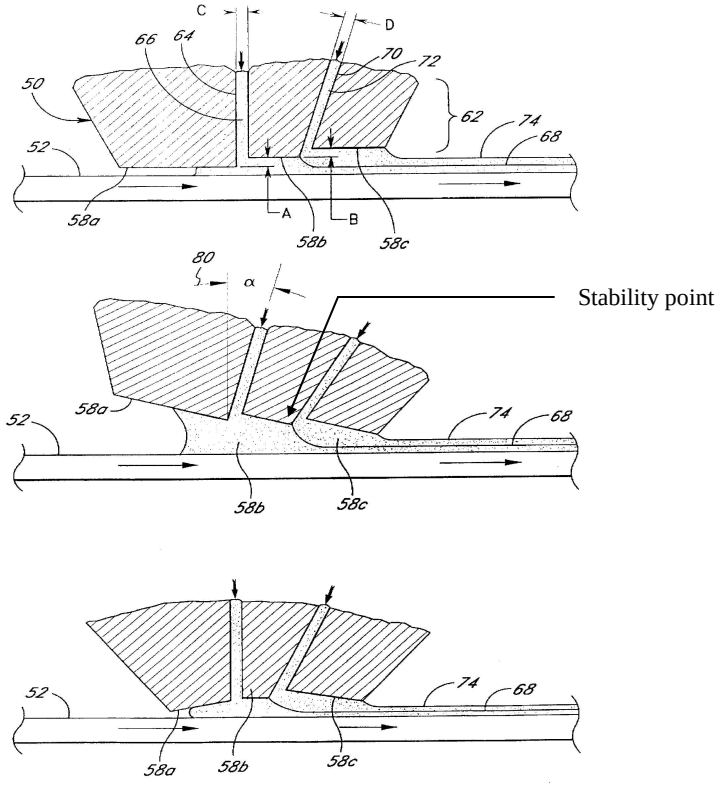

Fig. 6-2. Schematics of two layer slot coating lip configurations by Sartor et al. (1998)

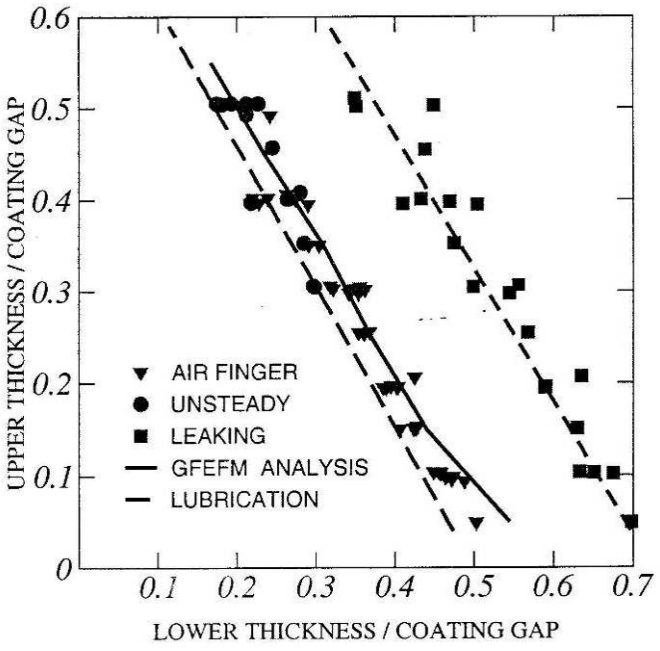

Fig. 6-3. Theoretical predictions and experimental determination of the low flow limit of the operation in two-layer slot coating. Conditions: Viscosity ratio = 1; P_{vac} = 0; Re = 2; Ca = 0.4. (from Musson 2001).

Musson(2001) analyzed two-layer slot coating by solving the Navier-Stokes equation system with Galerkin's method and finite element basis functions. He coupled two-dimensional model to arc-length continuation methods to trace out steady-state solution paths in the parameter space. Each steady state solution was checked for its stability and sensitivity to perturbations. He also made visualization experiments the results of which are shown in Fig. 6-3, where they are coupled with the results with theoretical prediction of his model. The dotted line in Fig. 6-3 shows the operating window prediction by Cohen (1990) from his

viscocapillary model, which agrees well with experimental data.

In the study of one parameter, the viscosity ratio (upper layer viscosity over lower layer viscosity), Musson found that only a limited range of viscosity ratio could be accommodated by the pressure difference between the downstream ambient air and the upstream vacuum chamber pressure. If the viscosity ratio was raised too much, the upstream meniscus moved toward upstream lip end and at above the upper limit of viscosity ratio, meniscus invaded the vacuum chamber. If the viscosity ratio was lowered too much, the upstream meniscus moved forward to the region under the lower-layer feed slot and at above the lower limit of the viscosity ratio the bead became unstable to three-dimensional disturbances. His frequency response analysis showed that the most detrimental disturbance in the two-layer slot coating is the fluctuation of coating gap and that the system becomes more sensitive to the coating gap disturbance as the top layer viscosity rises. In a two-parameter study, he tried to keep the upstream meniscus in same position as the viscosity ratio changed by manipulating other parameters, e.g. the upstream vacuum pressure; he checked the stability and sensitivity of the system to disturbances. He found that the system becomes unstable to a three-dimensional perturbation and sensitive to coating gap disturbances as the top layer viscosity falls.

Micro-vortices are undesirable to the coating quality because the liquid there would have infinite residence time if the flow is truly two-dimensional. When the coating liquid is a suspension, the particles tend to flocculate in these regions

and may periodically discharge large aggregates that cause defects. Sartor (1990) studied the microvortexes in the coating bead of the single layer slot coating and classified the microvortexes into four kinds according to their locations; under the downstream lip, under the upstream lip, on the downstream lip shoulder, and inside the feed slot. Some of these recirculations can fuse with each other. The most common class of microvortexes in tensioned-web slot coating appears to be those inside the feed slots, because the coating gap of tensioned-web coating is narrow compared to the gaps of fixed-gap slot coating and the feed rate is low. In his study on the microvortex inside a feed slot of single-layer fixed gap slot coating, Sartomer showed through his theoretical analysis with the Navier-Stokes system that the feed slot microvortex appears when the coating thickness is less than approximately one-fifth of the slot gap:

$$h_\infty < 0.2\, h_f \qquad (6\text{-}1)$$

where h_∞ is wet coating thickness and h_f is the width of feed slot.

Though the one-dimensional elastoviscocapillary modeling accounts well for the profile of the gap between web and die lips and the pressure profile along the gap, full two-dimensional Navier-Stokes theory is necessary to predict separation line location on the corner of the mid-lip accurately and occurrence of microvortexes around the feed slots. To reduce computational cost, the Navier-Stokes system for that region was hybridized with the elastoviscocapillary model so successful in the regions upstream of the bottom layer feed slot and downstream of the top layer feed slot. That is, the regions were matched at two

suitably positioned planes along the flow and all the governing equations, those of the elastoviscocapillary model upstream and downstream with those of the Navier-Sotkes theory in between, were solved together. Effects of layer flow rate ratio, viscosity ratio, and slot exit shape were examined with the hybrid model.

6.2. THEORY OF STEADY TWO-DIMENSIONAL FLOW

6.2.1. Navier-Stokes Equation System

The Navier-Stokes equation system of steady flow is comprised of the statements of mass and momentum conservation. In this study, only steady state flow is considered. Also, because the length scale of the coating is so small, the effects of gravity are neglected. The dimensionless, or unit-free, form of the momentum equation is

$$N_{RE}\mathbf{v}\cdot\nabla\mathbf{v}=\nabla\cdot\mathbf{T} \qquad (6\text{-}2)$$

where $\mathbf{v}$ is the velocity vector and $\mathbf{T}$ is the second rank Cauchy stress tensor. N_{RE} is Reynolds number, $N_{RE}\equiv\frac{\rho V_c L_c}{\mu_c}$, where ρ_c is the density, V_c is a characteristic speed, L_c is a characteristic length, and μ_c is the viscosity. If they are not specified, the characteristic length L_c is chosen to be the most representative radius of curvature of the die lips surfaces, V_c web moving speed, and ρ_c and μ_c the density and viscosity of bottom layer, respectively, and the

unit for the pressure and stress is chosen to be $\frac{\mu_c V_c}{L_c}$.

The coating flow are incompressible liquids, the conservation of mass equation reduces to the simple continuity equation.

$$\nabla \cdot \mathbf{v} = 0 \qquad (6\text{-}3)$$

The only liquids considered in this study are Newtonian liquids and the stress tensor in dimensionless form is

$$\mathbf{T} = -p\mathbf{I} + \nabla\mathbf{v} + \left(\nabla\mathbf{v}\right)^T \qquad (6\text{-}4)$$

where p is pressure. When the velocity and pressure gradient are non-zero only in parallel two-dimensional planes the equations simplify to the continuity equation and two components of momentum conservation equation in just three variables, namely pressure and two components of velocity.

6.2.2. Interfacial condition in multi-layer flow

When two immiscible liquids flow adjacent to one another, they are coupled by an interface whose location is generally unknown *a priori*. In steady state flow, the tractions acting on each side of the interface must balance the capillary pressure of the interface, the normal resultant of interfacial tension acting in a curved interface. Those tractions are each the vector sum of pressures, viscous traction stress and shear stress. The interfacial condition is

$$\mathbf{n} \cdot \mathbf{T}^A = \mathbf{n} \cdot \mathbf{T}^B + 2H\sigma\mathbf{n} \qquad (6\text{-}5)$$

where the superscript A and B are labels for the liquids, $\mathbf{n}$ is the unit normal

pointing from A to B, *H* is the mean curvature of the interface, positive when the interface is concave viewed from the B side, and σ is the interfacial tension.

However, when the two liquids in contact are miscible, there is no distinct phase boundary, but rather an interfacial zone that tends to thicken by diffusion between the two. This diffusion process can be slowed or even stopped, in most cases, solidifying the layers by curing or drying, as is done downstream in any coating process. The effect of miscibility is interdiffusion, which relaxes within picoseconds any composition gradient steep enough to produce interfacial tension, so that the interfacial condition reduces to

$$\mathbf{n} \cdot \mathbf{T}^A = \mathbf{n} \cdot \mathbf{T}^B \qquad (6\text{-}6)$$

Where the separating streamline meets a solid surface is called the separation line, at which all the viscous stresses disappear. The location of the separation line is unknown *a priori*, but it should be coincides with a streamline since no liquid flows across the interface between the layers. Therefore kinematic condition also should be satisfied along the interface. If Eq. (6-6) is expressed in stream line coordinate along the interface between the layers, the normal stress balance is

$$\left(p^A - p^B\right) = \left(\mu^A - \mu^B\right)\frac{\partial v_n}{\partial s_n} \qquad (6\text{-}7)$$

Where s_n is the arclength along a coordinate normal to the interface.

Scanlan (1990) studied the conditions for positioning separation line; he compared balancing the pressures on both sides and balancing normal stresses

of both sides at separation line. He found that pressure balance condition not only is correct, because it is derived from physical principles, but also is computationally robust. Continuous pressure condition is derived from Eq. (6-7) by applying zero viscous stress at separation line.

6.2.3. Membrane boundary condition on the liquid flow at the web surface

When the thickness of the web is so thin that, the stiffness number, $N_{SF} \equiv \frac{K}{R_0{}^2 N_0}$ (Eq. 2-53), is less than about 10^{-4}, the effects of bending moment (and twisting moment in three dimensions) become negligible, and the shell theory simplifies to the membrane theory. In this chapter only cases of thin web where membrane theory is effective are considered.

The tangential force balance of the membrane theory is that the derivative of tension is equal to the viscous stress on the web. Since in the condition of general tensioned-web slot die coating the tension change is not much, the tangential force balance is not used, and the web tension is set as constant. The normal force balance of the membrane theory is obtained by setting flexural rigidity as zero in Eq. (2-8):

$$\kappa_s N_0 - \Delta p = 0 \qquad (6\text{-}8)$$

where, $\Delta p = p - p_{atm}$ and κ_s is curvature. When arc-length coordinate ξ is defined along the web in the web's moving direction, curvature can be expressed in a base coordinate system, that is Cartesian coordinates x and y, and ξ

(Pranckh 1989):

$$\frac{d^2x}{d\xi^2} + \kappa_s \frac{dy}{d\xi} = 0\,, \quad \frac{d^2y}{d\xi^2} - \kappa_s \frac{dx}{d\xi} = 0 \qquad (6\text{-}9)$$

The other boundary condition for the liquid flow at the web surface is given as No slip boundary condition is given with no slip boundary condition.

$$\mathbf{t} \cdot \mathbf{v} = V \qquad (6\text{-}10)$$

where V is web moving speed, and **t** is tangential direction of the web shape.

6.2.4. Mesh deformation

When partial differential equations are to be solved with Galerkin's method and finite element basis function, those functions have to be deployed. The standard way is to divide the domain into sub-domains (elements). The unknown field variables are expressed as weighted sums of basis functions each of which is nonzero on only a limited number of subdomains. When the domain of interest is bounded by free surfaces, interfaces, or deformable solids, its shape is unknown *a priori*, and so it cannot be subdivided. That is, the discretization, or mesh, can not be prescribed. Because the configuration of subdomains generally changes as the shape of the domain changes, it becomes the part of problem. If the configuration of subdomains and the mesh consisting of their edges is governed by equations, they have to be solved as a part of solution. In other words the

equation system of the physics needs to be augmented with the equations that control the configuration of subdomains and their mesh.

The deployment scheme used in this chapter is the domain deformation or pseudo-solid method. The nodal points—the nodes—of the mesh are treated as material points on a fictitious elastic sheet which has the same shape as the domain of interest. When the boundary of the domain deforms to meet the physical requirement of the flow within it, the fictitious elastic material at any stage conforms to the shape of the domain. The mesh's nodes move along with the fictitious elastic medium as it deforms. Indeed, the moving mesh can be viewed as a node-connecting set of lines inscribed on deformable elastomeric sheet.

de Almeida and Scriven (1994) developed the concept of deformation mapping as means of generating boundary-fitted mesh. The concept was to couple a so-called variational mesh generation techniques (Thompson et al. 1985) with the deformation of elastic bodies, which can neither fold back on themselves nor tear. By inscribing a mesh on this elastic body, the mesh would not easily become defective.

The variational-based method from the standpoint of the physics of elasticity is to minimize an elastic potential energy of an elastic body, and thereby solve the equations of static equilibrium of the chosen elastic material. When W_e is elastic potential,

$$W_e = \int \omega(I, II, III) dV \qquad (6\text{-}11)$$

where ω is the stored energy function of the particular elastic medium under

imposed boundary conditions.

The deformation of the material depends on the relative motion of adjacent material particles. The local deformation of particles at **x** relative to their undeformed location **X** is described by the deformation tensor F.

$$F \equiv \left(\nabla_{\mathbf{X}} \mathbf{x}\right)^T \qquad (6\text{-}12)$$

where $\nabla_{\mathbf{X}}$ indicates the gradient operator with respect to location **X** in the referential state. The utility of F is that it relates the relative differential position vector $\mathbf{dx}$ in a deformed configuration to the relative differential position vector $\mathbf{dX}$ in reference configuration:

$$\mathbf{dx} = \left(\nabla_{\mathbf{X}} \mathbf{x}\right)^T \mathbf{dX} = \mathbf{F} \cdot \mathbf{dX} \qquad (6\text{-}13)$$

Green's strain tensor, $\mathbf{C}$, arises in the expression for the squared differential separation $(ds)^2$ of two neighboring particles with their separation $\mathbf{dX}$ in undeformed configuration:

$$(ds)^2 = \mathbf{dx} \cdot \mathbf{dx} = \mathbf{dX} \cdot \mathbf{F}^T \cdot \mathbf{F} \cdot \mathbf{dX} = \mathbf{dX} \cdot \mathbf{C} \cdot \mathbf{dX} \qquad (6\text{-}14)$$

Conversely, the original squared differential separation of a pair with length dS of that currently is $\mathbf{dx}$ is expressed in terms of deformed configuration

$$(dS)^2 = \mathbf{dX} \cdot \mathbf{dX} = \mathbf{dx} \cdot \mathbf{F}^{-\mathbf{T}} \cdot \mathbf{F}^{-\mathbf{1}} \cdot \mathbf{dx} = \mathbf{dx} \cdot \mathbf{B}^{-\mathbf{1}} \cdot \mathbf{dx} \qquad (6\text{-}15)$$

Here $\mathbf{B}$ is the Finger tensor and $\mathbf{B}^{-1}$ is the Cauchy strain tensor.

Now to decide how the elastic material deforms, a constitutive relation between stress and deformation is needed. Probably the simplest choice when

deformation is finite is the compressible neo-Hookean elastomer, which was employed by Musson (2001) for the material of the two-dimensional sheet-like domain. The stored energy function for such a material is

$$\varpi = aI_B + cIII_B - d\log_{10}\sqrt{III_B} \qquad (6\text{-}16)$$

I_B and III_B are the first and third invariants of the Finger tensor. He chosed the coefficients to be a = c = 0.5 and d = 8 ln(10) / 3. He wrote that the value of d guarantees that the energy always increases under either uniform compression or uniform dilation from the strain-free state. The corresponding stress-strain constitutive equation is given by a formula first derived by Finger (Truesdell and Noll 1965),

$$\mathbf{T}_\mathbf{c}^\mathbf{e} = \frac{2}{\sqrt{III_B}}\left[\left(II_B\frac{\partial\omega}{\partial II_B} + III_B\frac{\partial\omega}{\partial III_B}III_B\right)\mathbf{I} + \frac{\partial\omega}{\partial I_B}\mathbf{B} - III_B\frac{\partial\omega}{\partial II_B}\mathbf{B}^{-1}\right] \qquad (6\text{-}17)$$

here, $\mathbf{T}_\mathbf{c}^\mathbf{e}$ is the Cauchy stress tensor.

By substituting Eq. (6-16) into Eq. (6-17) Musson found the Cauchy stress of the elastomeric sheet on which a mesh was to be inscribed:

$$\mathbf{T}_\mathbf{c}^\mathbf{e} = \frac{2}{\sqrt{III_B}}\left[III_B\left(c - \frac{d}{2\ln 10\, III_B}\right)\mathbf{I} + a\mathbf{B}\right] \qquad (6\text{-}18)$$

Third invariant of the Finger tensor is

$$III_B = |\mathbf{B}| = |\mathbf{F}\cdot\mathbf{F}^{\mathrm{T}}| = |\mathbf{F}|^2 \qquad (6\text{-}19)$$

where $|\mathbf{B}|$ is determinant of B. Eq. (6-18) simplifies to

$$\mathbf{T}_{\mathbf{c}}^{\mathbf{e}} = \left(2c|\mathbf{F}| - \frac{d}{\ln 10 |\mathbf{F}|} \right) \mathbf{I} + \frac{2a}{|\mathbf{F}|} \mathbf{B} \qquad (6\text{-}20)$$

Deformation mapping is defined on static equilibrium. Since divergence of the stress tensor is a force per unit volume in its actual state, in static equilibrium, the momentum balance is expressed as

$$\nabla \cdot \mathbf{T}_{\mathbf{c}}^{\mathbf{e}} = 0 \qquad (6\text{-}21)$$

In some cases, such as in the case of large deformation, it is convenient to write the equation of static equilibrium as it maps onto the undeformed state, which is generally known whereas the deformed state is not. The mapped Cauchy stress tensor is called the first Piola-Kirchoff stress tensor. Piola-Kirchoff stress tensor, $\mathbf{T}_{PK1}^{\mathbf{e}}$, is related to the Cauchy stress tensor by (Malvern 1969) :

$$\mathbf{T}_{PK1}^{\mathbf{e}} = |\mathbf{F}| \mathbf{F}^{-1} \cdot \mathbf{T}_{c}^{\mathbf{e}} \qquad (6\text{-}22)$$

where $|\mathbf{F}|$ is determinant of **F.**

The equation of static equilibrium, Eq. (6-21), in the undeformed reference state is simply

$$\nabla_{\mathbf{X}} \cdot \mathbf{T}_{PK1}^{\mathbf{e}} = 0 \qquad (6\text{-}23)$$

Musson chose to solve the equations of domain deformation in the reference configuration, because it by definition is not distorted, which makes computing the mapping straightforward. In the present study Musson's version of domain

deformation was used to generate mesh; Eq. (6-23) was solved with Eq. (6-22) and Eq. (6-20).

The domain of elastic sheet should follow the changing shape of flow field. For this boundary conditions that control displacement of nodes in the direction perpendicular to the boundary are necessarily related to the physics of the underlying flow problem. At the boundary of membrane, free surface, or interface, the kinematic condition should be met since no fluid flow is allowed across the boundaries:

$$\mathbf{n} \cdot \mathbf{v} = 0 \qquad (6\text{-}24)$$

where $\mathbf{n}$ is the unit normal of the boundary.

The boundary conditions that control tangential displacement of nodes may be freely chosen, and are usually designed to produce a desirable node distribution from the distribution chosen on the reference domain. Two kinds of boundary conditions are used for node distribution. The first one is maintaining uniform stretch ratio along the boundary. The stretch along the boundary is

$$\lambda_{nn} = \left(\mathbf{t} \cdot \mathbf{B}^{-1} \cdot \mathbf{t}\right)^{-1/2} \qquad (6\text{-}25)$$

The desired condition for the uniform stretch is

$$\frac{\partial \lambda_{nn}}{\partial s} = 0 \qquad (6\text{-}26)$$

where s is the arclength.

The second boundary condition is to require that shear stress on the boundary of the mesh material to be zero:

$$\mathbf{tn} : \mathbf{T}_C^e = 0 \qquad (6\text{-}27)$$

Since shear stress is a function of the deformation gradient of the elastomeric material chosen for the domain that bears the mesh, it affects the angle at which the mesh lines meet the boundary; setting it zero, Eq. (6-27), ensures that any mesh line that meets the boundary at a right angle in the reference state does so in any deformed state.

6.3. Hybridizing 2D theory of the mid region with 1D elastoviscocapillary models upstream and downstream of it

The two-dimensional flow model based on the Navier-Stokes equation system of flow in the regions around and below the two feed slots was hybridized with the one-dimensional elastohydrodynamic model presented in Chapter 5 in order to study the important two-dimensional flow phenomena in computationally economic way. The phenomena of greatest importance are location of the separation line and appearance of microvortexes around the downstream, or top-layer feed slot, The base die shape was again chosen as a cylindrical one, almost same as that shown in the Fig. 5-5(a) except that the corners at the end of the top-layer feed slot were assigned to have radius of curvature, $0.0025R_0$.

6.3.1. Dividing zones

The overall structure of calculation domains were designed similar to that of the one-dimensional two-layer tensioned-web slot coating model shown in Fig. 5-4, except that the mid-lip zones, upstream feed-slot zone, and the downstream feed-slots zone were combined into the middle domain where the flow was treated as two-dimensional. The flow in the middle domain was matched to that in the downstream one at the radial plane, at Θ_{DM} = 5.57°; this position was chosen be approximately double the maximum downstream gap in the condition of this study to give enough length on the downstream lip of the two-dimensional zone that the flow there reached rectilinear flow at the downstream matching plane. Flow in the middle domain was matched to that in the upstream domain at the radial plane, Θ_{UM} = -0.06°, which was chosen to be very close to the downstream corner of upstream lip to avoid, as much as possible, the event of upstream meniscus's reaching the upstream matching plane. Since the main foci of the investigation with this hybridized model were the appearance of microvortex in the bottom layer feed slot and separation line position, the two-dimensional flow on the upstream lip was not seriously considered in this model,

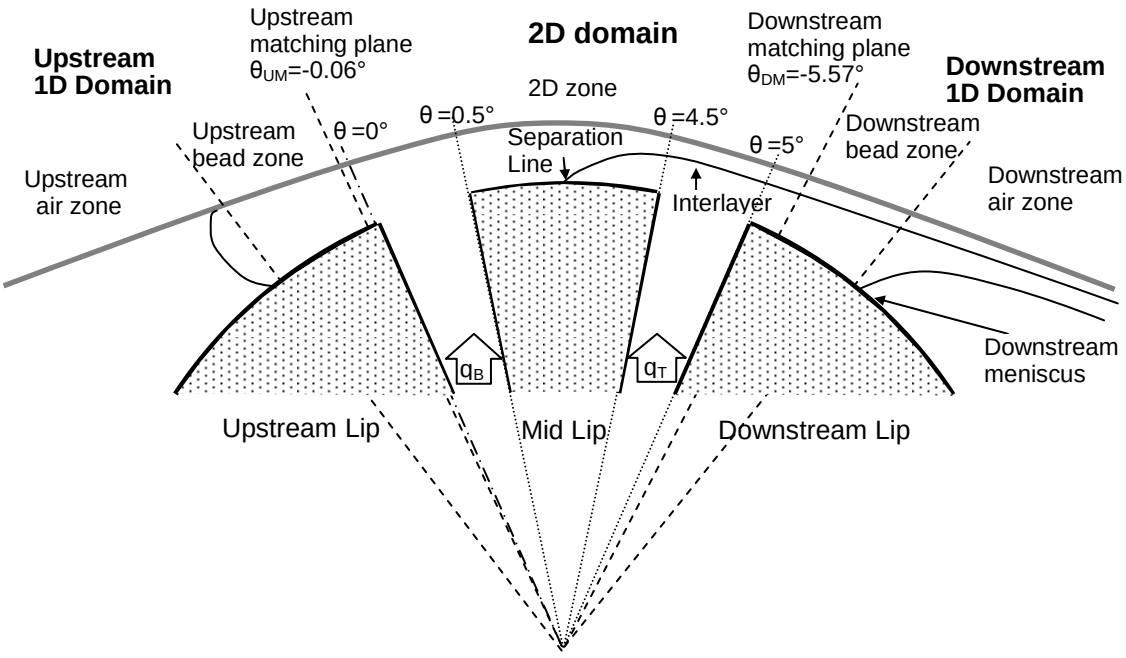

Fig. 6-4. Configuration of 1D/2D hybrid model of two-layer tensioned-web slot coating consisting of five zones, which were grouped into three domains: Upstream one-dimensional domain, two-dimensional domain in the middle, and the downstream one-dimensional domain.

6.3.2. Matching conditions and boundary conditions

Fig. 6-5 shows the boundary conditions on the domain of two-dimensional Navier-Stokes theory and the matching condition at the planes where it abuts the upstream and downstream domain of one dimensional elastoviscocapillary approximation. The discretization shown in Fig. 6-5 is the default mesh used in this study.

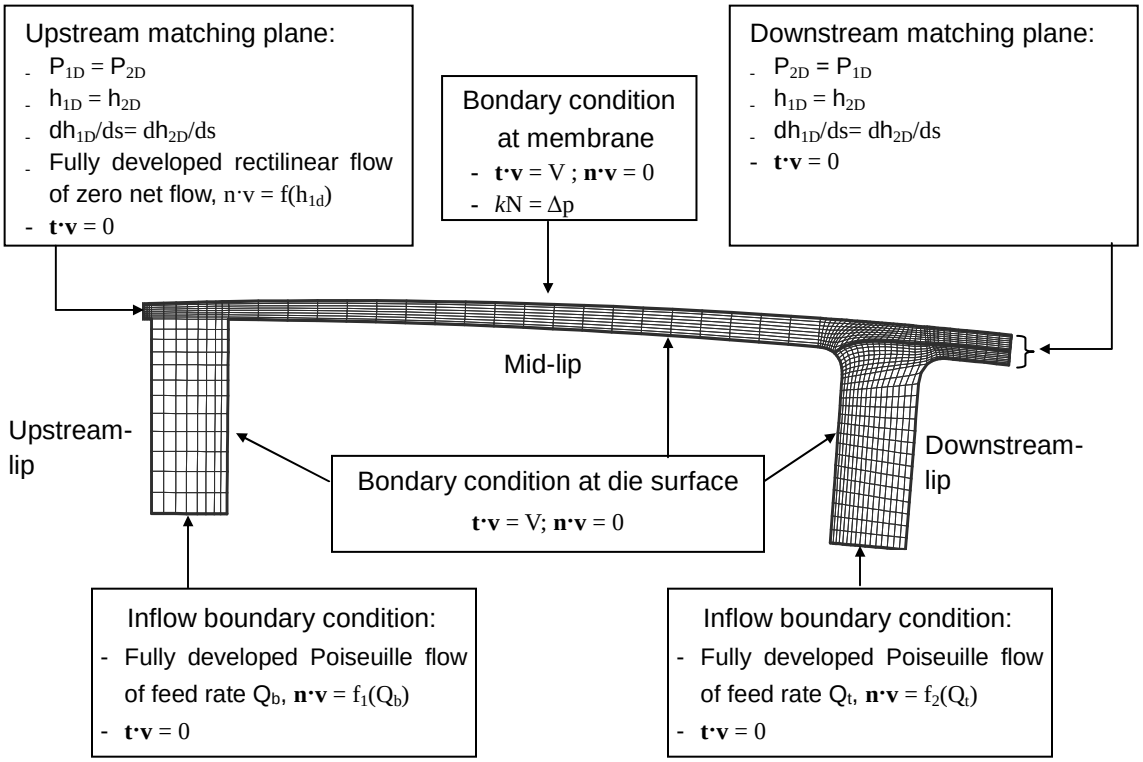

(a) Boundary conditions and matching conditions.

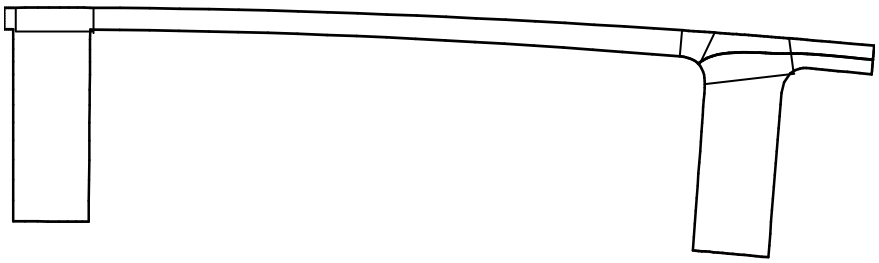

(b) Configuration of subdomains

Fig. 6-5. Boundary conditions and matching conditions in two-dimensional computation zone. The diagram also shows the default discretization used in this study, and the way it was assembled from subdomains. n is outward pointing unit normal, and t is tangential unit normal.

Depth of feed slot was set as two and half times of the width of feed gap, which is in general deep enough to assume fully-developed Poiseuille flow in the feed entry plane in the bottom.

At the bottom entry plane of each feed slot, the velocity was specified to be fully-developed Poiseuille flow of the volumetric flow rate per unit width imposed as feed rate at that slot. At the upstream matching plane, an open flow boundary, fully-developed rectilinear flow of zero net flow rate was specified. In the language of Galerkin finite element method, these are essential boundary conditions on the velocity profile.

The pressure profiles were matched at both matching planes. The pressure in the element right below the web at the upstream matching plane was chosen to match the pressure at the downstream end of upstream bead zone. At the downstream matching plane, normal viscous stress was assumed negligible and the pressure along the matching plane in 2D domain was equalized with the pressure from the downstream bead zone, P_{1D}.

$$P_{2D} = P_{1D} \qquad (6\text{-}29)$$

At both matching planes, the gap heights in the radial direction of the base polar coordinates of the one-dimensional calculation model were matched, and the slopes of the web were also matched.

6.3.3. Reducing the equations to algebraic ones

Galerkin's weighted residual method with finite element basis function was

employed to reduce the whole equation system to algebraic equations. That is, the residual of the differential equations from one-dimensional model upstream and downstream, of the two-dimensional Navier-Stokes theory in between, and of the domain deformation. In Galerkin's method the weight functions are the same as the basis functions used to represent the unknown field variables. Finite element basis functions are piecewise continuous polynomials of a particular order that are non-zero over at most a few adjacent elements. In the limit as a domain is subdivided into more and more elements, the growing number of polynomial basis functions, each nonzero at only one node of the mesh of elements, ultimately would become a complete set in the mathematical sense (Strang and Fix 1973). The pressure and velocity in the Navier-Stokes equations are expanded in necessarily truncated sets of these potentially complete basis functions:

$$\mathbf{v}(\mathbf{x}(\xi,\psi)) = \sum_{j=1}^{N_v} \mathbf{v}_j \phi_j(\xi,\psi) \qquad (6\text{-}30)$$

$$p(\mathbf{x}(\xi,\psi)) = \sum_{j=1}^{N_p} p_j \varphi_j(\xi,\psi) \qquad (6\text{-}31)$$

$$\mathbf{x}(\xi,\psi) = \sum_{j=1}^{N_x} \mathbf{x}_j \phi_j(\xi,\psi) \qquad (6\text{-}32)$$

Here N_v, N_p, and N_x are the number of basis functions for velocity, pressure, and the deformation of the reference domain necessary to represent the variables to the desired accuracy, given the distribution of the basis functions over the entire domain. Those distributions are the distributions of nodes of the finite element

mesh inscribed on the deformed domain. As described above, that mesh is determined by the chosen mesh on the undeformed domain, the constitutive relation chosen for the elasticity of the domain and the deformation of undeformed domain to the free boundary fitted deformed domain. $\mathbf{v}_i$, p_i, and $\mathbf{x}_i$ are the coefficients of the vector velocity, pressure, and vector mesh position, respectively. ϕ_j and φ_j are the chosen polynomial functions of space. Polynomials of lower degree in space are used to represent pressure than velocity in order to satisfy the Babuska-Brezzi condition (Sani et al. 1981). Biquadratic basis functions for velocity and bilinear discontinuous basis functions for pressure are used in this study.

The equations consisting of two-dimensional model are Eq. (6-2), Eq. (6-3), and Eq. (6-19), which are multiplied by basis functions and integrated over domain to produce the weighted residual equations:

$$\int_{\Omega} \left(N_{RE} \mathbf{v} \cdot \nabla \mathbf{v} - \nabla \cdot \mathbf{T} \right) \phi_i \, d\Omega = 0 \tag{6-33}$$

$$\int_{\Omega} \left(\nabla \cdot \mathbf{v} \right) \varphi_i \, d\Omega = 0 \tag{6-34}$$

$$\int_{\Omega} \left(\nabla_{\mathbf{x}} \cdot \mathbf{T}^{\mathbf{e}}_{PK1} \right) \phi_i \, d\Omega = 0 \tag{6-35}$$

The above weighted residual equation from two-dimensional Navier-Stokes theory and the residual equations from one-dimensional model were solved together by Newton iteration method as outline in chapter 2. The resultant linear equation system, average size of which was 15,000, was solved with a frontal

solver (Hood 1976). The convergence criterion in the Newton iteration was $1x10^{-7}$. Iteration was continued until both the L2-norm of residual and solution update are less than the tolerance. The initial estimate of solution in one-dimension part was brought from results of one-dimensional model described in Chapter 5. That of two-dimensional part was obtained by three steps. First, single phase flow field was solved in a fixed flow channel, the shape of which was brought from solution of one-dimensional model. Second, the interface position was solved with the membrane boundary still frozen. Third, membrane boundary position was solved together to make the first estimate of the solution of two-dimensional part.

Arc length continuation [see Chapter 2] was used to explore the parameter space.

6.4. Two-dimensional analysis on the flow in the double layer tensioned web coating.

6.4.1. Comparison with one-dimensional model

In the one-dimensional elastoviscocapillary model of two-layer tensioned web coating described in Chapter 5, the pressure directly over each of the feed slots was approximated as uniform. To spot check the validity of this approximation, the pressure profiles from Chapter 5's one-dimensional model were compared with those from the hybrid model, in which the feed slot pressure profiles fall in the middle region, i.e. where the flow is governed by the two-dimensional Navier-

Stokes system. The profiles are shown in Fig. 6-6.

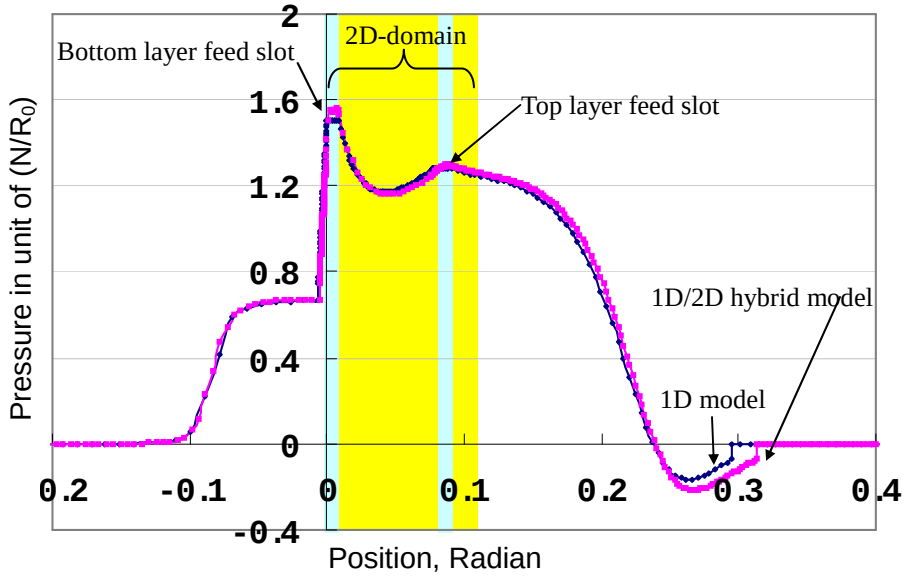

(a) Pressure profiles

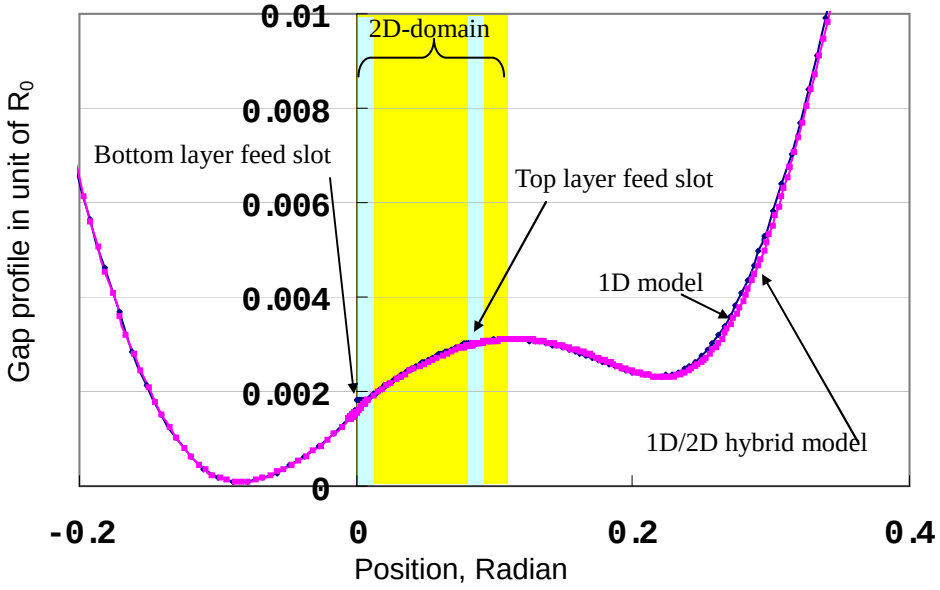

(b) Gap profiles

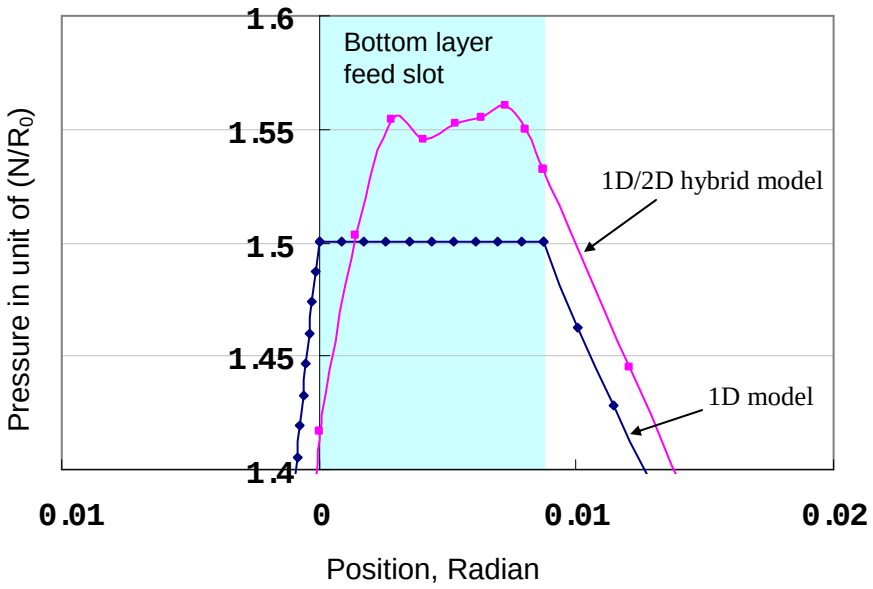

(c) Expanded pressure profiles around the bottom layer feed slot

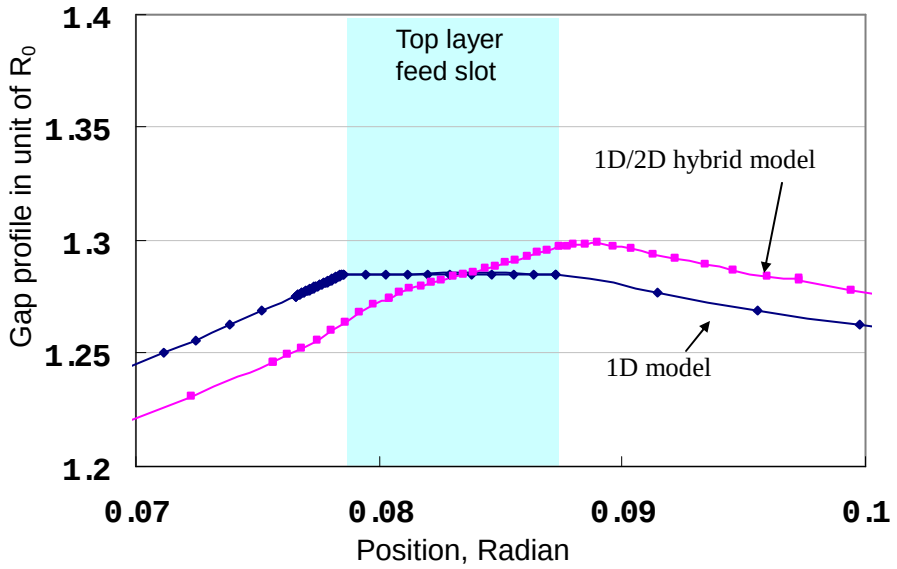

(d) Expanded pressure profiles around the top layer feed slot.

Fig. 6-6. Comparison of the prediction of the hybrid model with that of one-dimensional elastoviscocapillary model of Chapter 5. $N_{EL} = 4.6 \times 10^{-5}$, $\theta_A = 5^{\circ}, \theta_D = 7^{\circ}$, $N_{RE} = 0.87$, $Q_T = 0.76 \times 10^{-3}$, $Q_B = 2.5 \times 10^{-3}$, m = 1, and $N_{CA} = 0.145$.

As shown in Fig. 6-6 (a) and (b), the overall pressure and gap profiles predicted by the cruder and the more accurate models are seen to agree well except in a small zone near the downstream meniscus. The difference in the downstream meniscus location is rather big. This is thought to be from the differences in the two pressure profiles over the feed slot. Though the pressure differences in the feed slots are small when compared to the overall pressure level, the downstream meniscus location is sensitive to that level of pressure difference because the downstream meniscus is located in the area of wide gap where change of meniscus location doesn't make big difference in pressure profile. Fig. 6-6 (c) and (d) show the enlarged pressure profiles in bottom layer feed slot and top layer feed slot respectively. In both the areas, the pressure profile from hybrid model is lower than that from one dimensional model in the upstream side of feed slot but rises as the position goes to the downstream side of feed slot. These differences seem to be the effects of converging and diverging channel, which are ignored in one dimensional model, over the feed slot. In spite of these differences, which are rather small with respect to the overall pressure profile, assuming uniform pressure opposite feed slot seem to be reasonable in crude model.

6.4.2. Effect of the bottom layer feed rate

Shapes of flow channel of two different bottom-layer feed rates in whole 2D-zone computed with the hybrid model are shown in Fig. 6-7 with pressure

contour labeled with dimensionless pressure. Grey scale represents pressure level. As the feed rate rises, the gap expands to accommodate higher liquid flow rates. This is called self-adjusting gap, one of well-known features of the tensioned-web slot coating. Feeding raises the pressure around the feed slots. In both Fig. 6-7(a) and (b) the Qt was maintained low so that the pressure levels in the top layer feed slot is not high in both the figures. In the condition of Fig. 6-7(a), Q_b is maintained similar to the flow rate on the foil-bearing of similar condition, at which the radius of curvature and N_{EL} are same with that on the mid lip but the upstream and downstream pressures are ambient. The lubricant flow rate calculated from Eq. (2-1) in the foil bearing which has the radius of curvature and N_{EL} same with the mid-lip is 2.73×10^{-3}. No dominant pressure gradient exists on the mid lip besides the pressure peaks from the feed slot. But in Fig. 6-7(b) where feed rate in the bottom layer feed slot is given high, the strong negative pressure gradient forms on the mid lip.

In both cases, the pressure fields on the lips were almost one-dimensional, and no two-dimensional flow feature was found in the flows on the lips. The area of particular interest is near the top layer feed slot, where separation line and interface exist and microvortexes appear. To look at the flow closely, this area was zoomed and shown in Fig. 6-8.

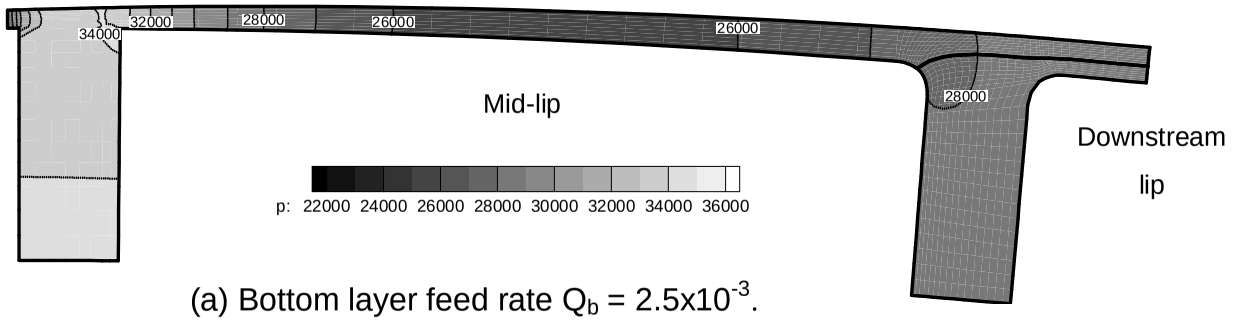

(a) Bottom layer feed rate $Q_b = 2.5 \times 10^{-3}$.

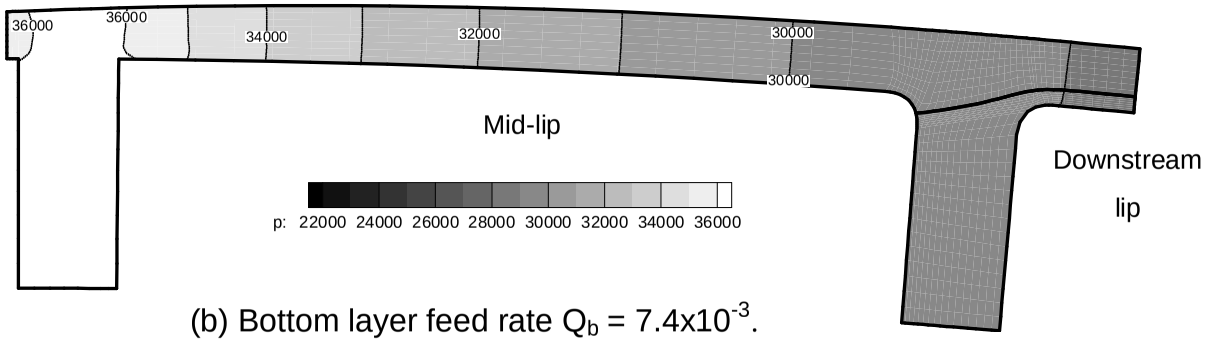

(b) Bottom layer feed rate $Q_b = 7.4 \times 10^{-3}$.

Fig. 6-7. Shape of the domain in 2D-zone. $Q_t = 0.76 \times 10^{-3}$, $N_{EL} = 4.6 \times 10^{-5}$, $N_{RE} = 8.7$, Web approach angle = 5°, Web departure angle = 7°, and viscosity ratio m = 1.

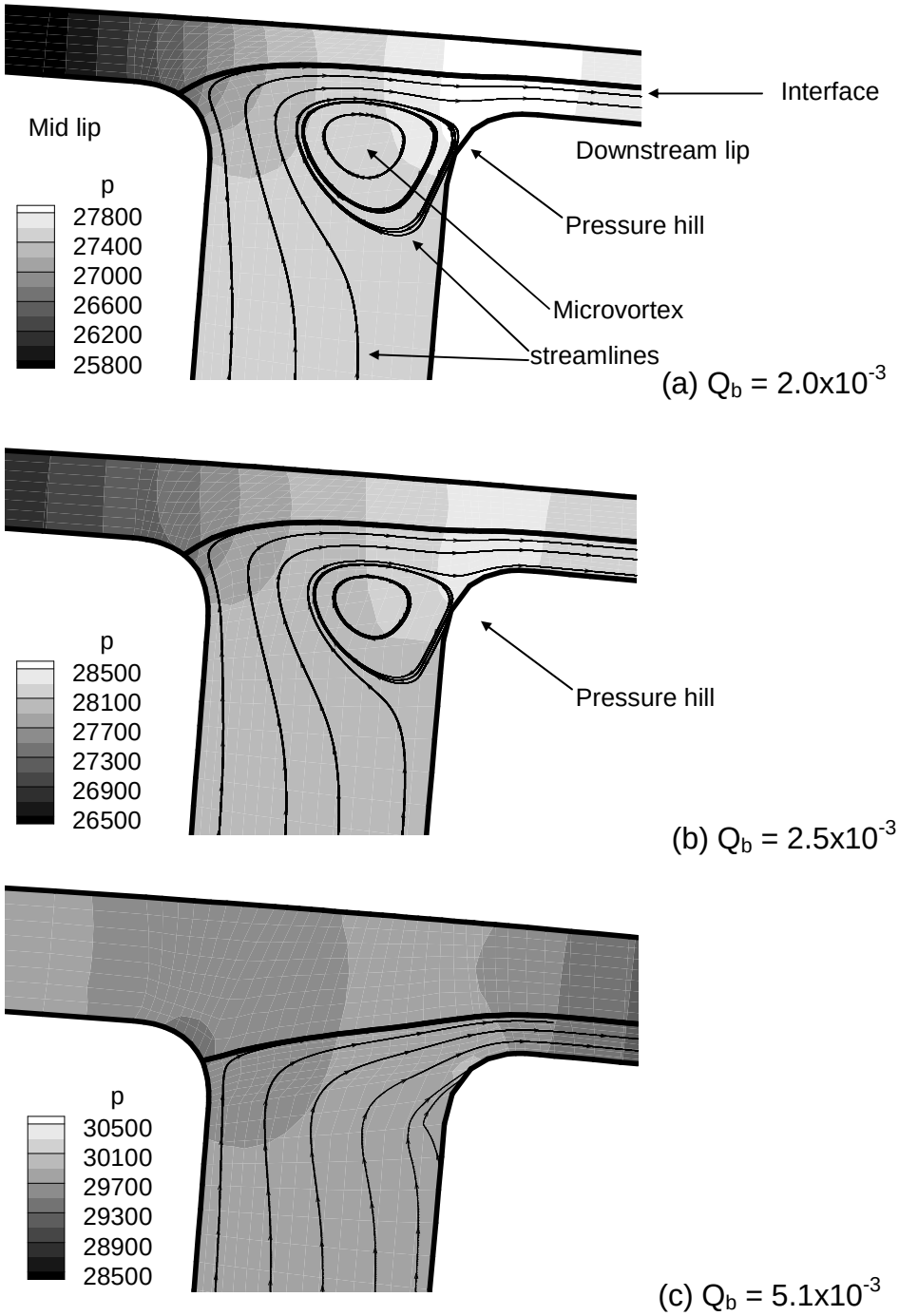

Fig. 6-8. Effect of bottom layer feed rate on the flow around the top-layer feed slot. Conditions are same with Fig. 6-7. (Grey scales represent pressure); Q_t = $0.76x10^{-3}$, N_{EL} = 4.6 x 10^{-5}, N_{RE} = 8.7, Web approach angle = 5°, Web departure angle = 7°, and viscosity ratio m = 1.

Fig. 6-8 shows the streamlines in the top-layer flow and the shape of the interface as the bottom layer feed rate varies. The microvortex shown near the corner of the downstream lip in the top layer feed slot disappears as the bottom-layer feed rate and the gap height around the top-layer feed slot rise. Contour plots of the pressure fields, which are represented as gray scale, shed hint on how the microvortex is formed. When the microvortex exists, a pressure hill appears in the fluid, inside the feed slot, near the downstream lip corner, making adverse pressure gradient along the downstream-side wall inside the feed slot. The adverse pressure gradient causes on the wall surface a backflow, which becomes a part of the microvortex.

The pressure hill inside the feed slot near the corner of the downstream lip might be simply seen as result of the converging channel which is formed by round corner of the downstream lip; though the corner radius was given sharp, $0.0025R_0$, it forms short converging channel when viewed in micro scale. One-dimensional flow model based on the lubrication flow assumption, one example of which can be found in section 5.2.4, has been effective in describing reveres flows in the lubrication-type flow in converging channel. But in this time one-dimensional flow model is not enough to explain the corner microvortex and the pressure hill causing it, because they’re totally two-dimensional flow phenomena. The detailed generation mechanisms of the pressure hill and the microvortex were studied in detail in section 6.5 with the two-dimensional flow model and fixed-gap flow channel designed for this study. Summary of the mechanism is given in Fig. 6-9. Moving substrate generates a viscous stress field that

penetrates into the feed slot and turns into a pressure hill at the downstream lip corner inside the feed slot. As the hill expands its area, the microvortex appears and grows.

The microvortex in Fig. 6-8 diminishes as the bottom-layer feed rate rises. Increase of bottom layer feed rate widens the overall gap between the web and the lips surfaces making it longer, the traveling distance for the viscous shear stress to get inside the feed slot. As a result, sizes of the pressure hill and the microvortex diminish as bottom feed rate rises.

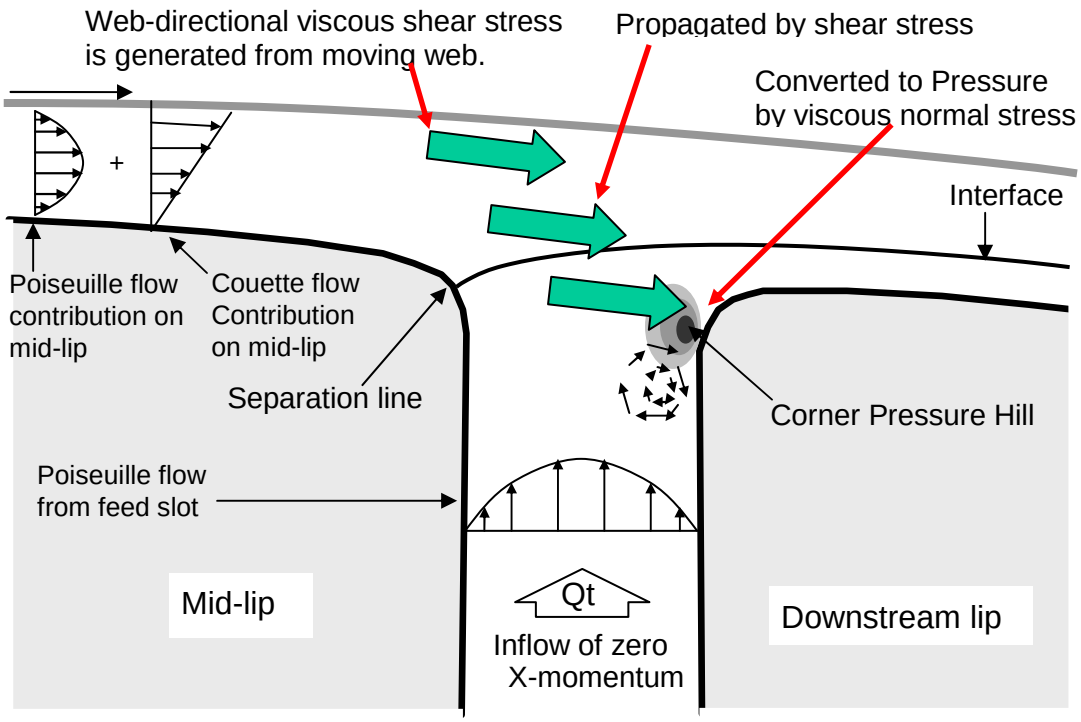

Fig. 6-9. Illustration about the generation of the pressure hill at the downstream corner of the top layer feed slot.

The separation line turns along the rounded surface of the downstream corner

of mid-lip as bottom layer feed rate changes. Separation line locates itself at a stagnant point where viscous stress disappear (Musson 2001). All viscous shear stresses should be balanced at the surface of separation point. Roughly there are three major contributions to the shear stress on the separation line: Couette flow from web movement, Poiseuille flows driven by the pressure gradient on the mid lip, and another Poiseuille flow by the pressure gradient from the top-layer feeding. When bottom-layer feed rate is high—the lubricant flow rate of foil bearing of the same surface curvature and elasticity number to those given on the mid-lip is fair criterion to judge if it is high or not—favorable pressure gradient forms along the mid lip as it is discussed earlier with Fig. 6-7. Fig. 6-8 (c), a case of favorable pressure gradient on the mid lip—shows that pressure gradient on mid-lip pushes the separation line toward the inside of the bottom-layer feed slot. But once the separation line gets inside of feed slot, it becomes less sensitive to the bottom layer feed rate. When top layer feed rate is not high the separation line seldom climbs onto the mid-lip surface since there is always forward viscous stress in the flow on the mid lip.

Under the conditions where the separation should locate on the upper surface of the mid lip, obtaining converged solution was not successful because of the big mesh distortion.

6.4.3. Effect of top layer feed rate

In this study the angle between the web movement and the flow direction in deep inside of feed slot is almost set near 90 degree as shown in Fig. 6-8 or Fig. 6-10; the angle change resulting from the web deformation is minor. In practical die shapes, angles of web to the feed slot direction, which is direction of feed slot wall in 2D cross-sectional view, will not always be close to the right angle. But in general the angle at which feed slot faces the web is within 20 degree from right angle, and discussion which follows in this section will hold true in most of the die shape.

Web-moving-directional velocity component of the feed flow deep inside the top layer feed slot is minor compared to the velocity component in the feed slot direction. When the shear stress generated at the surface of moving web propagates downward and penetrates into the feed slot, the feed flow of which the web-directional velocity component is zero would act against the shear stress penetration because it flushes the penetrated shear stress out of the feed slot. Fig. 6-10 shows the appearance and growth of microvortex which reflects the amount of shear stress penetration into the feed slot as the top-layer feed rate changes [detailed discussion on the shear stress penetration can be found in section 6.5]. Under the conditions given in Fig. 6-10, no microvortex is present when the top layer feed rate is high; but as it falls, a microvortex appears at the upstream corner of the downstream lip and grows to fill nearly the entire feed slot. Growth of microvortex is also accompanied by growth of pressure hill or adverse

pressure gradient along the downstream-side wall inside feed slot.

The increase in feed rate raises the pressure gradient along the feed channel, for more Poiseuille flow should be produced. Higher pressure gradient along the wall of the feed slot pushes the separation line back onto the upper surface of the mid-lip. The separation line moves towards the inside the feed slot as the top layer feed rate falls. But the location of separation line is rather insensitive while the bottom layer feed rate is close or smaller than the lubricant flow rate of the foil bearing in similar condition, same radius of curvature and same elasticity, [Fig. 6-10 (a) and (b)] since the change in pressure profile on the mid-lip is not so much in this condition.

The effects of same parameter, top layer feed rate, were check again at almost the same condition with that of Fig. 6-10 except that the bottom layer feed rate is set high to form a strong pressure gradient on the mid-lip. The results are shown in Fig. 6-11. When the bottom layer feed rate is high, separation line doesn't climb onto the upper surface of the mid-lip even with extraordinarily high top layer flow rate, Q_t = 15.2×10^{-3}, because shear stress from the web movement are backed by the pressure gradient developed on the mid-lip. In this condition, the microvortex disappears at lower level of top-layer feed rate than the case in Fig. 6-10 since thicker top layer increases the distance for the shear stress travel to get into the feed slot.

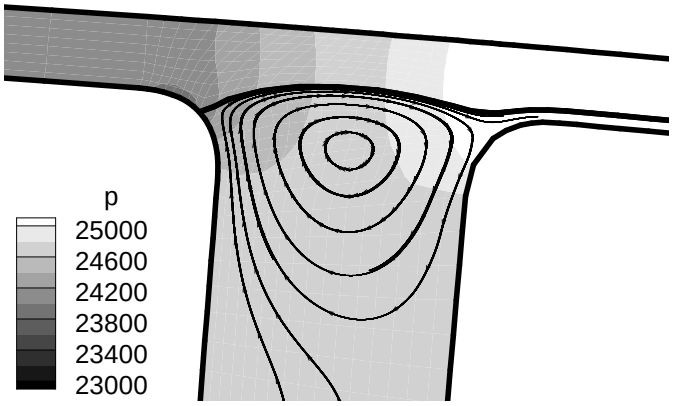

(a) $Q_t = 0.76 \times 10^{-4}$

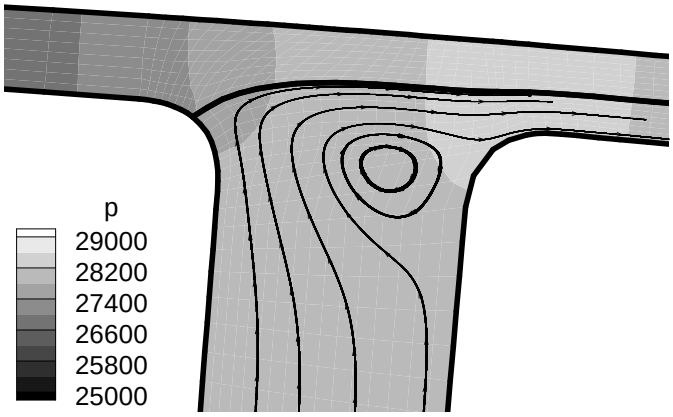

(b) $Q_t = 7.6 \times 10^{-4}$

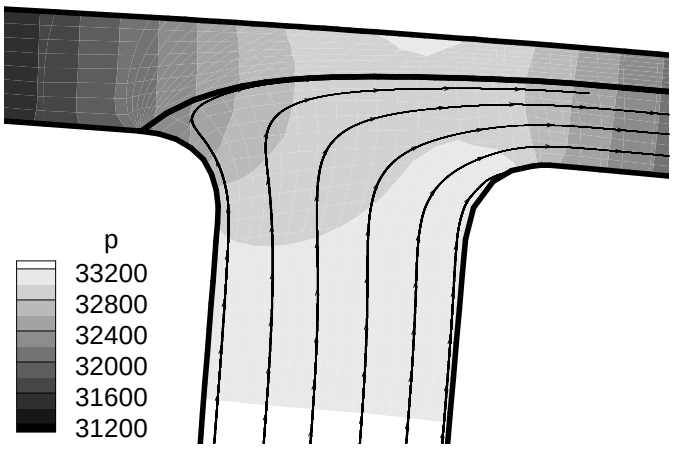

(c) $Q_t = 33 \times 10^{-4}$

Fig. 6-10. Effect of top layer feed rate on the flow around the top layer feed slot. $Q_b = 2.5 \times 10^{-3}$, $N_{EL} = 4.6 \times 10^{-5}$, $N_{RE} = 8.7$, $\Theta_A = 5^\circ$, $\Theta_D = 7^\circ$, and viscosity ratio m = 1.

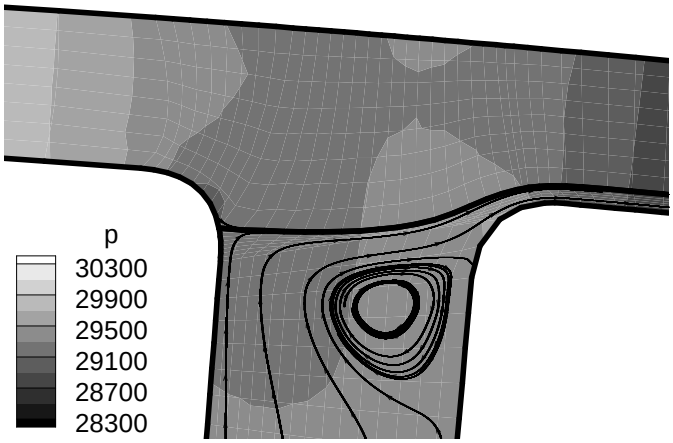

(a) $Q_t = 1.5 \times 10^{-4}$

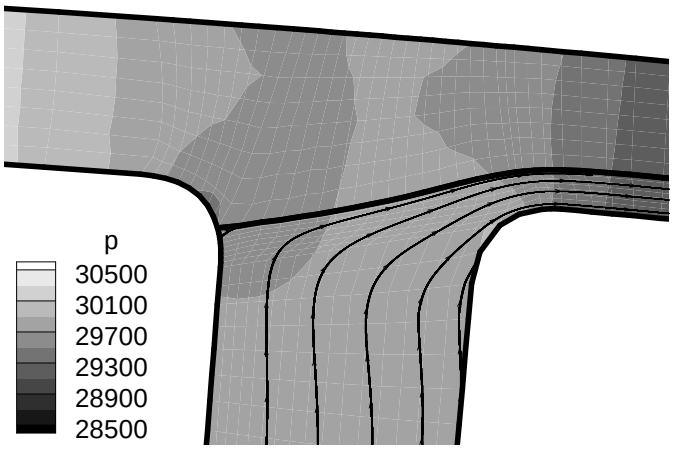

(b) $Q_t = 7.6 \times 10^{-4}$

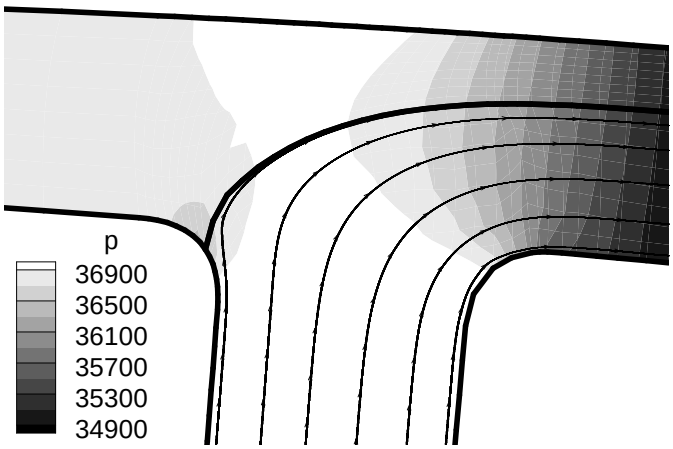

(c) $Q_t = 15.2 \times 10^{-3}$

Fig. 6-11. Effect of top layer feed rate on the flow around the top layer feed slot. $Q_b = 7.0 \times 10^{-3}$, $N_{EL} = 4.6 \times 10^{-5}$, $N_{RE} = 8.7$, $\Theta_A = 5^\circ$, $\Theta_D = 7^\circ$, and m = 1.

6.4.4. Effect of viscosity ratio

Changing viscosity ratio brings significant changes to the pressure distribution in the coating bead and affects the interface shape and the appearance of microvortex. Fig. 6-12 shows the changes in the bead flow as the top layer viscosity changes. When viscosity ratio, top layer viscosity to bottom layer viscosity, falls the microvortex inside the feed slot grows; conversely as the ratio rises the microvortex at the corner shrinks and disappears. Again the shear stress penetration into the feed explains the behavior of the microvortex. Since the web speed and the viscosity of bottom layer are kept same during this viscosity ratio continuation, the flux of shear stress produced at the web surface is same. When it is propagated to the top layer through the interface, the impact of the same amount of shear stress varies depending on the top layer viscosity. When the top layer viscosity rises, the momentum input needed to move the liquid in the top layer feed increase. It affects the penetration depth of shear stress, and the rise in top layer viscosity reduces the microvortex. On the contrary, when the viscosity ratio is low, the same flux of the shear stress induced at the substrate surface affects more in the top layer liquid than to the same viscosity liquid, and the microvortex grows.

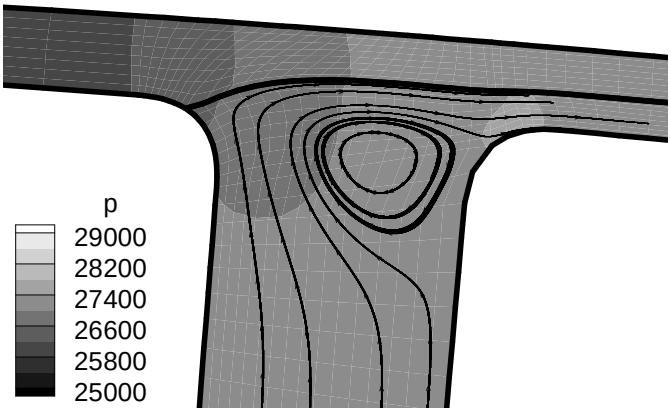

(a) m = 0.7

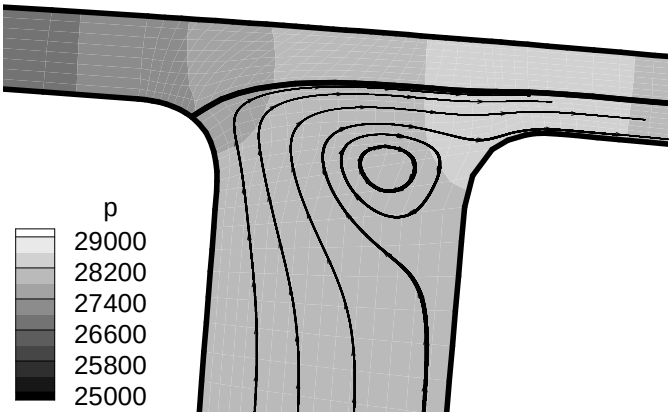

(b) m = 1

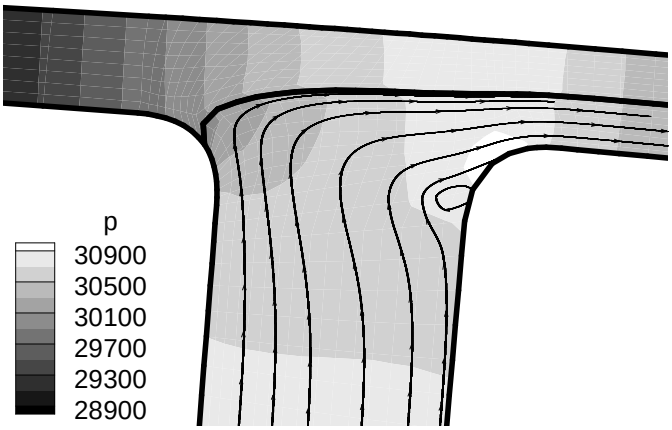

(c) m = 2.4

Fig. 6-12. Effect of viscosity ratio, top layer viscosity to bottom layer viscosity, on the bead flow around the top layer feed slot. μ_b = 25 cps, $Q_b = 2.5 \times 10^{-3}$, $Q_t = 0.76 \times 10^{-3}$, $N_{EL} = 4.6 \times 10^{-5}$, N_{RE} = 8.7, $\Theta_A = 5^\circ$, and $\Theta_D = 7^\circ$.

6.5. Microvortex inside feed slot

To study the generation of the microvortex inside the feed slot, two-dimensional Navier-Stokes equation system presented in section 6.2.1 was solved by Galerkin's method with finite element basis function for single phase flows inside the fixed channel of which the condition and the shape are similar to those around the feed slot of the slot coating. After the solutions were obtained elemental forces, which are the net viscous force, the inertia force, and the pressure force applied on each computational element, were calculated, and their effects on the microvortex were discussed.

6.5.1. Channel geometry and boundary conditions

Fig. 6-13 shows the shape of the flow channel and the boundary conditions used in calculation. All the corners in die shape were chosen to meet at right angle to simplify the analysis. Top wall movement, or web movement, is in x direction and the inner wall of the feed slot was laid in y direction.

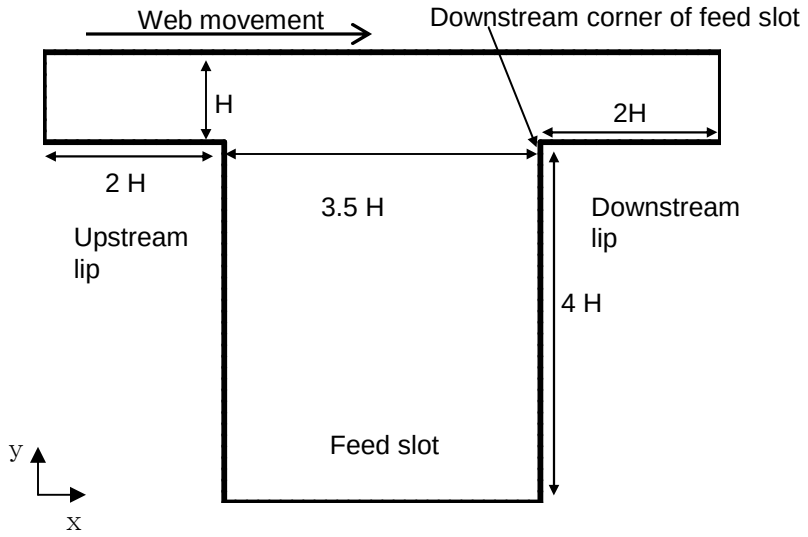

(a) Dimensions in units of the gap H.

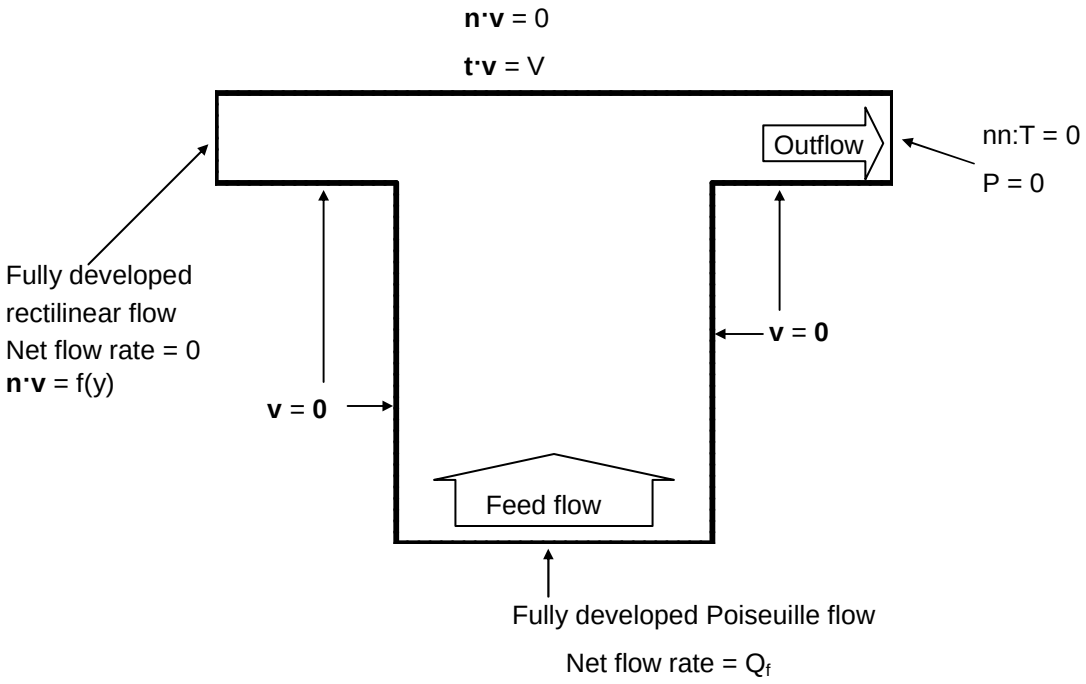

(b) Boundary conditions

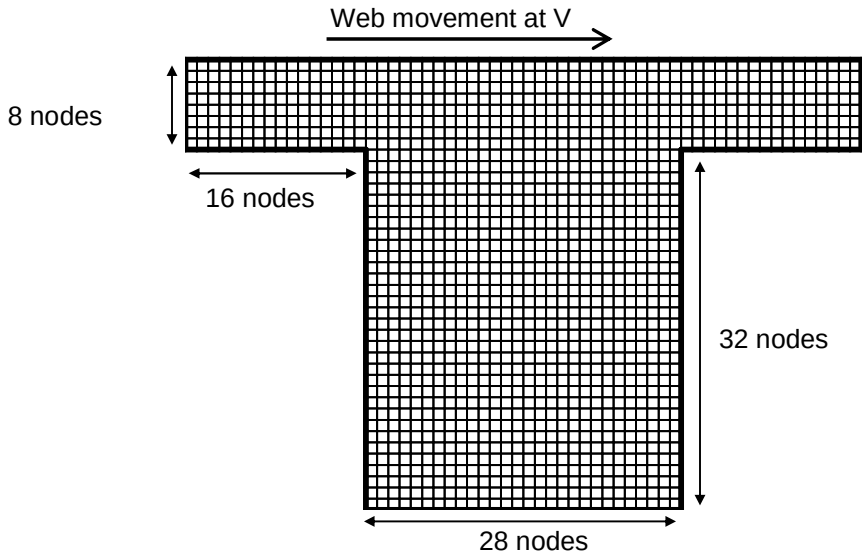

(c) Discretization for force analysis

Fig. 6-13. Shape of flow channel chosen for microvortex study and boundary condition applied in calculation.

Flow domain was uniformly discretized to assign same area in each element for fair comparison in the elemental force analysis. When flow field are solved without elemental force analysis, nodes are redistributed to increase the node density near the downstream lip corner by the feed slot. Galerkin's weighted residual method with finite element basis function was employed to solve Navier-Stokes equation system. Techniques used to obtain solution were same with that used in hybrid model study. Detailed information on the solution method can be found in section 6.3.3.

6.5.2. Elemental force analysis

When gravity is negligent, steady state Navier-Stokes equation is

$$\nabla \cdot [-\rho \mathbf{vv} - \mathbf{I}p + \mu(\nabla \mathbf{v} + \nabla \mathbf{v}^T)] = \mathbf{0} \qquad (6\text{-}36)$$

Since integration of Eq.(6-36) over any arbitrary control volume holds true, integration over computational element gives

$$\int_{Element} \nabla \cdot [-\rho \mathbf{vv} - \mathbf{I}p + \mu(\nabla \mathbf{v} + \nabla \mathbf{v}^T)] dV = \mathbf{0} \qquad (6\text{-}37)$$

After divergence theorem is applied, Eq. (6-37) becomes

$$\oint_{Element} \mathbf{n} \cdot [-\rho \mathbf{vv}] ds + \oint_{Element} \mathbf{n} \cdot [-\mathbf{I}p] ds + \oint_{Element} \mathbf{n} \cdot [\mu(\nabla \mathbf{v} + \nabla \mathbf{v}^T)] ds = \mathbf{0} \qquad (6\text{-}38)$$

Each term in Eq. (6-38) represents, respectively, net inertia force, net pressure force, and net viscous force applying on an element.

6.5.3. Pressure hill at the corner

The effect of Reynolds number on the behavior of microvortex is shown in Fig. 6-14 with streamlines of the flow and pressure contours in grey scale. The

microvortex appears in high Reynolds number condition. But it disappears as Reynolds number rises. What follows is the proposed explanation, which will be backed by elemental force analysis. The liquid issued from feed slot doesn't have x-directional momentum. When Reynolds number is low, i.e., the flow is viscous, the viscous shear stress induced at the moving-web surface not only moves the feed flow to x-direction but also penetrates into the feed slot. This penetrated viscous shear stress applies normal stress on the downstream wall of the feed slot and builds up pressure hill near the corner of the downstream feed slot.

Fig. 6-15 shows y-directional pressure gradient along the downstream wall of the feed slot. It shows that the pressure gradient is negative along the bottom wall of the feed slot for it should produce the Poiseuille flow of feeding and that pressure hill, or the area of positive pressure gradient near the top corner of the wall, increases as Reynolds number falls. Bigger pressure mountain causes bigger back flow along the wall, which becomes a part of microvortex. On the contrary, in high Reynolds number condition the microvortex diminishes or disappears. [Fig. 6-14 (b) and (c)]

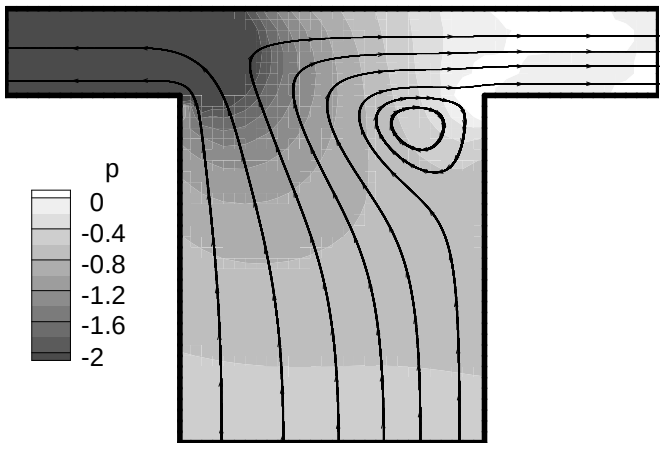

(a) N_{Re} = 0.001

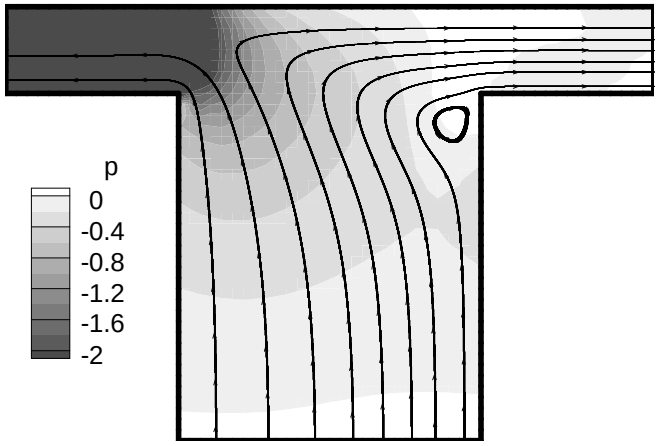

(b) N_{RE} = 8.6

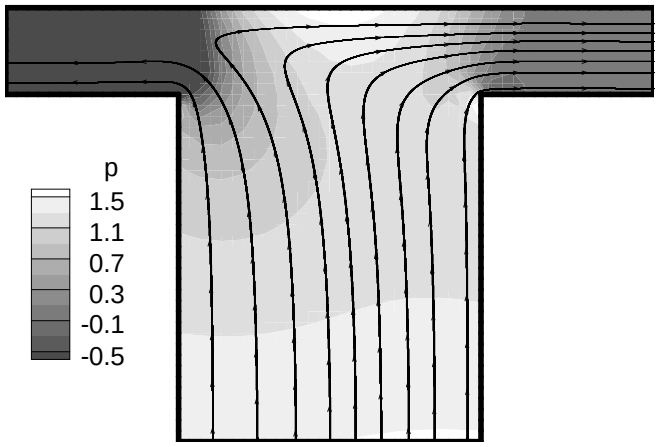

(c) N_{RE} = 22.5

Fig. 6-14 Effect of Reynolds number on the microvortex at the downstream corner of feed slot. Feed rate Q_f = 0.5 / VH. Unit of the pressure is [μV/H]. $N_{RE} \equiv \frac{H\rho V}{\mu}$.

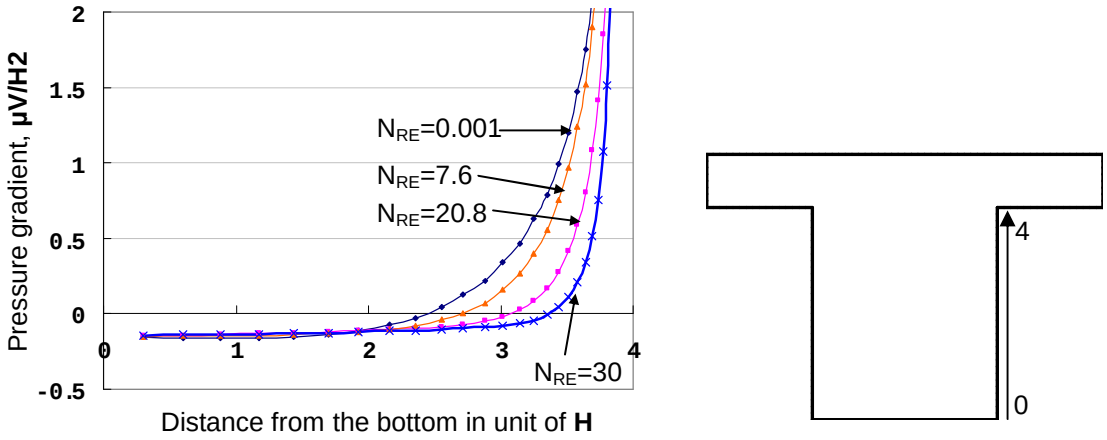

Fig. 6-15. Pressure gradient along the downstream wall of the feed slot. Feed rate Q_f = 0.5 / VH. Unit of the pressure is [μV/H].

The elemental force analysis gives evidences on the microvortex induced by shear stress penetration. Fig 6-16 shows contour plots of the x and y components of the elemental force vectors, obtained by integrating each terms in Eq. 6-38, in the flow field of low Reynolds number. The three forces in the Eq. 6-38 must balance each other. Since contribution of the inertia force to force balance is minor in low Reynolds number condition, as shown in Fig. 6-16(e) and (f), the pressure force and the viscous force counterbalance each other and take the mirror image of each other, i.e., their vector fields have same shape with opposite sign. As well as the grey scale, contour values are drawn by white solid lines for zero or positive contour values, and by white dotted line for negative contour values.

Positive value means the element receives net force in positive direction from the surrounding fluid. For example, the flow on the downstream lip in Fig. 6-16(a)

has mostly Couette flow. The rectangular element there receives positive viscous force at the top side and the same amount of negative viscous force at the bottom side. Therefore the net viscous force applied to an element on the downstream lip in Fig. 6-16(a) is almost zero. On the other hand, in the area above the feed slot and inside the feed slot denoted as shear stress penetration in fig. 6-16(a) the net x-directional viscous force applied to an element there is positive, which means the elements there receives more shear stress from the upper side than the amount it gives to the fluid below. The net x-directional viscous force applied in an element there is balanced by negative pressure force, which needs positive pressure gradient around the element. Since the negative x directional pressure force extends to the fluid near the downstream wall of the feed slot, positive pressure gradient in x direction forms from the shear stress penetration area to the downstream wall making pressure hill in the fluid near the downstream corner of the feed slot. Since the penetrated shear stress was originated by web movement, which is one of the primary sources of momentum in the given system, I concluded that the pressure hill near the downstream corner in the feed slot and the microvortex there is caused by the penetration of the viscous shear stress induced at the surface of moving web.

Fig. 6-17 shows same kinds of contour plots with Fig 6-16 for the high Reynolds number flow. Fig. 6-17(a) and (c) show that the penetration of the viscous shear stress into the feed slot is not so deep and that the pressure force near the downstream corner in the feed slot is very local. Since the three forces are in balance, it is not easy to see the interaction of the forces. Most of the x-momentum input from the viscous shear stress at the moving web seems to be supplied to fill up the x-directional inertia of the outflow in the high Reynolds condition.

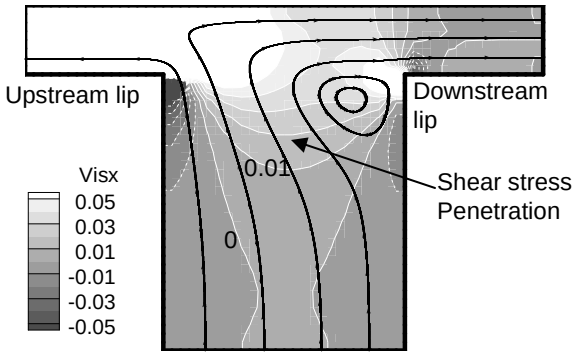

(a) Viscous force in x direction

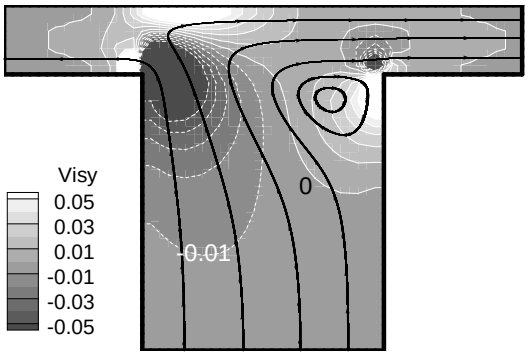

(b) Viscous force in y direction

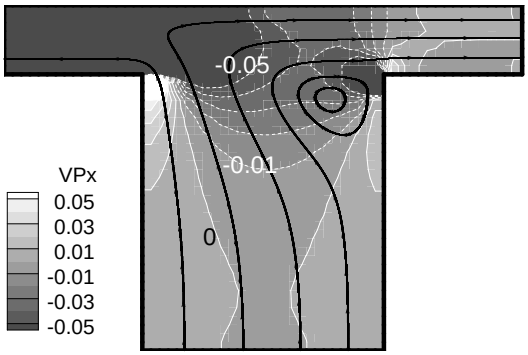

(c) Pressure force in x direction

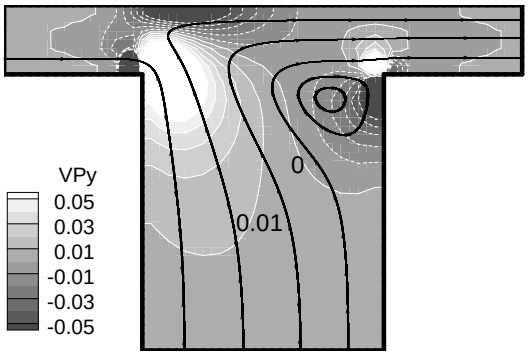

(d) Pressure force in y direction

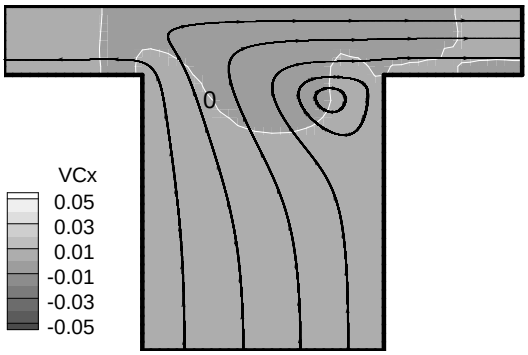

(e) Inertia force in x direction

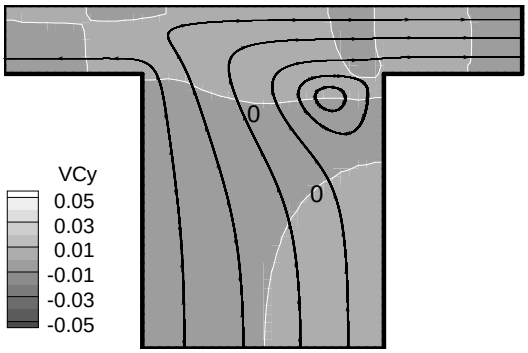

(f) Inertia force in y direction

Fig. 6-16. Contour plots of the x-directional and y-directional component of the net forces applied to the each computational element. N_{RE} = 0.001. Q_f = 0.5 / VH. Force unit is μV.

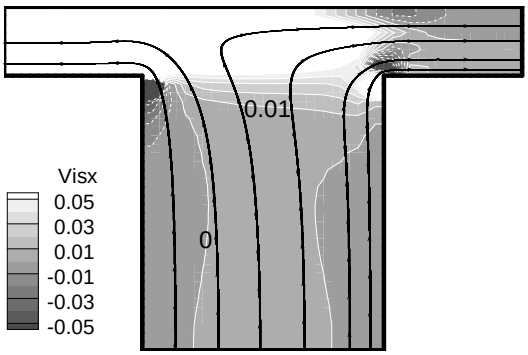

(a) Viscous force in x direction

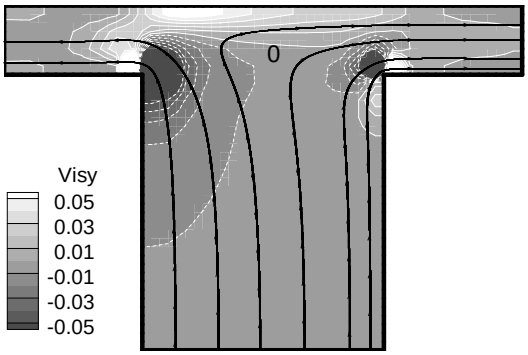

(b) Viscous force in y direction

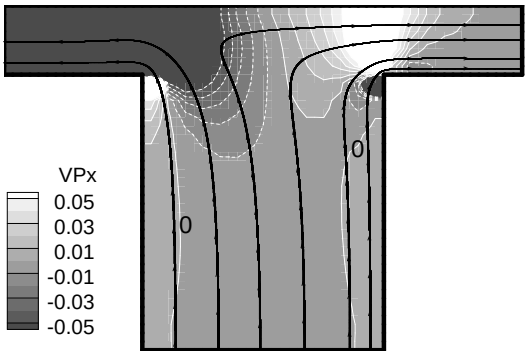

(c) Pressure force in x direction

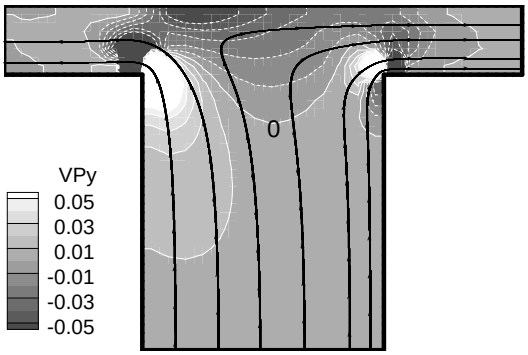

(d) Pressure force in y direction

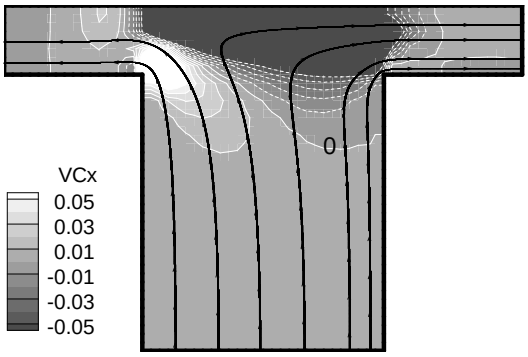

(e) Inertia force in x direction

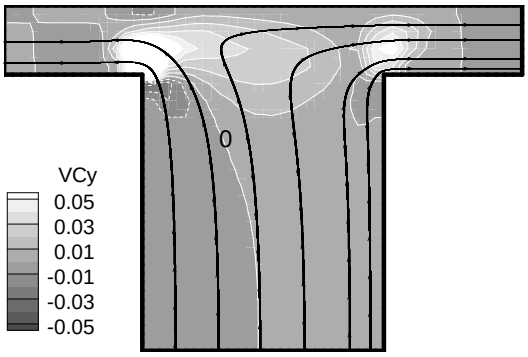

(f) Inertia force in y direction

Fig. 6-17. Contour plots of the x-directional and y-directional component of the net forces applied to the each computational element. N_{RE} = 22.5. Q_f = 0.5 / VH. Force unit is μV.

6.6. Conclusion

Separation line location and microvortex inside feed slot are important issues for successful two-layer coating in tensioned-web slot coating system. Previous researches on the double layer fixed-gap slot coating teach us to position the separation line on the downstream corner of mid-lip. Microvortex should be managed to be avoided or kept minimum as possible not to collect bubbles or foreign particles. Especially, fundamental configuration of the tensioned-web coating, thin coating gap, makes it susceptible to the microvortex.

The 1D/2D hybrid model study presented how the microvortex and the separation line react to the process parameters changes and showed how to control them. Through the study about the microvortex inside the feed, the explanation on the microvortex forming mechanism was suggested: the pressure hill at the corner seems to be made by the shear stress which is induced by the moving substrate and propagated by the viscous shear stress into the feed slot, provides adverse pressure gradient along the downstream wall of the feed slot, and causes backflow at the surface of the wall, which becomes important part of the microvortex. Elemental force analysis was performed to support the shear-stress-penetration explanation on the microvortex forming with flow channel designed similar to the fixed gap slot die. It gave us good evidence to the proposed mechanism.

Bibliography

BEGUIN, A. E. 1954 Method of coating strip material. U.S. Patent **2681294**.

BLOCK, H., VANROSSUM, J. J. 1953 The foil bearing – A new departure in hydrodynamic lubrication. *Lubrication Eng*. **9** 316.

CARVALHO, M. S. AND KHESHGI H. S. 2000 Low-flow limit in slot coating: Theory and experiment. *AIChE Journal* **46** 1907.

CHINO, N., HIRAKI, Y.,SATO T.,CHIKAMASA H. AND SHIBATA, N. 1988 Method of applying a liquid to a moving web. U.S. Patent **4717603**.

COHEN, D. 1993 *Two-layer Slot Coating: Flow Visualization and Modeling*. Master's thesis University of Minnesota.

DE ALMEIDA, V. 1995 *Gas-Liquid Counterflow through Constricted passages.* PhD thesis University of Minnesota. Published by University Microfilms International, Ann Arbor, MI.

ESHEL, A. AND ELROD, H. G. JR 1965 The theory of the infinitely wide, perfectly flexible, self-acting foil bearing. *Journal of Basic Engineering* **87** 831.

FENG, J. Q. 1998 Computational analysis of slot coating on a tensioned web. *AIChE Journal.* **44** 2137.

FLŰGG, W. 1973 Stresses in Shell. 2nd Edition Springer-Verlag, New York, USA.

GATE, I. D. 1999 *Slot Coating Flows: Feasibility, Quality.* PhD thesis University of Minnesota. Published by University Microfilms International, Ann Arbor, MI.

GILL, P. E., MURRAY, W. AND WRIGHT, M. H. 1981 Practical optimization. Academic Press Limited, London, U.K.

HIGGINS, B. G. AND SCRIVEN, L. E. 1981 Capillary pressure and viscous pressure drop set bounds on coating bead operability. *Chem. Eng. Sci.* **35** 673.

HIRAKI, Y., TAKAHASHI, S. AND CHINO, N. 1992 Apparatus for applying magnetic liquid to moving web. U.S. Patent **5083524.**

HOOD, P. 1976 Frontal solution program for unsymmetric matrices. *International Journal for Numerical Methods in Engineering* **20** 379-399.

KISTLER, S. F. 1983 *The fluid mechanics of curtain coating and related viscous free surface flows with contact lines.* PhD thesis University of Minnesota, Published by University Microfilms International, Ann Arbor, MI.

KISTLER, S., PALMQUIST, K., TOY, M. AND ULWELLING, W. 2000 Method and apparatus for coating plurality of wet layers on flexible elongated web. U.S. Patent **6033723**.

LACEY, C. 1992 Measurement and simulation of partial contact at the head/tape interface. *Journal of Tribology, ASME,* **114** 646.

Langlois, W. E. 1963 The lightly loaded foil bearing at zero angle of wrap. *IBM Journal of Research and Development* **7** 112-116

LANDAU, L. AND LEVICH, B. 1942 Dragging of a liquid by a moving plate. *Acta Physicochemica U.R.S.S* **XVII** 42.

LEE, H. 2001 Slot Coating Tensioned Web. Mater's thesis draft University of Minnesota.

LICHT, L 1968 An experimental study of elastohydrodynamic lubrication of foil bearings. Part 1-displacement in the central zone. *Journal of Lubrication Technology.* Jan. 199.

MATSUKAWA, J. AND ISHIKI, N. 1996 Coating apparatus. U.S. Patent **5534065**.

MUFTU, S. 2005, Mechanics of thin, flexible, translating media and their interactions with surrounding air. *JSME Journal* **48** 329

MUSSON, L. 2001 *Two-layer Slot Coating.* PhD thesis University of Minnesota, Published by University Microfilms International, Ann Arbor, MI.

PIPKIN, D. AND SCHAEFER, W. 1979 Method for applying a viscous fluid to a substrate. U.S. Patent **4142010**.

PRANCKH, F. R. 1989 *Elastohydrodynamics in coating flows*, PhD thesis University of Minnesota, Published by University Microfilms International, Ann Arbor, MI.

PRANCKH, F. R. AND COYLE, D. J. 1997 Elastohydrodynamic coating system. *Liquid*

Film Coating. Edited by Kistler, F. S. and Schweizer, P. M. Chapman & Hall, London, UK.

RENSHAW, A. A. 1999 An approximate analytical solution of the one-dimensional foil bearing problem. *Journal of Applied Mechanics* **66** 1028

RUSCHAK, K. J. 1976 Limiting flow in a pre-metered coating device. *Chemical Engineering Science* **31** 1057.

SARTOR, L.1990 *Slot Coating: Fluid Mechanics and Die Design.* PhD thesis University of Minnesota. Published by University Microfilms International, Ann Arbor, MI.

SARTOR, L., HUFF S. AND KISHI, C. 1998 Method for multiplayer coating using pressure gradient regulation. U.S. Patent **5728430**.

SCANLAN, D. J. 1990 *Two slot coater analysis: Inner layer separation issues in two-layer coating.* PhD thesis University of Minnesota. Published by University Microfilms International, Ann Arbor, MI.

SHIBATA, N. AND SATO, T. 1992 Coating method using an extrusion type coating apparatus. U.S. Patent **5108795**.

SHIBATA, N., TAKEDA, H., SATO, T. AND TANAKA, Y. 1987 Coating apparatus. U.S. Patent **4681062**.

SHIBATA, N., TAKEDA, H. AND SATO, T. 1990 Apparatus applying a liquid to a support. U.S. Patent **4907530**.

SILLIMAN, W. J. 1979 *Viscous film flows with contact lines: Finite element simulation, A basis for stability assessment and design optimization*. PhD thesis University of Minnesota. Published by University Microfilm International, Ann Arbor, MI.

SUN, S., MURRAY, C. B., WELLER D., FOLKS, L. AND MOSER, A. 2000 Monodisperse FePt nanoparticles and ferromagnetic FePt nanocrystal superlattices. *Science.* **28**7 1989.

TAKAHASHI, S. AND SHIBATA, N. 1992 Applicator device for applying thin liquids on carrier. U.S. Patent **5105760**.

TANAKA, Y., NODA, S. AND CHIKAMASA, H. 1984 Coating apparatus. U.S. Patent **4424762**.

TANAKA, Y. AND NODA, S. 1984 Coating apparatus. U.S. Patent **4480583**.

YOSHIDA, M. 1994 Extrusion type coater and coating method. U.S. Patent **5318804**.

TIMOSHENKO, S. 1940 Theory of Plate and Shells. 1st Ed. MaGraw-Hill Book Company, New York and London.

TOBISAWA, S., NAMIKI, T. AND KAWABE, S. 1991 Coating apparatus. U.S. Patent **5042422**.

TOMARU, M., SHIBATA, N. AND TAKAHASHI, S. 1997 Coating method application of a precoat solution in advance of coating composition. U.S. Patent **5677004**.

Appendix 2-A: Matching conditions in three-asymptotic-zone model.

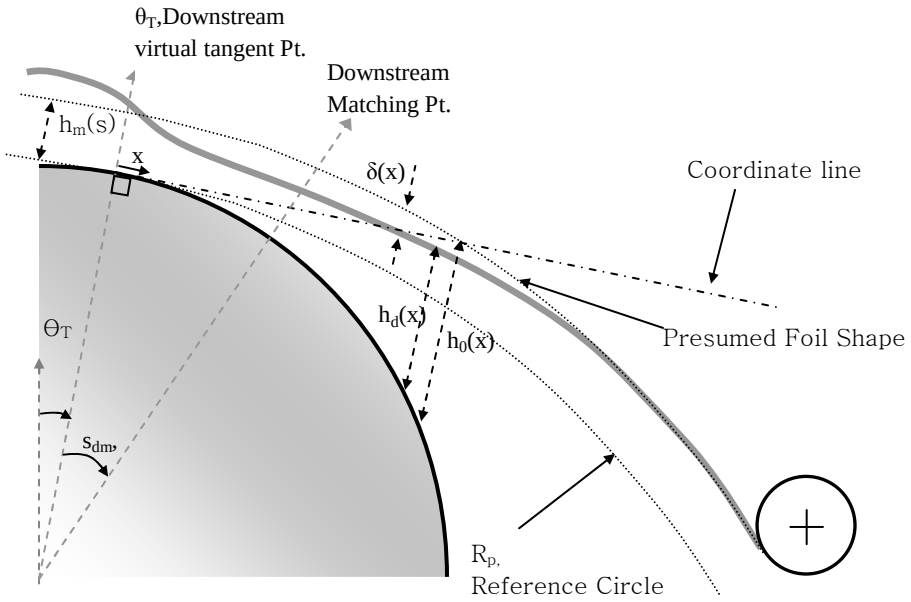

Uniform zone	:	Gap, h(s), is measured in radial direction.
Downstream zone	:	Gap is measured in perpendicular to the coordinate line.
Coordinate Line	:	On the tangent line sharing tangent point with reference circle

$\theta_T + s_{dm}$ is downstream matching position in radian. The x-coordinate on the downstream coordinate line is $x = Tan(s_{dm})$

1. Height Matching : Matching gap height in radial direction.

$$h_d(Tan(s_{dm})) = (h_{mid}(\theta_T + s_{dm}))Cos(s_{dm})$$

2. Slope Matching : Transforming into Cartesian coordinate system.

$$R(\theta) = R_0 + h_{mid}(\theta), \qquad \text{where} \quad \theta = \theta_T + s_{dm}$$

$$x = R(\theta)Sin(s_{dm})$$

$$y = R(\theta)Cos(s_{dm}) - (R_0)$$

$$\frac{dy}{dx} = \frac{\frac{dR}{d\theta}Cos(s_{dm}) - R(\theta)Sin(s_{dm})}{\frac{dR}{d\theta}Sin(s_{dm}) + R(\theta)Cos(s_{dm})}$$

3. Curvature Matching : Curvature doesn't change with coordinate change. Curvatures of polar coordinate and Cartesian coordinate were matched without transforming.